atmosphere

MDPI

Review

Green Leaf Volatiles in the Atmosphere—Properties, Transformation, and Significance

Kumar Sarang, Krzysztof J. Rudziński * and Rafał Szmigielski *

Institute of Physical Chemistry of the Polish Academy of Sciences, Kasprzaka Str. 44/52, 01-224 Warszawa, Poland; ksarang@ichf.edu.pl
* Correspondence: kjrudz@ichf.edu.pl (K.J.R.); ralf@ichf.edu.pl (R.S.)

Abstract: This review thoroughly covers the research on green leaf volatiles (GLV) in the context of atmospheric chemistry. It briefly takes on the GLV sources, in-plant synthesis, and emission inventory data. The discussion of properties includes GLV solubility in aqueous systems, Henry's constants, partition coefficients, and UV spectra. The mechanisms of gas-phase reactions of GLV with OH, NO_3, and Cl radicals, and O_3 are explained and accompanied by a catalog of products identified experimentally. The rate constants of gas-phase reactions are collected in tables with brief descriptions of corresponding experiments. A similar presentation covers the aqueous-phase reactions of GLV. The review of multiphase and heterogeneous transformations of GLV covers the smog-chamber experiments, products identified therein, along with their yields and the yields of secondary organic aerosols (SOA) formed, if any. The components of ambient SOA linked to GLV are briefly presented. This review recognized GLV as atmospheric trace compounds that reside primarily in the gas phase but did not exclude their transformation in atmospheric waters. GLV have a proven potential to be a source of SOA with a global burden of 0.6 to 1 Tg yr^{-1} (estimated jointly for (*Z*)-hexen-1-ol, (*Z*)-3-hexenal, and 2-methyl-3-buten-2-ol), 0.03 Tg yr^{-1} from switch grass cultivation for biofuels, and 0.05 Tg yr^{-1} from grass mowing.

Keywords: air quality; atmospheric chemistry; secondary organic aerosol; plant metabolites; emission inventory; rate constants; Henry's constants; UV spectra

Citation: Sarang, K.; Rudziński, K.J.; Szmigielski, R. Green Leaf Volatiles in the Atmosphere—Properties, Transformation, and Significance. *Atmosphere* **2021**, *12*, 1655. https://doi.org/10.3390/atmos12121655

Academic Editors: Joel F. de Brito and Michael Boy

Received: 21 October 2021
Accepted: 2 December 2021
Published: 9 December 2021

Contents

1. Introduction

Green leaf volatiles (GLV)—C_5 and C_6 aldehydes, alcohols, ketones, and esters—belong to inducible volatile organic compounds synthesized and emitted by green plants in response to mechanical wounding, herbivore attack, or abiotic stress [1–8]. They are synthesized rapidly via the lipoxygenase (LOX) pathway within minutes or seconds and can alert other plants fostering interplant communication [1,9]. Furthermore, they are responsible for the "green odor" of green leaves [10]. The first burst of volatiles often occurs when the leaves and stems are cut, followed by more intense and hours-long emissions from drying material [11]. Together with GLV, wounded plants emit methanol, acetaldehyde, acetone, butanone, and formaldehyde [12]. Plants also emit GLV upon the light-dark transition [13] and in high-light exposure [14].

The GLV include (*Z*)-3-hexenol, (*Z*)-3-hexenyl acetate, (*E*)-2-hexenal, (*Z*)-2-hexen-1-ol, (*Z*)-2-penten-1-ol and 1-penten-3-ol [12,13,15–20]. Jasmonic acid (JA), methyl jasmonate (MeJa), methyl salicylate (MeSa), and 2-methyl-3-butene-2-ol (MBO) also count as GLV [21,22]. However, they formally belong to other groups of plant volatiles [23,24]. Table 1 lists the compounds we included in this review as GLV (Table 1). Approximate yearly defense-initiated and cutting-drying emission of GLV in North America ranges from 1.5 to 2.6 Tg C yr^{-1} with estimated rates of 0.1 to 0.2 μg-C g^{-1} h^{-1} [25].

Table 1. Key Green Leaf Volatiles detected in plant emissions [a].

Name	Chemical Formula	MW g mol^{-1}	Structure	References
pentan-1-ol	$C_5H_{12}O$	88.15	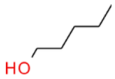	[9,26]
1-penten-3-ol	$C_5H_{10}O$	86.13		[9,16,18,26–30]
(*Z*)-2-penten-1-ol	$C_5H_{10}O$	86.13		[26,29–31]
(*E*)-2-pentenol	$C_5H_{10}O$	86.13	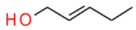	[28]
(*E*)-2-pentenal	C_5H_8O	84.12	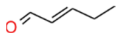	[28,30]
1-penten-3-one	C_5H_8O	84.12		[9,16,27–30]
(*Z*)-2-pentenyl acetate	$C_7H_{12}O_2$	128.17	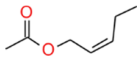	[31]
n-hexan-1-ol	$C_6H_{14}O$	102.16	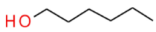	[16,26,28,32,33]
(*E*)-2-hexen-1-ol	$C_6H_{12}O$	100.16	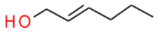	[26,28,32]
(*Z*)-2-hexen-1-ol	$C_6H_{12}O$	100.16	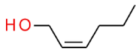	[18]
(*E*)-3-hexen-1-ol	$C_6H_{12}O$	100.16	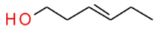	[28,32]

Table 1. *Cont.*

Name	Chemical Formula	MW g mol^{-1}	Structure	References
(*Z*)-3-hexen-1-ol (leaf alcohol)	$C_6H_{12}O$	100.16	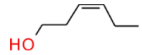	[9,10,12,13,16,18,26,28,31,32,34–37]
n-hexan-1-al	$C_6H_{12}O$	100.16	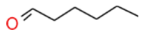	[3,18,26,28,30,32–34,36,38]
(*Z*)-3-hexen-1-al	$C_6H_{10}O$	98.14	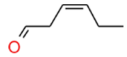	[9,12,13,18,26,28,32–34,37–39]
(*E*)-2-hexen-1-al (leaf aldehyde)	$C_6H_{10}O$	98.14	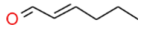	[9,10,18,26,28,31–33,35,36,38]
(*Z*)-2-hexenal	$C_6H_{10}O$	98.14		[16,28]
(*E*)-3-hexenal	$C_6H_{10}O$	98.14	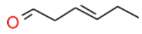	[28,32,37]
hexyl acetate	$C_8H_{16}O_2$	144.21	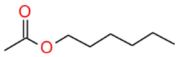	[33,37,40,41]
(*Z*)-2-hexenyl acetate	$C_8H_{14}O_2$	142.20	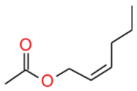	[18]
(*E*)-2-hexenyl acetate	$C_8H_{14}O_2$	142.20	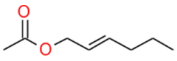	[28,37]
(*Z*)-3-hexenyl acetate (leaf acetate)	$C_8H_{14}O_2$	142.20	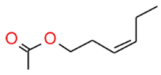	[12,13,16,18,26,28,31,32,34,37]
(*Z*)-3-hexenyl-propionate	$C_9H_{16}O_2$	156.22	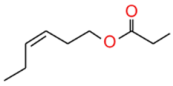	[28,30,42]
(*Z*)-3-hexenyl butanoate	$C_{10}H_{18}O_2$	170.25	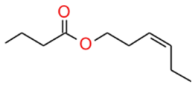	[30,37,40–43]
(*Z*)-3-hexenyl isobutanoate (isobutyrate)	$C_{10}H_{18}O_2$	170.25	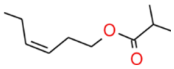	[30,40,42]
(*E*)-3-hexenyl butanoate	$C_{10}H_{18}O_2$	170.25	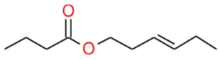	[41]
(*E*)-2-hexenyl butanoate	$C_{10}H_{18}O_2$	170.25	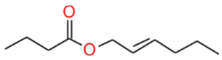	[37,42]
(*Z*)-3-hexenyl isopentanate	$C_{11}H_{20}O_2$	184.27	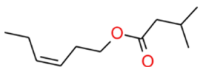	[40,42,44]
(*Z*)-3-hexenyl 2-methyl-2-butenoate	$C_{11}H_{18}O_2$	182.26	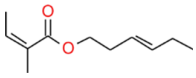	[40,42,44]
3-hexenyl hexanoate [b]	$C_{12}H_{22}O_2$	198.3	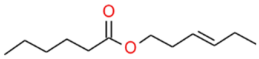	[41]
2-methy-3-buten-2-ol	$C_5H_{10}O$	86.13		[45–47]
1-octen-3-ol	$C_8H_{16}O$	128.21	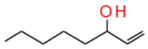	[18,28,48]
nonanal	$C_9H_{18}O$	142.24	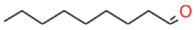	[44]
jasmonic acid	$C_{12}H_{18}O_3$	210.27	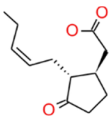	[26,39,49]
methyl jasmonate	$C_{13}H_{20}O_3$	224.30	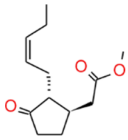	[26,49]

Table 1. *Cont.*

Name	Chemical Formula	MW g mol^{-1}	Structure	References
methyl salicylate	$C_8H_8O_3$	152.15	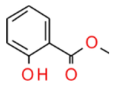	[7,30,40]

[a] for convenience of the audience, we used traditional GLV names rather than the latest IUPAC recommendations; [b] unspecified isomer.

The global annual emission of all BVOC reached 1087 Tg yr^{-1} estimated using the Community Land Model (CLM4) integrated with the MEGAN2.1 framework for estimating fluxes of biogenic compounds between terrestrial ecosystems and the atmosphere [50]. Isoprene was 535 Tg yr^{-1}, monoterpenes — 162 Tg yr^{-1}, and other compounds—390 Tg yr^{-1}. The modeling did not treat GLV as a separate group of compounds. It included some GLV in the stress VOC group (3-hexenal, 2-hexenal, 3-hexenol, 3-hexenyl acetate, hexanal, 1-hexenol, MeJa, and MeSa) and considered MBO individually. The emission of (*Z*)-3-hexenal was estimated as 4.9 Tg yr^{-1}, of (*Z*)-3-hexenol as 2.9 Tg yr^{-1}, and MBO as 2.2 Tg yr^{-1}. The annual emission of MBO calculated with MEGAN and averaged throughout 1980–2010 was 1.6 $\pm$ 0.1 Tg yr^{-1} [51].

Although the global emission of GLV is relatively small, the significance of local and seasonal emissions of GLV due to such events as harvests or grass mowing can be high for local air quality and SOA burden.

The emission budget of GLV can increase further if the GLV treatments become introduced to the world of agriculture, horticulture, and forestry. Prospective solutions are being investigated and discussed. Treatment of tomato with (*Z*)-3-hexenol prepared it for better defense against Tomato yellow leaf curl virus transmitted by whitefly [52]. Spraying with (*Z*)-3-hexenyl acetate reduced the salt stress in peanuts by a complex genetic mechanism increasing the photosynthetic rate, plant height, and shoot biomass [53]. Post-harvest fumigation of strawberries with (*E*)-2-hexenal and (*Z*)-3-hexenal decreased the mold infection rate [54]. Maize seedlings treated with physiological amounts of (*Z*)-3-hexenyl acetate showed less damage from cold stress and increased growth compared to untreated seedlings [55]. (*Z*)-3-hexenyl butyrate successfully modified the pre-harvest ripening of grapes [56].

Once in the atmosphere, GLV immediately encounter several reactants like OH and NO_3 radicals or O_3, which are ready to interact with unsaturated carbonyl compounds and contribute to the formation of secondary organic aerosols (SOAs) [57,58].

The modeling, which is the only way to estimate the global production and burden of SOA, provides mixed results. The intercomparison of 31 global chemistry-transport and general circulation models showed that the global annual output of SOAs varied from 13 to 121 Tg yr^{-1}, with a median value of 19 Tg yr^{-1} [59]. For the models which considered the semi-volatile character of SOAs, the global annual output of the SOAs varied from 16 to 121 Tg yr^{-1} with a much higher median of 51 Tg yr^{-1}. The STOCHEM model predicted 46.4 Tg yr^{-1} of SOAs, formed globally from sesquiterpenes (29 Tg yr^{-1}) and monoterpenes (162 Tg yr^{-1}) [60]. The corresponding SOA burden was 0.45 Tg. Approximately 0.010 Tg (2%) originated from isoprene, 0.188 Tg (44%) from monoterpenes, 0.187 Tg (41%) from both monoterpenes and sesquiterpenes, and 0.041 Tg (10%) from sesquiterpenes alone. Those results are consistent with GEOS-CHEM modeling based on the volatility basis set, which predicted 36.2 Tg yr^{-1} and 0.88 Tg of SOAs, including 21.5 Tg yr^{-1} and 0.53 Tg of biogenic SOA; as well as 14.7 Tg yr^{-1} and 0.35 Tg of anthropogenic and biomass burning SOAs [61]. The SOA production increased when modeling covered: the semi- and intermediately volatile OC; new SOA yields from chamber experiments; wet and dry deposition of organic vapors; and the photolytic and heterogeneous loss of SOAs. The new production of 132.2 Tg yr^{-1} included 8.8 Tg yr^{-1} from anthropogenic and biomass burning emissions, 97.5 Tg yr^{-1} from biogenic emissions, and 25.9 Tg yr^{-1} from semi- and intermediately volatile OC emissions. However, the SOA burdens have not changed and included 0.08,

0.59, and 0.21 Tg, respectively. Gas-phase processing of isoprene alone was estimated to contribute 6–30 Tg yr^{-1} of SOAs [62] with an additional 2 Tg yr^{-1} from aqueous-phase processing [63]. The CESM model with CAM5.3 and CLM4 components predicted 55.7 Tg yr^{-1} of isoprene SOA (1.07 Tg burden) for climate and emission conditions of 2000 [64]. Against all the quantities mentioned above, a less formal prediction of 1–5 Tg C yr^{-1} of SOA produced from GLV [65] seems overestimated and needs re-evaluation.

Major reviews published in the last decade provide little information on a GLV role in atmospheric chemistry and SOA formation. A special issue of Trends in Plant Science ("Induced plant volatiles: from genes to climate change") [66] discussed the BVOC emissions and their general relations with the environment with a focus on emissions [8,67,68]. The review on molecular identification of organic compounds in the atmosphere [69] mentioned the possibility of SOA formation from GLV based on four references. The extensive evaluation of the tropospheric aqueous-phase chemistry [70] included the rate constants for the aqueous-phase reactions with a few GLV, based on one work. The review on the atmospheric chemistry of oxygenated volatile compounds [71] provided the lifetimes of a few GLV due to the gas-phase reactions with OH, based on one reference. The opinion piece on plant-derived secondary organic material in the air [72] mentioned GLV as SOA precursors but did not go into any details.

The purpose of this review is to provide a practical background framework for designing future research on the role of GLV in atmospheric processes and specifically in the formation of SOAs.

2. Sources of GLV

2.1. Reasons or Causes of Emission

Plants release GLV when attacked by animals, insects, and microbes or exposed to abiotic stress or mechanical wounding [16,27,35,43,48,73,74]. For instance, trees and shrubs emitted (*E*)-2-hexenal upon wounding and in response to bacterial pathogenesis [6]. Emissions of *Pinus sylvestris* saplings infected with large pine aphid (*Cinara pinea* Mordviko) contained methyl salicylate and (*Z*)-3-hexenyl acetate [75]. Plants infected with pathogens probably emit methyl salicylate to activate disease resistance in neighboring plants and healthy tissues of the emitting plant [7]. Blande et al. [44] detected significant emission of MeSa from *Betula pendula* and *Alnus glutinosa* trees infested with *Euceraphis betulae* (Koch.) or *Pterocallis alni* (De Geer) aphids. The emission of volatiles depended quantitatively on the stress dose for both abiotic and biotic stressors [76].

Plants stimulated with GLV rapidly produced jasmonic acid (JA) and emitted anti-herbivore volatiles [34]. Plants pre-treated with GLV had more JA and sesquiterpenes when attacked by herbivores. The released GLV can inform the neighboring plant ecosystem of possible danger and prompt it to prepare its defense [4–6,34,77]. Experiments showed that intact undamaged corn seedlings produced JA and emitted sesquiterpenes when treated with GLV [34]. The GLV-primed defense initially suppresses the growth of plants, but after a few days, the growth significantly increases [78].

GLV can attract carnivores or parasitoids of herbivores that attack plants [79]. For instance, (*Z*)-3-hexenal attracted a chalcidoic wasp *Encarsia formosa*, a natural parasitoid of whitefly *Bemisia tabaci*, a herbivore pest of tomato plants [80]. Products of GLV reactions with ozone in the atmosphere also attract predators [81].

GLV emitted by plant seedlings can decrease their acceptability by herbivores (e.g., snails) [82]. Zhang et al. [41] showed that *Ips typographus* antennae responded strongly to green leaf alcohols (*Z*)-3-hexen-1-ol, 1-hexanol, and (*E*)-2-hexen-1-ol emitted by non-host plants such as *Betula pendula*, *B. pubescens*, and *Populus tremula*. Thus, the purpose of emission may be to direct the host-searching insect away.

(*Z*)-3-hexenyl butyrate controls the stomata closure to regulate CO_2 and water vapor transfer under abiotic stress like drought [56].

(*Z*)-3-hexenol, (*Z*)-3-hexenal, and (*Z*)-3-hexenyl acetate were also emitted by velvet mosquito plants upon the light-dark transition, probably due to the dark activation of 13-lipoxygenase enzymes in chloroplasts [13].

2.2. Synthesis in Plants

The GLV listed in Table 1 differ in the pathways by which they are synthesized [23,83]. Compounds traditionally considered to be GLV—C_6 aldehydes, alcohols, ketones, and esters, along with C_5 compounds and MeJa—are produced via the LOX pathway. MBO is a hemiterpene synthesized by the mevalonate or DMAPP pathway [24]. MeSa is an aromatic compound synthesized by the shikimic acid pathway [23]. (*Z*)-3-hexenyl-propionate, (*Z*)-3-hexenyl butyrate, and (*Z*)-3-hexenyl isobutyrate are esters probably synthesized from (*Z*)-3-hexenol by AAT [30,74].

The LOX pathway converts free fatty acids (linolenic, hexadecatrienoic, and linoleic acid) into C_6 GLV. Scheme 1 shows the reactions for linolenic acid [1,20,35,73,84]. This acid is oxidized to 13-hydroperoxodecatrienoic acid by molecular oxygen at position 13 in a reaction catalyzed by a non-heme iron-containing enzyme lipoxygenase (13-LOX). Then, hydroperoxyl lyase (HPL) converts the hydroperoxo acid into C_6 aldehyde (*Z*)-3-hexanal and a C12 oxo acid (*Z*)-9-traumatin. The aldehyde is converted to (*Z*)-3-hexenol by alcohol dehydrogenase (ADH). The latter is converted to (*Z*)-3-hexenyl acetate by alcohol acyltransferase (AAT). In an alternative pathway, isomerase converts (*Z*)-3-hexanal to (*E*)-2-hexanal. The ADH enzyme converts the latter isomer to (*E*)-2 hexenol, which in turn is converted to (*E*)-2-hexenyl acetate by AAT. Hexadecatrienoic acid follows a similar pathway, including (*Z*)-7-dinortraumatin as a counterpart to oxo acid (not shown here).

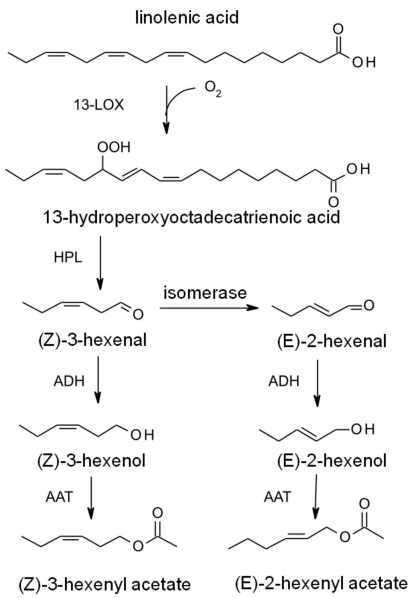

Scheme 1. Conversion of linoleic acid into hexenals, hexenols, and hexenyl acetates [84].

Interestingly, hexenals can also form directly from membrane lipids, without their conversion to fatty acids by lipase [1,85]. Linoleic acid follows a path similar to Scheme 1 with hexanal and hexanol produced (not shown here).

Scheme 2 explains the formation of C_5 GLV from 13-hydroperoxodecatrienoic acid [9]. First, lipoxygenase abstracts the OH group from OOH. The radical formed undergoes C_5–C_{13} β-scission to give 1-penten-3-ol. The latter is converted to 1-penten-3-one by ADH.

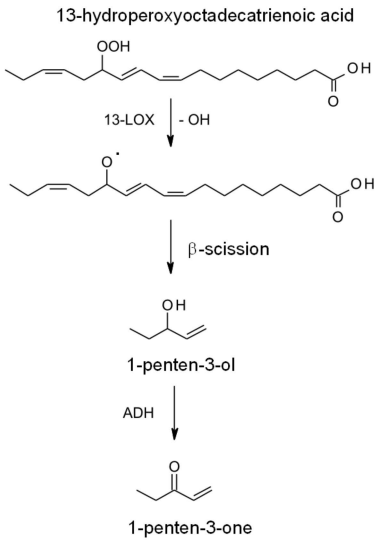

Scheme 2. Formation pathway of C_5 GLV [9].

13-hydroperoxodecatrienoic acid is also a precursor of JA and MeJa (Scheme 3) [9,32,49]. First, it is converted to alkene oxide by allene oxide synthase (AOS). Then, the oxide is cyclized to 12-oxophytodienoic acid by allene oxide cyclase (AOC). Finally, that acid is reduced and β-oxidized three times to give JA.

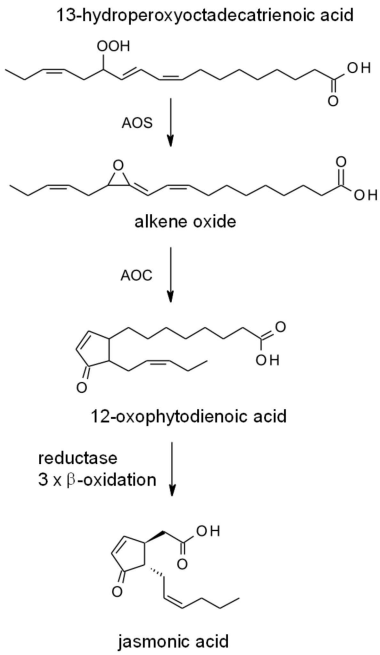

Scheme 3. Formation pathway of jasmonic acid [32].

2.3. Emission Data

The variety and quantity of emitted GLV vary between plant species [84]. The emission rates range from values below the detection limits to 100 μg g^{-1} fresh weight. The fraction of some components increased with the total amount of emitted GLV, without any general patterns. Table 2 collects emission values and emission rates of GLV and their mixtures measured in the field and laboratory experiments. Emission measures were a GLV mass per mass of leaves or plant material, dry or fresh, or a GLV mass per land area. Quantities that refer to the leaf area are used in quantifying the VOC emission from living vegetation and modeling atmospheric chemistry and aerosol formation. Values referring to the mass

of plant material help describe events like harvesting or grass mowing and compare VOC emission between species. Table 3 shows ambient concentrations of GLV and headspace concentrations measured in laboratory or field chambers.

Table 2. Emission and emission rates of atmospherically relevant GLV.

GLV	Emission or Emission Rate
pentan-1-ol	• 0.2 and 8.8 ng g DW^{-1} h^{-1} rape and blossoming rye, resp. (field enclosure) [86] [a]; 7.15 ± 0.46 pmol m^{-2} s^{-1} *L. pulmonaria* thalii: (intact); 18.4 ± 0.6, 28.0 ± 3.7, 56.3 ± 7.8 pmol m^{-2} s^{-1} after heat shock of 37, 46, and 51 °C, resp.; 68.6 ± 13.9 pmol m^{-2} s^{-1} (wounded) [87].
1-penten-3-ol	• 0.2 kg C ha^{-1} yr^{-1} switchgrass plantations (growth and harvest); 18 ± 9 ng g DW^{-1} h^{-1} (6 ± 3 pmol m^{-2} s^{-1}) mean before cutting; 91 ± 114 ng g DW^{-1} h^{-1} (31 ± 39 pmol m^{-2} s^{-1}) max after cutting; 48 ± 22 ng g DW^{-1} h^{-1} (17 ± 17 pmol m^{-2} s^{-1}) mean after cutting (including isoprene) [b] [88]. • 0.2, 0.3, 1.2 nmol m^{-2} s^{-1} *Couepia longipendula Pilg.* (detached leaves over Amazon Forest canopy, February, peak values at 7:30, 12:40, 16:40, resp.) [16]; • 17.4, 22.0, 4.8, 5.9, 1.9, and 37.7 ng g DW^{-1} h^{-1} rape, blossoming rape, rye, blossoming rye, grassland, and grassland after mowing, resp. (in a field enclosure) [86].
(*E*)-2-penten-1-ol	• 0.2 and 1.9 ng g DW^{-1} h^{-1} rape and blossoming rye (in a field enclosure) [86].
3-pentanone	• 0.2, 0.5, 2 nmol m^{-2} s^{-1} *Couepia longipendula Pilg.* (detached leaves over Amazon Forest canopy, February, peak values at 7:30, 12:40, 16:40, resp.) [16].
1-hexanol	• (3.5 ± 4.0), (18.2 ± 4.9), (0.5 ± 1.1) ng g DM^{-1} *Betula pendula*, *B. pubescens*, *Populus tremula*, resp. (dry leaves, June) [41]. • < 0.3 and 2.3 pmol m^{-2} s^{-1} Bel-W3 tobacco, before and after exposure to O_3 in a lab reactor [89]. • 0.1, 0.2, 0.3 nmol m^{-2} s^{-1} *Couepia longipendula Pilg.* (detached leaves over Amazon Forest canopy, February, peak values at 7:30, 12:40, 16:40, resp.) [16]. • 0.27 ± 0.04 pmol m^{-2} s^{-1} *L. pulmonaria* thalli: (intact); 0.27 ± 0.6, 0.33 ± 0.03, 0.52 ± 0.06 pmol m^{-2} s^{-1} after heat shock of 37, 46, and 51 °C, resp.; 0.46 ± 0.05 pmol m^{-2} s^{-1} (wounded) [87]. • 58.2 and 31.1 ng g DW^{-1} h^{-1} rye and blossoming rye (in a field enclosure) [86]. • 1.13 ± 1.13 ng g DW^{-1} h^{-1} *Betula pendula* [44]. • 0.6, 0.3 µg C g DW^{-1} h^{-1} rabbit brush, *Metasequoia glyptostroboides* (cut branches) [90]. • (0.4 ± 0.4)–(0.5 ± 0.5) ng g DW^{-1} h^{-1} *Pinus sylvestris* (various seedlings) [91].
(*E*)-2-hexen-1-ol	• (4.6 ± 1.4 | 1.3 ± 1.0), (4.2 ± 1.8 | 1.3 ± 1.0), (1.5 ± 1.0 | 0.6 ± 0.5), (- |1.0 ± 0.8) ng g $DW^{-1,}$ (June | August) *Betula pendula*, *B. pubescens*, *Populus tremula*, and *Sambucus nigra*, resp. (dry leaves) [41]. • 0.1–1.2 µg C g DW^{-1} h^{-1} various trees (cut branches) [90].
(*Z*)-3-hexen-1-ol	• 1.21 ± 0.06 µg m^{-2} mowed lawn [92]. • 9.6 and 163 pmol m^{-2} s^{-1} Bel-W3 tobacco, before and after exposure to O_3 in a lab reactor [89]. • 0.10 ± 0.03, 0.039 ± 0.006 pmol m^{-2} s^{-1} intact apple and grape foliage day mean, resp. [93]. • (108 ± 53), (2736 ± 546) ng/30 min from caterpillar-infested corn plant and its cut leaves, resp. (in a chamber) [34]. • 0.1, 0.3, 0.7 nmol m^{-2} s^{-1} *Couepia longipendula Pilg.* (detached leaves over Amazon Forest canopy, February, peak values at 7:30, 12:40, 16:40, resp.) [16]. • (3.4 ± 6.7), (30 ± 46) µg m^{-2} h^{-1} (1992), (1993), resp., from a test grassland in Argonne June–August average at variable locations, noon, sunny days [94]. • (0.85 ± 2.2), (54 ± 110) µg m^{-2} h^{-1} (1992), (1993), resp., from a test grassland in Argonne June-August average at fixed location, noon, sunny days [94]. • (29.0, 2.4), 20.1, 20.3, 33.9, 11.8, 0.5, 31.5, 48.4, 6.8, (0.8, 6.1, 7.5) and 23.6 ng g DW^{-1} h^{-1} (grape with fruits), rape, blossoming rape, rye, blossoming rye, beech, hornbeam, birch, oak, (grassland), grassland after mowing, resp. (in a field enclosure) [86]. • 0.2, 0.2, 0.06, 0.03, 0.05, 0.2, 0.07, 0.1, 0.06, 0.8, 1.3, 0.3, 0.3, 0.3, and 0.5 µg g DW^{-1} h^{-1} alfalfa, almond, apricot, bean, cotton, grape, nectarine, olive, orange, peach, pistachio, plum, walnut, valley oak, and whitehorn, resp. (in flow-through field enclosures) [95]. • 380 ± 180 ng μL^{-1} $(24\ h)^{-1}$ brussels sprout leaves infested by caterpillars [77].

Table 2. *Cont.*

GLV	Emission or Emission Rate
(*Z*)-3-hexen-1-ol	• 0, (2.5 ± 0.9) ng g DW^{-1} h^{-1} from intact and moth-damaged cabbage, resp. [81]. • 0.6 ± 0.1 µg g^{-1} h^{-1} cut sugarcane in a chamber [48]. • (55.5 ± 14.6 | 26.1 ± 20.1), (202 ± 68 | 62.7 ± 34.5), (8.8 ± 3.8 | -); (9.0 ± 15.2 | -) ng g DW^{-1} (June | August), *Betula pendula*, *B. pubescens*, *Populus tremula*, *Sambucus nigra*, resp., (dry leaves) [41]. • (247.08 ± 172.86)/(27.18 ± 6.67/16.95 ±6.97)/(218.05 ± 110.23) ng gDW^{-1} h^{-1} *Betula pendula* (control/aphid infested for 10 days/aphids removed/washed; resp.) [44]. • (43.22 ± 14.97) / (190.16 ± 47.64) ng g DW^{-1} h^{-1} *Betula pendula* (control/aphid infested for 21 days) [44]; • (14.42 ± 4.63) / (57.58 ± 31.53) ng g DW^{-1} h^{-1} *Alnus glutinosa* (control/aphid infested for 21 days) [44]. • 0.1–13.9 µgC g DW^{-1} h^{-1} various trees (cut branches) [90]. • 2.29–7.7 ng g $(foliage)^{-1}$ h^{-1} five tree species [40].
(*Z*)-3-hexenol + (*E*)-3-hexenol + (*E*)-2-hexenol	• 0.1 kg C ha^{-1} yr^{-1} from switchgrass plantations (growth and harvest); 6 ± 3 ng g DW^{-1} h^{-1} (1 ± 0.5 pmol m^{-2} s^{-1}) before cutting; 466 ± 144 ng g DW^{-1} h^{-1} (133 ± 35 pmol m^{-2} s^{-1}) after cutting; 149 ± 14 ng g DW^{-1} h^{-1} (42 ± 4 pmol m^{-2} s^{-1}) mean [88].
Hexanal	• 7.3, (25.3, 2.1), 10.4, 26.9, 19.2, 7.3, (6.4, 4.8), 6.3, 22.2, 13.6, (1.0, 3.1, 2.1), and 4.6 ng g DW^{-1} h^{-1} grape, (grape with fruits), rape, blossoming rape, rye, blossoming rye, (beech), hornbeam, birch, oak, (grassland), grassland after mowing, resp. (in a field enclosure) [86]. • 2 and 5 nmol g^{-1} fresh weight of intact and homogenized cucumber leaves [38]. • 4.7 ± 5.3, 1.3 ± 3.0 ng g^{-1} *Betula pendula*, *B. pubescens* (dry leaves), June [41]. • 0.6, 0.1 µgC g DW^{-1} h^{-1} rabbit brush, *Populus tremuloides* (cut branches) [90].
(*Z*)-2-hexenal	• 4.25 ± 0.64 pmol m^{-2} s^{-1} *L. pulmonaria* thalli (intact); 7.19 ± 1.98, 6.61 ± 0.16, 10.0 ± 1.9 pmol m^{-2} s^{-1} after heat shock of 37, 46, and 51 °C, resp.; 8.84 ± 1.31 pmol m^{-2} s^{-1} (wounded) [87] [b]. • 0.2, 0.3, 0.5 nmol m^{-2} s^{-1} *Couepia longipendula Pilg.* (detached leaves over Amazon Forest canopy, February, peak values at 7:30, 12:40, 16:40, resp.) [16].
(*E*)-2-hexen-1-al	• 8.6 nmol m^{-2} s^{-1} mountain grassland, cut [96]. • <0.4 and 9.8 pmol m^{-2} s^{-1} Bel-W3 tobacco, before and after exposure to O_3 in a lab reactor [89]. • 8.7, 0.8, 8.9 ng g DW^{-1} h^{-1} oak, grassland, and grassland after mowing (in a field enclosure) [86]. • 40, 5 nmol m^{-2} s^{-1} from Phragmite leaves exposed to 45 °C in normal and O_2-deprived atmosphere; 5, 6.8 nmol m^{-2} s^{-1} from Phragmite leaves and from Arabidopsis NPQ1 plants exposed to high light, resp. [14]. • 8, 28 nmol g^{-1} fresh weight of intact and homogenized cucumber leaves [38]. • (8.6 ± 11.1) / (0.7 ± 1.4) ng g DW^{-1} *Betula pendula* dry leaves, June/August [41].
(*Z*)-3-hexen-1-al	• 0.5 mg C g^{-1} of drying aspen leaves [33]. • 50 µgC g^{-1} h^{-1} cut and drying *Festuca rubra* (red fescue) [45]. • 1.6 and 49.3 pmol m^{-2} s^{-1} Bel-W3 tobacco, before and after exposure to O_3 in a lab reactor [89]. • 356 ± 95, 4872 ± 633 ng/30 min from caterpillar-infested corn plant and its cut leaves, resp. (in a chamber) [34]. • 2500 nmol g^{-1} fresh weight of homogenized Arabidopsis leaves [39]. • 25, 41 nmol g^{-1} fresh weight of intact and homogenized cucumber leaves, resp. [38].
(*Z*)-3-hexenal + (*E*)-2-hexenal	• 0.2 kg C ha^{-1} yr^{-1} from switchgrass plantations (growth and harvest); 4 ± 6 ng g DW^{-1} h^{-1} (0.6 ± 2 pmol m^{-2} s^{-1}) mean before cutting; 2666 ± 4787 ng g DW^{-1} h^{-1} (731 ± 1315 pmol m^{-2} s^{-1}) max after cutting; 486 ± 903 ng g DW^{-1} h^{-1} (133 ± 247 pmol m^{-2} s^{-1}) mean after cutting [88].
Hexyl acetate	• (14.4 ± 4.0 | 2.3 ± 4.5), (47.4 ± 13.6 | 13.9 ± 6.7) ng g DM^{-1} (June | August), *Betula pendula*, *B. pubescens*, resp. (dry leaves) [41]. • 0.43–3.16 ng g $(foliage)^{-1}$ h^{-1} five tree species [40].

Table 2. *Cont.*

GLV	Emission or Emission Rate
(*Z*)-3-hexenyl acetate	• 8.66 ± 0.08 µg m^{-2} mowed lawn [92]. • <0.3 and 39.6 pmol m^{-2} s^{-1} Bel-W3 tobacco, before and after exposure to O_3 in a lab reactor [89]. • 0.21 ± 0.06, 0.27 ± 0.02 pmol m^{-2} s^{-1} intact apple and grape foliage day mean, resp. [93]. • 595 ± 569, 3720 ± 1052 ng/30 min from caterpillar-infested corn plant and its cut leaves, resp. (in a chamber) [34]. • 0.1, 0.2, 2 nmol m^{-2} s^{-1} *Couepia longipendula Pilg.* (detached leaves over Amazon Forest canopy, February, peak values at 7:30, 12:40, 16:40, resp.) [16]. • 10.9, (114.1, 9.4), 37.5, 117.3, 11.1, (3.4, 4.1), 50.9, 95.0, 5.4, (1.8, 13.8, 13.1), and 29.6 ng g DW^{-1} h^{-1} grape, (grape with fruits), rape, blossoming rape, blossoming rye, (beech), hornbeam, birch, oak, (grassland), grassland after mowing, resp. (in a field enclosure) [86]. • 0.7, 1.9, 1.1, 0.4, ≤ 0.2, (0.8, 0.5), 0.1, 0.6, 0.2, 0.06, 3.4, 1.6, 0.4, 0.3, 0.2, and 3.3 µg g DW^{-1} h^{-1} alfalfa, almond, apricot, cherry, cotton (grape), lemon, nectarine, olive, orange, peach, plum, sorghum, walnut, valley oak, and whitehorn, resp. (in flow-through field enclosures) [95]. • 3608 ± 2076, 490 ± 220, 340 ± 200 ng μL^{-1} $(24\ h)^{-1}$ brussel sprout leaves infested by caterpillars, non-infested artificially damaged leaves from the infested plant, and undamaged leaves, resp. [77]. • 0, 8.4 ± 3.8 ng g DW^{-1} hr^{-1} from intact and moth-damaged cabbage, resp. [81]. • 1.22 ± 0.18 µg g^{-1} hr^{-1} cut sugarcane in a chamber [48]. • 7.35 ± 1.02 pmol m^{-2} s^{-1} *L. pulmonaria* thalli (intact); 7.36 ± 1.41, 12.1 ± 1.1, 17.5 ± 2.5 pmol m^{-2} s^{-1} after heat shock: 37 °C, 46 °C, 51 °C; 20.5 ± 1.4 pmol m^{-2} s^{-1} (wounded) [87]. • (130 ± 42.8/44.4 ± 40.0), (501 ± 246 / 26.4 ± 16.3), (67.6 ± 18.6/-), (14.3 ± 6.0/-ng) g DW^{-1} *Betula pendula*, *Populus tremula*, *B. pubescens*, *Sambucus nigra*, resp. (dry leaves), June/August [41]. • (41.18 ± 20.87)/(8.96 ± 1.61)/(6.90 ± 2.38)/(34.89 ± 13.66) ng g DW^{-1} h^{-1} *Betula pendula* (control/aphid infested for 10 days/aphids removed/washed) [44]. • (15.99 ± 5.08)/(62.38 ± 16.54) ng g DW^{-1} h^{-1} *Betula pendula* (control/aphid infested for 21 days) [44]. • (21.44 ± 6.11)/(43.91 ± 20.52) ng g DW^{-1} h^{-1} *Alnus glutinosa* (control/aphid infested for 21 days) [44]. • 0.3–19 µgC g DW^{-1} h^{-1} various trees (cut branches) [90]. • 6.28–71.39 ng g $(foliage)^{-1}$ h^{-1} five tree species [40]. • (75.5 ± 5.7) − (178.1 ± 31.3) ng g DW^{-1} h^{-1} *Pinus sylvestris* (various seedlings) [91].
(*E*)-2-hexenyl acetate	• (4.0 ± 2.1 / 0.4 ± 0.8); (38.7 ± 22.2/-) ng g^{-1} *Betula pendula*, *B. pubescens*, resp. (dry leaves), June/August [41]. • 0.1, 0.2 µg C h^{-1} g DW^{-1} ironwood (Accacia), slippery elm (Ulmus), resp. [90]. • 0.12 ± 0.07, 0.35 ± 0.17 ng g $(foliage)^{-1}$ h^{-1} blue ash, white fingertree [40].
(*Z*)-3-Hexenyl acetate + (*E*)-2-hexenyl acetate	• 3 ± 2 ng g DW^{-1} h^{-1} (0.5 ± 0.3 pmol m^{-2} s^{-1}) switchgrass, before cutting; 35 ± 50 ng g DW^{-1} h^{-1} (6 ± 8 pmol m^{-2} s^{-1}) after cutting; 13 ± 18 ng g DW^{-1} h^{-1} (2 ± 3 pmol m^{-2} s^{-1}) mean [88].
(*Z*)-3-hexenyl butanoate (butyrate)	• 0.0306 ± 0.0008 pmol m^{-2} s^{-1} intact apple foliage day mean [93]. • (-∣ 20.8 ± 10.1), (0.7 ± 1.1 ∣ -) ng g DW^{-1} (June ∣ August), *Betula pubescens*, *Populus tremula*, resp. (dry leaves) [41]. • (12.84 ± 8.86)/(0.48 ± 0.32)/(0.37 ± 0.37)/(4.45 ± 1.71) ng g DW^{-1} h^{-1} *Betula pendula* (control/aphid infested for 10 days/aphids removed/washed) [44]. • (0.19 ± 0.19)/(2.42 ± 1.04) ng g DW^{-1} h^{-1} *Betula pendula* (control/aphid infested for 21 days) [44]. • 0.2–5.2 µg C g DW^{-1} h^{-1} various trees (cut branches) [90]. • (0.9 ± 0.9) − (1.3 ± 0.9) ng g DW^{-1} h^{-1} *Pinus sylvestris* (various seedlings) [91].
(*E*)-3-hexenyl butanoate	• (7.3 ± 2.1 ∣ -), (33.8 ± 11.3 ∣ 7.3 ± 8.5), (4.8 ± 1.4 ∣ -) ng g DW^{-1} (June ∣ August), *Betula pendula*, *B. pubescens*, *Populus tremula*, resp. (dry leaves) [41].
(*Z*)-3-hexenyl 3-methylbutanoate (isovalerate)	• (0.46 ± 0.46)/(0.30 ± 0.30)/(0 ± 0)/(5.50 ± 1.70) ng g DW^{-1} h^{-1} *Betula pendula* (control/aphid infested for 10 days/aphids removed/washed) [44]. • 0.49 ± 0.49 ng g DW^{-1} h^{-1} *Betula pendula* [44]. • 0.3, 0.8 µg C g DW^{-1} h^{-1} *Artemisa tridentata*, *Betula alleghaniensis* (cut branches) [90].

Table 2. *Cont.*

GLV	Emission or Emission Rate
(*Z*)-3-hexenyl 2-methyl-2-butenoate (tiglate)	• (1.21 ± 0.54)/0.13 ng g DW^{-1} h^{-1} *Betula pendula* (control/aphid infested for 10 days [44].
3-hexenyl hexanoate [c]	• 2.9 ± 2.3 ng g DW^{-1} *Populus tremula* (leaves), June [41].
(*Z*)-3-hexenyl isobutyrate	• 0.03 ± 0.01, 0.40 ± 0.15, 0.03 ± 0.01 ng g^{-1} h^{-1} black ash, white fingertree, and olive tree, resp. (foliage) [40].
(*Z*)-3-hexenyl butyrate	• 0.15–0.66 ng g^{-1} h^{-1} five tree species (foliage) [40].
(*Z*)-3-hexenyl isovalerate	• 0.06–1.34 ng g^{-1} h^{-1} five tree species (foliage) [40].
(*Z*)-3-hexenyl isotiglate	• 0.02–0.38 ng g^{-1} h^{-1} four tree species (foliage) [40].
hexenyl type	• 140, 50, 0.06 µg (C) g DW^{-1} h^{-1} grass, clover (both cut and slashed), and over mowed grassland, resp [18].
1-octen-3-ol	• 9.0 ng g DW^{-1} h^{-1} blossoming rye in a field enclosure [86]. • (1.0 ± 0.6) − (44.6 ± 40.4) ng g DW^{-1} h^{-1} *Pinus sylvestris* (various seedlings) [91].
2-methyl-3-buten-2-ol	• 3.93 ± 1.70, 2.69 ± 1.24 nmol m^{-2} s^{-1} *Pinus ponderosa*, drought-stressed and watered [97]. • 6.933, 0.522 nmol m^{-2} s^{-1} mean, *Pinus ponderosa* and *Pinus nigra*, de novo synthesis [98]. • 1.6, 0.77 nmol m^{-2} s^{-1} (max, daily mean, resp.) *Pica abies* flux over mountain forest [99]. • 0.4–1.5 mg m^{-2} h^{-1} over mixed coniferous Roosevelt National Forest, Colorado (the lowest and peak values) [46]. • 76, 530 µg C m^{-2} h^{-1} *Pinus taeda* (plantation canopy level), mid-spring to summer and fall to early spring, resp. [47]. • 1.1 mg C m^{-2} h^{-1} *Pinus ponderosa* (plantation canopy level average), July [100]. • 1.37/0.01 mg C m^{-2} h^{-1} *Pinus ponderosa* (plantation average canopy level), daytime/nighttime, July to September [101]. • 1.0 mg C m^{-2} h^{-1} subalpine forest in the Rocky Mountains (canopy level average), July–August [102]. • 0.3–1.4 mg C m^{-2} h^{-1} *Pinus taeda* (canopy level, plantation near Chappel Hill) July [103]. • 2 mg C m^{-2} h^{-1} *Pinus ponderosa* (plantation canopy level average), July August; 18 µg C g^{-1} h^{-1} (max. at leaf level), at 30 °C and 1000 mmol m^{-2} s^{-1} PAR [104]. • 18 µg ± 7.4 C g^{-1} h^{-1} mean *Pinus ponderosa* at 30 °C and high irradiance [98]. • 25 µg C g^{-1} h^{-1} average *Pinus ponderosa* 1-year-old needles, intact [105]. • Over 20 mg C g^{-1} h^{-1} from leaves exposed to sunlight at 30 °C [45]. • 0.2, 0.3 µg C g DW^{-1} h^{-1} *Picea engelmanni*, *Pinus contorta* (cut branches) [90].
Nonanal	• (12.94 ± 0.95)/(12.57 ± 1.78)/(23.50 ± 3.09)/(25.12 ± 2.53) ng g DW^{-1} h^{-1} *Betula pendula* (control/aphid infested for 10 days/aphids removed/washed) [44]. • (6.51 ± 1.61)/(3.94 ± 2.76) ng g DW^{-1} h^{-1} *Betula pendula* (control/aphid infested for 21 days) [44]. • (3.92 ± 0.87)/(0.79 ± 0.50) ng g DW^{-1} h^{-1} *Alnus glutinosa* (control/aphid infested for 21 days) [44].
Methyl salicylate	• Up to 0.25 mg m^{-2} h^{-1} over walnut agroforest after cold night (7.5 °C) [106]. • <0.2 and 123 pmol m^{-2} s^{-1} tobacco Bel-W3 before and after exposure to O_3 in a lab reactor [89]. • 40 ± 17 pmol m^{-2} s^{-1} from drought-stressed *Alnus glutinosa* in a chamber; 63 ± 17 pmol m^{-2} s^{-1} with additional insect treatment; 14 ± 5 pmol m^{-2} s^{-1} after re-watering [107]. • 2.8 ng cm^{-2} h^{-1} from aphid-infested *Pinus sylvestris* saplings [75]. • (26.3 ± 22.0 | 1.2 ± 1.7), (9.2 ± 11.8 | -), (14.9 ± 3.8 |-), (0.7 ± 1.7 | -) ng g DW^{-1}, (June | August), *Betula pendula*, *B. pubescens*, *Populus tremula*, *Sambucus nigra*, resp. (dry leaves) [41]. • (25.45 ± 10.08)/(370.82 ± 99.35)/(551.32± 99.35)/(387.82 ± 77.14) ng g DW^{-1} h^{-1} *Betula pendula* (control/aphid infested for 10 days/aphids removed/washed) [44].

Table 2. *Cont.*

GLV	Emission or Emission Rate
Methyl salicylate	• (172.09 ± 120.115)/(721.63 ± 204.91) ng gDW^{-1} h^{-1} *Betula pendula* (control/aphid infested for 21 days) [44]. • (1.39 ± 1.39)/(137.98 ± 45.16) ng g DW^{-1} h^{-1} *Alnus glutinosa* (control/aphid infested for 21 days) [44]. • 0.5, 0.3 µg C g DW^{-1} h^{-1} *Fagus grandfolia, Quercus velutina* (cut branches) [90]. • 0.27–2.76 ng g^{-1} h^{-1} five tree species (foliage) [40].
Hexenals	• 0.07–0.417 µmol g DW^{-1} various cut grasses [108]. • 4 × 10^{-7} g m^{-2} s^{-1} hay after cutting and drying [109]. • 100–240 µg g DW^{-1} hay drying in a cuvette; 40–50 mg m^{-2} h^{-1} hay cutting in a chamber; 0.2–0.4 mg m^{-2} h^{-1} hay drying in a chamber; 0.1–1.5 mg m^{-2} h^{-1} 1st day of hay drying on a pasture in St. Johann, Tirol [110].
Pentenols and 2-methyl butanal	• 15 µg g DW^{-1} hay drying in a cuvette; 0.1–0.9 mg m^{-2} h^{-1} hay cutting in the chamber; 0.07–0.1 mg m^{-2} h^{-1} hay drying in the chamber; 0.1–0.7 mg m^{-2} h^{-1} 1st day of hay drying on a pasture in St. Johann, Tirol [110].
Pentenols and 3-methyl butanal	• 8 × 10^{-8} g m^{-2} s^{-1} hay cutting and drying [109].
Hexanal and (*E*)-2-hexenol	• 8 × 10^{-8} g m^{-2} s^{-1} hay cutting and drying [109].
Hexenols and hexanal	• 0.07–0.211 µmol g DW^{-1} various cut grasses [108]. • 30–60 µg g DW^{-1} hay drying in a cuvette; 1–3 mg m^{-2} h^{-1} hay cutting in the chamber; 0.1–0.3 mg m^{-2} h^{-1} hay drying in the chamber; 0.1–0.3 mg m^{-2} h^{-1} 1st day of hay drying on a pasture in St. Johann, Tirol [110].
Hexenyl acetates	• 0.10–0.844 µmol g DW^{-1} various cut grasses [108].
Hexyl acetates	• 0.003–0.015 µmol g DW^{-1} various cut grasses [108]. • 2.71 ± 0.05, 0.29 ± 0.07 pmol m^{-2} s^{-1} intact apple and grape foliage day mean, resp. [93].

[a] leaf (or plant material) dry weight (mass); [b] isoprene fragment was observed pre-cut and more 1-penten-3-ol fragment post-cut on MS; [c] unspecified isomer.

Table 3. Ambient and headspace concentrations of GLV.

GLV	Concentrations and References
1-penten-3-ol	• 17–54 ng dm^{-3} over freshly harvested tall fescue of various types in a headspace chamber [28].
(*E*)-2-penten-1-ol	• 236–1529 ng dm^{-3} over freshly harvested tall fescue of various types (in a headspace chamber); 1–9 ng dm^{-3} over sun-cured hay of tall fescue of various types (in a headspace chamber) [28].
(*E*)-2-pentenal	• 1–4 ng dm^{-3} over sun-cured hay of tall fescue of various types (in a headspace chamber) [28].
1-penten-3-one	• 7–55 ng dm^{-3} over freshly harvested tall fescue of various types (in a headspace chamber); 3–9 ng dm^{-3} over sun-cured hay of tall fescue of various types (in a headspace chamber) [28].
1-hexanol	• 1 ng dm^{-3} over sun-cured hay of tall fescue of various types (in a headspace chamber) [28]. • 0.04–0.12 ppbv at the canopy level (30 m) October-September 2010 in Amazon Rainforest [16].
(*E*)-2-hexen-1-ol	• 11–42 ng dm^{-3} over freshly harvested tall fescue of various types (in a headspace chamber); 0–1 ng dm^{-3} over sun-cured hay of tall fescue of various types (in a headspace chamber) [28].

Table 3. *Cont.*

GLV	Concentrations and References
(*Z*)-3-hexen-1-ol	• 958–3176 ng dm^{-3} over freshly harvested tall fescue of various types (in a headspace chamber); 2–5 ng dm^{-3} over sun-cured hay of tall fescue of various types (in a headspace chamber) [28]. • Max ~1000 ppbv, during cutting and drying grass and clover; 10–100 ppbv from red fescue grass; 5–100 ppbv from white clover leaves and stems, when cut and drying [12]. • 732 pptv mixing ratio over the canopy of tropical rainforest in Surinam [65].
(*E*)-3-hexenol	• 3–31 ng dm^{-3} over freshly harvested tall fescue of various types (in a headspace chamber) [28].
Hexanal	• 5–28 ng dm^{-3} over freshly harvested tall fescue of various types, in a headspace chamber [28].
(*E*)-2-hexenal	• 22–458 ng dm^{-3} over freshly harvested tall fescue of various types, in a headspace chamber; 4–12 ng dm^{-3} over sun-cured hay of tall fescue of various types, in a headspace chamber [28]. • 0.50–0.78 ppbv in 24 L of air at charcoal production workplace [111].
(*Z*)-2-hexenal	• 11–72 ng dm^{-3} over freshly harvested tall fescue of various types, in a headspace chamber; 0–1 ng dm^{-3} over sun-cured hay of tall fescue of various types, in a headspace chamber [28].
(*E*)-3-hexenal	• 26–165 ng dm^{-3} over freshly harvested tall fescue of various types, in a headspace chamber; 1–2 ng dm^{-3} over sun-cured hay of tall fescue of various types, in a headspace chamber [28].
(*Z*)-3-hexenal	• 18–698 ng dm^{-3} over freshly harvested tall fescue of various types, in a headspace chamber; 0–1 ng dm^{-3} over sun-cured hay of tall fescue of multiple types, in a headspace chamber [28]. • <100 pptv, ~16–20 ppbv, before and after lawn mowing [112]. • Max ~1000 ppbv, during cutting and drying grass and clover; 10–1000 ppbv from red fescue grass; 10–100 ppbv from white clover leaves and stems when cut and dried in a lab chamber [12]. • Up to 650 ppbv from cut aspen leaves in a chamber [33]. • Up to 160 ppbv over cut drying bluegrass leaves (25–30 °C) [29].
(*E*)-2-hexenyl acetate	• 49–102 ng dm^{-3} over freshly harvested various types of tall fescue in a headspace chamber [28].
(*Z*)-3-hexenyl acetate	• 10,195–24,816 ng dm^{-3} over freshly harvested tall fescue of various types, in a headspace chamber; 0–2 ng dm^{-3} over sun-cured hay of tall fescue of various types, in a headspace chamber [28]. • 165.3–353.7 pptv on a spring day; 213.3–790.2 pptv in spring night, over flowering orange tree [113]. • 1–10 ppbv from red fescue grass, 0.5–9 ppbv from white clover leaves and stems, when cut and dried in a lab chamber [12].
(*Z*)-3-hexenyl propionate	• 1–5 ng dm^{-3} over freshly harvested tall fescue of various types, in a headspace chamber [28].
1-octen-3-ol	• 6–18 ng dm^{-3} over freshly harvested tall fescue of various types, in a headspace chamber. 1–2 ng dm^{-3} over sun-cured hay of tall fescue of various types, in a headspace chamber [28].
2-methyl-3-buten-2-ol	• 19 ppbv max., 0.2–2 ppbv avg. *Pinus ponderosa* plantation canopy level [104]. • 0–7 ppbv *Pinus ponderosa* plantation in the Sierra Nevada, canopy level, July to September [101]. • 50–200 pptv day (mixing ratio) Niwot Ridge, Colorado, June 1991 [114].
Methyl salicylate	• Mixing ratio up to 14 ppbv over walnut agroforest after cold night (7.5 °C) [106].

Several researchers developed models that predict emission fluxes of volatile compounds, including GLV. The most comprehensive is the Model of Emission of Gases and Aerosols from Nature version 2.1 (MEGAN) [50,115], which aimed to estimate fluxes of biogenic compounds between terrestrial ecosystems and the atmosphere. MEGAN divided BVOC into 19 classes. There is no separate GLV class, but the "Stress VOC" class includes 3-hexenal, 2-hexenal, 3-hexenol, 3-hexenyl acetate, hexanal, 1-hexenol, MeJa, and MeSa. 2-Methyl-3-buten-2-ol is a separate class alone. MEGAN requires the input of meteorological, radiation, and land cover data, including the emission factors for 15 predefined classes of vegetation.

Heiden et al. [116] studied the emission dynamics of (*Z*)-3-hexenol, (*Z*)-3-hexenal, (*E*)-3-hexenol, (*E*)-2-hexenol, (*E*)-2-hexenal, hexanal, and 1-hexanol produced by various plants (tobacco, corn, pine, tomato, sunflower, broadleaf bean) after exposure to various stresses (ozone, pseudomonas infection, wounding) in a laboratory reactor. They obtained a general correlation:

$$\frac{\phi}{\phi_{max}} = A[\exp(-k_1 t) - \exp(-k_2 t)] \quad (1)$$

where ϕ is the actual emission rate, ϕ_{max} is the maximum emission rate in mol cm^{-2} s^{-1}, A is the scaling factor to force $\phi = \phi_{max}$ at the correct experimental time, t is time in h, k_1 and k_2 measured in h^{-1} are empirical factors. For sunflower and broadleaf bean, the equation without the k_1 term provided a good approximation. The parameters in Equation (1) are available in the original publication.

Kirstine and Galbally [19] developed a model for estimating BVOC emission from uncut and cut grass in urban environments. They estimated that hexenyl-type compounds (C_6 GLV alcohols and aldehydes) constituted more than 70% of total BVOC emission upon initial wounding of grass and 22–40% during drying of cut material. For Sydney and Melbourne, Australia, the total emissions were 2.9×10^9 g yr^{-1} and 2.9×10^9 g yr^{-1}, respectively, from uncut grass, 4.5×10^9 g yr^{-1} and 5.4×10^9 g yr^{-1} from cut grass, and 1.2×10^{11} g yr^{-1} and 2.0×10^{11} g yr^{-1} from other biogenic sources. The diurnal variation of BVOC flux varied from 0 in the night to peak values between 2 and 3 pm. Maximum emissions occurred in November and December.

Karl et al. [46] provided several model correlations for estimating MBO fluxes over vegetation, based on sensible heat (ωT) and latent heat fluxes (ωq), temperature (T), and two linear models (GLM1, GLM2) using temperature and light (PAR). The correlations utilized VOC fluxes measured at the Niwot Ridge AmeriFlux site in the Roosevelt National Forest in the Rocky Mountains of Colorado, USA, using the eddy covariance approach with PTR-MS instrument as a VOC sensor.

Geron et al. [47] provided a formula estimating the temperature dependence of MBO emission on temperature:

$$M = M_S e^{[\beta(T - T_s)]} \quad (2)$$

where M is the emission rate of MBO in mg C m^{-2} h^{-1} at temperature T in °C, M_s is the emission rate at standard temperature T_s = 30 °C, β is the temperature response factor (average β = 0.17, for the growing season β = 0.1).

Harley et al. [98] developed a model that described the diurnal emission of MBO and other BVOC from trees at varying temperatures and incident photosynthetic photon flux densities based on several fitted parameters like energies of activation and deactivation, and temperature and light scalars.

3. Physical Properties of GLV

3.1. Solubility in Water and Partition Coefficients

Henry's constants, 1-octanol/water partition coefficients, and 1-octanol/air partition coefficients are collected in Table 4. Along with the experimental values, the table contains estimates obtained here using the EPI suite HENRYWIN v3.20 freely available from the US EPA [117]. EPI estimates Henry's constants using three different methods (the bond estimation method, the group estimation method [118], and the VaporPressure/WaterSolubility estimation method. Estimates in Table 4 are the mean values from those three methods with standard deviations taken as uncertainties. The Log KOW procedure ver. 1.68 and Log Octanol-Air KOAWIN procedure ver. 1.1 were used to estimate the partition coefficients. The reviews of other estimation methods are provided elsewhere [119–121].

Table 4. Henry's constant, 1-octanol/water partition coefficient (K_{OW}), and 1-octanol/air partition coefficient (K_{OA}) for GLV in water and aqueous solutions.

GLV	Henry's Constant				Octanol/Water Partition Coefficient		Octanol/Air Partition Coefficient	
	H M atm^{-1}	T K	I M	Ref.	Log (K_{OW})	Ref.	Log (K_{OA})	Ref.
pentan-1-ol	87.7 ± 8.9	298	0	[120] [c]	1.5	[122]	4.7	[123]
	84.4 ± 7.0	298		[124] [a]	1.34	[125]	[f] 4.8	[117] [i]
	46.1 ± 2.1	306						
	11.9 ± 0.3	323						
	3.8 ± 0.1	343						
	71.9 ± 3.6	298		[117] [g]	1.3	[117] [h]	4.6	[117] [i]
1-penten-3-ol	72.5 ± 40.6	298		[117] [g]	0.84	[126]	4.5	[117] [i]
					0.81	[125]		
					1.1	[117] [h]		
(*Z*/*E*)-2-penten-1-ol	119.8 ± 34	298	0	[117] [g]	1.1	[117] [h]	4.4	[117] [i]
(*E*)-2-pentenal	17.3 ± 12.3	298		[117] [g]	1.1	[117] [h]	3.6	[117] [i]
1-penten-3-one	28.5 ± 23.2	298		[117] [g]	0.9	[117] [h]	3.8	[117] [i]
(*Z*)-2-pentenyl acetate	2.8 ± 0.8	298		[117] [g]	2.1	[117] [h]	3.8	[117] [i]
n-hexan-1-ol	61.8 ± 16.3	298	0	[120] [c]	1.84	[125]	5.2	[123]
	59.6 ± 2.8	298		[124] [a]	2.03	[122]	5.0	[117] [i]
	32.7 ± 1.1	306						
	8.0 ± 0.3	323						
	2.53 ± 0.01	343						
	55.5 ± 3.5	298		[117] [g]	1.8	[117] [h]		
n-hexan-1-al	3.2 ± 0.4	295	0	[127]	1.78	[122]	4.4	[123]
	5 ± 1	298		[128]	1.8	[117] [h]	[f] 3.8, 3.9	[117] [i]
	5.2 ± 0.5		freshwater	[129]				
	4.4 ± 0.4		25% seawater					
	3.4 ± 0.3		50% seawater					
	3.6 ± 0.2		75% seawater					
	3.2 ± 0.1		100% seawater					
	4.5 ± 1.0		0	[120] [c]				
	3.9 ± 1.0			[117] [g]				

Table 4. *Cont.*

GLV	Henry's Constant				Octanol/Water Partition Coefficient		Octanol/Air Partition Coefficient	
	H M atm^{-1}	T K	I M	Ref.	Log (K_{OW})	Ref.	Log (K_{OA})	Ref.
hexyl acetate	1.5 ± 0.2	298	0	[127]	2.59	[126]	4.6	[123]
	1.4 ± 0.2			[117] [g]	2.8	[117] [h]	4.5 [f], 4.4	[117] [i]
hexenol [b]	25	298	0	[33]				
(*E*/*Z*)-2-hexen-1-ol	94.4 ± 35.2			[117] [g]	1.6	[117] [h]	4.8	[117] [i]
(*Z*)-3-hexen-1-ol	113 ± 7.1	298	0	[130]	1.6	[117] [h]	4.8	[117] [i]
	140 ± 18		0.01					
	132 ± 11		1					
	83.4 ± 8.3	303	0					
	62.7 ± 3.0	308	0					
	129.9 ± 65.6	298		[117] [g]				
(*E*)-2-hexenal	14.5 ± 1.7	298	0	[127]	1.6	[117] [h]	4.3 [f], 4.0	[117] [i]
	20			[128,131]				
	13.6 ± 7.3			[117] [g]				
(*Z*)-3-hexenal	6			[33]	1.6	[117] [h]	3.7	[117] [i]
	4.1 ± 1.9			[117] [g]				
hexenyl acetate [b]	1			[33]				
(*E*/*Z*)-2-hexenyl acetate	1.8 ± 0.7			[117] [g]	2.6	[117] [h]	4.2	[117] [i]
(*Z*)-3-hexenyl acetate	3.1 ± 0.4	298	0	[127]	2.6	[117] [h]	4.2	[117] [i]
	3.62 ± 0.22	298	0	[130]				
	3.29 ± 1.1		0.01					
	2.32 ± 0.17		1					
	3.21 ± 0.17	303	0					
	2.56 ± 0.19	308	0					
	3.3 ± 2.4	298		[117] [g]				

Table 4. *Cont.*

GLV	Henry's Constant				Octanol/Water Partition Coefficient		Octanol/Air Partition Coefficient	
	H M atm^{-1}	T K	I M	Ref.	Log (K_{OW})	Ref.	Log (K_{OA})	Ref.
(*E*)-3-hexenyl acetate	3.3 ± 0.4	298	0	[127]				
	3.3 ± 2.4			[117] [g]				
(*Z*)-3-hexenyl-propionate	2.4 ± 1.6			[117] [g]	3.1	[117] [h]	4.6	[117] [i]
(*E*/*Z*)-3-hexenyl butyrate	1.8 ± 1.1			[117] [g]	3.6	[117] [h]	4.9	[117] [i]
(*Z*)-3-hexenyl isobutyrate	1.3 ± 0.6			[117] [g]	3.5	[117] [h]	4.9	[117] [i]
(*E*)-2-hexenyl butanoate	1.2 ± 0.3			[117] [g]	3.6	[117] [h]	4.9	[117] [i]
(*Z*)-3-hexenyl 3-methylbutanoate	1.1 ± 0.6			[117] [g]	4.0	[117] [h]	5.2	[117] [i]
(*Z*)-3-hexenyl 2-methyl-2-butenoate	1.8 ± 0.6			[117] [g]	3.9	[117] [h]	5.4	[117] [i]
3-hexenyl hexanoate	1.0 ± 0.5			[117] [g]	4.6	[117] [h]	5.7	[117] [i]
2-methyl-3-buten-2-ol	73 ± 3	296 ± 2	0	[132]	1.1	[117] [h]	4.2 [f], 4.5	[117] [i]
	38 ± 7		40% wt H_2SO_4					
	48 ± 26		55% wt H_2SO_4					
	48 [a]	298	0	[119]				
	52.9 ± 5.1		0					
	38.7 ± 2.2	303	0.01	[130]				
	21.8 ± 4.4	308	1					
	40.2 ± 5.4		0					
	31.7 ± 2.2		0					
	65 ± 3.5	303	0	[128,133]				
	62 ± 0.8	303	22.7 mM KNO_3 + 7.42 mM $CaSO_4$	[133]				
	59.8 ± 58.6 [d]			[117] [g]				

Table 4. *Cont.*

GLV	Henry's Constant				Octanol/Water Partition Coefficient		Octanol/Air Partition Coefficient	
	H M atm^{-1}	T K	I M	Ref.	Log (K_{OW})	Ref.	Log (K_{OA})	Ref.
1-octen-3-ol	13.2 44.5 ± 1.7	>378 K	0	[120,134] [117] [g]	2.6	[117] [h]	5.6	[117] [i]
nonanal	1.3 ± 0.2 1.2 ± 0.1 0.51 ± 0.03 0.38 ± 0.03 1.6 ± 0.4	298 298	0 Freshwater 50% seawater 100% seawater	[120] [c] [129] [117] [g]	3.3	[117] [h]	[f] 4.8, 5.0	[117] [i]
Jasmonic acid [e]					2.5	[117] [h]	9.7	[117] [i]
methyl jasmonate [e]	5081 ± 1003 8091 ± 1121 5454 ± 520 3869 ± 261 6716 ± 1272 4837 ± 272	298 298 298 298 303 308	0 0 0.01 1 0	[106] [130]	2.8	[117] [h]	7.5	[117] [i]
methyl salicylate [e]	33.5 ± 4.0 37.9 ± 2.1 26.7 ± 3.4 20.1 ± 1.6 16.4 ± 0.9 10.0 ± 4.2	298 298 298 298 303 308	0 0.01 1 0	[106] [130]	2.6	[117] [h]	5.0 [f], 6.3	[117] [i]

[a] recalculated from the original data; [b] unspecified structure; [c] mean of experimental values summarized by Sander 2015; [d] EPI suite could not estimate the value using group estimation method, so the difference between bond estimation value and VP/WSol resulted in large std. deviation; [e] the predicted KH values are unreasonable and therefore not included [f] Log KOA (octanol/air): estimated within EPI suite using one of the experimental values; [g] mean of bond est., group est., and VP/Wsol est. values by EPI suite (HENRYWIN v3.20) for which standard deviation is provided as error; [h] calculated with EPI suite HENRYWIN v3.20, Log KOW (version 1.68 estimate); [i] calculated with EPI suite HENRYWIN v3.20, Log Octanol-Air (KOAWIN v1.10).

The octanol/water partition coefficient represents the equilibrium in a two-phase three-component system solute-water-octanol—it is a ratio of the solute concentration in the octanol-rich phase to the solute concentration in the water-rich phase [122]. It shows the balance between the lipophilicity and hydrophilicity of a solute. The octanol/air partition coefficient represents the equilibrium in a two-phase three-component system solute-air-octanol—it is a ratio of a solute concentration in octanol to the solute concentration in the air. It estimates the partitioning of a solute between air and various environmental matrices like soil, vegetation, and aerosol particles [135].

Table 5 presents the GLV solubility in water and equilibrium vapor pressure either determined experimentally or calculated using EPI MPBPVP and WSKOW suites [117].

Table 5. Solubility in water and vapor pressure of GLVs at 298 K, experimental and estimated with EPI suite (MPBPVP (v1.43), mean of Antoine and Grain methods, and WSKOW v1.42 method, resp.).

GLV	Solubility		Vapor Pressure	
	mmol dm^{-3}	Ref.	Atm	Ref.
1-pentanol	245.5	[136]	2.9×10^{-3}	[137]
	307	[138]	3.7×10^{-3}	[138]
	257	[126]	3.49×10^{-3}	[117] [b]
	236.98	[117] [a]		
1-penten-3-ol	1047.1	[126]	1.20×10^{-2}	[117] [b]
	1035.1	[125]		
	525.48	[117] [a]		
(*Z*/*E*)-2-penten-1-ol	530.83	[117] [a]	3.46×10^{-3}	[117] [b]
(*E*)-2-pentenal	178.08	[117] [a]	2.43×10^{-2}	[117] [b]
1-penten-3-one	260.34	[117] [a]	5.03×10^{-2}	[117] [b]
(*Z*)-2-pentenyl acetate	11.23	[117] [a]	4.14×10^{-3}	[117] [b]
n-hexan-1-ol	57.5	[136]	1.22×10^{-3}	[139]
	61.3	[125]	1.16×10^{-3}	[117] [b]
	67.39	[117] [a]		
n-hexanal	56.3 [c]	[117] [b]	1.49×10^{-2}	[139]
	49.9	[140]	1.39×10^{-2}	[140]
	35.21	[117] [a]	1.26×10^{-2}	[117] [b]
hexyl acetate	3.5	[141]	1.74×10^{-3}	[142]
	8.9	[126]	1.91×10^{-3}	[117] [b]
	2.14	[117] [a]		
hexenol [f]	159.74	[117] [a]		
(*E*/*Z*)-2-hexen-1-ol	159.74	[117] [a]	1.20×10^{-3}	[117] [b]
(*Z*)-3-hexen-1-ol	162 ± 6	[130]	1.23×10^{-3}	[117] [b]
	159.74	[117]		
(*E*)-2-hexenal	53.61	[117] [a]	6.21×10^{-3}	[117] [b]
(*Z*)-3-hexenal	53.61	[117] [a]	1.97×10^{-2}	[117] [b]
(*E*/*Z*)-2-hexenyl acetate	3.38	[117] [a]	2.61×10^{-3}	[117] [b]
(*Z*)-3-hexenyl acetate	3.12 ± 0.17	[130]	1.50×10^{-3}	[117] [b]
	3.38	[117] [a]		
(*E*)-3-hexenyl acetate	3.38	[117] [a]	1.50×10^{-3}	[117] [b]
(*Z*)-3-hexenyl-propionate	1.02	[117] [a]	5.50×10^{-4}	[117] [b]
(*E*/*Z*)-3-hexenyl butyrate	0.31	[117] [a]	2.05×10^{-4}	[117] [b]
(*Z*)-3-hexenyl isobutyrate	0.35	[117] [a]	3.71×10^{-4}	[117] [b]

Table 5. *Cont.*

GLV	Solubility mmol dm^{-3}	Ref.	Vapor Pressure Atm	Ref.
(*E*)-2-hexenyl butanoate	0.31	[117] [a]	2.05×10^{-4}	[117] [b]
(*Z*)-3-hexenyl 3-methylbutanoate	0.11	[117] [a]	1.39×10^{-4}	[117] [b]
(*Z*)-3-hexenyl 2-methyl-2-butenoate	0.13	[117] [a]	7.53×10^{-5}	[117] [b]
3-hexenyl hexanoate	0.03	[117] [a]	3.04×10^{-5}	[117] [b]
2-methyl-3-buten-2-ol	1959 ± 36 565.89	[130] [117] [a]	3.08×10^{-2}	[117] [b]
1-octen-3-ol	14.32	[117] [a]	3.13×10^{-4}	[117] [b]
nonanal	0.7 0.93	[140] [117] [a]	4.87×10^{-4} 5.13×10^{-4} 7.42×10^{-4}	[139] [140] [117] [b]
Jasmonic acid	3.53	[117] [a]	2.41×10^{-8} [d] 1.79×10^{-7} [e]	[117] [b]
methyl jasmonate	4.52 ± 0.09 0.64	[130] [117] [a]	4.43×10^{-7} [d] 1.24×10^{-6} [e]	[117] [b]
methyl salicylate	5.11 ± 0.06 4.6 [c] 12.32	[130] [141] [117] [a]	7.03×10^{-5}	[117] [b]

[a] estimated with EPI suite (WSKOW v1.42); [b] estimated with EPI suite (MPBPVP (v1.43), mean of Antoine and Grain methods); [c] 308 K; [d] selected VP with modified grain method; [e] subcooled liquid VP with modified grain method; [f] unspecified structure.

The Henry's constants in Table 4 attributed to Sander [120] are actually the mean values of the constants determined by several authors: for pentan-1-ol [118,119,138,143–148], hexanal [129,140,144,149,150], and nonanal [140,144,149,150]. One of the values for nonanal [149] seems an outlier compared to the other latest values and therefore was skipped in calculating the mean.

There are no experimental Henry's constants for 1-penten-3-one (ethyl vinyl ketone). Still, the EPI estimate at 298 K in Table 4 is close to the mean empirical constant of (30.4 ± 10.1) M atm^{-1} determined for the structurally similar methyl vinyl ketone [120]. Similarly, the EPI estimate of the Henry's constant for (*Z*)-2-pentenyl acetate at 298 K (Table 4) is close to the (2.7 ± 0.4) and (2.3 ± 0.4) M atm^{-1} values determined for the homolog amyl acetate and isoamyl acetate, respectively [120].

Hansel et al. [21] estimated Henry's constant for several intermediate and final products of methyl jasmonate and methyl salicylate reactions with OH radicals (not shown here).

A few studies provided the temperature dependence of the GLV Henry's constants, and most of them were for pentanol and hexanol. Gupta et al. [151] developed the classical van't Hoff equations for dimensionless Henry's constants based on empirical determination and valid between 313–363 K (Equations (3a) and (3b)):

$$ln\left(K_{H,\ pentanol}\right) = 14.233 - \frac{6559.6}{T} \quad (3a)$$

$$ln(K_{H,\ hexanol}) = 11.705 - \frac{5538.7}{T} \quad (3b)$$

where K_H was the ratio of the solute molar concentrations in the gas and aqueous phases.

Falabella et al. [152] correlated the experimental Henry's constants determined in water and aqueous solutions of Na_2SO_4 for the temperature range 313–363 K using a modified theory of dilute solutions [153,154] (Equations (4a) and (4b)):

$$ln\left(K_{H,\ pentanol}\right) = ln\left(P^{sat}_{H2O}\right) + \frac{10.04}{T_r} - 14.51\frac{(1-T_r)^{0.355}}{T_r} + 2.72\frac{exp(1-T_r)}{T_r^{0.41}} + 0.91x \quad (4a)$$

$$ln(K_{H,\ hexanol}) = ln\left(P^{sat}_{H2O}\right) + \frac{9.57}{T_r} - 10.61\frac{(1-T_r)^{0.355}}{T_r} + 0.64\frac{exp(1-T_r)}{T_r^{0.41}} + 1.11x \quad (4b)$$

where K_H is in kPa, $P^{sat}{}_{H2O}$ is the saturation pressure of water in kPa, $T_r = T/T_{critical}$ is the reduced temperature, and x is the concentration of Na_2SO_4 in mol kg^{-1} water.

Dohnal et al. [155] provided a correlation for the temperature dependence of the thermodynamic Henry's constant for pentanol at 273–373 K (Equation (5)).

$$ln\left(K^o_{H,\ pentenol}\right) = 78.7049 - \frac{99.5059}{\tau} - 97.8025\ ln(\tau) + D\tau \quad (5)$$

where $K^0{}_H$ is in kPa and τ = T/298.15.

Equation (6) approximates the temperature variation of the Henry's Law constant for MBO in water [132]:

$$ln[\mathrm{H_{MBO}}] = \frac{(7230 \pm 190)}{T} - (20.2 \pm 0.7),\ T = 275 - 295\ \mathrm{K} \quad (6)$$

where H is in M atm^{-1}. The corresponding enthalpy of solvation is $\Delta H_{sol} = -(60 \pm 7)$ kJ mol^{-1}. Equation (6) calculated the constants at 298 K and 303 K (58 and 38.9 M atm^{-1} resp.) that were lower than the experimental values from other authors (Table 4).

Zhou et al. [129] determined the temperature dependence of the Henry's constant for hexanal (Equations (7a) and (7b)) and nonanal (Equations (8a) and (8b)) in freshwater and seawater across the range of 283–318 K:

$$\log \mathrm{H}_{\text{hexanal, seawater}} = -8.35 + 2645/\mathrm{T} \quad (7a)$$

$$\log \mathrm{H}_{\text{hexanal, freshwater}} = -8.76 + 2819/\mathrm{T} \quad (7b)$$

$$\log \mathrm{H}_{\text{nonanal, seawater}} = -9.01 + 2555/\mathrm{T} \quad (8a)$$

$$\log \mathrm{H}_{\text{nonanal, freshwater}} = -9.81 + 2929/\mathrm{T} \quad (8b)$$

where H is in M atm^{-1} and covers all possible hydrated forms of the solutes.

Liyana-Arrachchi et al. [156,157] simulated the behavior of MBO, MeSa, (Z)-3-hexen-1-ol, and (Z)-3-hexenylacetate at air-water interfaces using molecular dynamics approaches. The surface concentrations of GLV at the same bulk concentration decreased in the following order: (Z)-3-hexenyl acetate, (Z)-3-hexen-1-ol, MBO, and MeSa. The models accurately reproduced the experimental values of 1-octanol/water partition coefficients and the surface tension of solutions at 298 K and 0.01 MPa. The models indicated that all four GLV tended to remain at water-air interfaces with polar groups oriented towards the water. The observation indicated that the atmospheric reactions of those GLV may proceed at the aqueous interfaces rather than in the bulk gas or aqueous phases.

3.2. UV Spectra

UV spectroscopy is often used to follow the concentrations of reactants quantitatively in laboratory systems. The UV spectra of compounds quickly inform us about the possible photodegradation of these products. The energy flux of solar UV radiation is practically null below 290 nm [158], so compounds that do not absorb light above this value do not undergo photolysis in the atmosphere. The absorption cross-sections in the gas phase and

the extinction coefficients in the aqueous phase were defined with Equations (9a) and (9b), resp. Formally, Equation (9c) converts both quantities between each other.

$$\sigma(\lambda) = -\frac{ln[I(\lambda)/I_0(\lambda)]}{Lc} \tag{9a}$$

$$\varepsilon(\lambda) = -\frac{ln[I(\lambda)/I_0(\lambda)]}{Lc} = \frac{A(\lambda)}{Lc} \tag{9b}$$

$$\varepsilon = \sigma N \times 10^{-3} \tag{9c}$$

where σ (λ) is the absorption cross-section in cm^2 molecule^{-1} at wavelength λ, $\varepsilon(\lambda)$ is extinction coefficient in cm^{-1} M^{-1}, L is the optical path in cm, C is the concentration of absorbing gas in molecule cm^{-3}, c is the concentration of absorbing solute in M, $I(\lambda)$ and $I_0(\lambda)$ are the light intensities in the presence and absence of absorbing gas, resp., $A(\lambda)$ is the absorbance of a solute at λ, N is Avogadro's number.

Jiménez et al. [57] determined the absolute UV absorption cross-sections of pure gaseous 1-penten-3-ol (1.5–6.5 mmHg), 1-penten-3-one (1.1–7.4 mmHg), and (*Z*)-3-hexen-1-ol (0.2–0.4 mmHg) in a Pyrex absorption cell with quartz windows at 298 K (Figures 1 and 2). Jiménez et al. [159] used a similar setup to determine the UV absorption cross-sections of pure vapors of hexanal (0.9–7.0 mmHg) and (*E*)-2 hexenal (0.6–3.5 mmHg) at room temperature (Figures 3 and 4).

Xing et al. [160] determined the UV absorption cross-section of gaseous (*Z*)-3-hexenal (0.2–7.0 mmHg) at 298 K using a Horiba Jobin Yvon, Triax-320 spectrophotometric setup (Figure 5). Absorption followed the Beer's Law in the range 240–340 nm.

O'Connor et al. [161] determined the UV absorption cross-sections of gaseous (*E*)-2-hexenal and hexanal in a Pyrex cell with quartz windows at 297 ± 3 K (Figures 3 and 4). They used both a static and a dynamic method. The cell was either filled with a given amount of aldehyde or flushed continuously with a mixture containing 1.7 × 10^{16}–8.8 × 10^{16} molecule cm^{-3} of aldehyde and nitrogen. The cell pressure varied between 1.0 and 5.8 mmHg. The dynamic method failed for (*E*)-2-hexenal, probably because of leaks. The absorption cross-sections were slightly lower than [159], but the main absorption peaks appeared at the same wavelength.

Kalalian et al. [162] determined the UV absorption cross-sections for gaseous (*E*)-2-pentenal (0.2–9 mmHg) and (*E*)-2-hexenal (0.2–3 mmHg) at 298 K (Figures 1 and 4). Their results agree well with [159,161] in terms of peak wavelengths and with [159] in terms of intensities. Absorption below 245 nm resulted from the π-π * transition and the absorption band between 270 and 370 nm–to the n-π* transition of the carbonyl group absorption.

Richards-Henderson et al. [22] determined the UV absorption coefficients for (*Z*)-3-hexen-1-ol, (*Z*)-3-hexenyl acetate, MeSa, MeJa, and 2-methyl-3-butene-2-ol in aqueous solutions of pH = 5.5 ± 03 at 298 K (Figure 2, Figure 6, and Figure 7). Their results agree well with [163] and this work regarding peak location, while differences in the intensities can result from experimental errors [163].

Canosa-Mas et al. [164] recorded a UV spectrum of MeSa vapors at equilibrium with liquid phase at 293 K (Figure 6d).

Sarang et al. [163] presented UV spectra of 1-penten-3-ol, (*Z*)-2-hexen-1-ol, and (*E*)-2-hexen-1-al in aqueous solutions at 298 K and pH = 7 (Figures 1, 4 and 8). The spectra were recorded with a double-beam Lambda 900 UV/VIS/NIR spectrometer (Perkin Elmer Instruments). We also included unpublished spectra of (*E*)-2-hexenal, (*Z*)-2-hexen-1-ol, (*Z*)-3-hexenyl acetate, MBO, and MeSa in aqueous solutions recorded at 295 K with a double-beam Jasco V-570 UV-VIS-NIR spectrophotometer using water as a reference medium (Figures 4 and 6–8).

Rudich et al. [165] determined the UV absorption cross-section of MBO in the gas phase using a flow-through cell at 10 mmHg to minimize the influence of isoprene formed by the decomposition of MBO (Figure 7a).

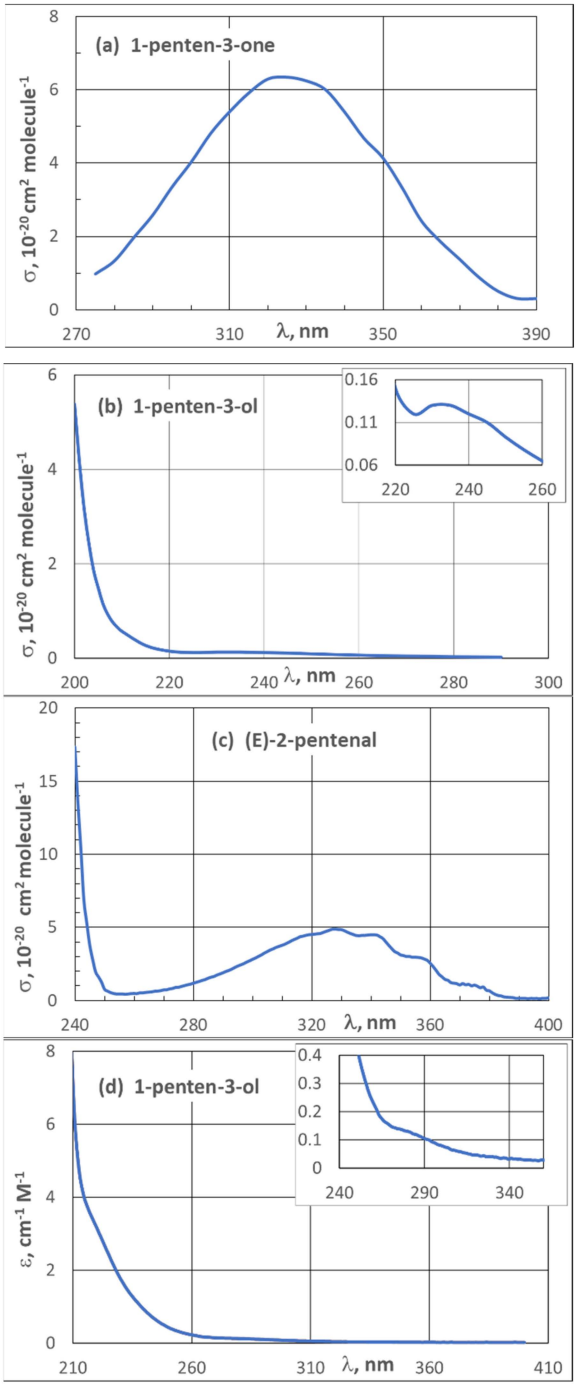

Figure 1. Absorption cross-sections σ of (**a**) 1-penten-3-one, (**b**) 1-penten-3-ol [57], and (**c**) (*E*)-2-pentenal [162] in the gas phase at 298 K, and absorption coefficients ε of (**d**) 1-penten-3-ol in the aqueous phase at 298 K and pH = 7 [163].

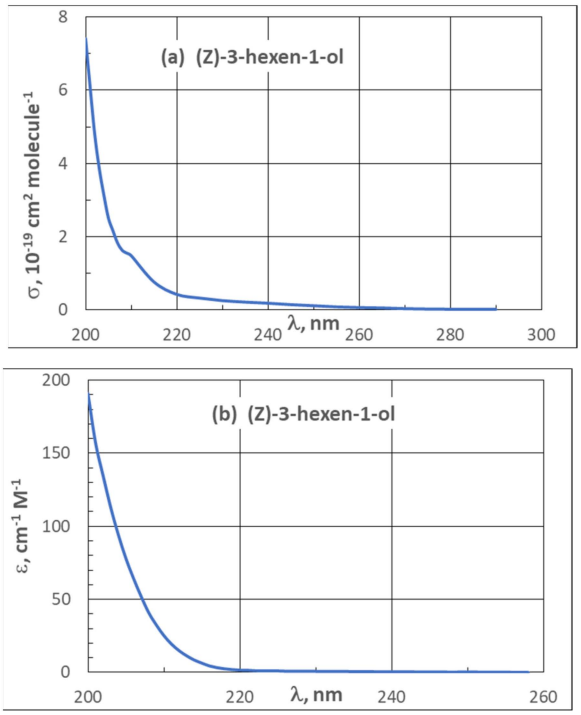

Figure 2. (*Z*)-3-hexen-1-ol: absorption cross-sections σ in the gas phase [57] (**a**) and absorption coefficient ε in the aqueous phase at 298 K and pH = 5.5 [22] (**b**).

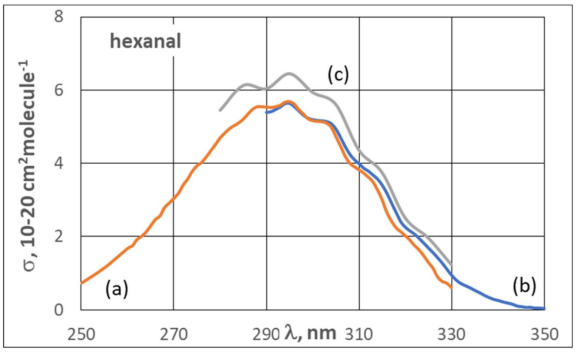

Figure 3. Absorption cross-sections σ of hexanal in the gas phase (**a**) [159], (**b**) at 297 K [161], and (**c**) at room temperature [166].

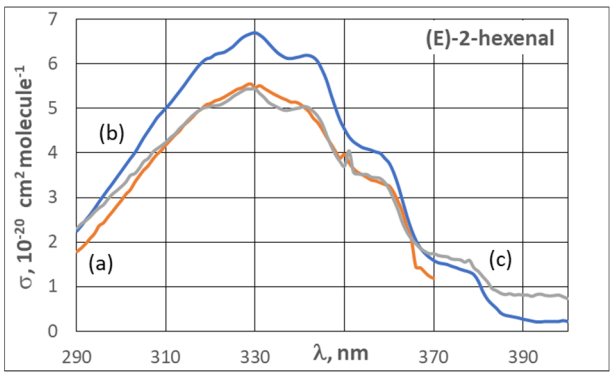

Figure 4. *Cont.*

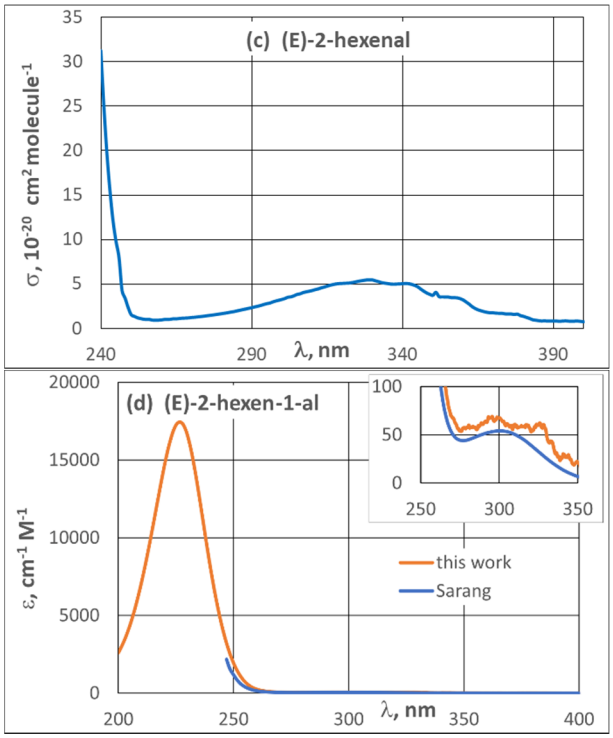

Figure 4. (*E*)-2-hexenal: absorption cross-sections σ in the gas phase (**a**) at 298 K [159], (**b**) at 297 ± 3 K [161], ((**c**), top and middle plate) at 298 K [162], and (**d**) absorption coefficients ε in the aqueous phase at 298 K and pH = 5.5 Sarang [163] and this work.

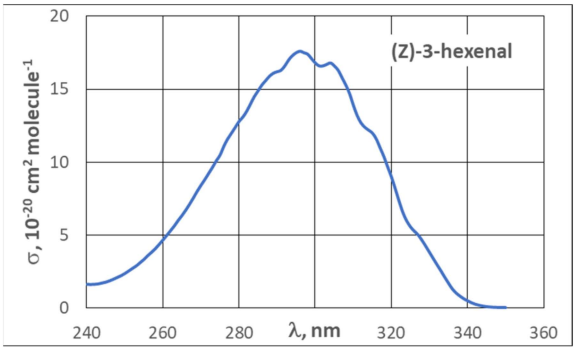

Figure 5. Absorption cross-sections σ of (*Z*)-3-hexenal in the gas phase at 298 K [160].

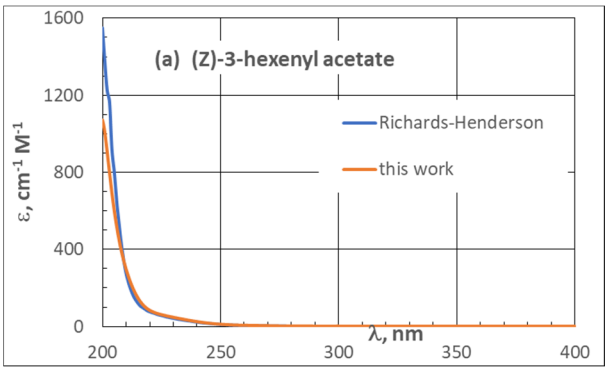

Figure 6. *Cont.*

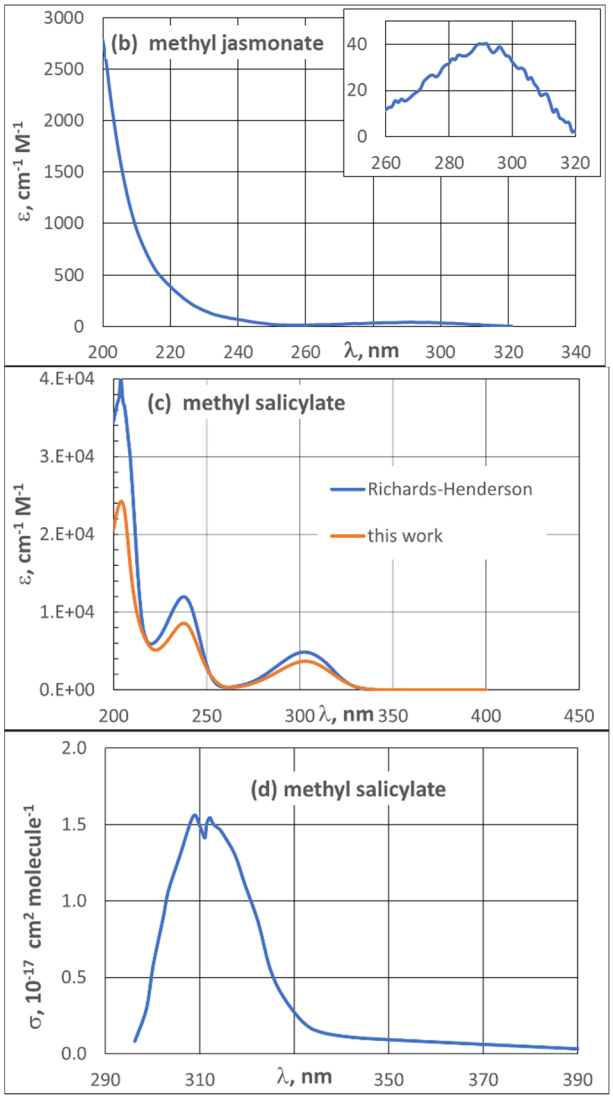

Figure 6. Absorption coefficients ε of (**a**) (*Z*)-3-hexenyl acetate, (**b**) methyl jasmonate, and (**c**) methyl salicylate in aqueous solutions at 298 K and pH = 5.5 (Richards-Henderson [22]) and pH = 7 (this work), and (**d**) absorption cross-sections of methyl salicylate vapor at 293 K [164].

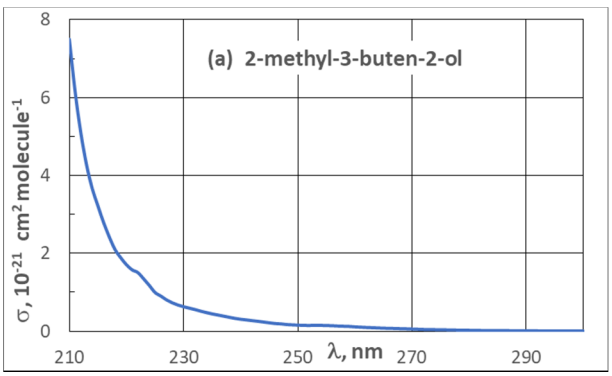

Figure 7. *Cont*.

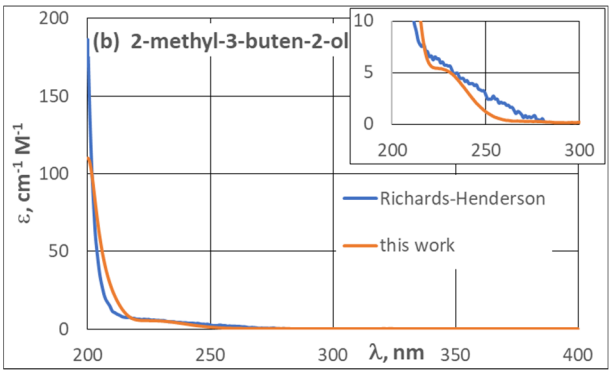

Figure 7. 2-methyl-3-buten-2-ol: absorption cross-sections σ of 2-methyl-3-buten-2-ol in the gas phase [165] (**a**) and absorption coefficients ε in the aqueous phase at 298 K and pH = 5.5 (Richards-Henderson [22]) and pH = 7 (this work) (**b**).

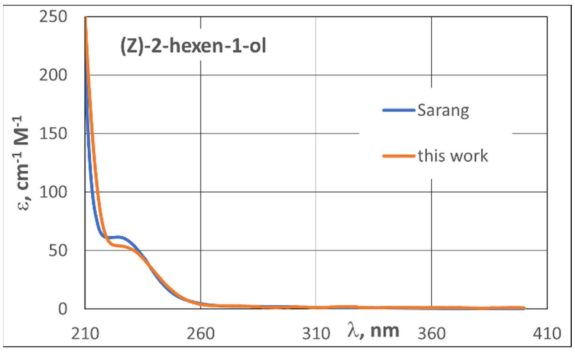

Figure 8. (*Z*)-2-hexen-1-ol: absorption coefficients ε in the aqueous phase at 298 K and pH = 7 Sarang [163] and this work.

4. Gas-Phase Chemistry

GLVs undergo reactions with oxidants such as hydroxyl (OH) radicals, nitrate (NO_3) radicals, ozone (O_3), and Cl atoms in the atmospheric air.

Atkinson and Arey [167,168] reviewed the literature on mechanisms and kinetics of gas-phase atmospheric reactions of VOC and BVOC but included no data on GLV except hexanal and hexenols. Section 4 discusses detailed mechanisms and products of GLV reactions with OH, NO_3, O_3, and Cl. This review did not aim to cover the theoretical modeling of atmospheric reactions. Interested readers may see an excellent review by Vereecken et al. [169].

4.1. Products and Mechanisms

Volatile organic compounds react with radicals X following the general Scheme 4 [168,170], which begins with the formation of an alkyl radical by adding X to a double C=C bond or by hydrogen abstraction. The alkyl radical reacts with oxygen to form the alkylperoxy radical RO_2. The fate of RO_2 depends on available reactants. RO_2 self-reacts with another RO_2 and gives a carbonyl and alcohol or an alkoxy radical. The reaction with HO_2 radicals leads to hydroperoxides, while the reaction with NO_2- to the peroxynitrate. The reaction of RO_2 with NO gives either the nitrate or the alkoxy radical, which reacts further to various products.

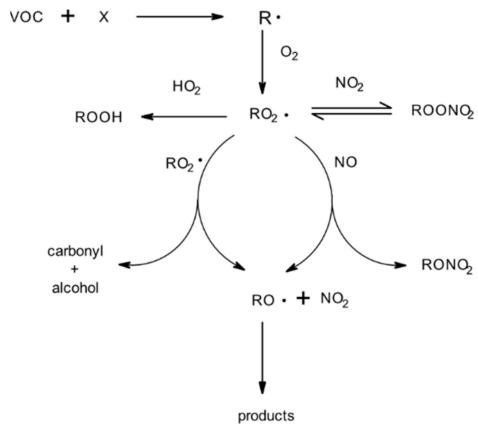

Scheme 4. Reactions that most often occur when alkene reacts with an atmospheric oxidant X (OH, NO_3, O_3, Cl) in the presence of oxygen and nitrogen oxides [168].

4.1.1. Reactions with OH

GLV reactions with OH radicals begin with the OH addition to the C=C bond or the hydrogen abstraction by OH. Almost all experimental works cited in this section illustrate their results using the addition mechanisms. However, Gai et al. [171] compared both channels in reactions of several hexenols with OH radicals at CCSD(T)/6-311++G(2d,2p)//BH&HLYP/6-31 G(d,p) level of theory. The hydrogen abstraction channel included 11 abstractions at all C sites and excluded the OH group. The addition channel generally appeared faster, and the branching ratios of the abstraction channel ranged from 0.16 to 0.59 (Table 6). The overall theoretical rate constants (abstraction + addition) differed by (−46) to 82% from the experimental rate constants determined by those authors (Section 4.2.1, Table 15). Tables 7 and 8 show the products of GLV–OH reactions and the corresponding experiments.

Table 6. Theoretical rate constants (cm^3 $molecule^{-1}$ s^{-1}) for reactions of hexenols with OH radicals through the OH addition and hydrogen abstraction channels [171].

Reactant	$k_{OH\ addition}$	$k_{H\ abstraction}$	k_{total}	H-Abstraction Branching Ratio	k_{total} Deviation from Experimental Values %
(*E*)-2-hexen-1-ol	4.97×10^{-11}	9.76×10^{-12}	5.95×10^{-11}	0.16	26.4
(*Z*)-2-hexen-1-ol	5.34×10^{-11}	2.19×10^{-11}	7.53×10^{-11}	0.29	11.7
(*E*)-3-hexen-1-ol	2.45×10^{-11}	3.50×10^{-11}	5.95×10^{-11}	0.59	34.6
(*Z*)-3-hexen-1-ol	1.17×10^{-10}	3.07×10^{-11}	1.48×10^{-10}	0.21	−46.5
(*E*)-4-hexen-1-ol	4.74×10^{-11}	1.30×10^{-11}	6.04×10^{-11}	0.22	15.4
(*Z*)-4-hexen-1-ol	1.10×10^{-10}	2.73×10^{-11}	1.37×10^{-10}	0.20	82.6

On the contrary, Du and Zhang [172] performed quantum chemical modeling of the OH radical reaction with MBO. The reaction proceeded mainly through the equally fast additions of OH to two unsaturated C atoms in MBO and the formation of C_4 and C_3 adducts. Both intermediates reacted further with oxygen and finally gave two primary products: glycolaldehyde CH_2OHCHO and propanone CH_3COCH_3. The minor products, formaldehyde HCHO and 2,3-dihydroxy-3-methyl propanal $(CH_3)_2COHCHO$, formed through the C_4 adduct [172].

Among the experimentalists, only Davis et al. [173] considered the hydrogen abstraction channel in reactions of GLV aldehydes with OH (Schemes 5–7). First, an alkyl radical forms and reacts with molecular oxygen to give the peroxy radical (Scheme 5).

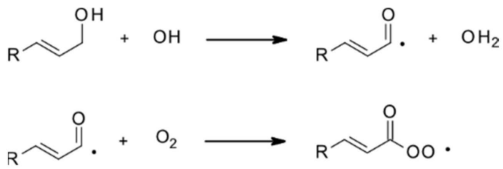

Scheme 5. Hydrogen abstraction from a GLV aldehyde and formation of a peroxy radical [173].

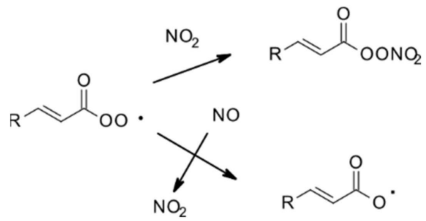

Scheme 6. Reactions of the peroxy radicals with NO_2 and NO produce a peroxynitrate and an alkoxy radical, resp. [173].

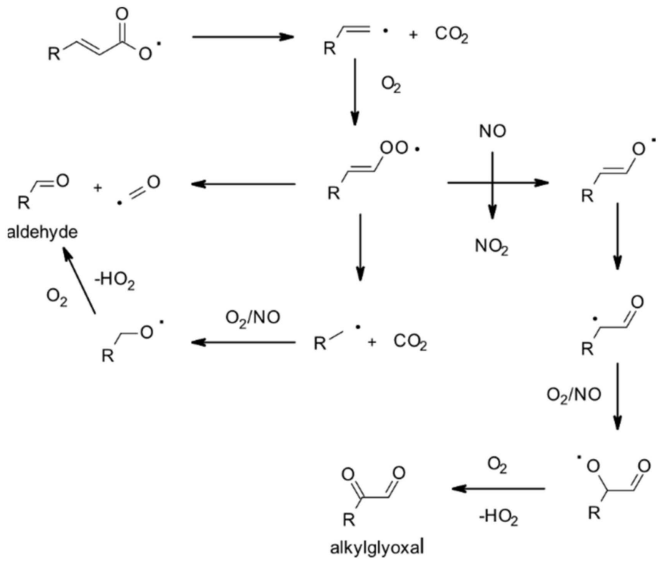

Scheme 7. Reactions of the alkoxy radical leading to the formation of an aldehyde and an alkylglyoxal [173].

In the presence of NO_x, the peroxy radical reacts with NO_2 to produce a peroxynitrate or reacts with NO to afford an alkoxy radical by oxygen abstraction (Scheme 6). The alkoxy radical enters a series of reactions with O_2 and NO that lead to the formation of an aldehyde and alkyl glyoxal (Scheme 7).

We explain the principles of the OH addition mechanism using (*Z*)-3-hexen-1-ol as an example. The references quoted may refer to other GLV but includes the same mechanism principle. First, the OH radicals add to the C=C bond producing two isomeric alkoxy radicals. Those radicals react with molecular oxygen to form two isomeric peroxy radicals (Scheme 8) [95].

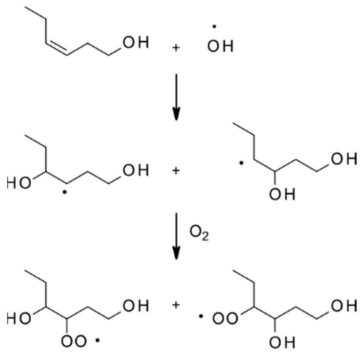

Scheme 8. The OH radical addition to the C=C bond in (*Z*)-3-hexen-1-ol [95].

In the absence of NOx, the peroxy radicals undergo a self-reaction that produces isomeric alkoxy radicals (Scheme 9), as shown for similar hexenals [174–176] and MBO [177].

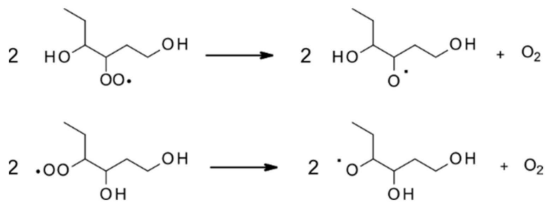

Scheme 9. Self-reaction of peroxy radicals [95] and other references in this section.

If NO is present, it reacts with peroxy radicals either to subtract one oxygen atom and produce two alkoxy radicals [95,173–182] or to afford two organic dihydroxy nitrates by addition [178,180] (Scheme 10).

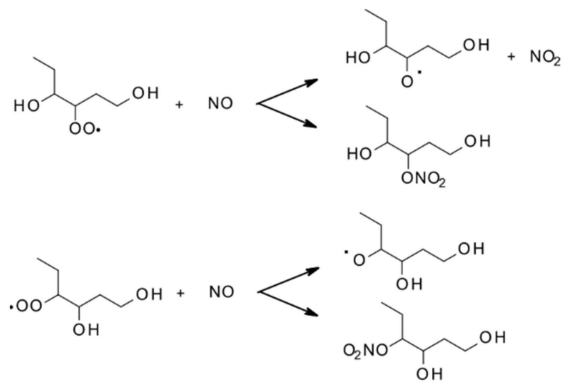

Scheme 10. Reactions of peroxy radicals from (*Z*)-3-hexen-1-ol with NO lead to the formation of organic nitrates and alkoxy radicals [95,173–182].

The alkoxy radicals can isomerize [180,183], decompose [95,174–176,180], or undergo hydrogen abstraction [175,176] (Scheme 11). The products formed include respectively: (i) 3,4-dihydroxyhexanal, (ii) propanal and 3-hydroxypropanal, and (iii) two dihydroxyhexanones and one trihydroxyhexanone.

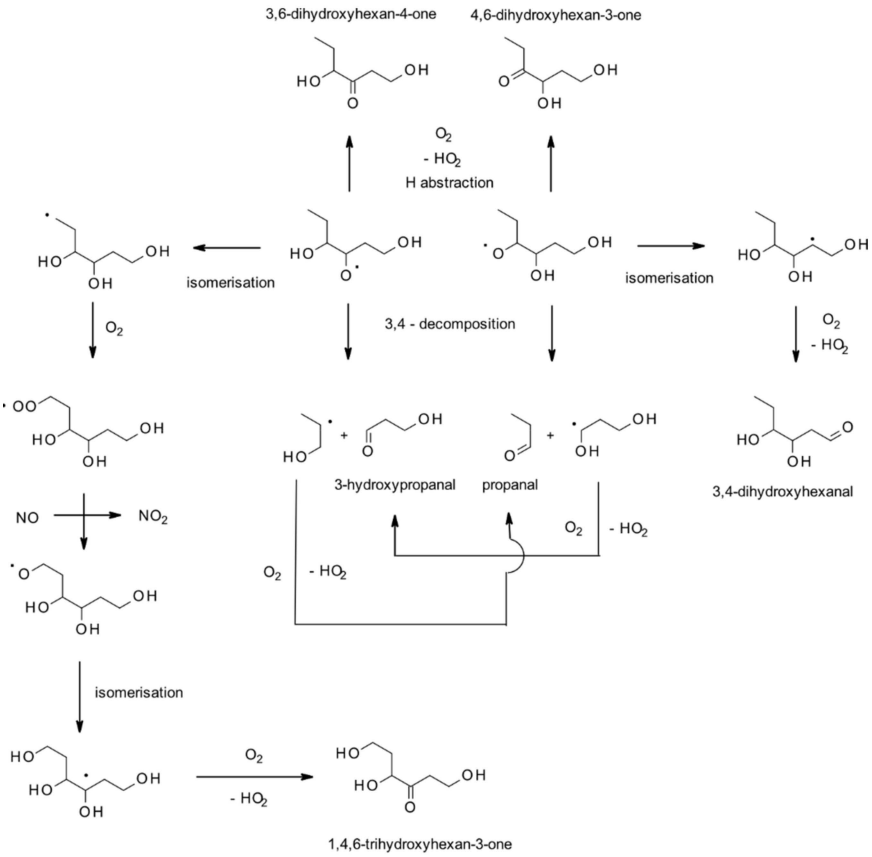

Scheme 11. Reactions of alkoxy radicals derived from (*Z*)-3-hexen-1-ol [95,174–176,180,183].

Propanal can react further with OH, O_2, and NO_x to give peroxynitrates, formaldehyde, and CO_2 [95].

MBO reacts with OH like (*Z*)-3-hexen-1-ol, and final products include glycolaldehyde, acetone, formaldehyde, hydroxymethylpropanal, and trihydroxybutanal. Scheme 12 shows the plausible reaction paths for MBO-derived alkoxy radicals [177,178,180,182].

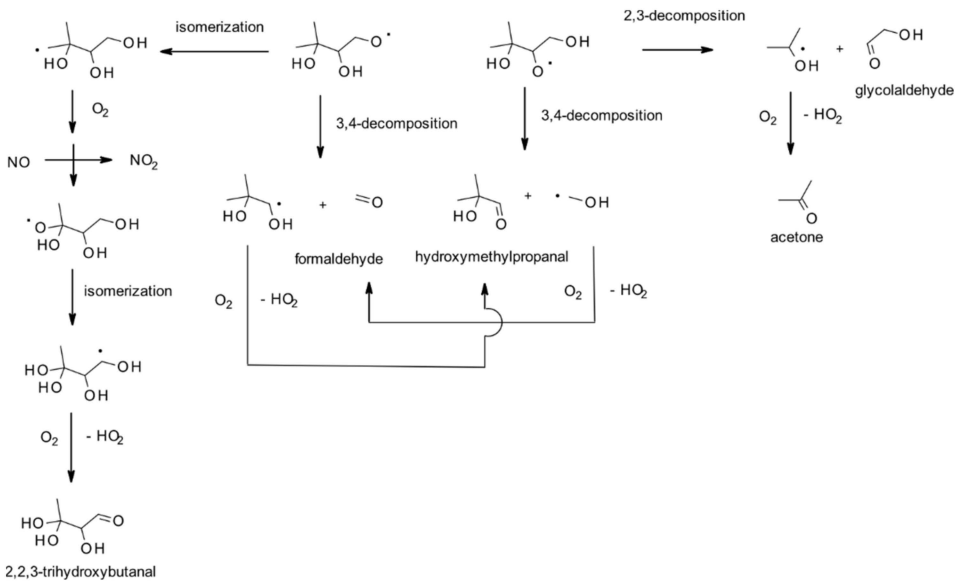

Scheme 12. Reactions of MBO-derived alkoxy radicals: 2,3-decomposition, 3,4-decompositions, and isomerization [177,178,180,182].

Furthermore, the MBO-derived peroxy radicals can react with NO to give MW 165 dihydroxynitrates (Scheme 13) [180].

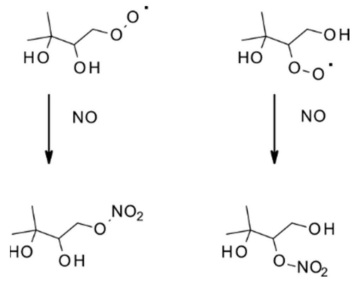

Scheme 13. Reactions of MBO-derived peroxy radicals with NO produce MW 165 dihydroxynitrates [180].

The OH radicals add to GLV aldehydes like they do to GLV alcohols and lead to aldehydes, alkylglycolaldehydes, glyoxal, and CO (Scheme 14) [173]. Yet, an alternative decomposition of the alkoxy radical leads to aldehyde, alkylglyoxal, and CO_2 (Scheme 7).

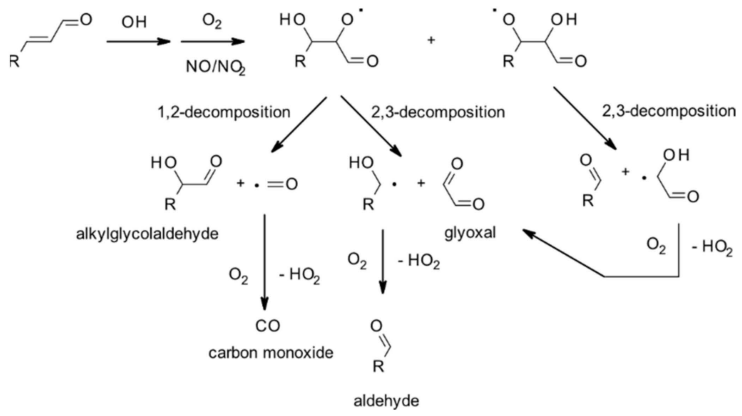

Scheme 14. The mechanism of OH radical addition to GLV aldehydes includes several decompositions of alkoxy radicals [173].

A saturated GLV pentan-1-ol reacts with OH by the hydrogen abstraction from a CH_2-group at position 2 and subsequent reaction with oxygen, leading to a β-hydroxyalkoxy radical. The latter can isomerize to 1,5-dihydroxy-2-pentanone, decompose to butanal, or get autoxidized to 1-hydroxy-2-pentanone [184]. Initial hydrogen abstraction at position 3 leads to 3-hydroxypropanal, and at position 4, to 5-hydroxy-2-pentanone and 4-hydroxypentanal.

Table 7. Products from gas-phase reactions of GLV with OH radicals.

GLV	Product	Yield %	Expt Table 8	Ref.
Pentan-1-ol	Pentanal	40.5 ± 8.2	X	[184]
	Butanal	16.2 ± 3.7		
	Propanal	8.1 ± 1.9		
	Etanal	18.1 ± 4.2		
	Formaldehyde	25.1 ± 1.3		
	5-hydroxy-2-pentanone	observed		
	3-hydroxypropanal	observed		

Table 7. *Cont.*

GLV	Product	Yield %	Expt Table 8	Ref.
1-penten-3-ol	Formaldehyde	35 ± 4	I	[185]
	Glycolaldehyde	47 ± 6		
(*Z*)-2-penten-1-ol	Formaldehyde	11 ± 2		
	Propanal	91 ± 13		
	Glycolaldehyde	87 ± 11		
(*E*)-2-hexen-1-ol	Butanal	Main	II	[176]
(*E*)-3-hexen-1-ol	Propanal	Main	II	[176]
		37 ± 7	III	[175]
(*Z*)-3-hexen-1-ol	Propanal	Main	II	[176]
		58 ± 8	IV	[180]
		74.6 ± 6.7	VIII	[183]
	3-hydroxypropanal	101 ± 24	IV	[180]
		48 + 48/−24	VIII	[183]
	3,4-dihydroxyhexanoic acid	Observed	IV	[180]
	Dihydroxynitrates MW 179 (see Scheme 10)	Observed	IV, VIII	[180,183]
	Hydroxycarbonyl MW 132 (see Scheme 11)	Observed	VIII	[183]
(*Z*)-3-hepten-1-ol	Butanal	33 ± 3	III	[175]
(*E*)-2-hexenylacetate	Butanal	Observed	XI	[186]
2-methyl-3-buten-2-ol	Acetone	14.1 ± 0.2	V	[182]
		52 ± 5 molar	VI	[179]
		58 ± 4	VII	[178]
		observed	IV	[180]
		67 ± 5	IX	[177]
	Formaldehyde	9.3 ± 3.3	V	[182]
		35 ± 4 molar	VI	[179]
		29 ± 3	VII	[178]
		observed	IV	[180]
	Formic acid	33 ± 3	IX	[177]
		9.3 ± 3.3	V	[182]
		28.0 ± 2.8	V	[182]
	Glycolaldehyde	50 ± 5 molar	VI	[179]
		61 ± 9	VII	[178]
		78 ± 20	IX	[177]
		66 ± 2	XIII a	[187]
		29 ± 5	XIII a	[187]
	2-hydroxy-2-methylpropanal	19 ± 7	VII	[178]
		31 ± 4	IV	[180]
		31 ± 11	IX	[177]
		12 ± 2	XIII a	[187]
		37 ± 7	XIII b	[187]
	Dihydroxynitrates MW 165 (see Scheme 13)	observed	IV	[180]
	Organic nitrates	5 ± 2	VII	[178]
	Glyoxal	26	XIII a	[187]
		37	XIII b	[187]
	CO	observed	V	[182]
	CO_2	observed	V	[182]
Nonanal	1-nitooxy octane	40	XII	[188]

Table 8. Experiments used to determine the rate constants listed in Table 7.

Expt	Photoreactor Type	Vol. dm^3	Material	Detection	Temp. K	*p* atm	OH Source	Ref.
I	Chamber	47	Steel	LP FTIR	298	1	Ethyl nitrite	[185]
II	Bag	80	Teflon	GC-FID (SPME)	298	1	H_2O_2	[176]
III	Chamber	1080	Quartz	LP FTIR	298	1	H_2O_2	[175]
IV	Chamber	7000	Teflon	GC-FID, GC-MS, API-MS	296	0.97	Methyl nitrite	[180]
V	Chamber	480	Teflon	LP FTIR	295	0.97	H_2O_2	[182]
VI	Chamber	47	Steel	LP FTIR	295		Methyl nitrite	[179]
VII	Chamber	5800	Teflon	LP FTIR, GC-FID, GC-MS, API-MS/MS	298	1	Ethyl nitrite	[178]
VIII	Chamber	6500–7900	Teflon	GC-FID, GC-MS, API-MS	298	1	Methyl nitrite	[183]
IX	LISA CRAC EUPHORE			LP FTIR	298	1	HONO, n-propyl nitrite	[177]
X	Reactor	480	Duran	LF FIR, GC-PI	298	0.97	Methyl nitrite	[184]
XI	Bag	80	Teflon	GC-FID	298	1	H_2O_2	[186]
XII	Chamber	5000	Teflon	GC-FID	298	1	Isopropyl nitrite	[188]
XIII a XIII b	Chamber	28,000	Teflon	LIP	294–298		Cyclohexane Cyclohexane NO_x	[187]

Priya and Senthilkumar [189] theoretically studied the reaction of MeSa with OH radicals using DFT methods with B3LYP, M06-2X [50], and MPW1K [51] functionals, and 6-311++G(d,p) basis set. The dominating hydrogen abstraction channel was the abstraction of OH hydrogen (Scheme 15). The dominating addition channel was the OH addition at para position (Scheme 16).

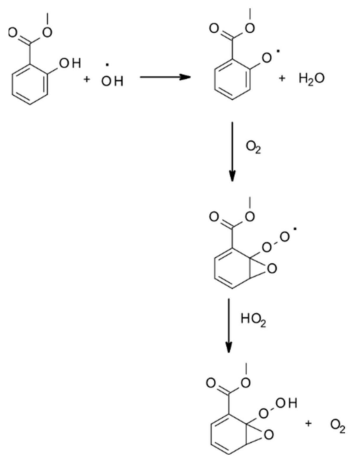

Scheme 15. Dominating hydrogen abstraction channel in the reaction of MeSa with OH radicals [189].

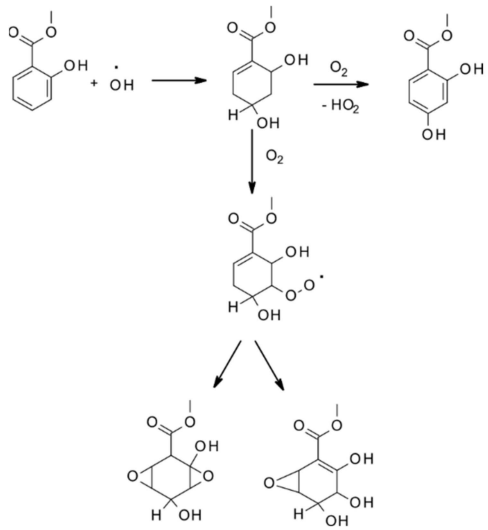

Scheme 16. Dominating addition channel in the reaction of MeSa with OH radicals [189].

On the contrary, Seif et al. [190] theoretically found that the addition at the ipso position had the largest branching ratio and the addition at the para position, the smallest one. The rate constants k_i for the individual addition channels calculated at 298 K and 1 atm using RRKM theory at MN15-L/aug-cc-pVTZ level with Eckart tunneling were 4.65, 2.02, 1.01, 0.24, 3.27, and 0.57 10^8 M^{-1} s^{-1}, respectively for the positions from 1 to 6. The hydrogen abstraction mechanism appeared negligible because of the high Gibbs potential.

4.1.2. Reactions with NO_3

There are not many papers on the mechanisms of GLV reactions with NO_3. General principles can emerge from the works on reactions with other alkenes [168,170]. The reaction begins with the NO_3 addition to a double C=C bond which yields two isomeric alkyl radicals (Scheme 17). The following steps are like those in the GLV-OH mechanism. Fantechi et al. proposed a similar mechanism for the reaction of MBO with NO_3 radicals (Scheme 18) [182]. That mechanism includes an additional decomposition of alkoxy radicals, which leads to acetone. More decomposition steps for MBO-derived alkoxy radicals were proposed (Scheme 19) [191].

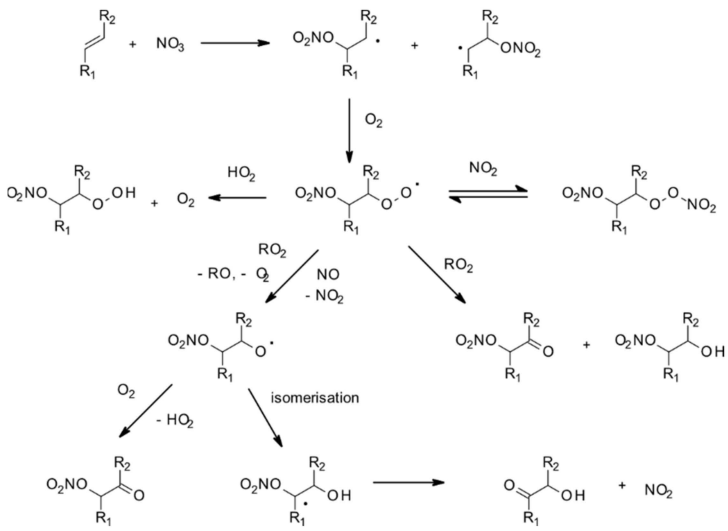

Scheme 17. Possible pathways in reactions of GLV with NO_3 radicals (for simplicity, the scheme shows the transformation of only one isomeric alkyl radical) [168,170].

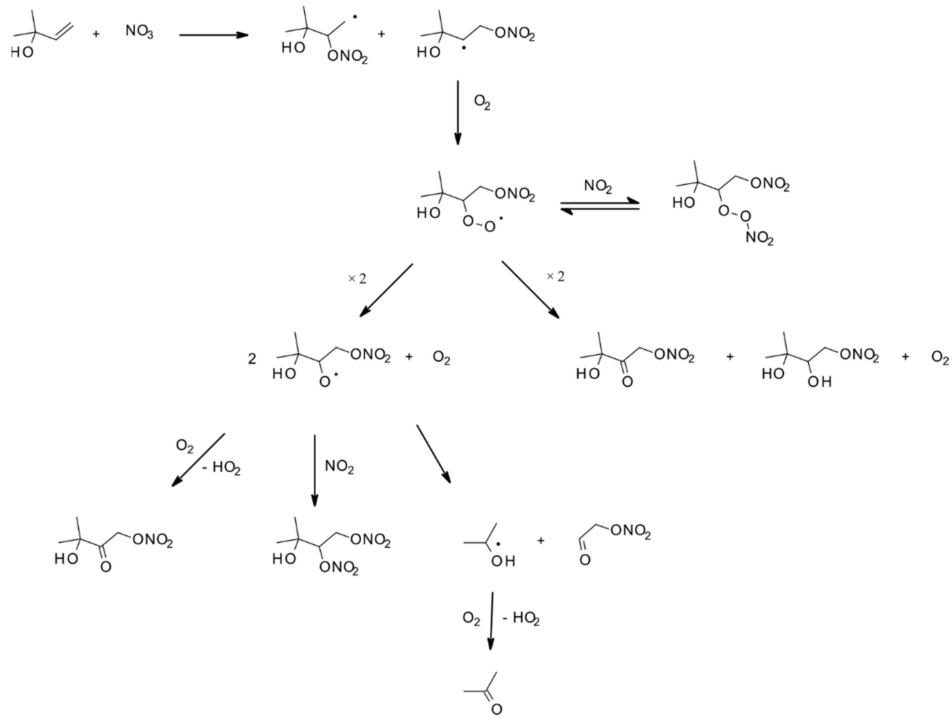

Scheme 18. Mechanism of MBO reaction with NO_3 radicals (for simplicity, the scheme shows the transformation of only one isomeric alkyl radical) [182].

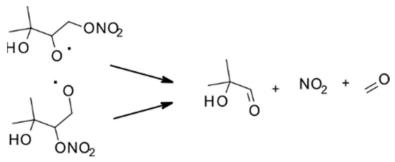

Scheme 19. Alternative decomposition steps of MBO-derived nitrate alkoxy radicals [191].

Products obtained from reactions of GLV with NO_3 are listed in Table 9, while Table 10 briefly describes the corresponding experiments.

Table 9. Products observed in reactions of GLV with NO_3.

GLV	Product	Yield, % Molar	Expt TabLe 10	Ref.
1-penten-3-ol, (*Z*)-2-penten-1-ol	2-pentenyl nitrate	observed	I a	[192]
	Ethyl vinyl nitrate	observed		
	2-penten-1-ol	observed	I b	
(*E*)-2-hexenal	PAN analogue	100 ± 2.5	II	[193]
	CO	6.4 ± 4.2		
	Formic acid	observed		
MBO	Acetone	63	III	[191]
		68.7 ± 7.1	IV	[182]
	1-nitroxyacetaldehyde	67	III	[191]
	Formaldehyde	4	III	[191]
	Organic nitrates	12.5–13.5	IV	[182]
	Hydroxy-aldehyde nitrates, peroxynitrates, carbonyl nitrates, nitroxyalcohols, dinitrates	observed		

Table 10. Experiments used to determine the rate constants listed in Table 9.

Expt	Photoreactor			Detection	T	p	NO_3 Source	Ref.
	Type	Vol. dm^3	Material		K	atm		
I a I b	Chamber	80	Teflon	GC-MS	298	1	N_2O_5 NO_2	[192]
II	Reactor	977	Pyrex	LP FTIR, UV	294	1	N_2O_5	[193]
III	Reactor	153	Glass	LP FTIR	297	1	N_2O_5	[191]
IV	Chamber	480	Teflon	LP FTIR	295	0.97	N_2O_5	[182]

4.1.3. Reactions with O_3

The ozonolysis of alkenes generally begins with a primary ozonide formation by O_3 addition to a double C=C bond, which decomposes to Criegee biradicals and carbonyl products (Scheme 20) [194–197]. Those products can recombine to form a secondary ozonide.

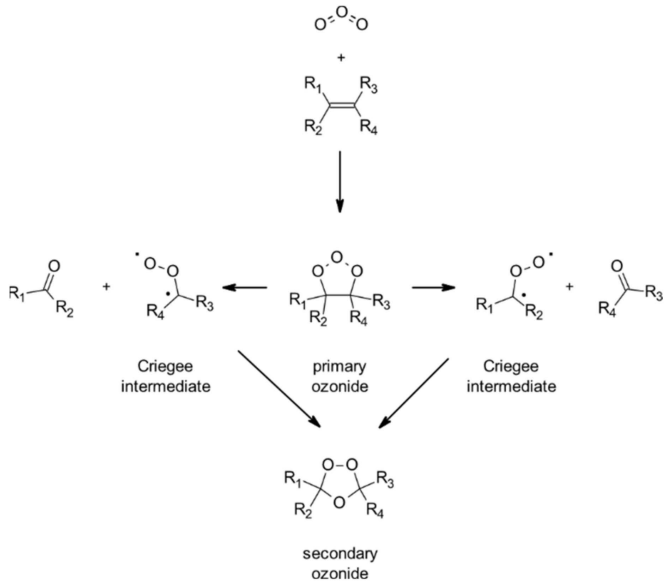

Scheme 20. General mechanism of the O_3 reactions with alkenes, including GLV [195,197].

Criegee biradicals stabilize by a range of reactions that depend on the R substituents and are presented below for individual GLV.

The basic mechanism of the ozonolysis of (*Z*)-3-hexenol includes the formation of propanol, 3-hydroxypropanal, and Criegee intermediates that stabilize by hydration and dehydration, leading to propanoic and 3-hydroxypropanoic acids (Scheme 21) [92,198].

Scheme 22 shows additional hydroperoxide product channels. They begin with Criegee stabilization by isomerization and include OH-driven abstraction steps, which may be plausible [198]. Further schemes present more isomerization channels of hexenylacetates.

Scheme 23 shows the basic mechanism for O_3 reaction with (*Z*)-3-hexenyl acetate [92,196,198–200]. The primary carbonyls formed are propanal and 3-oxypropyl acetate, while Criegee intermediates stabilize, leading to propanoic and 3-acetoxy propanoic acids.

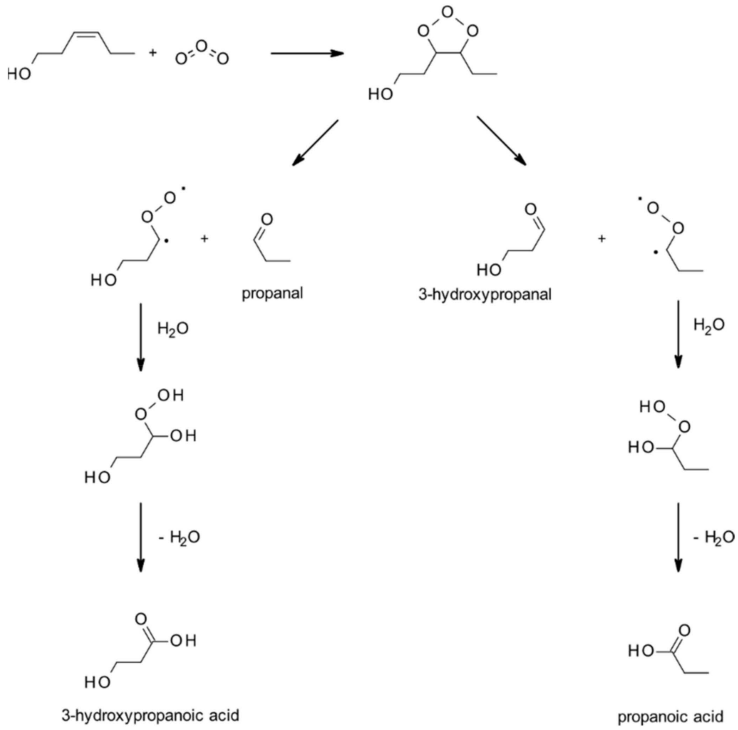

Scheme 21. The basic mechanism of the O_3 reaction with (*Z*)-3-hexenol [92,198].

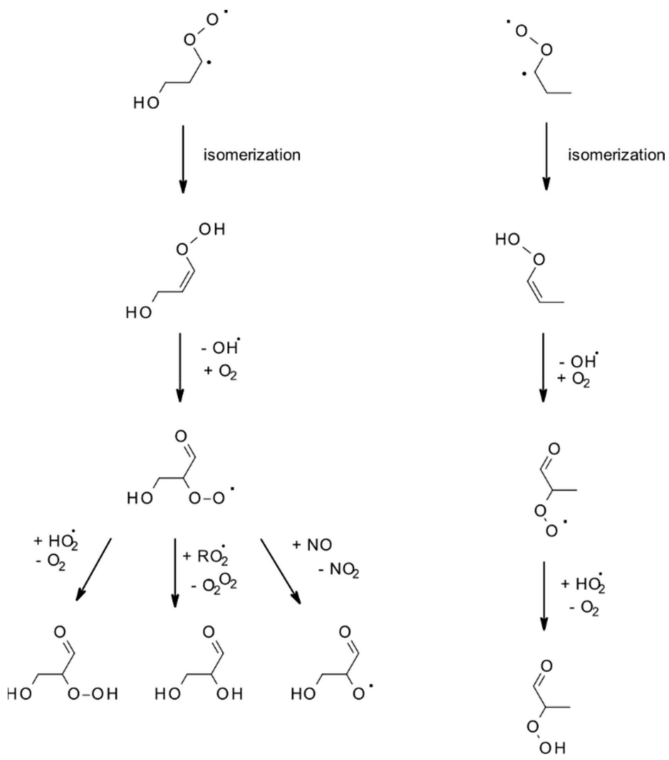

Scheme 22. Proposed hydroperoxide channels in the O_3 reaction with (*Z*)-3-hexenol [198].

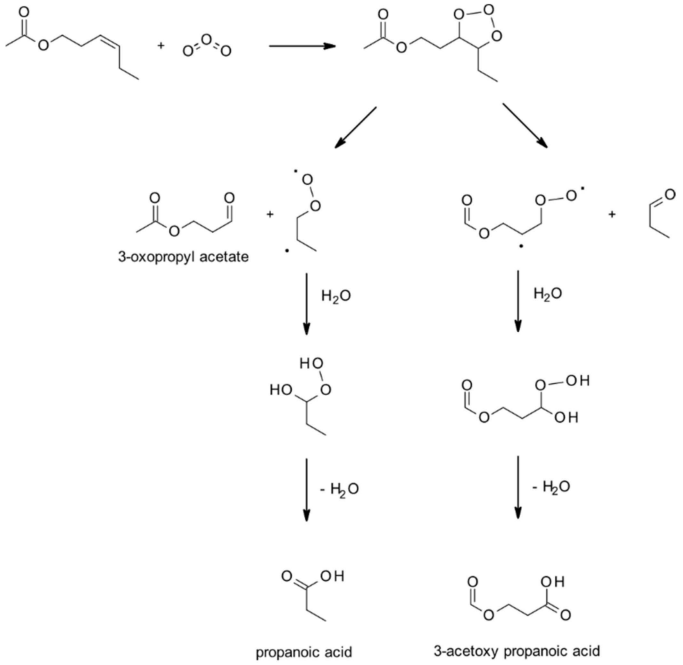

Scheme 23. The basic mechanism of the O_3 reaction with (*Z*)-3-hexenyl acetate [92,196,198–200].

Schemes 24 and 25 show the theoretically predicted stabilization pathways of Criegee intermediates, which afford several carbonyl products [196].

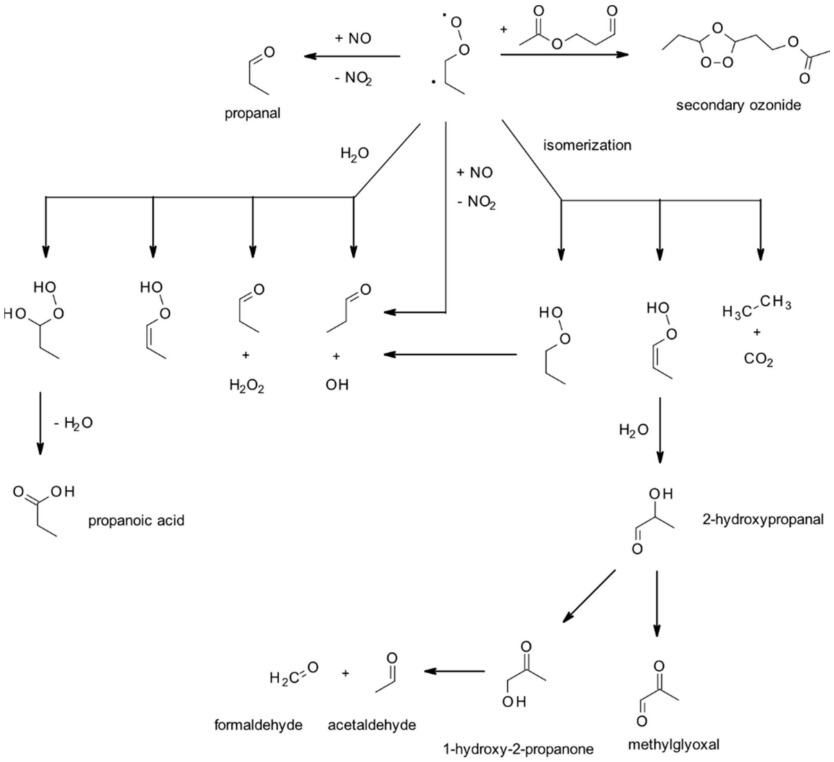

Scheme 24. Theoretically predicted stabilization channels of Criegee intermediates from (*Z*)-3-hexenyl acetate [196].

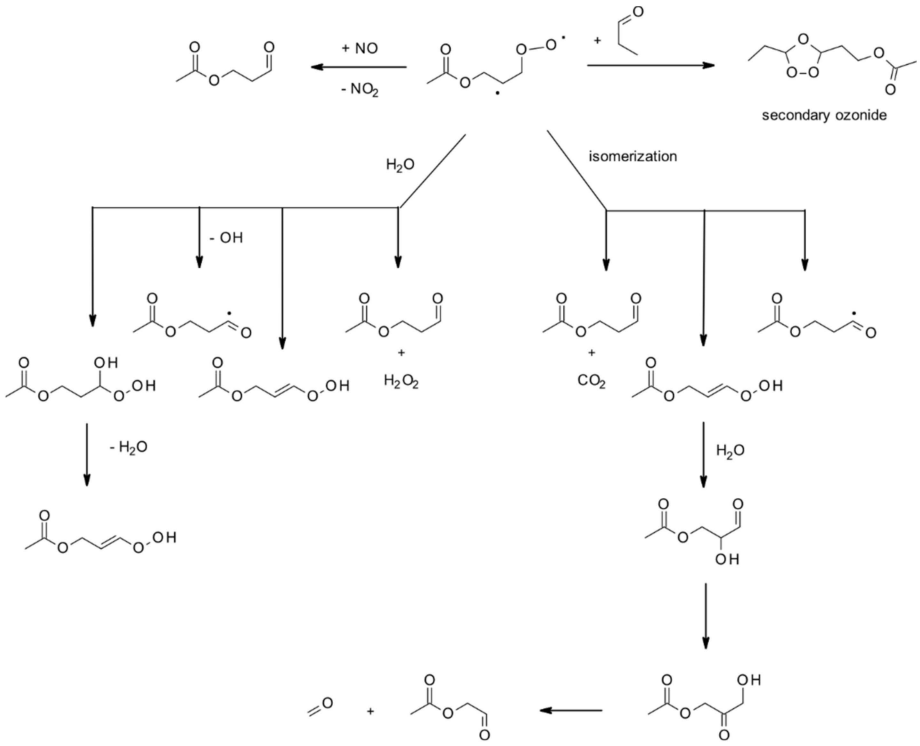

Scheme 25. More theoretically predicted stabilization paths of Criegee intermediates from (*Z*)-3-hexenyl acetate [196].

Scheme 26 shows the mechanism of the MBO ozonolysis. Smog chamber experiments confirmed some channels only at dry conditions [177,182].

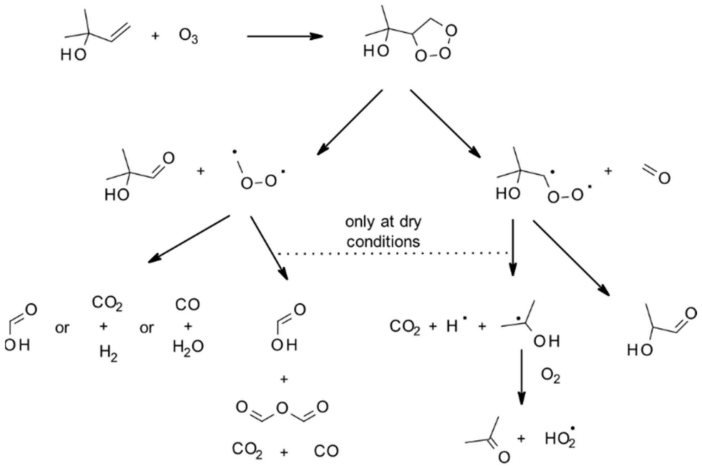

Scheme 26. Mechanism of MBO reaction with ozone [177,182].

Priya et al. [189] studied the ozonolysis of MeSa based on a simplified chemical mechanism. It contained the cycloaddition of ozone to the C_5-C_6 bond and abstraction of one oxygen by H_2 (Scheme 27). They managed to estimate the rate constants for those steps that were close to the experimental values.

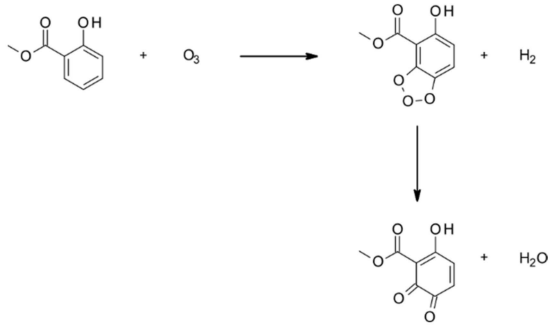

Scheme 27. Simplified mechanism of MeSa ozonolysis [189].

Products observed in GLV reactions with ozone are collected in Table 11. Table 12 briefly describes the corresponding experiments. The formation of SOA particles during ozonolysis of GLV and their composition are discussed in Section 6.1.

Table 11. Products observed in reactions of GLV with ozone.

GLV	Product	Yield, Molar	Expt Table 12	Ref.
1-penten-3-ol	Formaldehyde	0.49 ± 0.02	I	[201]
		0.34 ± 0.04	IX	[199,200]
	2-hydroxybutanal	0.46 ± 0.03	I	[201]
		0.30 ± 0.05 [a]	IX	[199,200]
	Propanal	0.15 ± 0.02	I	[201]
		0.12 ± 0.01	IX	[199,200]
(*Z*)-2-penten-1-ol	Propanal	0.39 ± 0.03	I	[201]
		0.493 ± 0.075	V	[183]
		0.51 ± 0.02	IX	[199,200]
	3-hydroxypropanal	0.33 + 0.33/−0.16	V	[183]
	Glycolaldehyde	0.43 ± 0.04	I	[201]
	2-hydroxyacetaldehyde [b]	0.53 ± 0.04	IX	[199,200]
	Formaldehyde	0.07 ± 0.02	IX	[199,200]
	Acetaldehyde	0.08 ± 0.01	IX	[199,200]
	methylglyoxal	0.04 ± 0.01	IX	[199,200]
1-penten-3-one	Formaldehyde	0.37 ± 0.02	I	[201]
	2-oxobutanal	0.49 ± 0.03	I	[201]
	SOA	0.13–0.17	I	[201]
(*Z*)-3-hexen-1-ol	Propanal	Observed	II	[92]
		0.43 ± 0.02	VIII	[202]
		0.59	IX	[199,200]
	Propanoic acid	Observed	II	[92]
	2-propenal	Observed	II	
	Acetaldehyde	Observed	II	
	Ethane	0.069 ± 0.005	VIII	[202]
	OH	0.26	VI	[174]
		0.28 ± 0.06	VIII	[202]
(*E*)-2-hexenal	OH	0.62	VI	[174]
	Butanal	0.53	IX	[199,200]
		0.527 ± 0.055	IX	[203]
	Glyoxal	0.56		[199,200]
		0.559 ± 0.037	IX	[203]
	2-oxobutanal [c]	0.074 ± 0.006		
	acetaldehyde	0.109 ± 0.020		
	Propanal	0.067 ± 0.008		
	cyclohexanone	0.032 ± 0.003		

Table 11. *Cont.*

GLV	Product	Yield, Molar	Expt Table 12	Ref.
(*Z*)-3-hexenal	Propanal	0.35 ± 0.01	VIII	[202]
	Ethane	0.079 ± 0.004		
	OH	0.32 ± 0.07		
(*Z*)-3-hexenyl acetate	Propanal	Observed	II	[92]
		0.76 ± 0.04		
	Propanoic acid	Observed	II	[92]
	2-propenal	Observed	II	
	Acetic acid	Observed	II	
	OH	0.16	VI	[174]
	acetaldehyde	0.05 ± 0.01	IX	[199,200]
	methylglyoxal	0.05 ± 0.01		
	Acetone	0.04 ± 0.01		
	glyoxal	0.003 ± 0.001		
(*E*)-2-hexenyl acetate	butanal	0.47	IX	[199,200]
		0.473 ± 0.023	IX	[203]
	1-oxyethyl acetate	0.58	IX	[199,200]
		0.583 ± 0.141 [c]	IX	[203]
	Glyoxal	0.209 ± 0.004		
	Propanal	0.102 ± 0.002		
	2-oxobutanal [c]	0.091 ± 0.007		
	Acetaldehyde	0.039 ± 0.003		
	Cyclohexanone	0.090 ± 0.004		
3-metyl-2-buten-3-ol	Acetone	0.083 ± 0.050	III	[182]
		Observed	IV	[178]
		0.67 ± 0.05	VII a	[177]
		0.23 ± 0.06	IX	[199,200]
	Formaldehyde	0.467 ± 0.055	III	[182]
		0.29 ± 0.03	IV	[178]
		0.44 ± 0.05	VII a	[177]
		0.55 ± 0.03	VII b	[177]
		0.36 ± 0.09	IX	[199,200]
	Formic acid	Observed	III	[182]
		0.14 ± 0.04	VII a	[177]
	Formic anhydride	0.16 ± 0.07		
	2-hydroxy-2-methylpropanal	0.30 ± 0.060.47 (FTIR)	IV	[178]
		0.43 ± 0.12	VII a	[177]
		0.84 ± 0.08	VII b	[177]
		0.30 ± 0.02	IX	[199,200]
	Acetaldehyde	0.01 ± 0.01		
	CO	0.343 ± 0.024	III	[182]
	CO_2	0.232 ± 0.015	III	
	OH	0.19	IV	[178]

[a] measured as 2-oxobutanal; [b] measured as glyoxal; [c] tentative.

Table 12. Experiments used to determine the rate constants listed in Table 11.

Expt	Type	Photoreactor Vol. dm^3	Material	Detection	Temp. K	*p* atm	Additions	Ref.
I	CRAC LISA	3910 977	FEP Pyrex	LP FTIR	293 [b] 295 [c]	1	CO [a]	[201]
II	Chamber	775	Teflon	GC-MS	296	1		[92]
III	Chamber	480	Teflon	LP FTIR	295	0.97		[182]
IV	Chamber	7000–8000, 5800	Teflon	API-MS/MS, GC-FID, GC-MS, GC-FTIR, LP_FTIR	298	0.97		[178]

Table 12. *Cont.*

Expt	Type	Photoreactor Vol. dm^3	Material	Detection	Temp. K	*p* atm	Additions	Ref.
V	Chamber	6500–7900	Teflon	GC-FID, GC-MS	298		Cyclohexane [a]	[183]
VI	Chamber	6700, 7900	Teflon	GC-FID	296	0.97	Cyclohexane [a] (*E*)-2-butene [d]	[174]
VII a	LISA CRAC	980 3910	Pyrex FEP	LP-FTIR GC-MS	298 [e]	1	CO [a]	[177]
VII b	CRAC	3910	FEP	LP-FTIR GC-MS	298 [f]	1	CO [a]	[177]
VIII	Chamber	6000		LP FTIR	298	1	1,3,5-trimethyl benzene [a]	[202]
IX	Chamber	3700–3900	Teflon	LC-UV	282–296	1	Cyclohexane [a]	[199,200]

[a] OH scavenger; [b] RH < 0.4%; [c] RH < 1%; [d] reference reactant; [e] RH <0.2%; [f] RH ≈30%.

4.1.4. Reactions with Cl

The gas-phase reaction of Cl atoms with GLV follows a mechanism like that for OH radicals, which includes the Cl addition to a double bond or hydrogen abstraction by Cl at a C atom with the formation of HCl [179,204,205]. Quantum-mechanical modeling showed that the addition is the dominant pathway while the hydrogen abstraction cannot be excluded [205,206]. A few studies have focused on the GLV-Cl reaction products (Tables 13 and 14).

Table 13. Products from gas-phase reactions of GLV with Cl radicals.

GLV	Product	Yield %	Expt Table 14	Ref.
1-penten-3-ol	Chloroacetaldehyde	33 ± 1	I	[205]
	Propanal	39 ± 1		
	Acetaldehyde	8 ± 3		
	1-penten-3-one	<2		
(*Z*)-2-penten-1-ol	2-chlorobutanal	19 ± 1	I	[205]
	Propanal	27 ± 1		
	Acetaldehyde	18 ± 2		
	(*Z*)-2-pentenal	36 ± 1		
(*E*)-2-hexenyl acetate	butanal formaldehyde propanal	not quantified	V	[186]
2-methyl-3-buten-2-ol	Acetone	47 ± 5	II	[179]
		48 ± 4	III	[207]
		38.5 ± 20.6	IV	[204]
	chloroacetaldehyde	53 ± 5	II	[179]
		47 ± 5	III	[207]
	formyl chloride	<11	II	[179]
		6.8 ± 5.9	IV	[204]
	formaldehyde	6 ± 2	II	[179]
		7.2 ± 0.6	III	[207]
	glycolaldehyde	2.1 ± 0.2	III	[207]
	formic acid	Below the quantification limit	III	[207]
		1.8 ± 0.1	IV	[204]
	HCl	15.7 ± 13.5	IV	[204]
	CO	20 ± 9.3		
	CO_2	<15		

Table 14. Experiments used to identify the products listed in Table 13.

Expt	Type	Photoreactor Vol. dm^3	Material	Detection	Temp. K	*p* Atm	Cl Source	Ref.
I	Bag	400	Teflon	GC-FID, GC-MS	298	1	Trichloroacetyl chloride	[205]
II	Chamber	47	Steel	LP FTIR	295		Cl_2	[179]
III	Chamber	140	Pyrex	FTIR	296 ± 2	0.92	Cl_2	[207]
IV	Chamber	480	Teflon	FTIR	298 ± 2	0.97	Cl_2	[204]
V	Bag	80	Teflon	GC-FID, GC-MS (SPME)	298	1	oxalyl chloride	[186]

Scheme 28 shows the Cl addition to 1-penten-3-ol at two possible positions accompanied by the formation of alkyl radicals that can either isomerize or react with O_2 molecules to form the peroxy radicals [205].

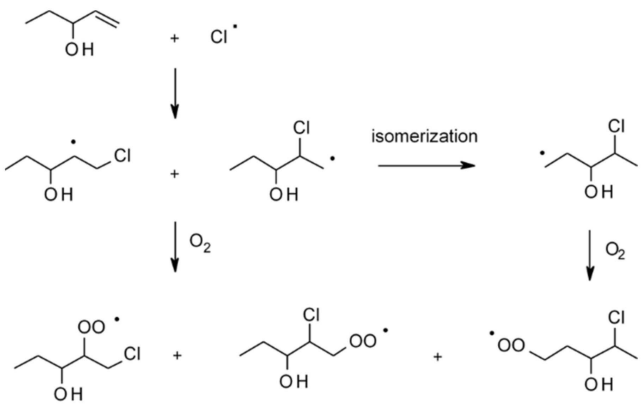

Scheme 28. The Cl radical addition to the C=C bond in 1-penten-3-ol followed by isomerization or reaction with molecular oxygen [205].

The peroxy radicals formed can isomerize or enter a self-reaction to decompose (Scheme 29). The products of those reactions can further decompose or react with molecular oxygen to give stable products and release HO_2 radicals (Scheme 30).

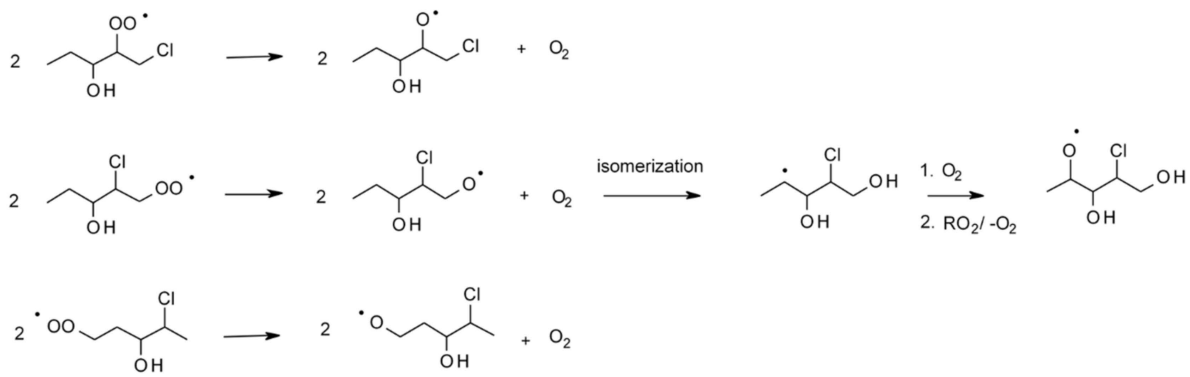

Scheme 29. The self-reaction and isomerization peroxy radicals derived from 1-penten-3-ol in the absence of NO [205].

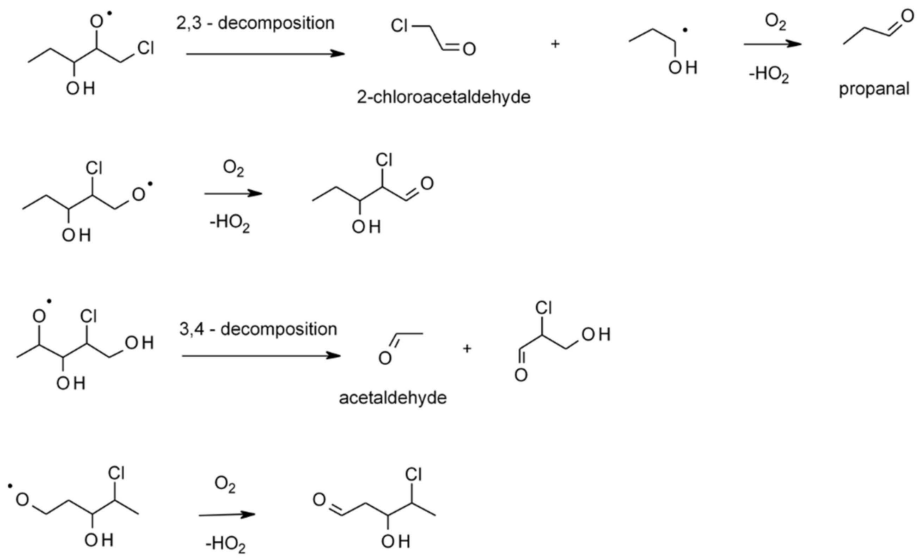

Scheme 30. Reactions of alkoxy radicals in the mechanism of the reaction of 1-penten-3-ol with Cl. [205].

The hydrogen abstraction in 1-penten-3-ol occurs preferentially at C_3 position, followed by the formation of peroxy radicals that self-react to form the alkoxy radicals. The latter can also self-react to afford 1-penten-3-one with the release of H_2O_2 (Scheme 31) [205].

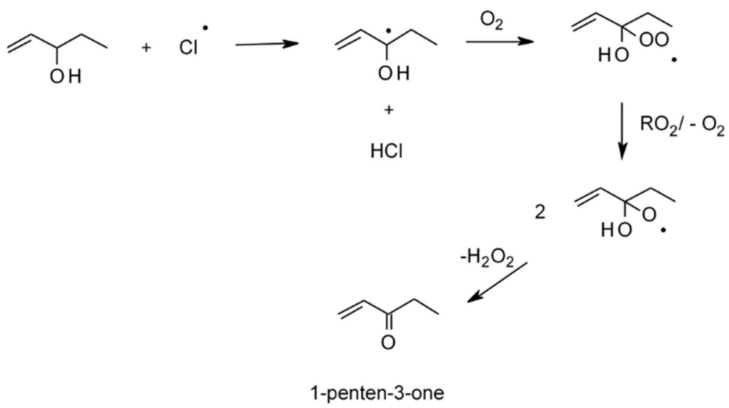

Scheme 31. Hydrogen abstraction from 1-penten-3-ol by a Cl radical, followed by the formation of a peroxy radical and a self-reaction leading to the formation of 1-penten-3-one [205].

Scheme 32 shows the reaction pathways for the alkoxy radicals derived from the Cl radical addition and hydrogen abstraction reactions of (*Z*)-2-penten-1-ol [205]. In both cases, acetaldehyde is a secondary product.

Shashikala and Janardanan [208] studied the reaction of (*E*)-2-hexenal with Cl radicals using the density functional theory. The geometry optimization used the MP2/6-31G * level of theory (B3), and later single point energies of all MP2/6-31G * optimized stationary points were computed using BHANDHLYP/6–311 + G** (B2) level of theory. They found that the Cl radical was more reactive towards (*E*)-2-hexen-1-al than other atmospheric oxidants (OH, O_3, NO_3), both in the Cl addition and H abstraction channels.

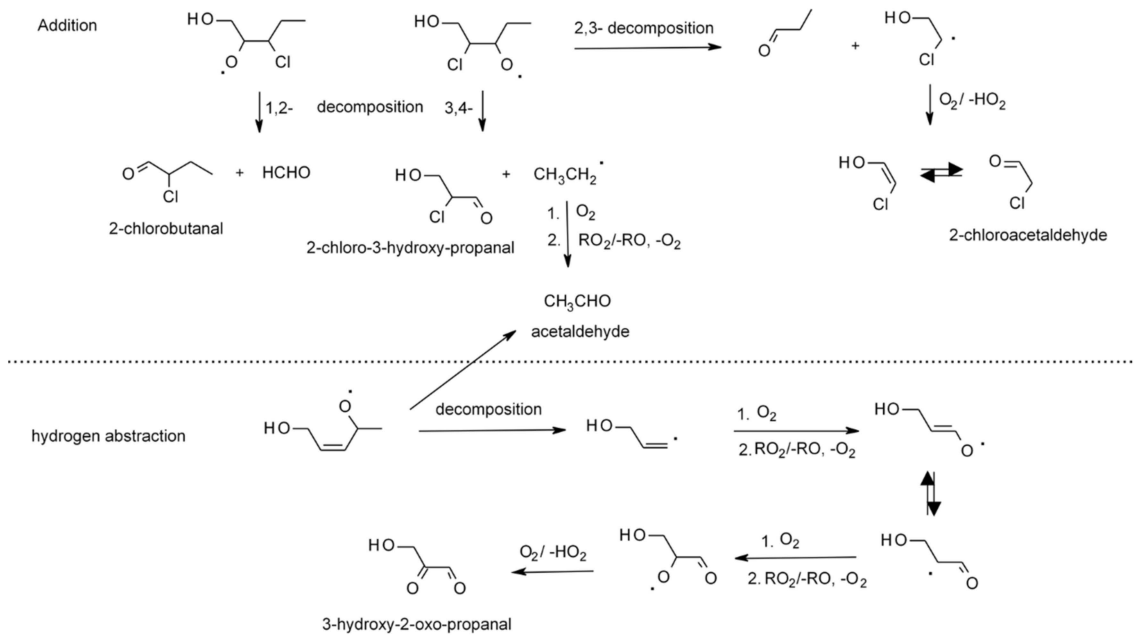

Scheme 32. Reaction of alkoxy radicals produced in the addition and hydrogen abstraction channel of the (*Z*)-2-penten-1-ol reaction with Cl radicals [205].

The reaction of MBO with Cl was studied experimentally [179,207] and theoretically at the MP2(full)/6-311G(d,p) and CCSD(T)/6-311þG(d,p) level of theory [206]. In the absence of NO, the Cl addition appeared more favorable than the hydrogen abstraction. The addition at the C_4 position provided almost 50% of the products by the molar yield. The identification of glycolaldehyde and formic acid among the products revealed the formation of intermediate OH radicals [207]. Scheme 33 shows the plausible transformation of the alkoxy radicals produced from the initial reactions of MBO with Cl.

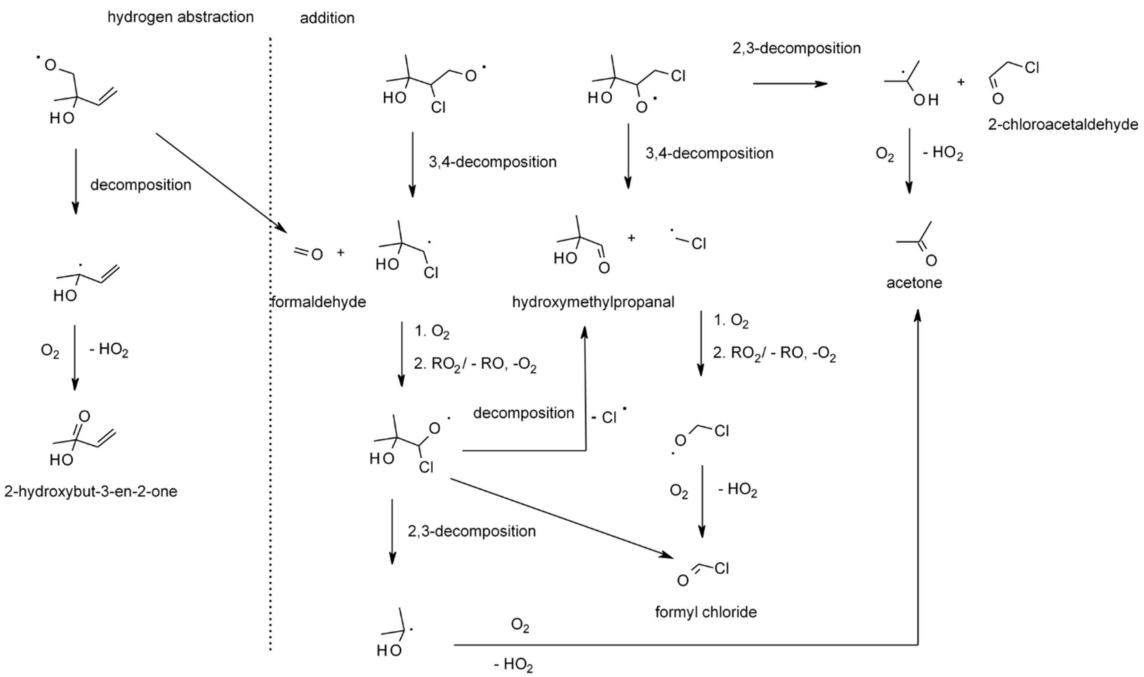

Scheme 33. The reaction of the alkoxy radicals derived from the MBO reactions with Cl (the addition and hydrogen abstraction channels) in the absence of NO [179,206,207].

In NO's presence, the peroxy radicals derived from the MBO reaction with Cl convert to alkoxy radicals (Scheme 34) [204]. Schemes 35 and 36 show further reactions of the alkoxy radicals.

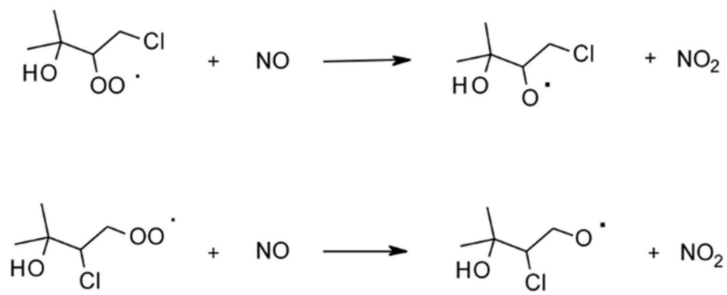

Scheme 34. Reactions of peroxy radicals from the MBO-Cl reaction with NO lead to alkoxy radicals' formation [204].

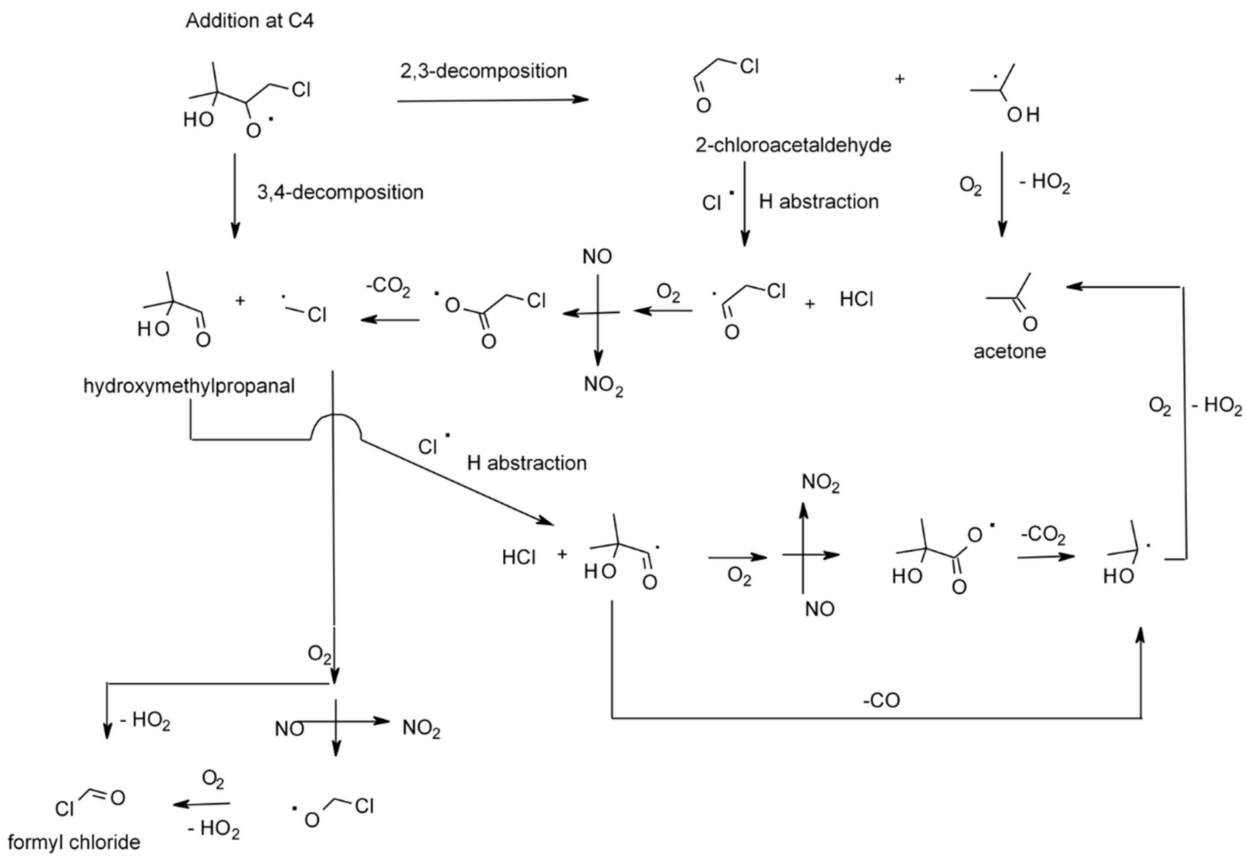

Scheme 35. Reactions of alkoxy radicals resulting from the Cl addition to MBO at the C_4 position in the presence of NO and O_2 [204].

Scheme 37 shows the reactions of the alkoxy radicals formed by the hydrogen abstraction from MBO [204].

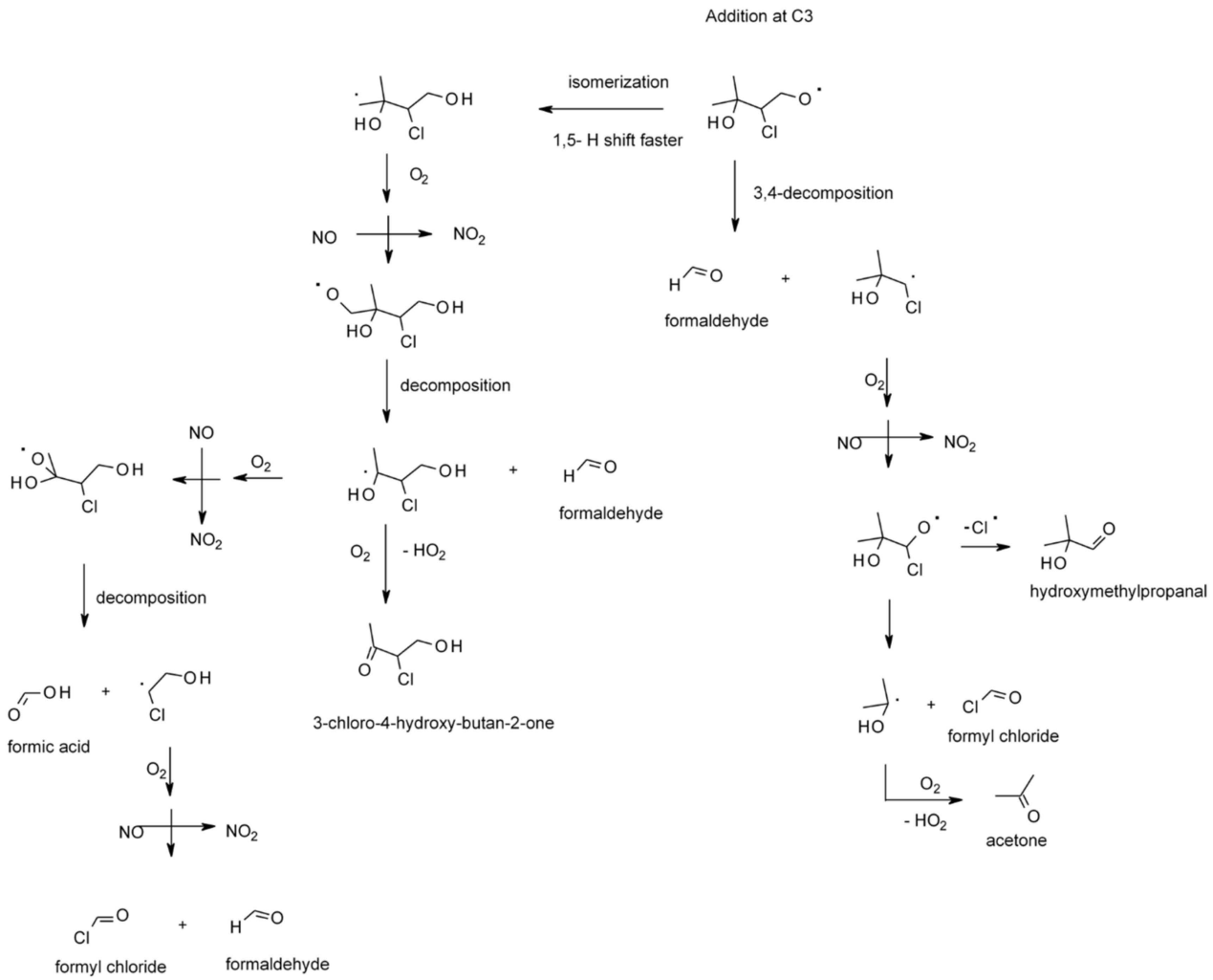

Scheme 36. Reactions of alkoxy radicals resulting from the Cl addition to MBO at the C_3 position in the presence of NO and O_2 [204].

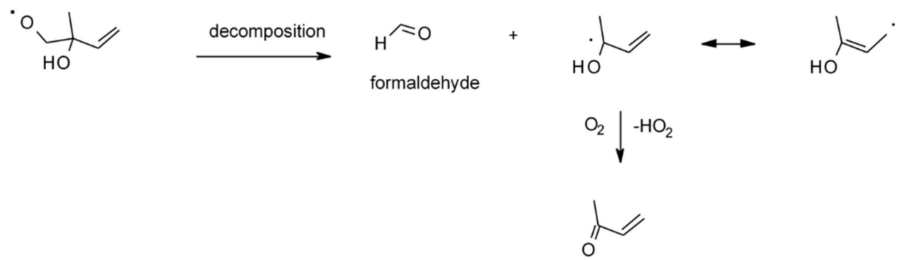

Scheme 37. The reaction of an alkoxy radical generated by the hydrogen abstraction from MBO at the methyl group in the presence of NO and O_2 [204].

Elizabeth Gaona-Colmán et al. [186] studied the Cl addition to (*E*)-2-hexenyl acetate. Scheme 38 shows the plausible transformation of the alkoxy radicals formed by that reaction.

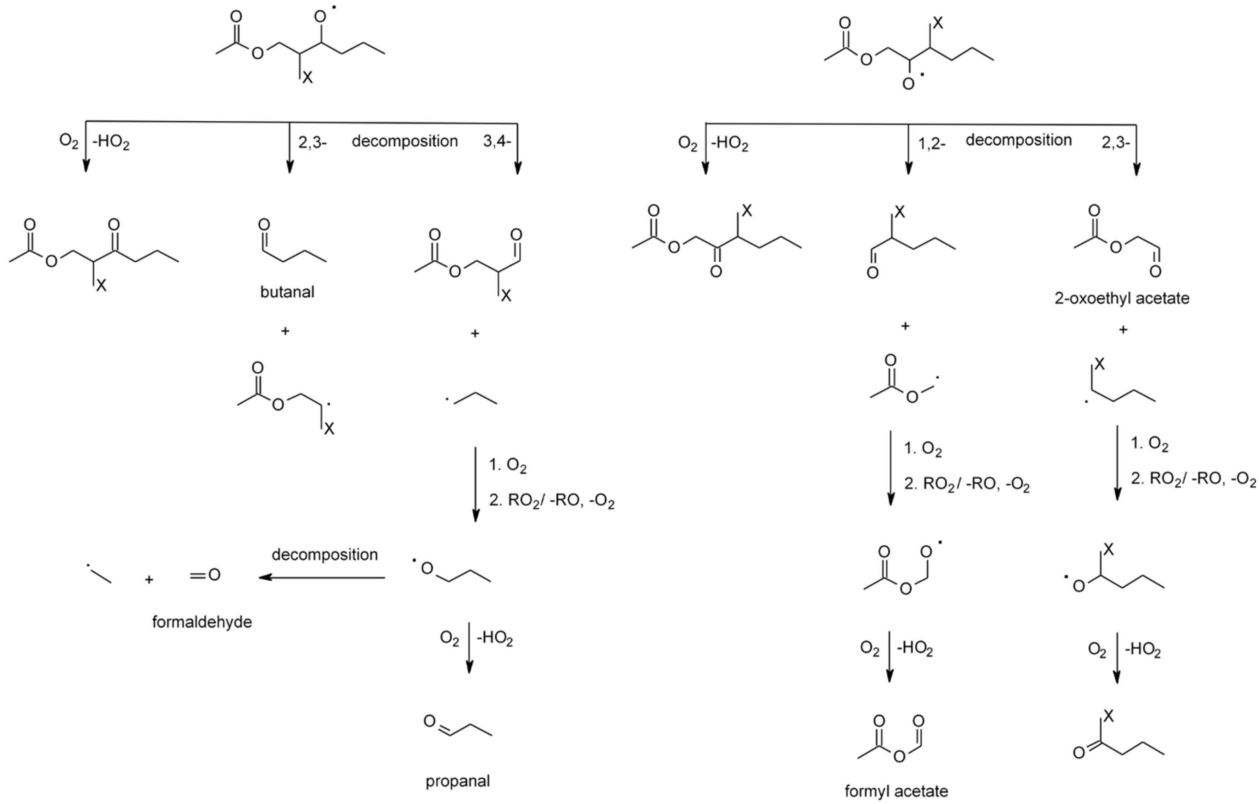

Scheme 38. Reaction of alkoxy radicals derived from the (*E*)-2-hexenyl acetate reaction with Cl radicals: decomposition and addition of molecular oxygen followed by removal of HO_2 [186].

Priya and Senthilkumar [209] theoretically studied the mechanism of Cl radical reactions with MeSa using density functional theory at B3LYP and M06-2X levels of theory with 6-311++G(d,p) basis set. They found that the reaction involved the hydrogen abstraction at the meta position throughout all courses. They concluded that the reaction of MeSa with a Cl radical via hydrogen abstraction from the aromatic ring followed by reaction with O_2 results in the formation of methyl 3-peroxy-2-hydroxy benzoate radical intermediate via a barrierless reaction (Scheme 39).

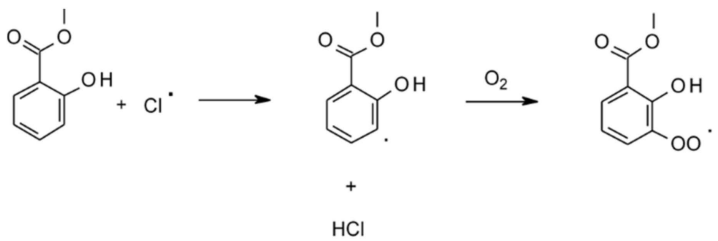

Scheme 39. Dominating hydrogen abstraction channel at the meta position of MeSa and formation of peroxy radicals [209].

The authors evaluated reactions of methyl 3-peroxy-2-hydroxy benzoate radicals with HO_2, NO_2, and NO. The reaction with NO was the most favorable, with the lowest energy barrier close to 6.7 kJ mol^{-1} (Scheme 40) [209].

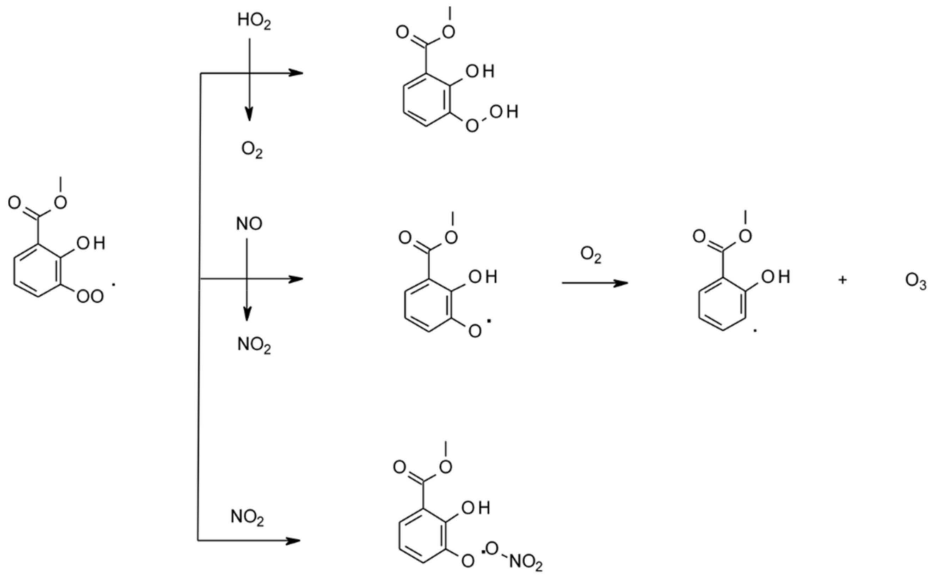

Scheme 40. Possible reaction pathways of MeSa-based peroxy radicals in the presence of NO [209].

4.1.5. Gas-Phase Photolysis

O'Connor et al. [161] analyzed the sunlight photolysis of (*E*)-2-hexenal, (*Z*)-3-hexenal and (*E*,*E*)-2,4-hexadienal in a Euphore smog chamber in dry purified air (0.05–1.0% RH and 286–294 K) using LP FTIR, GC-FID, and GC-MS with EI ionization. The samples were preconcentrated on glass beads at −160 °C, then rapidly desorbed onto the chromatographic column. The authors found that CO was the major product (34% yield) of the photolysis of (*Z*)-3-hexenal (which gave small amounts of products) according to the Norrish type 1 mechanism (Scheme 41). The (*Z*)-2-pentenyl radical form reacted with O_2 to produce the pentenyl peroxy radical, which, in turn, self-reacted to a pentenyl oxy radical. The pentenyl oxy radical reacted with oxygen to finally give (*Z*)-3-pentenal, which showed in the experiments. On the other hand, (*E*)-2-hexen-1-al was reversibly converted to (*Z*)-2-hexen-1-al.

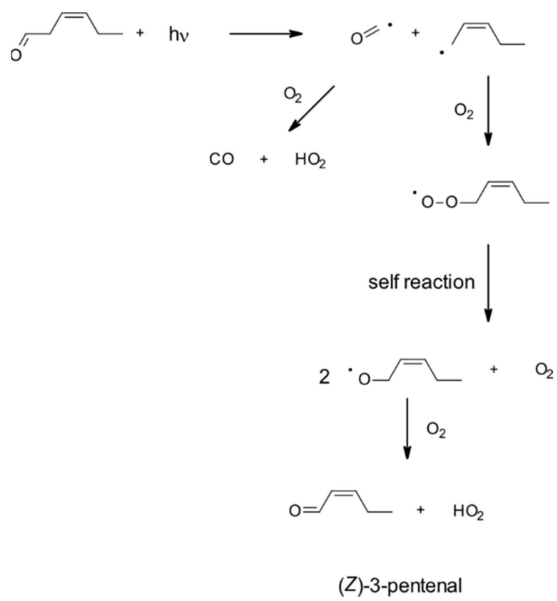

Scheme 41. Photolysis of (*Z*)-3-hexenal in the presence of oxygen [161].

Tang and Zhu [166] studied the formation of HCO radicals from the gas-phase photolysis of n-hexanal (and n-heptanal) using cavity ring-down spectroscopy. Scheme 42 shows thermodynamically feasible dissociation pathways after UV excitation of n-hexanal. The radical yields ranged from 0.1 to 0.08 for 2–8 mmHg partial pressures of hexenal. Furthermore, they used mass spectrometry to identify several other products: acetaldehyde CH_3CHO and butene C_4H_8 (yield 0.28–0.31); CO and pentane C_5H_{12} (yield 0.20); C_5H_{11}, 2-methylcyclopentanol (yield 0.12); and 2-ethylcyclobutanol (yield 0.3).

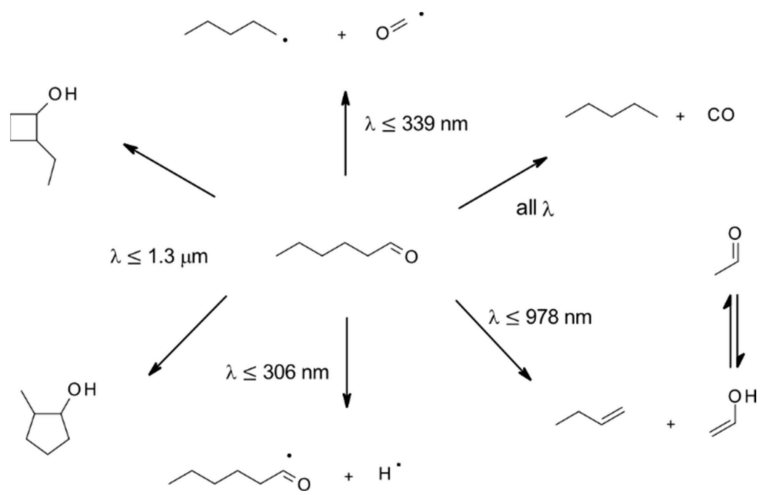

Scheme 42. Thermodynamically feasible dissociation pathways after UV excitation of n-hexanal [166].

4.2. Gas-Phase Kinetics

This section presents the rate constants for gas-phase reactions of GLV with OH and NO_3 radicals, O_3, and Cl atoms, and the photolysis rate constants. The rate constants were determined either by the relative or absolute approach. The relative method compares a GLV reaction with an oxidant to the oxidant reaction with another compound for which the rate constant is known. From that comparison, the method derives a relative rate constant for the GLV-oxidant reaction. The absolute method directly follows the decay of GLV and the oxidant to determine its absolute rate constant.

4.2.1. Gas-Phase Reactions with OH Radicals

Table 15 contains the rate constants for gas-phase reactions of GLV with OH radicals determined experimentally at single temperatures, Table 16 briefly describe the experiments carried out to determine the constants. Table 17 shows the Arrhenius parameters for reactions studied over temperature ranges, Table 18 briefly describe the experiments carried out to determine the constants. The OH radicals were generated using several methods: photolysis of H_2O_2 at 248, 252, or 254 nm; photolysis of H_2O at 165 nm; photolysis of methyl nitrite CH_3ONO at 300 nm (Equation (15)); photolysis of ethyl nitrite CH_3CH_2ONO; photolysis of HNO_3 at 248 nm; photolysis of HONO at 355 nm; reaction of F atoms with H_2O or H atoms with NO_2.

Table 15. Relative and absolute ([a]) rate constants for gas-phase reactions of GLV with OH at single temperatures.

GLV	k cm^3 $molecule^{-1}$ s^{-1}	T K	P Atm	Expt Table 16	Ref.
Pentan-1-ol	$(1.0 \pm 0.1) \times 10^{-11}$	298	1	I	[210]
	$(1.08 \pm 0.11) \times 10^{-11}$ [a]	296	0.03–0.07	II	[211]
	$(1.20 \pm 0.16) \times 10^{-11}$ [a]	298 ± 2	1	III	[212]
	$(1.05 \pm 0.13) \times 10^{-11}$	ibid		IV	
	$(1.11 \pm 0.11) \times 10^{-11}$	298 ± 2	740 mmHg	V	[184]
	$(1.23 \pm 0.10) \times 10^{-11}$	295 ± 2	1	VI	[213]
	$(1.26 \pm 0.07) \times 10^{-11}$ $(1.20 \pm 0.06) \times 10^{-11}$	298 ± 2	1	VII	[214]
1-penten-3-ol	$(6.7 \pm 0.9) \times 10^{-11}$	298	1	VIII	[185]
(*Z*)-2-penten-1-ol	$(1.06 \pm 0.15) \times 10^{-10}$				
(*E*)-2-pentenal	$(2.35 \pm 0.21) \times 10^{-11}$ [a]	298	0.132–0.526	IX	[85]
1-penten-3-one	3.6×10^{-11} [b]	298	1	X	[215]
Hexan-1-ol	$(1.58 \pm 0.35) \times 10^{-11}$	296 ± 2	1	XI	[216]
(*Z*)-2-hexen-1-ol	$(1.1 \pm 0.4) \times 10^{-10}$	296 ± 2		XII	[217]
	0.95×10^{-10} [b]	298			
	$(8.53 \pm 1.36) \times 10^{-11}$ [e]	298	1	XIII	[171]
(*E*)-2-hexen-1-ol	$(1.0 \pm 0.3) \times 10^{-10}$	298	1	XIV	[176]
	$(8.08 \pm 1.33) \times 10^{-11}$ [e]	298	1	XIII	[171]
(*Z*)-3-hexen-1-ol	$(1.2 \pm 0.2) \times 10^{-10}$	298	1	XIV	[176]
	$(9.57 \pm 2.42) \times 10^{-11}$ [a]	298		XV	[57]
	$(1.08 \pm 2.2) \times 10^{-10}$	296 ± 2	0.974	XVI	[174]
	$(1.01 \pm 0.16) \times 10^{-10}$ [e]	298	1	XIII	[171]
(*E*)-3-hexen-1-ol	$(1.4 \pm 0.3) \times 10^{-10}$	298	1	XIV	[176]
	$(1.14 \pm 0.14) \times 10^{-10}$	298 ± 2	1	XVII	[175]
	$(0.8 \pm 0.1) \times 10^{-10}$	296 2	0.98 ± 0.01	XII	[217]
	1.28×10^{-10}	298			
	$(9.10 \pm 1.50) \times 10^{-11}$ [e]	298	1	XIII	[171]
(*E*)-4-hexen-1-ol	$(7.14 \pm 1.20) \times 10^{-11}$ [e]	298	1	XIII	[171]
(*Z*)-4-hexen-1-ol	$(7.86 \pm 1.30) \times 10^{-11}$ [e]				
n-hexanal	$(2.60 \pm 0.21) \times 10^{-11}$ [a]	298	0.132–0.526	IX	[85]
	$(2.86 \pm 0.13) \times 10^{-11}$	298 ± 2	1.00 ± 0.01	XVIII	[218]
	$(3.17 \pm 0.15) \times 10^{-11}$	296 ± 2	1	XIX	[219]
	$(2.71 \pm 0.20) \times 10^{-11}$	298 ± 2	1	XX	[220]
(*E*)-2-hexenal	$(0.681 \pm 0.049) \times 10^{-11}$	296 ± 2	0.974	XVI	[174]
	$(2.95 \pm 0.45) \times 10^{-11}$ [a]	298	0.132–0.526	IX	[85]
	$(3.95 \pm 0.17) \times 10^{-11}$	298 ± 2	1	XXI	[221]
(*Z*)−3-hexenal	$(6.9 \pm 0.9) \times 10^{-11}$	298	1	XXII	[160]
(*Z*)- 3-hexenyl formate	$(4.61 \pm 0.07) \times 10^{-11}$	298	1	XXIII	[222]
	$(4.24 \pm 0.07) \times 10^{-11}$ [b]				
(*E*)-2-hexenylacetate	$(6.88 \pm 1.41) \times 10^{-11}$	298 ± 1	750 mmHg	XXIV	[186]
(*Z*)- 3-hexenyl acetate	$(1.21 \pm 0.71) \times 10^{-11}$	296 ± 2	0.974	XVI	[174]
(*Z*)-3-hepten-1-ol	$(1.28 \pm 0.23) \times 10^{-10}$	298 ± 2	1	XVII	[175]
2-methyl-3-buten-2-ol	$(6.9 \pm 1.0) \times 10^{-11}$	295 ± 1	0.921	XXV	[179]
	$(5.67 \pm 0.13) \times 10^{-11}$	296 ± 2	0.974	XIX	[223]
	$(3.9 \pm 1.2) \times 10^{-11}$	298 ± 2	0.974 ± 0.007	XXVI	[224]
	$(6.6 \pm 0.5) \times 10^{-11}$	298 ± 2	1	XXVII	[225]
	$(5.6 \pm 0.6) \times 10^{-11}$	298 ± 2	1	XXVIII	[177]
	$(5.49 \pm 0.44) \times 10^{-11}$ [a] $(6.32 \pm 0.27) \times 10^{-11}$ [a,d] $(6.61 \pm 0.66) \times 10^{-11}$ [a,c]	300	5	XXIX	[226]

Table 15. *Cont.*

GLV	k cm^3 $molecule^{-1}$ s^{-1}	T K	P Atm	Expt Table 16	Ref.
(*Z*)-3-octen-1-ol	$(1.49 \pm 0.35) \times 10^{-10}$	298 ± 2	1	XVII	[175]
Nonanal	$(3.6 \pm 0.7) \times 10^{-10}$	298	1	XXX	[188]
	$(2.88 \pm 0.20) \times 10^{-11}$	298 ± 2	1	XX	[220]
Methyl salicylate	$(3.20 \pm 0.46) \times 10^{-12}$	298	1	XXXI	[227]

[a] absolute rate constant; [b] from SAR or LFER; [c] reaction with OD; [d] with 15% of O_2 added; [e] theoretical rate constants for the addition and hydrogen abstraction channels are given in Section 4.1.1 (Table 6).

Table 16. Experiments used to determine the rate constants listed in Table 15.

Expt	Photoreactor Type	Vol. dm^3	Material	Detection	OH Source	Add.	Reference Reactants	Ref.
I	Bag	140	Teflon	GC-FID	H_2O_2		Pentane 1,3-dioxolane Cyclohexane	[210]
II	Bulbs	5	Pyrex	RF	H_2O		no	[211]
III	Cylinder	50	Teflon	GC-FID	H_2O_2 or CH_3ONO		Cycloxexane	[212]
IV	Cell	1	Steel	LP UV			no	
V	Cylinder	480	Duran	LP FTIR; GC-PI	CH_3ONO	NO [a]	Cycloxexane	[184]
VI	Bag	100	Teflon	GC-FID	H_2O_2		Propane; hexane	[213]
VII	Bag	100	Tedlar	GC-MS	CH_3ONO		Cyclohexane; p-xylene	[214]
VIII	Chamber	47	Steel	LP FTIR	CH_3CH_2ONO		propene	[185]
IX	Cell PLP	0.2	Pyrex	LIF	H_2O_2		no	[85]
X	SSR LFER							[215]
XI	Chamber	7600	Teflon	GC-FID	CH_3ONO	NO [a]	Cyclohexane	[216]
XII	Bag	200	Teflon	GC-FID	H_2O_2		Allyl ether Cycloxexane 1-methyl-cyclohexane	[217]
XIII	Bag	150	Teflon	GC-FID	H_2O_2		Cyclohexane 2-methyl-3-buten-1-ol	[171]
XIV	Bag	80	Teflon	GC-FID, SPME	H_2O_2		Methyl methacrylate (*E*)-2-buten-1-ol	[176]
XV	Cell PLP	0.2	Pyrex	UV, LIF	H_2O_2		no	[57]
XVI	Chamber	6700 7900	Teflon	GC-FID	CH_3ONO	NO [a]	(*E*)-2-butene	[174]
XVII	Chamber	1080	Quartz	LP FTIR	H_2O_2		(*E*)-2-butene isobutene	[175]
XVIII	Reactor	250	Steel	LP FTIR	CH_3ONO Other nitrites		Propene 1-butene	[218]

Table 16. *Cont.*

Expt	Photoreactor			Detection	OH Source	Add.	Reference Reactants	Ref.
	Type	Vol. dm^3	Material					
XIX	Chamber	7000	Teflon	GC-FID	CH_3ONO	NO [a]	1,3,5-trimethylbenzene Methyl vinyl ketone	[219, 223]
XX	Cylinder	108O	Pyrex	LP FTIR	CH_3ONO		(*E*)-2-butene; Methylvinyl ketone	[220]
XXI	Bag	100	Tedlar	GC-MS	CH_3ONO		2-methyl-2-butene, β-pinene	[221]
XXII	Chamber	6000	PFA	LP FTIR	CH_3ONO		1,3,5-trimethylbenzene	[160]
XXIII	Bag	400	Teflon	GC-FID	H_2O_2		Cyclohexane, n-octane, 1-butene	[222]
XXIV	Bag	80	Teflon	GC-FID	H_2O_2		(*E*)-3-hexen-1-ol 2-buten-1-ol	[186]
XXV	Chamber	47	Steel	LP FTIR	CH_3ONO		Ethylene, propylene	[179]
XXVI	Chamber	480	Teflon	LP FTIR	H_2O_2		Isoprene, propene	[224]
XXVII	Chamber	6000	Teflon	LP FTIR	CH_3ONO	NO [a]	di-n-butyl ether, propene	[225]
XXVIII	LISA CRAC EUPORE	980, 3910 2×10^5	Pyrex FEP Teflon	LP FTIR	HONO H_2O_2	NO_x	Isoprene	[177]
XXIX	Discharge-flow reactor	0.02	Pyrex	LIF	F + H_2O, H + NO_2		no	[226]
XXX	Chamber	5000	Teflon	GC-FID	Isopropyl nitrite	NO_x	Octane	[188]
XXXI	ICARE-CHRS chamber	7300	Teflon	HR PTR-TOF-MS	CH_3ONO		Methyl ethyl ketone; Toluene; Di-n-butyl ether	[227]

[a] suppresses the O_3 formation.

Table 17. Absolute ([a]) rate constants for gas-phase reactions of GLV with OH radicals—Arrhenius parameters and values at selected temperature T.

GLV	A cm^3 Molecule^{-1} s^{-1}	E_A/R K	k_T cm^3 Molecule^{-1} s^{-1}	T K	T Range K	P Atm	Expt Table 18	Ref.
Pentan-1-ol	$(6.7 \pm 3.8) \times 10^{-12}$ [a]	$-(132 \pm 176)$	$(1.04 \pm 0.59) \times 10^{-11}$ [a]	298	273–373	100 mmHg	I	[210]
1-penten-3-ol	$(6.8 \pm 0.7) \times 10^{-12}$ [a]	$-(690 \pm 20)$	$(7.12 \pm 0.73) \times 10^{-11}$ [a]	297	243–404	20–100 mmHg	II	[228]
	$(7.7 \pm 1.6) \times 10^{-12}$ [a]	$-(606 \pm 60)$ [a]	$(5.65 \pm 0.76) \times 10^{-11}$ [a]					
(*E*)-2-penten-1-ol	$(6.8 \pm 0.8) \times 10^{-12}$ [a]	$-(680 \pm 20)$	$(6.76 \pm 0.70) \times 10^{-11}$ [a]	298	263–353		III	[57]
1-penten-3-one	$(4.4 \pm 2.8) \times 10^{-12}$ [a]	$-(507 \pm 180)$ [a]	$(2.36 \pm 0.47) \times 10^{-11}$ [a]					
(*E*)-2-pentenal	$(7.9 \pm 1.2) \times 10^{-12}$ [a]	$-(510 \pm 20)$	$(4.3 \pm 0.6) \times 10^{-11}$ [a]	297	244–374	0.03–0.197	IV	[173]
(*E*)-2-hexen-1-ol	$(5.4 \pm 0.6) \times 10^{-12}$ [a]	$-(690 \pm 20)$	$(6.15 \pm 0.75) \times 10^{-11}$ [a]	298	263–353		III	[57]
(*Z*)-3-hexen-1-ol	$(1.3 \pm 0.1) \times 10^{-11}$ [a]	$-(580 \pm 10)$	$(1.06 \pm 0.12) \times 10^{-10}$ [a]	297	243–404	20–100 mmHg	II	[228]
hexanal	$(4.2 \pm 0.8) \times 10^{-12}$ [a]	$-(565 \pm 65)$	$(2.78 \pm 0.50) \times 10^{-11}$ [a]	298	263–353	0.066	IV	[159]
(*E*)-2-hexenal	$(7.5 \pm 1.1) \times 10^{-12}$ [a]	$-(520 \pm 30)$	$(4.4 \pm 0.5) \times 10^{-11}$ [a]	297	244–374	0.03–0.197	IV	[173]
	$(9.8 \pm 2.4) \times 10^{-12}$ [a]	$-(455 \pm 80)$	$(4.68 \pm 0.50) \times 10^{-11}$ [a]	298	263–353	0.066	IV	[159]
2-methyl-3- buten-2-ol	$(8.2 \pm 1.2) \times 10^{-12}$ [a] 8.43×10^{-12} [b]	$-(610 \pm 50)$ -619.4 [b]	$(5.4 \pm 0.4) \times 10^{-11}$ [a] $(6.4 \pm 0.6) \times 10^{-11}$ [b]	299 298	254–410 254–360	1.3	IV	[165]
Methyl salicylate	5.0962×10^{-11} [a,c,d]	917	1.9595×10^{-12} [a,c,d]	298	278–298	1	V	[190]
	1.54×10^{-12} [a,d,e]	5053.9	6.64×10^{-20} [a,d,e]	298	278–350	1	VI	[189]

[a] absolute rate constants; [b] values for reactions with OD radicals; [c] converted from the original units; [d] calculated theoretically; [e] initial OH addition, the paper contains Arrhenius equations for other steps of the reaction mechanism.

Table 18. Experiments used to determine the rate constants listed in Table 17.

Expt	Photoreactor			Detection	OH Source	Ref.
	Type	Vol. dm^3	Material			
I	Cell, LFP		Pyrex	LIF	H_2O_2	[210]
II	Cell, LFP	0.15	Pyrex	LIF	H_2O_2	[173,228]
III	Cell PLP	0.2	Pyrex	UV, LIF	H_2O_2	[57,159]
IV	Cell, PLP	0.15	Pyrex	LIF	HONO, DONO	[165]
V	RKKM theory at MN15-L/aug-cc-pVTZ level with Eckart tunneling correction					[190]
VI	DFT theory using B3LYP, M06-2X, and MPW1K functionals with 6-311++G(d,p) basis set.					[189]

Most of the reactions have negative activation energies, as their rate decreases with increasing temperature. The exception is methyl salicylate, which is the only aromatic compound studied. In some cases, evaluated theoretically, the additional channel of a GLV-OH reaction had a positive activation energy while the hydrogen abstraction channel had a negative one [189].

Gibilisco et al. [176] correlated the rate constants for reactions of OH radicals with unsaturated alcohols obtained experimentally ((*E*)-2-hexen-1-ol, (*E*)-3-hexen-1-ol, and (*Z*)-3-hexen-1-ol, Table 15 and from the literature with the energy of the highest occupied molecular orbital (HOMO) of those alcohols calculated with the Gaussian package:

$$\ln k_{OH}\ (cm^3\ molecule^{-1}\ s^{-1}) = -(1.3 \pm 0.1)\ E_{HOMO} - (10.3 \pm 1.3) \quad (10)$$

Based on their results and the literature data, Gibilisco et al. [175] correlated the rate constants for reactions of GLV with OH radicals against those for reactions with Cl atoms:

$$\log k_{OH} = (0.29 \pm 0.04) \log k_{Cl} - 10.8 \quad (11)$$

Peirone et al. [217] showed that the SAR relation [229] based on group-reactivity factors provided an estimation close to the experimental rate constants (Table 15).

Basandorj et al. [226] showed that the gas-phase reactions of OH and OD radicals with 2-methyl-3-buten-2-ol were faster by 15% in the presence of O_2. At temperatures higher than 335 K, that rate constant of those reactions depended on the total pressure and was analyzed for the dependence on the concentration of an inert gas component. The ab initio theoretical calculation supported the analysis. The second-order rate constant for OH radicals decreased with pressure and temperature according to Equation (12):

$$k^{II} = \left(\frac{k_0(T)[M]}{1 + \frac{k_0(T)[M]}{k_\infty(T)}} \right) F_c^{\left(\frac{1}{1+[\log(k_0(T)[M]/k_\infty(T))]^2} \right)} \quad (12)$$

where k_0 is the thermolecular rate constant at the low-pressure limit, k_∞ is the rate constant at the high-pressure limit, F_c is the collisional broadening factor, and M is the inert gas. For $k_\infty = 8.3 \times 10^{-12} \exp(610/T)$ cm^3 $molecule^{-1}$ s^{-1} at 100 mmHg [165] and $F_c = 0.6$, the temperature dependence of k_0 was evaluated from the experimental data:

$$k_0 = (2.5\ \pm 7.4) \times 10^{-32} \exp\left[\frac{4250 \pm 1150}{T} \right] cm^6 molecule^{-2} s^{-1} \quad (13)$$

The kinetic Equation (13) was consistent with a Lindemann-Hinshelwood mechanism:

$$OH + MBO \rightarrow HO - MBO^* \quad (14a)$$

$$OH + MBO \rightarrow HO - MBO^* \quad (14b)$$

$$\text{HO-MBO*} + \text{M} \rightarrow \text{HO} - \text{MBO} + \text{M*} \quad (14c)$$

DFT calculations showed that the radical formed by the addition of OH to the internal carbon was more stable than that formed by the addition to the terminal carbon. Additionally, the authors provided geometries, energies, and vibrational frequencies of all structures considered.

Formation of OH radicals by photodissociation of methyl nitrite often used to generate OH radicals in laboratory experiments follows the mechanism below (e.g., [225]):

$$CH_3ONO + h\nu \rightarrow CH_3O + NO \quad (15a)$$

$$CH_3O + O_2 \rightarrow CH_2O + HO_2 \quad (15b)$$

$$HO_2 + NO \rightarrow OH + NO_2 \quad (15c)$$

Methyl nitrite can be synthesized by the dropwise addition of 50% sulfuric acid to a saturated solution of $NaNO_2$ in methanol.

4.2.2. Gas-Phase Reactions with NO_3 Radicals

Table 19 contains the rate constants for gas-phase reactions of GLV with OH radicals determined experimentally at single temperatures, Table 20 briefly describe the experiments in which the constants were determined. Table 21 shows the Arrhenius parameters for reactions studied over temperature ranges, Table 22 briefly describe the experiments in which the constants were determined. Methods used to generate the NO_3 radicals include thermal decomposition of N_2O_5, the reaction of F atoms with HNO_3, and the reaction of NO_2 with O_3.

Table 19. Relative and absolute ([a]) rate constants for gas-phase reactions of GLV with NO_3 at single temperatures.

GLV	k cm^3 $molecule^{-1}$ s^{-1}	T K	P Atm	Expt. Table 20	Ref.
1-penten-3-ol	$(1.39 \pm 0.19) \times 10^{-14}$ [a]				
(*Z*)-2-penten-1-ol	$(1.53 \pm 0.23) \times 10^{-13}$ [a]	298 ± 3	1.00 ± 0.03	I a	[192]
	$(3.5 \pm 1.9) \times 10^{-13}$			I b	
	$(3.11 \pm 0.11) \times 10^{-13}$	295 ± 2	1	II	[230]
(*E*)-2-pentenal	$(1.93 \pm 0.40) \times 10^{-14}$				
1-penten-3-one	3.39×10^{-14} [f]	298	1	III	[215]
(*Z*)-4-hexen-1-ol	$(2.93 \pm 0.58) \times 10^{-13}$ [a]	298 ± 3		I a	[231]
(*Z*)-3-hexen-1-ol	$(2.67 \pm 0.42) \times 10^{-13}$ [a]				
	$(2.72 \pm 0.83) \times 10^{-13}$	296 ± 2	0.974	IV	[174]
(*E*)-3-hexen-1-ol	$(4.43 \pm 0.91) \times 10^{-13}$ [a]	298 ± 3		I a	[231]
	$(5.2 \pm 1.8) \times 10^{-13}$ [g]			I b	
(*Z*)-2-hexen-1-ol	$(1.56 \pm 0.24) \times 10^{-13}$ [a]			I a	
	$(4.05 \pm 0.45) \times 10^{-13}$ [d]	295 ± 2	1	II	[230]
	$(3.57 \pm 0.62) \times 10^{-13}$ [e]				
(*E*)-2-hexen-1-ol	$(1.30 \pm 0.24) \times 10^{-13}$ [a]	298 ± 3		I a	[231]
hexanal	$(1.14 \pm 0.14) \times 10^{-14}$	298 ± 2	1.00 ± 0.01	V	[218]
	$(1.73 \pm 0.18) \times 10^{-14}$	298 ± 2	1	V	[232]
	$(4.75 \pm 0.62) \times 10^{-14}$ [b]	296 ± 2	1	VI	[219]
	$(1.07 \pm 0.12) \times 10^{-14}$ [c]				
	$(1.7 \pm 0.1) \times 10^{-14}$	297 ± 2	1	VII a	[233]
(*Z*)-2-hexenal	$(1.36 \pm 0.29) \times 10^{-14}$	295 ± 2	1	II	[230]
(*E*)-2-hexenal	$(1.21 \pm 0.10) \times 10^{-14}$	296 ± 2	0.974	IV	[174]
	$(4.7 \pm 1.5) \times 10^{-15}$ [a]	294 ± 3	1	VIII	[193]
(*Z*)-3-hexenylacetate	$(2.46 \pm 0.75) \times 10^{-13}$	296 ± 2	0.974	IV	[174]
2-methyl-3-buten-2-ol	$(2.1 \pm 0.3) \times 10^{-14}$ [a]	294	1	IXa	[234]
	$(1.6 \pm 0.6) \times 10^{-14}$			IX b	
	$(0.86 \pm 0.29) \times 10^{-14}$	298 ± 2	0.974 ± 0.007	X	[224]
Nonanal	$(1.8 \pm 0.\ 2) \times 10^{-14}$	297 ± 2	1	VII b	[233]
	$(2.2 \pm 0.\ 3) \times 10^{-14}$			VII c	
Methyl salicylate	$(4.19 \pm 0.92) \times 10^{-15}$	298	1	XI	[227]

[a] absolute rate constant; [b] methacrolein reference; [c] 1-butene reference, [d] (*E*)-2-butene reference, [e] cyclopentene reference; [f] estimated from SAR or LFER; [g] overestimated (see text).

Table 20. Experiments used to determine the rate constants listed in Table 19.

Expt	Photoreactor Type	Photoreactor Vol. dm^3	Photoreactor Material	Detection	NO_3 Source	Reference Reactants	Ref.
I a	Discharge flow tube			Off-axis continuous-wave CEAS	F + HONO	no	[192]
I b	Bag	56	Teflon	GC-FID	N_2O_5	(*E*)-2-butene, 1-butene	
II	Flow-tube	0.005	Glass	CI MS	N_2O_5	(*E*)-2-butene, Cyclopen-tane, 1,3-butadiene	[230]
III	SRR, LFER						[215]
IV	Chamber	6700 7900	Teflon	GC-FID	N_2O_5	(*E*)-2-butene, propene	[174]
V	Reactor	250	Steel	LP FTIR	N_2O_5	Propene 1-butene	[218,232]
VI	Chanber	6500	Teflon	GC-FID	N_2O_5	Methacrolein, 1-butene	[219]
VII a VII b VII c	Bag	100	PVF	(a) FTIR (b,c) GC (SPME)	N_2O_5	(a) propene (b) butanal (c) 1-butene	[233]
VIII	Reactor	977	Pyrex	FTIR, UV	N_2O_5	no	[193]
IX a	Flow tube FFD			LP FTIR	F + HNO_3	no	[234]
IX b	Reactor	153			N_2O_5	propene	
X	Chamber	480	Teflon	LP FTIR	N_2O_5	propene	[224]
XI	ICARE-CHRS chamber	7300	Teflon	HR PTR-TOF-MS	NO_2 + O_3	acetaldehyde	[227]

Table 21. Absolute rate constants for gas-phase reactions of GLV with NO_3 radicals—Arrhenius parameters and values at temperature T.

GLV	A Molecules cm^{-1} s^{-1}	EA/R K	k_T Molecules cm^{-1} s^{-1}	T K	T Range K	P mmHg	Expt Table 22	Ref.
(*E*) -2-pentenal	$(5.40 \pm 0.30) \times 10^{-12}$	1540 ± 200	$(2.88 \pm 0.29) \times 10^{-14}$	298	298–433	1	I	[235]
(*E*) -2-hexenal	$(1.2 \pm 0.3) \times 10^{-12}$	926 ± 85	$(5.49 \pm 0.95) \times 10^{-14}$	298	298–433	1		[235]
2-methyl-3-butene-2-ol	4.6×10^{-14}	400	$(1.2 \pm 0.09) \times 10^{-14}$	298	267–400	1.2–8.8	II	[236]

Table 22. Experiments used to determine the rate constants listed in Table 21.

Exp	Photoreactor Type	Photoreactor Vol. dm^3	Photoreactor Material	Detection	OH Source	Add.	Reference Reactants	Ref.
I	Flow tube FFD			LIF	F + HNO_3		no	[235]
II	Flow tube			LP VIS	N_2O_5		no	[236]
III								
IV								

Pfrang et al. [192,231] showed that relative rate constants for the gas-phase reactions of NO_3 with (*Z*)-2-hexen-1-ol, (*E*)-3-hexen-1-ol, (*Z*)-2-penten-1-ol, and 1-penten-3-ol at 298 ± 3 K obtained using N_2O_5 as a source of NO_3 were higher than the absolute rate constants obtained using off-axis continuous-wave cavity-enhanced absorption spectroscopy (CEAS) using the reaction of F atoms with HNO_3 as a source of NO_3. That was caused by

slow reactions of N_2O_5 with GLV ($(5.0 \pm 2.8) \times 10^{-19}$ cm^3 molecule^{-1} s^{-1} for (*Z*)-2-penten-1-ol; $(9.1 \pm 5.8) \times 10^{-19}$ cm^3 molecule^{-1} s^{-1} for 1-penten-3-ol; and $(3.1 \pm 2.3) \times 10^{-18}$ cm^3 molecule^{-1} s^{-1} for (*E*)-3-hexen-1-ol).

4.2.3. Gas-Phase Reactions with O_3

Table 23 contains the rate constants for gas-phase reactions of GLV with O_3 determined experimentally at single temperatures, Table 24 describe the experiments carried to determine the constants. Table 25 shows the Arrhenius parameters for reactions studied over temperature ranges, Table 26 briefly describe the experiments carried to determine the constants. In each experiment, external devices generated ozone.

Table 23. Relative and absolute ([a]) rate constants for gas-phase reactions of GLV with O_3 at single temperatures.

GLV	k cm^3 molecule^{-1} s^{-1}	T K	P atm	Expt Table 24	References
pentan-1-ol	$(2.9 \pm 0.2) \times 10^{-17}$	298	1		[210]
1-penten-3-ol	$(1.64 \pm 0.15) \times 10^{-17}$ [a]	298	1	I	[201]
	$(1.79 \pm 0.18) \times 10^{-17}$ [a]	289 ± 1	1	II	[237]
(*Z*)-2-penten-1-ol	$(11.5 \pm 0.66) \times 10^{-17}$ [a]	298	1	I	[201]
	$(1.69 \pm 0.25) \times 10^{-16}$ [a]	288 ± 1	1	II	[237]
1-penten-3-one	$(1.17 \pm 0.15) \times 10^{-17}$ [a]	298	1	I	[201]
(*Z*)-2-hexen-1-ol	$(7.44 \pm 1.03) \times 10^{-17}$ [a]	298	1	III a	[238]
	10.4×10^{-17}	298		III b	
(*E*)-2-hexen-1-ol	$(5.98 \pm 0.73) \times 10^{-17}$	298	1	IV	[239]
	$(1.66 \pm 0.22) \times 10^{-16}$ [a]	298	1	III a	[238]
	2.86×10^{-16}	298		III b	
(*Z*)-3-hexen-1-ol	6.7×10^{-17}	296	1	V	[92]
	6.4×10^{-17}				
	$(1.05 \pm 0.95) \times 10^{-16}$ [a]	258		II	[237,240]
	$(6.4 \pm 1.7) \times 10^{-17}$	296 ± 2	0.974	VI	[174]
	$(6.04 \pm 0.07) \times 10^{-17}$	298	1	IV	[239]
	$(5.47 \pm 0.71) \times 10^{-17}$ [a]	298	1	III a	[238]
	4.40×10^{-17}	298		III b	
(*E*)-3-hexen-1-ol	$(5.83 \pm 0.86) \times 10^{-17}$	298	1	IV	[239]
	$(6.19 \pm 0.72) \times 10^{-17}$ [a]	298	1	III a	[238]
	5.8×10^{-17}			III b	
(*Z*)-4-hexen-1-ol	$(7.09 \pm 0.91) \times 10^{-17}$ [a]	298	1	III a	[238]
	8.38×10^{-17}			III b	
(*E*)-4-hexen-1-ol	$(1.05 \pm 0.14) \times 10^{-16}$ [a]			III a	
	0.88×10^{-16}			III b	
(*E*)-2-hexenal	$(1.28 \pm 0.28) \times 10^{-18}$	287.3 ± 1.4	1	II	[203]
	$(3.0 \pm 2.1) \times 10^{-18}$	296 ± 2	0.974	VI	[174]
(*Z*)-3-hexenal	$(3.45 \pm 0.30) \times 10^{-17}$	298	1	VII	[160]
(*Z*)-3-hexenyl formate	$(4.06 \pm 0.66) \times 10^{-17}$ [a]	298	1	VIII a	[241]
	6.60×10^{-17} [a,b]			VIII b	
(*E*)-2-hexenyl acetate	$(2.18 \pm 0.28) \times 10^{-17}$	288.4 ± 0.4	1	II	[203]
(*Z*)-3-hexenyl acetate	3.6×10^{-17}; 5.4×10^{-17}	296	1	V	[92]
	$(5.4 \pm 1.4) \times 10^{-17}$	296 ± 2	0.974	VI	[174]
	$(5.77 \pm 0.70) \times 10^{-17}$ [a]	298	1	VIII a	[241]
	6.84×10^{-17} [a,b]			VIII b	
(*Z*)-3-hexenyl propionate	$(7.62 \pm 0.88) \times 10^{-17}$ [a]	298	1	VIII a	[241]
	1.084×10^{-16} [a,b]			VIII b	
(*Z*)-3-hexenyl butyrate	$(1.234 \pm 0.159) \times 10^{-16}$ [a]			VIII a	
	1.789×10^{-16} [a,b]			VIII b	

Table 23. *Cont.*

GLV	k cm^3 $molecule^{-1}$ s^{-1}	T K	P atm	Expt Table 24	References
2-methyl-3-buten-2-ol	$(1.0 \pm 0.03) \times 10^{-17}$ [a]	291 ± 1		II	[237]
	$(8.3 \pm 1.0) \times 10^{-18}$ [a]	293 ± 2	1	IX	[242]
	$(8.6 \pm 2.9) \times 10^{-18}$	298 ± 2	0.974 ± 0.007	X	[224]
	$(8.6 \pm 1.0) \times 10^{-18}$ [a]	298 ± 2	1	XI	[177]
1-octen-3-ol	$(5.00 \pm 0.58) \times 10^{-24}$ [a]	298	1	XII	[48]
Methyl salicylate	$\sim 4 \times 10^{-21}$ [c]	298 ± 5	1	XIII	[164]
	$(3.33 \pm 2.01) \times 10^{-19}$	298	1	XIV	[227]

[a] absolute rate constant; [b] calculated theoretically; [c] rough estimate due to low conversion of the reference reactant toluene.

Table 24. Experiments used to determine the rate constants listed in Table 23.

Expt	Photoreactor			Detection	Addition	Reference Reactants	Ref.
	Type	Vol. dm^3	Material				
I	Cork LISA	3910 977	Teflon Pyrex	LP FTIR, O_3 analyzer		no	[201]
II	Chamber	3500–3700	Teflon	UV photometer	Cyclohexane [a]	no	[203,237,240]
III a III b				O_3 analyzer DFT method at the BH&HLYP/6-31+G(d,p) level of theory	Cyclohexane [a]	no	[238]
IV	Chamber	480	Pyrex	LP FTIR	No [b]	1,4-cyclohexadiene, isoprene	[239]
V	Chamber	775	Teflon	GC-MS	Fluorobenzene [c]	no	[92]
VI	Chamber	6700 7900	Teflon	GC-FID	Cyclohexane [a]	(*E*)-2-butene, propene, 2-methyl-2-butene	[174]
VII	Chamber	6000	PFA	LP FTIR	CO [a]	1,3,5-trimethylbenzene	[160]
VIII a VIII b	Flow tube	0.012		O_3 analyzer DFT calculations with the BHandHLYP functional and the 6-311+G(d,p) basis sets at the BHandHLYP/6-311+G(d,p) level of theory.		no	[241]
IX	Reactor	977	Pyrex	LP FTIR	CO [a]	no	[242]
X	Chamber	480	Teflon	LP FTIR	Propane [a]	Propene, isobutene	[224]
XI	LISA CRAC	980 3910	Pyrex FEP	LP FTIR GC-MS	CO [a]	no	[177]
XII	Chamber	775 8000	Teflon	NIR LDI MS, O_3 analyzer		no	[48]
XIII	Chamber	50	Teflon	GC-FID		Toluene	[164]
XIV	ICARE-CHRS chamber	7300	Teflon	HR PTR-TOF-MS		3,3,3-trifluoropropene	[227]

[a] OH scavenger; [b] see comment in the text; [c] internal standard.

Table 25. Relative rate constants for gas-phase reactions of GLV with O_3_ Arrhenius parameters and values at selected temperature T (obtained by relative methods if not marked absolute).

GLV	A Molecules cm^{-1} s^{-1}	EA/R K	k_T Molecules cm^{-1} s^{-1}	T K	T Range K	P Atm	Expt Table 26	Ref.
1-penten-3-ol	$(1.82 \pm 2.08) \times 10^{-16}$	730 ± 348	$(1.61 \pm 0.21) \times 10^{-17}$	298 ± 2	273–333	1	I a	[243]
			$(1.75 \pm 0.25) \times 10^{-17}$	298 ± 2			I b	
			0.20×10^{-17}	298			I c	
(*Z*)-2-penten-1-ol	$(2.32 \pm 1.94) \times 10^{-15}$	902 ± 265	$(11.90 \pm 1.40) \times 10^{-17}$	298 ± 2	273–333	1	I a	[243]
			$(9.07 \pm 1.29) \times 10^{-17}$	298 ± 2			I b	
			1.50×10^{-17}	298			I c	
(*E*)-2-penten-1-al	$(1.38 \pm 0.73) \times 10^{-16}$ [a]	1406 ± 163	$(1.24 \pm 0.06) \times 10^{-18}$ [a]	298	233–373	0.8–1	II	[244]
(*E*)-3-hexen-1-ol	$(1.74 \pm 1.65) \times 10^{-15}$	1020 ± 300	$(5.97 \pm 0.99) \times 10^{-17}$	298 ± 2	273–333	1	I a	[243]
			$(6.50 \pm 0.95) \times 10^{-17}$	298 ± 2			I b	
			1.48×10^{-17}	298			I c	
(*E*)-2-hexenal	$(1.79 \pm 0.54) \times 10^{-16}$ [a]	1457 ± 90	$(1.37 \pm 0.03) \times 10^{-18}$ [a]	298	233–373	0.8–1	II	[244]
(*Z*)-2-hexenyl acetate	$(2.02 \pm 0.65) \times 10^{-15}$ [c]	1306 ± 44 [c]	2.50×10^{-17} [b]					
(*E*)-2-hexenyl acetate	$(7.21 \pm 0.93) \times 10^{-15}$ [c]	1856 ± 33 [c]	1.39×10^{-17} [b]	298	200–370	0.996	III	[196]
(*Z*)-3-hexenyl acetate	$(2.83 \pm 0.39) \times 10^{-15}$ [c]	993 ± 35 [c]	9.84×10^{-17} [b]					
(*E*)-3-hexenyl acetate	$(1.68 \pm 0.23) \times 10^{-14}$ [c]	925 ± 34 [c]	7.37×10^{-16} [b]					
Methyl salicylate	2.97×10^{-12} [b,d]	6185.6	2.9×10^{-21} [d]	298	278–350	1	IV	[189]

[a] absolute rate constant; [b] practically did not depend on pressure in the range of 0.01–10,000 mmHg; [c] evaluated based on the reference data; [d] formation of primary ozonide.

Table 26. Experiments used to determine the rate constants listed in Table 25.

Exp	Photoreactor Type	Photoreactor Vol. dm^3	Photoreactor Material	Detection	Add.	Reference Reactants	Ref.
I a	Flow tube	63	Pyrex	LP FTIR	Cyclohexane [a]	2,3-dimethyl-1,3-butadiene	[243]
I b				GC-MS (SPME)		1-heptene	
I c	DFFT method with M06–2X functional and 6-311 þ G(d,p) triple split valence basis set						
II	Flow tube	63	Pyrex	LP FTIR	Cyclohexane [a]	no	[244]
III	DFT and modified RRKM						[196]
IV	DFT using B3LYP, M06-2X and MPW1K functionals with 6-311++G(d,p) basis set.						[189]

[a] OH scavenger.

Gibilisco et al. [239] studied the gas-phase reactions of O_3 with (*Z*)-3-hexen-1-ol, (*E*)-3-hexen-1-ol, and (*E*)-2-hexen-1-ol without any OH scavengers added because they assumed that OH radicals formed during ozonolysis affect both the major and the reference reactants and OH influence is self-canceling and marginal. That assumption is not exact because the amounts of reactants consumed by OH radicals add to the quantities consumed by O_3 and thus are not self-canceling:

$$\frac{\Delta_{R1,\,total} - \Delta_{R1,\,OH}}{\Delta_{R2,\,total} - \Delta_{R2,\,OH}} \neq \frac{\Delta_{R1,\,ozone}}{\Delta_{R2,\,ozone}} \quad (16)$$

Several authors showed that the rate constants calculated with DFT methods agreed well with the experimental constants [238,241]. Besides, Zhang et al. [241] found that the theoretical and empirical rate constants for gas-phase reactions of O_3 with (*Z*)-3-hexenyl esters increased with the length of the ester group.

4.2.4. Gas-Phase Reactions with Cl Radicals

Table 27 contains the rate constants for gas-phase reactions of GLV with Cl radicals determined experimentally at single temperatures, Table 28 briefly describe the experiments carried out to determine the constants. Table 29 shows the Arrhenius parameters for reactions studied over temperature ranges, Table 30 briefly describe the experiments carried out to determine the constants.

Table 27. Relative rate constants for gas-phase reactions of GLV with Cl at single temperatures.

GLV	K cm^3 $Molecule^{-1}$ s^{-1}	T K	P Atm	Expt Table 28	Ref.
Pentan-1-ol	$(2.9 \pm 0.2) \times 10^{-10}$	298	1	I	[210]
	$(2.51 \pm 0.13) \times 10^{-10}$	298 ± 2	1	II	[212]
	$(2.57 \pm 0.25) \times 10^{-10}$	295 ± 2	1	III	[213]
1-penten-3-ol	$(2.96 \pm 1.22) \times 10^{-10}$	258 ± 1	1	IV	[205]
	$(2.37 \pm 0.38) \times 10^{-10}$	262 ± 1	1		[205]
	$(2.40 \pm 0.54) \times 10^{-10}$	273 ± 1	1		[205]
	$(2.35 \pm 0.31) \times 10^{-10}$	298 ± 1	1		[205]
	$(2.78 \pm 0.30) \times 10^{-10}$	313 ± 1	1		[205]
	$(2.57 \pm 0.28) \times 10^{-10}$	333 ± 1	1		[205]

Table 27. *Cont.*

GLV	K cm^3 $Molecule^{-1}$ s^{-1}	T K	P Atm	Expt Table 28	Ref.
(*Z*)-2-penten-1-ol	$(2.99 \pm 0.53) \times 10^{-10}$	296 ± 2	1	V	[245]
	$(3.00 \pm 0.49) \times 10^{-10}$	298 ± 1	1	IV	[205]
	$(2.66 \pm 0.47) \times 10^{-10}$	313 ± 1	1		[205]
	$(3.26 \pm 0.48) \times 10^{-10}$	333 ± 1	1		[205]
(*E*)-2-pentenal	$(1.31 \pm 0.19) \times 10^{-10}$	298	1	VI	[246]
1-penten-3-one	$(2.91 \pm 1.10) \times 10^{-10}$	298	1	VII	[247]
	$(1.9 \pm 0.4) \times 10^{-10}$	297–400	1	VIII	[248]
(*E*)-2-hexen-1-ol	$(3.41 \pm 0.65) \times 10^{-10}$	296 ± 2	1	V	[245]
	$(3.49 \pm 0.82) \times 10^{-10}$	298 ± 3	1	IX	[249]
(*Z*)-3-hexen-1-ol	$(3.15 \pm 0.58) \times 10^{-10}$	296 ± 2	1	V	[245]
	$(2.94 \pm 0.72) \times 10^{-10}$	298 ± 3	1	IX	[249]
(*E*)-3-hexen-1-ol	$(3.05 \pm 0.59) \times 10^{-10}$	296 ± 2	1	V	[245]
	$(3.42 \pm 0.79) \times 10^{-10}$	298 ± 3	1	IX	[249]
(*Z*)-3-hepten-1-ol	$(3.80 \pm 0.86) \times 10^{-10}$	298 3	1		[249]
Hexanal	$(2.88 \pm 0.37) \times 10^{-10}$	298	1	VI	[246]
	$(3.23 \pm 0.15) \times 10^{-10}$	298 ± 2	1	X	[220]
(*E*)-2-hexenal	$(1.92 \pm 0.22) \times 10^{-10}$	298	1	VI	[246]
(*Z*)-3-hexenyl formate	$(2.45 \pm 0.15) \times 10^{-10}$	298	1	IV	[222]
	4.94×10^{-10} [a]	298	1		[222]
(*E*)-2-hexenylacetate	$(3.10 \pm 1.13) \times 10^{-10}$	298 ± 1	750 mmHg	XI	[186]
2-methyl-3-buten-2-ol	$(4.7 \pm 1.0) \times 10^{-10}$	298 ± 2	0.974 ± 0.007	XII	[224]
	$(3.3 \pm 0.4) \times 10^{-10}$	295 ± 1	0.921	XIII	[179]
1-octen-3-ol	$(4.03 \pm 0.77) \times 10^{-10}$	296 ± 2	1	V	[245]
(*Z*)-3-octen-1-ol	$(4.13 \pm 0.68) \times 10^{-10}$	298 ± 3	1	IX	[249]
Nonanal	$(4.82 \pm 0.20) \times 10^{-10}$	298 ± 2	1	X	[220]
methyl salicylate	$(2.8 \pm 0.44) \times 10^{-12}$	298 ± 5	1	XIV	[164]
	$(1.65 \pm 0.3) \times 10^{-12}$	298	1	XV	[227]

[a] from SAR or LFER.

Table 28. Experiments used to determine the rate constants listed in Table 27.

Expt	Photoreactor			Detection	Cl Source	Add.	Reference Reactants	Ref.
	Type	Vol. dm^3	Material					
I	Bag	140	Teflon	GC-FID	Cl_2		Pentane 1,3-dioxolane	[210]
II	Cylinder	50	Teflon	GC-FID	Cl_2, $COCl_2$		Cyclohexane Cycloxexane	[212]
III	Bag	100	Teflon	GC-FID	Cl_2		Propane; hexane	[213]
IV	Chamber	400	Teflon	GC-FID	CCl_3COCl		Octane, propene, cyclohexane	[205,222]
V	Chamber	600	Teflon	Ion flow tupe MS	Cl_2		Tetrahydrofuran, propan-1-ol, octane	[245]
VI	Chamber	200	Teflon	GC-FID	Cl_2		Ethene; propene; 1-butene	[246]
VII	Bag	80	Teflon	GC-FID	ClC(O)C(O)Cl		Chloroethene 1,1-dichloroethene acrylonitrile	[247]
VIII	Bulb	0.5	Pyrex	GC-FID; GC-MS; FTIR	Cl_2		Ethane	[248]

Table 28. *Cont.*

Expt	Photoreactor			Detection	Cl Source	Add.	Reference Reactants	Ref.
	Type	Vol. dm^3	Material					
IX	Chamber	480	Pyrex	LP FTIR	Cl_2		1-butene, isobutene	[249]
X	Cylinder	108O	Pyrex	LP FTIR	Cl_2		(*E*)-2-butene; Methy lvinyl ketone	[220]
XI	Bag	80	Teflon	GC-FID	ClC(O)C(O)Cl		(n-butyl methacrylate n-butyl acrylate	[186]
XII	Chamber	480	Teflon	LP-FTIR	Cl_2		Ethene	[224]
XIII	Chamber	47	Steel	LP-FTIR	Cl_2		Ethane, cyclohexane	[179]
XIV	Chamber	50	Teflon	GC-FID	Cl_2		Acetone	[164]
XV	ICARE-CNRS chamber	7300	Teflon	HR PTR-TOF-MS	Cl_2		Acetone	[227]

Table 29. Relative and absolute ([a]) rate constants for gas-phase reactions of GLV with Cl atoms—Arrhenius parameters and values at selected temperature T.

GLV	A	EA/R	k_T	T	T Range	P	Expt	Ref.
	cm^3 Molecule^{-1} s^{-1}	K	cm^3 Molecule^{-1} s^{-1}	K	K	Atm	Table 30	
hexanal	$(7.91 \pm 0.66) \times 10^{-11}$ [a]	$-(349 \pm 51)$	$(2.56 \pm 0.24) \times 10^{-11}$ [a]	298	265–381	1	I	[250]
2-methyl-3-butene-2-ol	$(2.83 \pm 2.50) \times 10^{-14}$	$-(2670 \pm 249)$	$(2.13 \pm 0.19) \times 10^{-10}$	298	256–298	1	II	[251]
methyl salicylate	1.2703×10^{-8} [a,b,c]	1438.4	1.01×10^{-10} [a,b,c,d]	298	278–350	1	III	[209]

[a] absolute rate constants; [b] determined theoretically; [c] calculated here from the reference data; [d] 100 times higher than experimental values from Table 23 [209].

Table 30. Experiments used to determine the rate constants listed in Table 29.

Expt	Photoreactor			Detection	Cl Source	Add.	Reference Reactants	Ref.
	Type	Vol. dm^3	Material					
I	Cell (PLP)	0.2	Pyrex	RF	Cl_2	No	No	[250]
II	Chamber	400	Teflon	GC-FID	CCl_3COCl		Cycloxexane, methanol, propene, 1-butene	[251]
III	DFT methods at B3LYP and M06-2X levels of theory with 6-311++G(d,p) basis set							[209]

Gibilisco et al. [249] correlated the rate constants for gas-phase reactions of Cl with various unsaturated VOC against the energy of the highest occupied molecular orbital (E_{HOMO}) calculated with the Gaussian package (Equation (12)).

$$\ln k \left(\mathrm{cm^3 molecule^{-1} s^{-1}}\right) = -(0.3 \pm 0.1) E_{HOMO} - (19.0 \pm 0.4) \quad (17)$$

4.2.5. Gas-Phase Photolysis

Table 31 shows the experimental rates of GLV photolysis, absolute or relative to the NO_2 photolysis rate. All constants were based on the measured UV spectra of GLV (Section 3.2). Table 32 provides more details.

Table 31. GLV photolysis rate constants j, absolute, and relative to the photolysis rate constant of NO_2, determined at given effective quantum yields Φ and zenith angles θ.

GLV	j s^{-1}	j/j(NO_2)	Φ	θ °	T K	Expt Table 32	Ref.
1-penten-3-ol	$(1.61–2.36) \times 10^{-6}$ [a]		1		298	I	[57]
(*E*)-2-pentenal	3.06×10^{-4}		1	20	298	II	[162]
	2.87×10^{-4}			30			
	2.58×10^{-4}			40			
	2.18×10^{-4}			50			
	1.63×10^{-4}			60			
	9.73×10^{-5}			70			
1-penten-3-one	$(0.36–1.39) \times 10^{-5}$ [a]		1		298	I	[57]
n-hexanal	1.7×10^{-5}	0.2×10^{-2}	0.28		286–294	III	[161]
	1.14×10^{-5}		0.28		298	I	[159]
	$(1.81 \pm 0.10) \times 10^{-5}$		0.31 ± 0.02	17	298	IV	[220]
(*Z*)-3-hexenal	2.1×10^{-5}	0.4×10^{-2}	0.34		286–294	III	[161]
	$(2.61 \pm 0.08) \times 10^{-5}$	$(4.7 \pm 0.4) \times 10^{-3}$	0.25 ± 0.06		298	V	[160]
(*E*)-2-hexenal	1.0×10^{-4}	1.8×10^{-2}	0.36		286–294	III	[161]
	3.80×10^{-4}		1	20	298	II	[162]
	4.05×10^{-4}			30			
	3.80×10^{-4}			40			
	3.42×10^{-4}			50			
	2.89×10^{-4}			60			
	2.17×10^{-4}			70			
(*Z*)-3-hexen-1-ol	$(1.61–2.36) \times 10^{-5}$ [a]		1		298	I	[57]
Methyl salicylate	$(2.82 \pm 0.26) \times 10^{-5}$ [b]				298	VI	[227]
	Insignificant [c]						

[a] upper limits, 0–10 km above the Earth's surface; [b] at 254 nm; [c] at 365 nm and > 300 nm.

Table 32. Experiments used to determine the rate constants listed in Table 31.

Expt	Photoreactor Type	Vol. dm^3	Material	Detection	Additions	Ref.
I	Calculation conditions: clear-sky, July noon, Ciudad Real (Spain). The actinic flux was based on the TUV model [a].					[57,159]
II	The actinic flux was based on the TUV model [a].					[162]
III	EUPHORE	2×10^5	PTFE	LP-FTIR, GC-FID, GC-MS		[161]
IV	EUPHORE	2×10^5	PTFE	LP-FTIR		[220]
V	Chamber	6000	PFA	LP-FTIR	CO [b], isoprene [c]	[160]
VI	ICARE-CNRS	7300	FEP	HR PTR-TOF-MS		[227]

[a] Tropospheric Ultraviolet Model [252]; [b] OH scavenger; [c] OH tracer.

Photolysis was an insignificant degradation path in the troposphere for 1-penten-3-ol and (*Z*)-3-hexen -1-ol [57], (*Z*)-3-hexen-1-al [161], MBO [165], and MeSa [227]. Photodegradation of (*Z*)-3-hexenal was faster than its reaction with O_3 (1×10^{12} molecule cm^{-3}) and slower than its reaction with OH (2×10^6 molecule cm^{-3}). Substantial photodegradation occurred for (*E*)-2-pentenal and (*E*)-2-hexenal [162] as well as for 1-penten-3-one and hexanal [57].

4.2.6. SAR and LFPR Methods

We did not intend to review the methods of estimating the rate constants based on structure-activity or linear free energy relationships. The interested readers are referred to the original publications on the correlations for gas-phase reactions of organic compounds

with OH radicals [222,229,253–255], with OH, O_3, and NO_3 radicals [215,255–259], with Cl radicals [215,222,245,260], and with O_3 [255,261]. Besides, SAR correlations were proposed for some aqueous-phase reactions [262–264].

5. Aqueous-Phase Kinetics

There is little data published on the aqueous-phase reactions of GLV, so we present all findings in one section. Reaction mechanisms are discussed in Section 6.3, together with multiphase experiments. Rate constants determined are collected in Tables 33–35.

Table 33. Relative rate constants for aqueous-phase reactions of GLV with OH radicals—Arrhenius parameters and values at 298 K and pH = 5.4, and yields of SOA products.

GLV	A 10^{11} M^{-1} s^{-1}	E_A kJ mol^{-1}	T Range K	pH	$k_{298\,K}$ [a] 10^8 M^{-1} s^{-1}	SOA %	Ref.
1-penten-3-ol	10.4 ± 0.3	13 ± 2	278–318	7	6.3 ± 0.1	-	[163]
1-penten-3-one					7.2 [b]	-	[215]
(*Z*)-2-hexen-1-ol	2.6± 0.1	9 ± 2	273–318	7	6.7 ± 0.3	-	[163]
(*Z*)-3-hexen-1-ol	8.1 ± 0.9	12 ± 0.3	278–298	5.4	5.1 ± 0.8	52	[22]
(*E*)-2-hexenal	5.2 ± 0.1	12 ± 1	273–318	7	4.8 ± 0.3	-	[163]
(*Z*)-3-hexenyl acetate	190 ± 40	17 ± 2	278–298	5.4	8.7 ± 1.1	8	[22]
methyl salicylate	58 ± 40	14 ± 1	278–298	5.4	7.8 ± 0.5	87	
methyl jasmonate	58 ± 9	15 ± 2	278–298	5.4	6.8 ± 0.8	67	
2-methyl-3-butene-2-ol	23 ± 5	13 ± 2	278–298	5.4	7.5 ± 1.4	20	

[a] experimental values; [b] estimated from SAR or LFER.

Table 34. Relative rate constants for aqueous-phase reactions of GLV with SO_4^- and NO_3 radicals at pH = 7—Arrhenius parameters (278–318 K) and values at 298 K [163].

GLV	X	A 10^9 M^{-1} s^{-1}	E_A kJ mol^{-1}	$k_{298\,K}$ 10^8 M^{-1} s^{-1}
1-penten-3-ol	SO_4^-	7.9 ± 0.1	5 ± 1	9.4 ± 1.0
	NO_3	150 ± 10	17 ± 2	1.5 ± 0.2
(*Z*)-2-hexen-1-ol	SO_4^-	110 ± 10	10 ± 2	28.3 ± 3
	NO_3	38 ± 1	9 ± 1	8.4 ± 2.3
(*E*)-2-hexenal	SO_4^-	2.9 ± 0.1	4 ± 1	4,8 ± 0.2
	NO_3	31 ± 1	17 ± 2	0.28 ± 0.07

Table 35. Relative rate constants for aqueous-phase reactions of GLV with singlet molecular oxygen $^1O_2$ * and ^3C * triplet state (^3DMB * and ^3MAP *) at pH = 5.4, and yields of some SOA products [265].

GLV	$^1O_2$ * A M^{-1} s^{-1}	$^1O_2$ * E_A kJ mol^{-1}	$^1O_2$ * $k_{298\,K}$ 10^6 M^{-1} s^{-1}	^3DMB * k 10^6 M^{-1} s^{-1} pH = 2.1 298 K	^3DMB * k 10^6 M^{-1} s^{-1} pH = 5.1 278–298 K	SOA %	^3MAP * k 10^6 M^{-1} s^{-1} pH = 5.1
(*Z*)-3-hexen-1-ol	6.1×10^{20}	82 ± 7.4	2.5 ± 0.3	0.33 ± 0.04	0.24 ± 0.1	-	1.2 ± 0.8
(*Z*)-3-hexenyl acetate	2.2×10^{15}	50 ± 7.2	3.9 ± 0.8	14 ± 2	14 ± 7	38	7.3 ± 2
methyl salicylate	-	-	≤ 0.1	29 ± 2	12 ± 4	80	8.0 ± 0.8
methyl jasmonate	3.6×10^{23}	96 ± 4.8	6.0 ± 0.7	3.6 ± 0.5	4.2 ± 3	84	1.2 ± 0.5
2-methyl-3-butene-2-ol	6.7×10^9	22 ± 1.7	7.5 ± 1.4	0.28 ± 0.1	0.13 ± 0.07	-	0.55 ± 0.2

Richards-Henderson et al. [22] studied the aqueous-phase oxidation of (*Z*)-3-hexen-1-ol, (*Z*)-3-hexenyl acetate, MeSa, MeJa, and MBO induced by OH radicals formed by the photodissociation of H_2O_2. Control experiments without H_2O_2 showed that the photodegradation of reactants did not occur. The total mass yield of SOA products was determined gravimetrically after blowing the post-reaction solutions to dryness with N_2. Unreacted GLV in dry residues was determined chromatographically after the recon-

stitution of samples with water. Rate constants for reactions were determined using a competitive kinetics technique against sodium benzoate (Table 33).

Sarang et al. [163] determined the relative rate constants for the aqueous-phase reactions of 1-penten-3-ol, (*Z*)-2-hexen-1-ol, and (*E*)-2-hexenal with OH, NO_3, and SO_4^- radicals (Tables 33 and 34). They used the Laser Flash Photolysis-Laser Long Path Absorption (LFP-LLPA) technique over the 278–318 K temperature range. The rate constants weakly increased with temperature. The impact of diffusion of reactants on the rate constants was: 30–60% (reactions with OH radicals); 5–23% (reactions with SO_4^- radicals); and 0.2–8% (reactions with NO_3 radicals).

Richards-Henderson et al. [265] determined the relative rate constants for reactions of several GLV with ^3C * triplet state and $^1O_2$ * singlet molecular oxygen generated by irradiation of organic chromophores—3,4-dimethoxybenzaldehyde (DMB) or methoxyacetophenone (MAP) and Rose Bengal, resp.—with simulated sunlight. They used a competitive kinetics method against the reference reactants phenol or syringol (for ^3C *) and tyrosine or furfuryl alcohol (for $^1O_2$ *). The results are in Table 33. The yields of SOA products were determined using the procedure applied in the experiments with OH radicals [22] (see above). All $^1O_2$ * reactions and reactions of ^{3}DMB * with hexenol and methylbutenol were too slow to produce measurable amounts of SOA.

Mael et al. [266] synthesized intermediate products of the oxidation of 1-metyl-3-buten-1-ol—(3,3-dimethyloxiran-2-yl)methanol (2-methyl-3-buten-1-ol 2,3-epoxide), 2-(oxiran-2-yl)propan-2-ol (2-methyl-3-buten-1-ol 3,4-epoxide), and 3-methylbutane-1,2,3-triol), and (2,3-dihydroxyiso-pentanol, DHIP)—to study their aqueous-phase reactions with sulfates and nitrates as well as hydrolysis thereof. Products obtained from reactions of both epoxides in 1 M solutions of sulfate included DHIP and its sulfuric acid esters (two isomers). Products of reactions of 3,4 epoxide in 1 M nitrate solutions included two isomers of nitric acid esters of DHIP (Section 6.3, Scheme 44).

In addition, those authors determined the rate constants for the following reactions: (i) acid (H^+) catalyzed hydrolysis of 2,3-epoxide $(4.075 \pm 0.004) \times 10^{-1}$ M^{-1} s^{-1}; (ii) acid (H^+) catalyzed hydrolysis of 3,4-epoxide $(4.36 \pm 0.13) \times 10^{-3}$ M^{-1} s^{-1}; (iii) neutral hydrolysis of tertiary sulfuric acid ester from 2,3-epoxide $(4.42 \pm 0.20) \times 10^{-6}$ s^{-1}; (iv) neutral hydrolysis of tertiary nitric acid ester from 3,4-epoxide $(2.10 \pm 0.14) \times 10^{-3}$ s^{-1}; (v) neutral hydrolysis of primary sulfuric acid ester from 3,4-epoxide $< 2 \times 10^{-7}$ s^{-1}; (vi) neutral hydrolysis of primary nitric acid ester from 3,4-epoxide $< 2 \times 10^{-7}$ s^{-1}; and D_2SO_4 esterification of DHIP $(1.292 \pm 0.047) \times 10^{-4}$ s^{-1}, probably at room temperature.

Noziere et al. [132] found that a chemical reaction accompanied the uptake of MBO in aqueous solutions of sulfuric acid (Section 3.1). The first-order rate constant for that reaction increased with the concentration of the acid:

$$n(\mathrm{k}) = (0.19 \pm 0.02)\mathrm{W} - (14.6 \pm 1.3)\ \ \mathrm{s}^{-1} \tag{18}$$

where W = 40–62% is the weight concentration of sulfuric acid. The reaction product was assigned to the mass spectrometer signal m/z 87 recorded in solutions. The proposed chemical mechanism included a pinacol rearrangement of protonated MBO leading to 3-methyl butanone (Section 6.3, Scheme 50). Liu et al. [267] used a rotated wetted wall reactor coupled with TOF MS with single-photon ionization to study uptake and aqueous-phase reactions of 2-methyl-3-buten-2-ol with H_2O_2 (0.1–1.0% wt) in aqueous solutions of sulfuric acid (40–60% wt) at 293 K and 5–108 mm Hg total pressure. MBO was monitored as the MBO^+-CH_3 ion cluster (m/z 71). The uptake coefficient was defined as the probability of MBO loss (from the gas phase) per collision with the aqueous surface (Equation (19)).

$$\gamma = \frac{4\mathrm{kV}}{\omega \mathrm{A}} \tag{19}$$

where ω (m s^{-1}) is the mean molecular speed of MBO, V (cm^3) is the volume of the reaction zone, A (cm^2) is the surface area of solution, and k (s^{-1}) is the first-order rate constant for the removal of MBO from the gas phase defined by Equation (20).

$$ln\left(\frac{S}{S_0}\right) = -\frac{kL}{v_{av}} \tag{20}$$

where S and S_0 are MS signals of MBO with and without loss from the gas phase, L (cm) is the contact distance between the gas and the solution, and v_{av} (cm s^{-1}) is the average gas flow velocity. In the absence of H_2O_2, the uptake of MBO was reversible at 40% acid concentration, irreversible (reactive) at 60% acid, and mixed at 50% acid. The addition of H_2O_2 at concentrations higher than 1% substantially increased the reactive character of the uptake. The uptake coefficient increased with the concentration of both sulfuric acid and H_2O_2. Equations (21a)–(21d) approximated the original data.

$$ln(\gamma) = 0.1591W - 18.059, R^2 = 0.9909,\ at\ [H_2O_2] = 0 \tag{21a}$$

$$ln(\gamma) = 0.167W - 17.656, R^2 = 0.9891, at\ [H_2O_2] = 0.1\ \%\ wt \tag{21b}$$

$$ln(\gamma) = 0.2159W - 19.04, R^2 = 0.9633, at\ [H_2O_2] = 0.5\ \%\ wt \tag{21c}$$

$$ln(\gamma) = 0.2188W - 18.468, R^2 = 0.9935, at\ [H_2O_2] = 1.0\ \%\ wt \tag{21d}$$

where *W* (% wt) is the weight concentration of H_2SO_4.

The gas-phase products accompanying the MBO uptake were determined online using MS and GC approaches and offline using FTIR. Isoprene was the only gaseous product during MBO uptake in sulfuric acid solutions. The products identified during the uptake in the mixed solutions of H_2O_2 and H_2SO_4 were acetaldehyde, acetone, and a product observed online that decomposed into isoprene when analyzed offline. Scheme 44 (Section 6.3) includes the mechanism proposed by the authors.

Ren et al. [268] studied the aqueous-phase reactions of MBO with sulfate radical-anions generated from $K_2S_2O_8$ either by the photodissociation at 254 nm or by thermal dissociation at room temperature. Due to essentially different rates of dissociation, the photo experiments lasted for 1 hour while the thermal experiments—up to 150 days. The same products were identified in both types of experiments, albeit in different proportions (Section 6.1, Tables 39 and 40 (organosulfates)). The reaction mechanism is discussed in Section 6.3.

Liyana-Arachchi et al. [269] analyzed the behavior of MBO molecules and OH radicals at an air-water interface using a molecular dynamics approach. They found that encounters of the species at the interface were sufficiently numerous to indicate a possibility of a chemical reaction.

Heath et al. [270] determined the pseudo-first-order rate constants for the reaction of MeJa with OH radicals in irradiated aqueous solution (bulk) and thin aqueous films. The OH radicals were generated by the photolysis of H_2O_2. The extent of the reaction was followed by measuring the concentration of MeJa with HPLC-UV/DAD. The rate of reaction in the films was more significant than in bulk and increased with decreasing film thickness (Table 36). The readers may doubt whether the illumination of the bulk solution and thin films was equally effective.

Table 36. Pseudo-first order rate constant for the aqueous-phase reaction of MeJa with OH radicals in bulk solutions and aqueous films.

Film Thickness, μm	∞ (Bulk)	193.1	77.2	38.6
k_{1st}, 10^{-4} min^{-1}	2.83 ± 0.02	9.62 ± 0.43	11.0 ± 0.5	12.7 ± 0.6

Hansel et al. [21,271] applied HPLC-ESI-MS techniques to identify several intermediate and final low-volatile products formed in the aqueous-phase oxidation of MeJa and MeSa by OH obtained by the photodissociation of H_2O_2 and proposed plausible formation mechanisms (Section 6.3, Schemes 47 and 48, resp.).

In summary, the rate constants for aqueous-phase reactions of GLV with OH radicals were high (~10^9 M^{-1} s^{-1}) and close to the diffusional limit (Table 33). Rate constants for reactions with SO_4^- were a little lower but still close to the diffusional limit (Table 32). Reactions with NO_3 were still slower, with rate constants of the order 10^8 M^{-1} s^{-1}. Reactions with singlet molecular oxygen and excited triple-state carbon appeared the slowest, with rate constants ranging between 10^5 and 10^7 M^{-1} s^{-1}. All reactions of GLV with radicals weakly accelerated with temperature had energy of activation between 4 and 20 kJ mol^{-1}.

6. Multiphase and Heterogeneous Transformation

6.1. Smog-Chamber Studies

Products of GLV processing in smog chambers are listed in: Table 37 (photooxidation and ozonolysis of (*Z*)-3-hexen-1-ol), Table 38 (ozonolysis of (*Z*)-3-hexenyl acetate), Table 39 (photooxidation of 2-methyl-3-buten-2-ol and ambient samples), Table 40 (organosulfates from various experiments and ambient samples). One should remember that compounds identified in aerosol samples may have multiple precursors. The experiments are briefly described below.

Table 37. Products identified in smog chamber oxidation of (*Z*)-3-hexen-1-ol by OH and O_3.

Name	Oxidant	MW	Formula	Structure	Phase	Ref.
acetaldehyde		44	C_2H_4O			
2-propenal		56	C_3H_4O			
propanal		58	C_3H_6O		gas	[92]
acetic acid		60	$C_2H_4O_2$			
2-propenoic acid		72	$C_3H_4O_2$			
3-hydroxypropanal		74	$C_3H_6O_2$	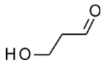	PM	[198]
propionic acid	O_3	74	$C_3H_6O_2$		Gas, PM	[92,198]
2-hydroxyacetic acid		76	$C_2H_4O_3$	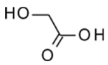		
3-hydroxy-2-oxopropanal		88	$C_3H_4O_3$	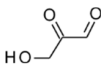		
2,3-di-hydroxypropanal		90	$C_3H_6O_3$	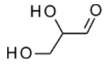	PM	[198]
2-hydro-peroxypropanal		90	$C_3H_6O_3$	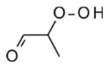		
3-hydroxy-2-oxopropanoic acid		104	$C_3H_4O_4$	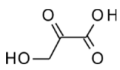		
2-hydroperoxy-3-hydroxypropanal		106	$C_3H_6O_4$	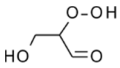		

Table 37. *Cont.*

Name	Oxidant	MW	Formula	Structure	Phase	Ref.
2-ethyl-1,3-dioxan-4-ol		132	$C_6H_{12}O_3$	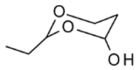		[65,198]
3-(2-hydroxy ethoxy) propanoic acid	OH, O_3	134	$C_5H_{10}O_4$	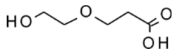	PM	[65]
2-(2-hydroxyethyl)-1,3-dioxan-4-ol		148	$C_6H_{12}O_4$	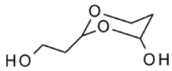		[65,198]
2-(1,3-dioxin-2-yl) ethylformate	O_3	158	$C_7H_{10}O_4$	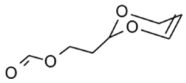	PM	[198]
3-(3–hydroxy propanoyloxy) propanoic acid	OH, O_3	162	$C_6H_{10}O_5$	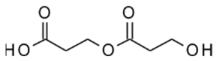	PM	[65]
2-(4-hydroxy-1,3-dioxan-2-yl)ethyl formate		176	$C_7H_{12}O_5$	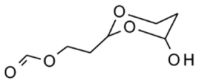		
2-(1,3-dioxin-2-yl) ethyl propionate		186	$C_9H_{14}O_4$	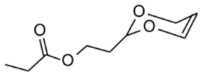		
1-((2-ethyl-1,3-dioxan-4-yl)oxy)propan-1-ol	O_3	190	$C_9H_{18}O_4$	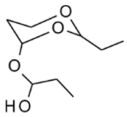	PM	[198]
2-(2-((3-hydroxyprop-1-en-1-yl)oxy)ethyl)-1,3-dioxan-4-ol		204	$C_9H_{16}O_5$	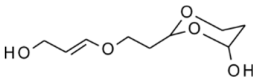		
2-(4-hydroxy-1,3-dioxan-2-yl)ethyl propionate		204	$C_9H_{16}O_5$	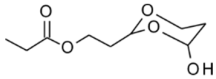		
3-(3-(2-hydroxyethoxy) propanoyloxy) propanoic acid	OH, O_3	206	$C_8H_{14}O_6$	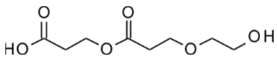	PM	[65]
3-(formyloxy)-3-(2-oxoethoxy) propyl propionate	O_3	218	$C_9H_{14}O_6$	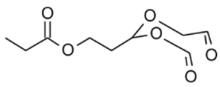	PM	[198]
3-(3-(2-hydroxy ethoxy)-3-oxopropanoyloxy) propanoic acid		220	$C_8H_{12}O_7$	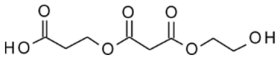		
3-(3-(2-hydroxyethoxy)-3-hydroxypropanoyloxy) propanoic acid		222	$C_8H_{14}O_7$	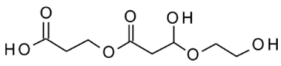		
1-(2-(4-hydroxyl-1,3-dioxan-2-yl)-ethoxy)-propane-1,3-diol	OH, O_3	222	$C_9H_{18}O_6$	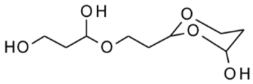	PM	[65]
1,3-dihydrox-3-(2-hydroxyethoxy) propyl- 3- hydroxy propanoate		224	$C_8H_{16}O_7$	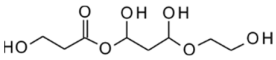		
3-(3-(3-hydroxy propanoyloxy) Propanoyloxy propanoic acid		234	$C_9H_{14}O_7$	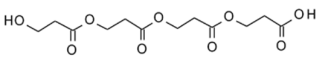		

Table 37. *Cont.*

Name	Oxidant	MW	Formula	Structure	Phase	Ref.
3-(carboxyoxy)-3-(2-oxoethoxy) propyl propionate	O_3	234	$C_9H_{14}O_7$	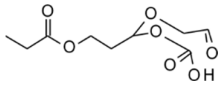	PM	[198]
1-(1-((2-ethyl-1,3-dioxan-4-yl)oxy)propoxy) propan-1-ol		248	$C_{12}H_{24}O_5$	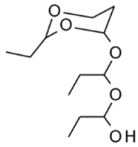		
3-(3-(3-(3-hydroxy propanoyloxy) propanoyloxy) propanoy-loxypropanoic acid	OH, O_3	306	$C_{12}H_{18}O_9$	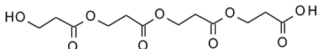	PM	[65]

Table 38. Products identified in smog chamber ozonolysis of (Z)-3-hexenyl acetate.

Name	MW	Formula	Structure	Phase	Ref.
2-propenal	56	C_3H_4O		Gas	[92]
Propanal	58	C_3H_6O			
Acetic acid	60	$C_2H_4O_2$			
2-propenoic acid	72	$C_3H_4O_2$			
Propionic acid	74	$C_3H_6O_2$		Gas, PM	[92,198]
2-hydroperoxy propanal	90	$C_3H_6O_3$	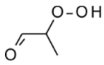	PM	[198]
3-oxo-propyl acetate	116	$C_5H_8O_3$	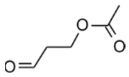	PM	[272]
2-acetoxyacetic acid	118	$C_4H_6O_4$	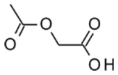	PM	[198]
2,3-dioxopropyl acetate	130	$C_5H_6O_4$	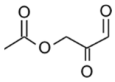		
2-hydroxy-3-oxopropyl acetate	132	$C_5H_8O_4$	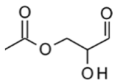		
3-acetoxy-propanoic acid	132	$C_5H_8O_4$	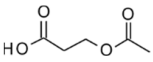	PM	[198,272]
3-acetoxy-2-oxopropanoic acid	146	$C_5H_6O_5$	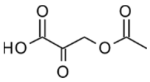	PM	[198]
2-hydroperoxy-3-oxopropyl acetate	146	$C_5H_8O_5$	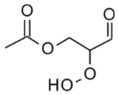		

Table 38. *Cont.*

Name	MW	Formula	Structure	Phase	Ref.
3-acetoxypropane peroxoic acid	148	$C_5H_8O_5$	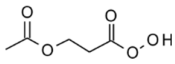	PM	[272]
3,4-dioxohexyl acetate	172	$C_8H_{12}O_4$	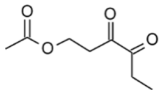	PM	[198]
2-hydroxyethyl 3-acetoxypropanoate	176	$C_7H_{12}O_5$	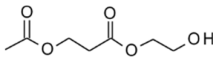	PM	[272]
2-(3-oxopropyl)ethyl 3-acetoxy propanoate	232	$C_{10}H_{16}O_6$	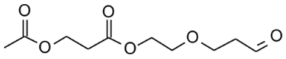	PM	[272]
3-acetoxypropanoyl 3-acetoxypropanoate	246	$C_{10}H_{14}O_7$	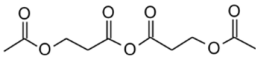	PM	[198]
2-(2-(3-acetoxy propanoyloxy)ethoxy) propanoic acid	248	$C_{10}H_{16}O_7$	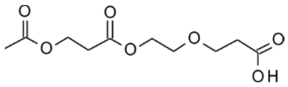	PM	[272]
5-acetoxy-3-oxopentyl-3-acetoxypropanoate	274	$C_{12}H_{18}O_7$	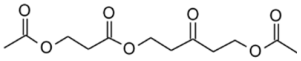		
2-(3-acetoxypropanoyloxy)ethyl 3-acetoxypropanoate	290	$C_{12}H_{18}O_8$	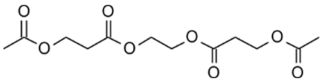		
[3-[2-(3- acetoxypropoxy)ethoxy]-3-oxo-propyl] 3-acetoxypropanoate	348	$C_{15}H_{24}O_9$	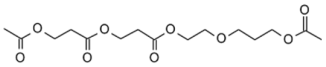		

Table 39. Products identified in SOA from smog-chamber and aqueous-phase reactions of 2-methyl-3-buten-2-ol and ambient SOA samples (except organosulfates listed in Table 40).

MW	Name	Formula	Structure	Phase	Ref.	Ambient Aerosol
30	formaldehyde	CH_2O		Gas	[273,274]	
32	methanol	CH_4O		Aqu	[268] [b]	
44	acetaldehyde	C_2H_4O		Gas	[273]	
46	formic acid	CH_2O_2		Aqu	[268] [b]	
48	formaldehyde hydrated (methanediol)	CH_4O_2				
58	acetone	C_3H_6O		Gas, aqu	[268,273,274] [b]	
58	glyoxal	$C_2H_2O_2$		Gas	[187,273]	
60	glycolaldehyde	$C_2H_4O_2$				
61	acetic acid	$C_2H_4O_2$		Aqu	[268] [b]	
72	methylglyoxal	$C_3H_4O_2$		Gas	[273]	
74	glyoxylic acid	$C_2H_2O_3$				

Table 39. *Cont.*

MW	Name	Formula	Structure	Phase	Ref.	Ambient Aerosol
76	glycolic acid	$C_2H_4O_3$	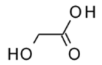	Aqu	[268] [b]	
78	glycolaldehyde hydrated	$C_2H_6O_3$				
86	1,3-butanedione	$C_4H_6O_2$		Gas	[273]	
86	2-oxopropanedial	$C_3H_2O_3$	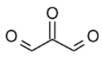			
88	2-hydroxy-2-methylpropanal	$C_4H_8O_2$		Gas	[187,273]	
88	2-hydroxypropaneial	$C_3H_4O_3$	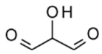	Gas	[273]	
100	2,3-dioxobutanal	$C_4H_4O_3$				
114	2,3-dioxobutane-1,4-dial	$C_4H_2O_4$	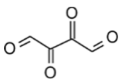			
116	2-oxovaleric acid	$C_5H_8O_3$	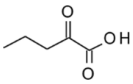			
118	1,3-dihydroxy-3-methyl-butan-2-one	$C_5H_{10}O_3$	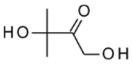	Gas, PM		
118	2,3-dihydroxy-3-methylbutanal	$C_5H_{10}O_3$	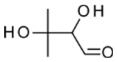	Gas		
120	2,3-dihydroxyisopentanol	$C_5H_{12}O_3$	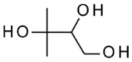	PM, aqu	[266] [a], [268] [b], [273]	$PM_{2.5}$ [273,275]
132	2,3-dihydroxy-2-methylbutane dialdehyde	$C_5H_8O_4$	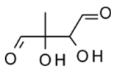	Gas, PM	[273]	
134	2,3-dihydroxy-3-methyl-butanoic acid	$C_5H_{10}O_4$	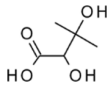			
134	2-hydroxy-2-methylpropenedioic acid	$C_4H_6O_5$	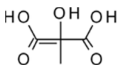			
136	2-methylerythritol	$C_5H_{12}O_4$	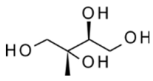	PM		$PM_{2.5}$ [273,275]
136	2-methylthreitol	$C_5H_{12}O_4$	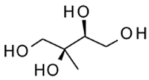			$PM_{2.5}$ [273,275]
164	2,3-dihydroxy-2-methylsuccinic acid [c]	$C_5H_8O_6$	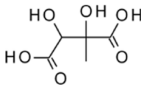			$PM_{2.5}$ [276]

[a] aqueous phase reactions of methylbutenol epoxides (Section 5); [b] aqueous-phase addition of sulfate radical anions (Section 5); [c] and isomers.

Table 40. Organosulfates identified in smog chamber and aqueous-phase experiments with GLV, eventually confirmed in samples of ambient aerosols.

MW	Name	Product Formula	Structure	Parent Compound	Formation Process	Ref.	Ambient Aerosol
140	Glycolaldehyde sulfate	$C_2H_4O_5S$	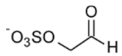	MBO	SO_4^- addition	[268] [b]	$PM_{2.5}$ [277] PM_{10} [278]
154	Hydroxyacetone sulfate	$C_3H_6O_5S$	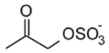	(*Z*)-3-hexen-1-ol	OH photolysis, ozonolysis	[279]	PM_1 [280,281], $PM_{2.5}$ [277,279,282–285], PM_{10} [278]
156	Glycolic acid sulfate	$C_2H_4O_6S$	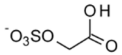	MBO	SO_4^- addition	[268] [b]	PM_1 [280,281,286], $PM_{2.5}$ [277,282–285,287,288]
158	Hydrated glycol sulfate	$C_2H_6O_6S$	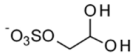	MBO	SO_4^- addition	[268] [b]	
170	Lactic acid sulfate	$C_3H_6O_6S$		(*E*)-2-pentenal	Ozonolysis	[289]	PM_1 [280,286], $PM_{2.5}$ [277,282–284,287,289–292]
170	1-sulfooxy-2-hydroxybutane	$C_4H_{10}O_5S$	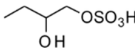	(*E*)-2-pentenal	Ozonolysis	[289]	$PM_{2.5}$ [289]
170	2-Sulfoxy-3-hydroxy-propanal	$C_3H_6O_6S$	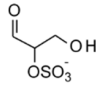	(*Z*)-3-hexen-1-ol	OH photolysis, ozonolysis	[279]	$PM_{2.5}$ [279]
186	3-sulfoxy-2-hydroxy-propanoic acid	$C_3H_6O_7S$	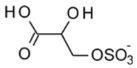	(*Z*)-3-hexen-1-ol	OH photolysis, ozonolysis	[279]	$PM_{2.5}$ [279]
198	3-hydroxy-3-methyl-butan-2-one sulfate	$C_5H_{10}O_6S$	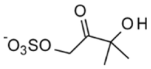	MBO	SO_4^- addition	[268] [b]	
198	4-sulfoxy-1-hydroxy-3-m3thyl-butan-2-one	$C_5H_{10}O_6S$	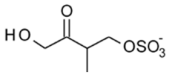	MBO	SO_4^- addition	[268] [b]	$PM_{2.5}$ [277], $PM_{2.5}$ [288]
200	2,3-dihydroxy-3-methyl-butane sulfate	$C_5H_{12}O_6S$	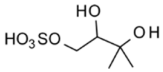	MBO	OH photolysis SO_4^- addition	[266] [a], [268] [b],[293]	PM_1 [280,281] [?], $PM_{2.5}$ [277,283,293], [288] [?]
210	(*Z*)-5-sulfoxy-hex-3-enoic acid	$C_6H_{10}O_6S$	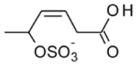	(*Z*)-3-hexen-1-ol	OH photolysis, ozonolysis	[279]	PM_1 [280,281] [?], $PM_{2.5}$ [279], PM_{10} [278] [?]

Table 40. *Cont.*

MW	Name	Product Formula	Structure	Parent Compound	Formation Process	Ref.	Ambient Aerosol
212	6-(sulfoxy) hexanoic acid	$C_6H_{12}O_6S$	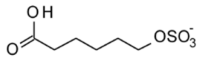	(*Z*)-3-hexen-1-ol	OH photolysis, ozonolysis	[279]	PM_1 [280,281] [?], $PM_{2.5}$ [279]
214	3-sulfoxy-2-hydroxypentanoic acid	$C_5H_{10}O_7S$	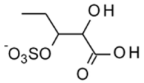	(*E*)-2-pentenal (*E*)-2-pentenoic acid	Ozonolysis, SO_4^- (aqu)	[289]	PM_1 [280] [?], $PM_{2.5}$ [289]
214	2-sulfoxy-3-hydroxypentanoic acid	$C_5H_{10}O_7S$	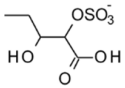	(*E*)-2-pentenal	Ozonolysis	[289]	PM_1, [280,281] [?], $PM_{2.5}$ [289]
226	(*E*)-5-sulfoxy-4-hydroxy-hex-2-enoic acid	$C_6H_{10}O_7S$	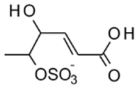	(*Z*)-3-hexen-1-ol	OH photolysis, ozonolysis	[279]	$PM_{2.5}$ [279]
226		$C_6H_{10}O_7S$	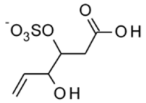	(*Z*)-3-hexenal	Ozonolysis	[294]	$PM_{2.5}$ [294]
230	3-sulfooxy-2,4-dihydroxypentanoic acid	$C_5H_{10}O_8S$	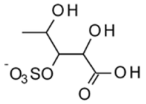	(*E*)-2-pentenal, (*Z*)-3-hexenal (*Z*)-2-hexenal	Ozonolysis ozonolysis	[289]	$PM_{2.5}$ [289]
270		$C_9H_{18}O_7S$	-	(*Z*)-3-hexen-1-ol	OH photolysis, ozonolysis	[279]	$PM_{2.5}$ [279]

[a] aqueous phase reactions of methylbutenol epoxides (Section 5); [b] aqueous-phase addition of sulfate radical anions (Section 5); [?] unresolved structure.

Barbosa et al. [279] studied the formation of SOA from the hydroxyl radical (OH)-initiated oxidation and ozonolysis of (*Z*)-3-hexen-1-ol. They used either non-acidified or acidified sulfate seed aerosols under different relative humidity conditions (12–95% and 5–52%, resp.) and 291–300 K temperatures. The OH radicals were generated by the photolysis of isopropyl nitrite. SOA yields in OH–GLV experiments varied from 13 to 34.2 μg m^{-3} (0.8–2%) for acidic seeds and from 15.2 to 32.1 μg m^{-3} (0.9–2%) for nonacidic seeds, with weak maxima at intermediate RH (~30%). The dependence is biased by the variation of other parameters, notably the NO and NO_x concentrations. SOA yields in O_3–GLV experiments varied from 5 to 52 μg m^{-3} (0.5–5.1%) for acidic seeds and from 5 to 30 μg m^{-3} (0.5–2.9%) for nonacidic seeds, and were significantly higher at low RH (0.7~5% at RH = 4–5% vs. 0.5–1% at RH = 44–51%). They discovered the formation of several organosulfates (Table 40) and confirmed their presence in $PM_{2.5}$ field samples (Section 6.2).

Hamilton et al. [65] studied the SOA formation during ozonolysis or OH initiated oxidation of (*Z*)-3-hexen-1-ol and (*Z*)-3-hexenylacetate in the European Photoreactor chamber in Valencia. They used isoprene as a reference compound. The photolysis of HONO generated the OH radicals. The authors used the LC-ITMS approach to identify the products contained in SOA particles collected on quartz-fiber filters [272]. Ozonolysis of (*Z*)-3-hexenyl acetate produced 3-acetoxypropanal, 3-acetoxypropanoic acid, 3-acetoxypropane peroxic acid, and a range of oligomers with ester and ether linkages (Table 38). Almost all oligomers contained a terminal acetate group, which prevented further oligomeric growth. Ozonolysis of (*Z*)-3-hexen-1-ol produced a vast number of oligomers originating from 3-hydroxypropanal and 3-hydroxypropanoic acid (Table 37), according to the mechanism in (Section 6.3, Scheme 51).

Aerosol mass yields in the OH–GLV experiments were 43.2 μg m^{-3} (3.1%) for (*Z*)-3-hexen-1-ol, 9.7 μg m^{-3} (0.93%) for (*Z*)-3-hexenylacetate, and 18.5 μg m^{-3} (1.2%) for isoprene (initial concentrations 449, 498, and 511 ppbv, resp.). Aerosol mass yields from ozonolysis of GLV were 854 μg m^{-3} (9.6%) for (*Z*)-3-hexen-1-ol and 800 μg m^{-3} (8.5%) for (*Z*)-3-hexenylacetate.

O'Dwyer et al. [201] observed SOA formation during ozonolysis of 1-penten-3-ol, (*Z*)-2-penten-1-ol and 1-penten-3-one at 298 K and atmospheric pressure in a 3910 dm^3 smog chamber (see Section 4.1.3). They used dry conditions and no seed aerosol. A burst of new particles, 30–50 nm in diameter, was observed immediately after the ozone introduction (~180 s). The particles' number decreased in time, but their size increased to 130–150 nm at ~1.2 hours. The aerosol mass yields were 0.136–0.166 for 1-penten-3-ol, 0.156–0.164 for (*Z*)-2-penten-1-ol, and 0.028–0.034 for 1-penten-3-one.

Hamilton et al. [272] studied the composition of SOA obtained from the ozonolysis of (*Z*)-3-hexenylacetate in the EUPHORE chamber at 292 K (average). FTIR followed the decay of hydrocarbons. The formation and growth of SOA was followed by a scanning mobility particle sizer, condensation particle counter, and differential mobility analyzer. Samples of SOA were collected on quartz fiber filters using a high-volume pump. The filters were extracted by sonication with water, methanol, tetrahydrofuran, or acetonitrile. The extracts were evaporated to dryness and reconstituted with a water/methanol solvent (50:50 vol) for LC-MS/MS analysis with Li^+ cationization. The major products identified are listed in Table 38. Fifteen other oligomers were distinguished, all with 3-acetoxypropanoic acid monomer units.

Jain et al. [198] observed the formation of SOA from ozonolysis of (*Z*)-3-hexen-1-ol, (*Z*)-3-hexenyl acetate, or effluents from grass clippings (Festuca, Lolium, and Poa) in a 775 l Teflon chamber at 298 ± K. Ozone was generated externally with a corona discharge apparatus. The initial molar ratio of O_3 and GLV was 1:1. They measured the particle number and mass size distribution using a scanning mobility particle sizer. In grass clipping experiments, SOA formed immediately after ozone injection into the chamber. The mass loading of SOA reached 16 μg m^{-3} from (*Z*)-3-hexenyl acetate and 12 μg m^{-3} from (*Z*)-3-hexen-1-ol. The addition of propionaldehyde enhanced the SOA formation indicating it was a precursor of condensing products (Section 6.3, Scheme 51). They analyzed the

particle composition using near-infrared laser desorption/ionization mass spectrometry. Compounds observed in SOA from grass clipping experiments included first-generation products (m/z 70–150) and later products (m/z 150–300).

Fischer et al. [48] determined the (1.03 ± 0.07%) SOA mass yields from gas-phase ozonolysis of 1-octen-3-ol in two Teflon chambers (see Section 4.2.3) equipped with scanning mobility particle sizers and electrical low power impactors. Ozone and 1-octen-3-ol mixing ratios were 200 ppb. They also observed SOA formation from ozonolysis of volatiles emitted in situ from cut sugarcane. The sugarcane volatiles included toluene, 3-hexenal, 2-hexenal, (*Z*)-3-hexenyl acetate, (*Z*)-3-hexen-1-ol, and 1-octen-3-ol. The gas-phase ozonolysis products included methyl ester of butanoic acid, heptanal, octanal, nonanal, and decanal, all identified against the NIST spectral library. The maximum SOA concentration observed was 1.6 ± 0.2 μg m^{-3}. Several particle-phase products were identified using NIR-LDI-AMS (Section 6.3, Scheme 53). The SOA particles had a non-liquid character shown by the bounce-factor determinations.

Faiola et al. [295] investigated the SOA formation during dark ozonolysis and OH-induced photooxidation of *Pinus sylvestris* emissions. They compared the emissions from healthy plants and plants infested by large pine aphids (*Cinara pinea* Mord.). The initial concentration of MeSa was one of the parameters measured. SOA yield from ozonolysis ranged from 6.3 to 14.6% and did not depend on the infestation. SOA yield from the OH photooxidation of the emissions was: 10.5–23.2% for healthy plants and 17.8–26.8% for the aphid-infested plants.

Waza [296] studied the ozonolysis of (*E*)-2-hexenal, (*Z*)-3-hexen-1-ol, and (*Z*)-3-hexenylacetate in a rectangular 9.8 m^3 Teflon-film chamber at ambient temperature and pressure and 50% RH. He observed the formation and growth of SOA particles. The SOA yields were smaller than those observed for α-pinene in comparable experiments.

Joutsensaari et al. [297] demonstrated the formation and growth of SOA particles from ozonolysis of emissions of white cabbage cultivars sprayed with MeSa in an illuminated 2.6 m^3 growth chamber. The emissions contained terpenes, sesquiterpenes, (*Z*)-3-hexen-1-ol, (*E*)-2-hexenal, and (*Z*)-3-hexenyl acetate.

Shalamzari et al. [294] studied the growth of SOA on seed aerosol during the ozonolysis of (*Z*)-3-hexenal in a 14.5 m^3 steel chamber with Teflon-coated walls. Relative humidity and acidity of seed aerosols varied. The OH radicals were generated from the NO_x-mediated photooxidation of organic precursors. SOA samples were collected on Teflon-impregnated glass fiber filters. The methanol extracts of the filters were obtained using sonication, preconcentrated with a rotary evaporator, filtered, and evaporated to dryness with nitrogen stream. The residue was reconstituted with methanol, dried again, reconstituted with methanol/water solvent (1:1 col), and analyzed with UPLC-MS using reversed-phases or ion-pairing techniques. A significant MW 226 organosulfate was identified as a SOA-bound component from the ozonolysis of (*Z*)-3-hexenal (Table 40).

In a similar study, Shalamzari et al. [289] studied SOA from ozonolysis of (*E*)-2-pentenal, (*Z*)-3-hexenal, and (*Z*)-2-hexenal. They identified the following organosulfates, which could be related to (*E*)-2-pentenal: 3-sulfooxy-2,4-dihydroxy pentanoic acid (MW 230); 2-sulfooxy-3-hydroxy pentanoic acid and 3-sulfooxy-2-hydroxy pentanoic acid (MW214); lactic acid sulfate (MW 170); and 1-sulfooxy-2-hydroxy butane (MW 170) (Table 40). Those organosulfates were also produced during ozonolysis of (*Z*)-3-hexenal and (*Z*)-2-hexenal. 3-sulfoxy-2-hydroxy pentanoic acid was also formed during aqueous-phase sulfation of (*E*)-2-pentenoic acid with sulfate radical anions. The formation mechanisms of those products were suggested.

Harvey et al. [92] observed the formation of SOA from ozonolysis of (*Z*)-3-hexenol, (*Z*)-3-hexenylacetate, their mixtures, and emissions from turf grass (Festuca, Lolium, and Poa). They used a 775 l Teflon chamber at 296 K. Using a scanning mobility particle sizer, they measured total aerosol mass, aerosol particle number, and mass size distribution. The recorded SOA yields were 0.26 ± 0.01 and 0.24 ± 0.08%, respectively. For each GLV, the

products identified included: propanoic acid, propenoic acid, acetic acid, propanal, and 2-propenal (from each GLV). Acetaldehyde was produced only from hexenyl acetate.

Carrasco et al. [177] studied the SOA formation during the gas-phase reactions of MBO with O_3 and with OH radicals in the presence of NO. Experiments with ozone were carried out in the CRAC chamber, while experiments with OH–in the 204 m^3 EUPHORE outdoor chamber with natural sunlight illumination (Section 4.2, Tables 16 and 24). The chambers had multireflection optical systems coupled to FTIR spectrometers for monitoring the concentrations of gaseous reactants and products and the analyzers for monitoring O_3, NO_x, and NO_y. Scanning mobility analyzers monitored the number, concentration, and size distribution of SOA particles. No significant yields of SOA occured in the reactions with OH radicals. Ozonolysis produced 9–25 μg m^{-3} aerosol mass at wet conditions (RH = 20–30%) and 74 μg m^{-3} at dry conditions equivalent to 0.3–1.5% and 1.8% yields, resp.

Chan et al. [187] studied SOA formation during photooxidation of 2-methyl-3-buten-1-ol initiated by OH radicals at 293–298 K, 4–66% RH, and high NO_x or low NO_x conditions in 28 m^3 Caltech dual indoor chambers. The OH radicals were generated by the HONO photooxidation at high NO_x and H_2O_2 photooxidation at low NO_x. GC-FID, chemical ionization MS, and laser-induced phosphorescence were used to determine the concentration of 2-methyl-3-buten-1-ol, gas phase products, and glyoxal, resp. The mass yield of SOA was 0.001–0.0014 in the low NOx experiments and lower than 0.001 in the high NO_x experiments.

Jaoui et al. [273] used a 14.5 m^3 steel chamber with Teflon coated walls to study the photooxidation of 2-methyl-3-buten-2-ol initiated by OH radicals in the presence and absence of NO_x and SO_2. They generated OH radicals by the in situ photolysis of H_2O_2 or methyl nitrite and added ammonium sulfate seed aerosol to promote the condensation of low volatile products. In some experiments, they added SO_2 as well. The reactants and gas-phase carbonyl products were determined using GC-FID and GC-MS. The aerosol particles were collected on quartz filters for further analysis of composition and EC/OC contents. The samples were extracted from filters, derivatized with BSTFA, and analyzed using GC-MS approaches. Size distribution, volume, and total number density of aerosol particles were measured during experiments with a scanning mobility particle sizer. Besides, samples of ambient $PM_{2.5}$ aerosol were collected on quartz filters in the Research Triangle Park, NC USA, extracted, derivatized, and analyzed for composition. Conversion of MBO in all experiments was 70%, the yield of SOA was 0.7% (one experiment), and the yield of secondary organic carbon (SOC) ranged from 0.2 to 0.9%. The gas products identified included formaldehyde, acetaldehyde, glyoxal, glycolaldehyde, methylglyoxal, glyoxylic acid, 2,3butanedione, 2-oxopropane-1-3-dial, 2-hydroxy-2-methylpropanal, 2-hydroxypropane-1,3-dial, 2,3-dioxobutanal, 2,3-dioxobutane-1,4-dial, 3-hydroxy-2-oxo-isopentanol, 2,3-dihydroxy-3-methylbutanal, 2,3-dihydroxy-2-methylbutane dialdehyde, and 2-oxovaleric acid. Table 39 shows products identified in the particle phase.

Zhang et al. 2012 [293] studied the photooxidation of 2-methyl-3-buten-2-ol initiated by OH radicals in the presence of low NO in a 274 m^3 outdoor smog chamber with natural sunlight. The OH radicals were generated from H_2O_2. Neutral or acidic seed aerosol was prepared from ammonium sulfate and sulfuric acid. Aerosol was sampled on glass-fiber filters. The samples were extracted with methanol and analyzed using LC-MS techniques. The SOA yield increased with the acidity of seed aerosol up to 1%. The main product identified–MW 200 organosulfate–was also determined in ambient SOA (Section 6.2). The same product was identified in aerosol samples from smog-chamber experiments with the uptake of (3,3-dimethyloxiran-2-yl) methanol (a 2-metyl-3-buten-1-ol epoxide) on seed aerosols carried out to confirm the epoxide pathways of SOA formation [298].

Novelli et al. [274] studied the photooxidation of MBO by O_3 in the presence of NO in the 270 m^3 outdoor chamber SAPHIR. They followed the evolution of OH and HO_2 radicals and showed it was consistent with box modeling based on the MCM 3.3.1 mechanism. The hydrogen-shift pathways suggested by [299] were insignificant due to relatively low reaction rates. The major products observed in the chamber were acetone and formaldehyde.

6.2. Ambient Aerosols

Many compounds linked to the atmospheric transformation of GLV were firmly identified in ambient aerosol samples. In this section, we present the results from campaigns that intentionally regarded the reactions involving GLV.

Barbosa et al. [279], in a study supporting their chamber experiments, discovered several organosulfates in $PM_{2.5}$ samples collected on prebaked quartz filters in the Atlantic Forest area (open tropical rainforest type) of the Botanical Garden in Rio de Janeiro in 2016 (Table 40). They identified organosulfates also in the companion smog-chamber experiments.

Ambient aerosol samples collected in K-puszta in summer 2003 contained 2,3-dihydroxypentanoic acid, which could originate from 2-pentenal [300], a product of (*Z*)-3-hexenal [161] photolysis.

Shalamzari et al. [294] analyzed $PM_{2.5}$ samples collected in K-puszta from May to June 2006 (BIOSOL campaign). They used high-volume dichotomous $PM_{2.5}$ samplers with quartz-fiber filters and sampled separately during days and nights. Punches from the filters were extracted with methanol, preconcentrated, filtered, and evaporated to dryness. The residues were reconstituted in methanol, divided in portions, and evaporated to dryness. Before the UPLC-MS analysis, the residues were reconstituted in methanol/water (1:4 vol) solvent. A characteristic MW 226 organosulfate $H_2C{=}C{-}CH(OH){-}CH(OSO_3H){-}CH_2{-}C(O)OH$ was identified in the samples, which could form by ozonolysis of (*Z*)-3-hexenal as shown in companion chamber experiments (Section 6.1, Table 40).

Shalamzari et al. [289] continued the analysis of K-puszta aerosol samples. They identified the following organosulfates linked to GLV in the companion chamber studies (Section 6.1, Table 40): 3-sulfoxy-2,4-dihydroxypentanoic acid (MW 230), 2-sulfoxy-3-hydroxypentanoic acid (MW 214), lactic acid sulfate (MW 170), 1-sulfooxy-2-hydroxybutane (MW 170).

Zhang et al. [293] collected ambient $PM_{2.5}$ aerosol samples using high-volume samplers in Manitou Forest Observatory in the Rocky Mountains in 2011. The samples were extracted from filters with methanol and analyzed using LC-MS techniques. The MW 200 organosulfate was identified, which also formed from MBO in companion smog-chamber experiments (Section 6.1, Table 40). The compound was suggested as a plausible marker of MBO SOA.

6.3. Aqueous and Multiphase Mechanisms

GLV and products of their gas-phase reactions (Section 4.1) can partition into aqueous solutions or particle aqueous-phases. They can hydrolyze or react with other dissolved species by various mechanisms reviewed in this section.

GLV epoxides form by the oxidation of GLV in the gas phase. Scheme 43 shows the formation of MBO epoxides, including the 1,5-hydrogen shift and elimination of HO_2 radical [266,298].

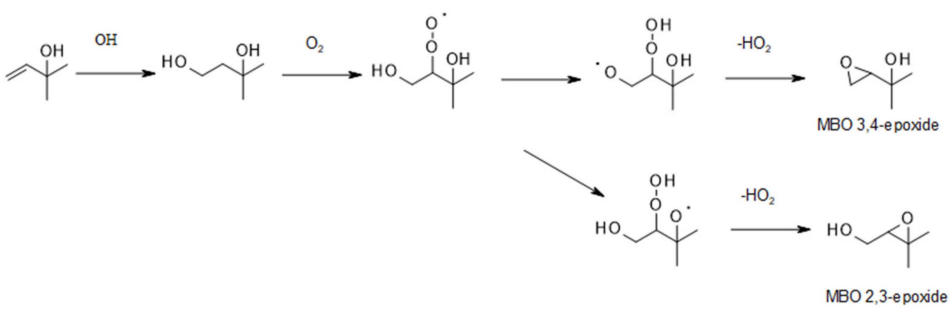

Scheme 43. Formation of 2-methyl-3-buten-2-ol epoxides in the gas phase.

In the aqueous phase, GLV epoxides can hydrolyze or react with acids or acidic anions like sulfate or nitrate as reported for MBO (Scheme 44) [266,267], (*Z*)-3-hexenal [294], and (*E*)-2-pentenal [289]. Hydrolysis is acid-catalyzed [267].

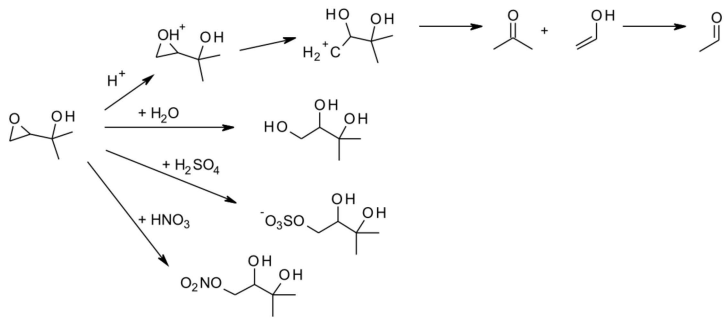

Scheme 44. Hydrolysis, sulfation, and nitration of MBO 3,4-epoxide [266,267].

GLV-derived hydroperoxides form during the ozonolysis or photooxidation of GLV in the gas phase [279]. After partitioning to the aqueous phase, they can react with acids (Scheme 45).

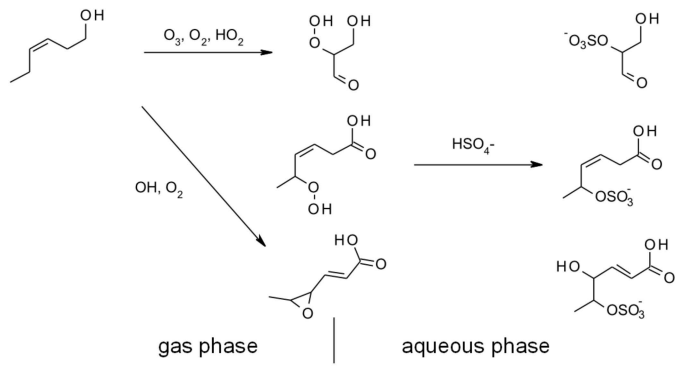

Scheme 45. Aqueous-phase reactions of hydroperoxides and epoxides from the gas-phase oxidation of (*Z*)-3-hexenol [279].

Aqueous-phase reactions of GLV with radicals and radical-anions can proceed by the addition of a radical to a C=C double bond, electron transfer, or hydrogen abstraction. The addition mechanisms lead to many products and are most interesting. The mechanism involving sulfate radical-anions and oxygen was proposed for isoprene [301,302], methyl vinyl ketone [303], (*Z*)-2-pentenoic acid [289], and recently for olefins, including MBO [268]. Scheme 46 shows the reaction mechanism for MBO based on the latter citation. The reaction starts with the addition of SO_4^- to the double C=C bond in MBO and the formation of carbon-centered alkyl sulfate radical (two isomers). Oxygen molecule adds to a radical center to form the peroxyalkyl sulfate radical, which can enter a self-reaction [181] and turn into the sulfate butanediol and hydroxybutanone sulfate products. In an alternative path, the peroxyradical loses one oxygen atom to some available reducing agent and turns into the alkoxy sulfate radical. The alkoxy sulfate radical can undergo electron transfer from a suitable donor and turn into the sulfate butanediol product or can undergo hydrogen abstraction by an oxygen molecule and turn into the hydroxybutanone product. Besides, the alkoxy sulfate radical can participate in several fragmentation processes to give smaller molecules like glycolic sulfates, acetic acid, formic acid, and methanol.

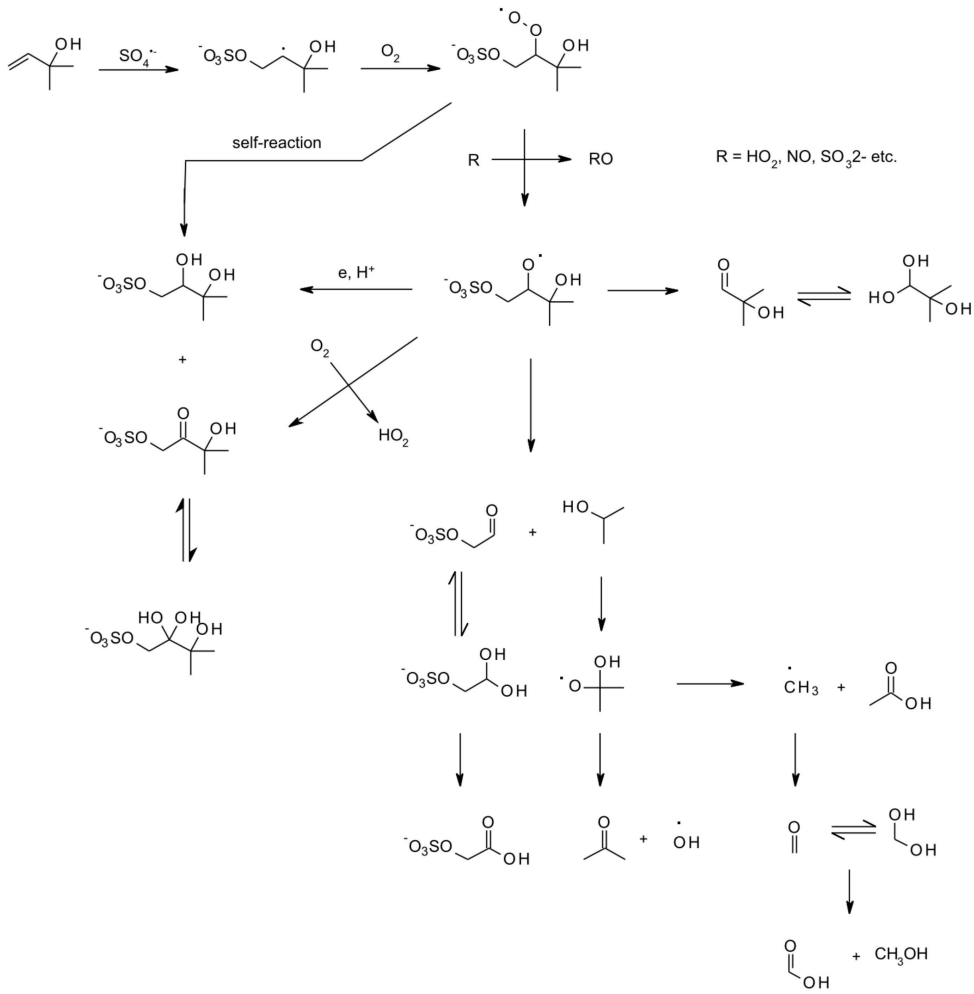

Scheme 46. Mechanism of SO_4^- addition to MBO (based on [268]) shows pathways starting from one of two possible isomers of the alkyl sulfate radical.

Hansel et al. [21,271] proposed the chemical mechanisms of aqueous-phase transformation of MeJa and MeSa. For MeJa, the mechanism started with the addition of OH radical to a double C=C bond producing four isomeric hydroxyalkyl radicals (Scheme 47). Then, an O_2 molecule is added to each isomer to give four isomers of a hydroperoxide radical. Each hydroperoxide isomer could either react with other peroxy radicals present to give alcohols, carbonyls, and organic peroxides, or react with HO_2 radicals and lose O_2 to produce hydroyperoxides. MeSa could react with OH radicals by two distinct paths. They start with the OH addition to the aromatic ring and the phenolic hydrogen abstraction by OH (Scheme 48). In the first path, 1,2- and 1,4-dihydroxycyclohexadienyl radicals formed, which reacted with molecular oxygen to give the peroxyl radicals. The peroxyl radical decomposed by elimination of an HO_2 radical to give dihydroxybenzene. The latter could similarly react with OH and O_2 to afford trihydroxybenzene products. Dihydroxycyclohexadienyl radicals could also lose an H_2O molecule and form an H-adduct radical, converting to phenoxyl radical. The two radicals can recombine to form dimers. In the hydrogen abstraction path, the phenoxyl radical forms directly from MeSa. Trihydroxybenzene products can from peroxy radicals via an alternative pathway (Scheme 49).

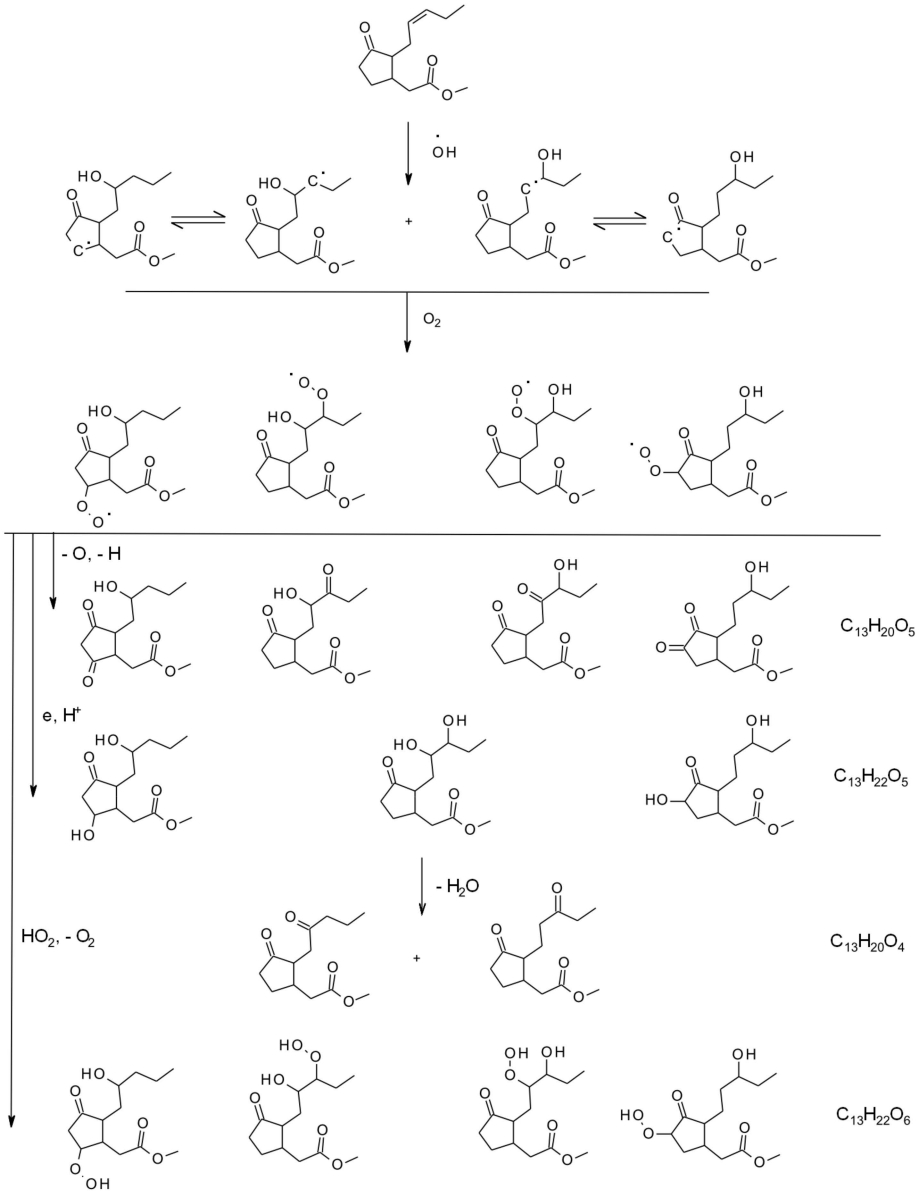

Scheme 47. A plausible mechanism of MeJa reactions initiated by OH radicals in the aqueous phase (elemental formulas annotate products identified in laboratory experiments) [21,271].

An interesting concept was the pinacol rearrangement of protonated MBO, which led to carbonyl derivatives (Scheme 50) [132].

The ozonolysis of GLV has been studied in multiphase chamber experiments but not in the aqueous phase alone [48,92,198,279]. Hydroperoxides formed in the gas phase possibly partitioned to the particle aqueous-phase, and participated in acid-catalyzed sulfation (Scheme 45) [279]. 3-Hydroxypropanal, produced by the decomposition of primary (*Z*)-3-hexen-1-ol ozonide, reactively partitioned to the particle phase. Therein, it plausibly entered several oligomerization reactions to give higher molecular weight products (Scheme 51) [65,198]. A similar mechanism is valid for the particle-phase oligomerization of 3-oxopropyl acetate and propanal (Scheme 52) [92]. Both compounds originated from the gas-phase ozonolysis of (*Z*)-3-hexenyl acetate. The formation of several particle-phase products from 1-octen-3-ol through Criegee intermediates was proposed based on AMS analyses of SOA (Scheme 53) [48].

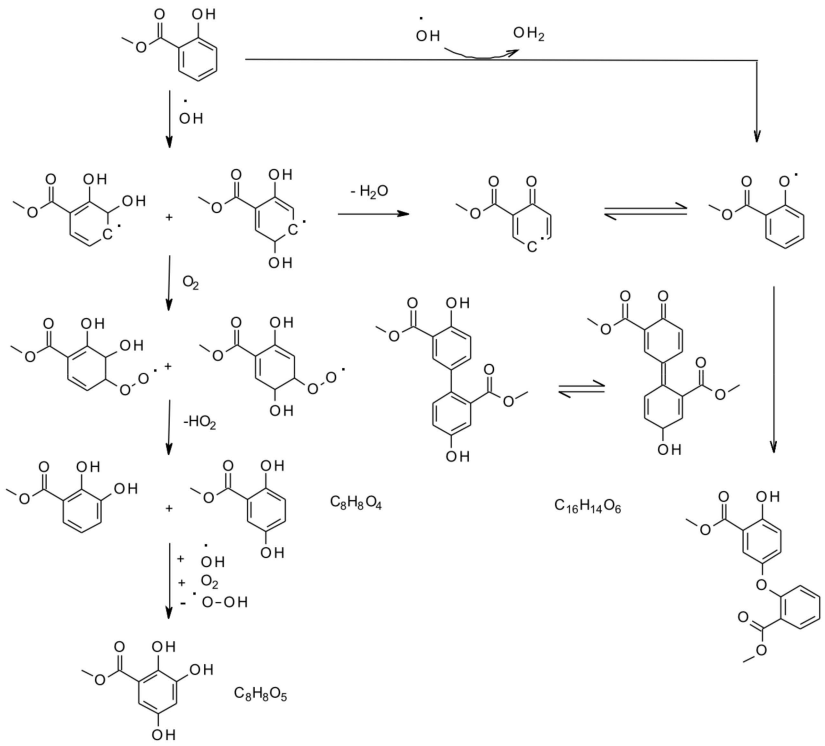

Scheme 48. A plausible mechanism of MeSa reactions initiated by OH radicals in the aqueous phase (elemental formulas mark the products identified in laboratory experiments) [21,271]. The $C_8H_8O_5$ products can also form by an alternative path (Scheme 49).

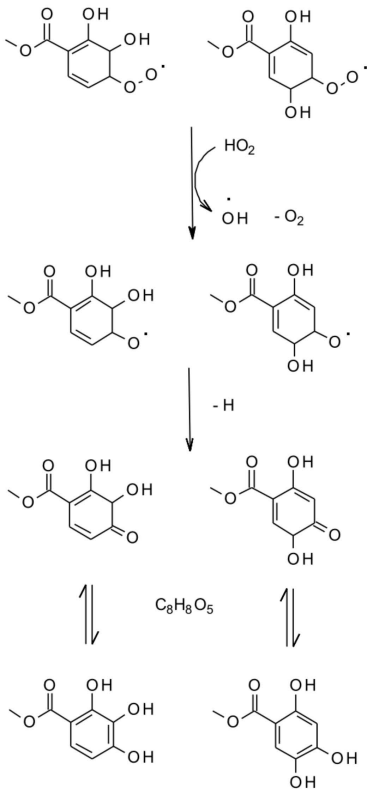

Scheme 49. An alternative mechanism of $C_8H_8O_5$ formation in the oxidation of MeSa initiated by OH radicals [21,271].

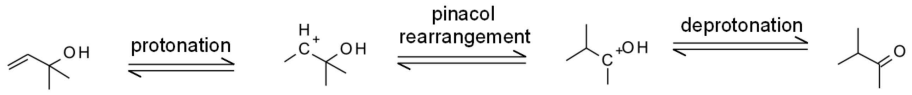

Scheme 50. Pinacol rearrangement in aqueous transformation of MBO [132].

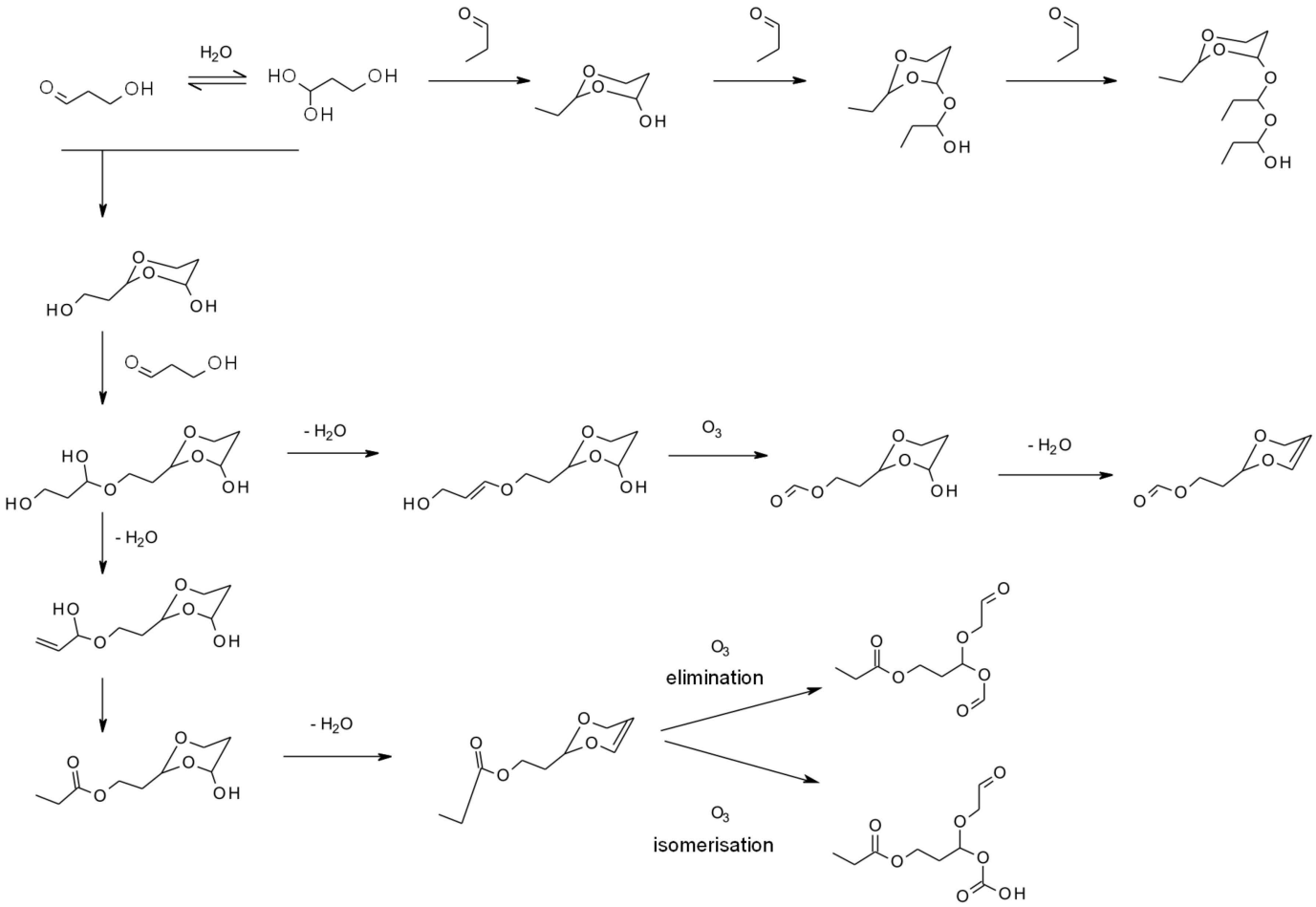

Scheme 51. Particle-phase formation of HMW compounds from 3-hydroxypropanal produced by ozonolysis of (Z)-3-hexen-1-ol [65,198].

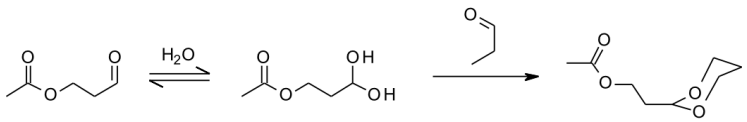

Scheme 52. Particle-phase oligomerization of 3-oxopropyl acetate and propanal that are produced by the gas-phase ozonolysis of (Z)-3-hexenyl acetate [92].

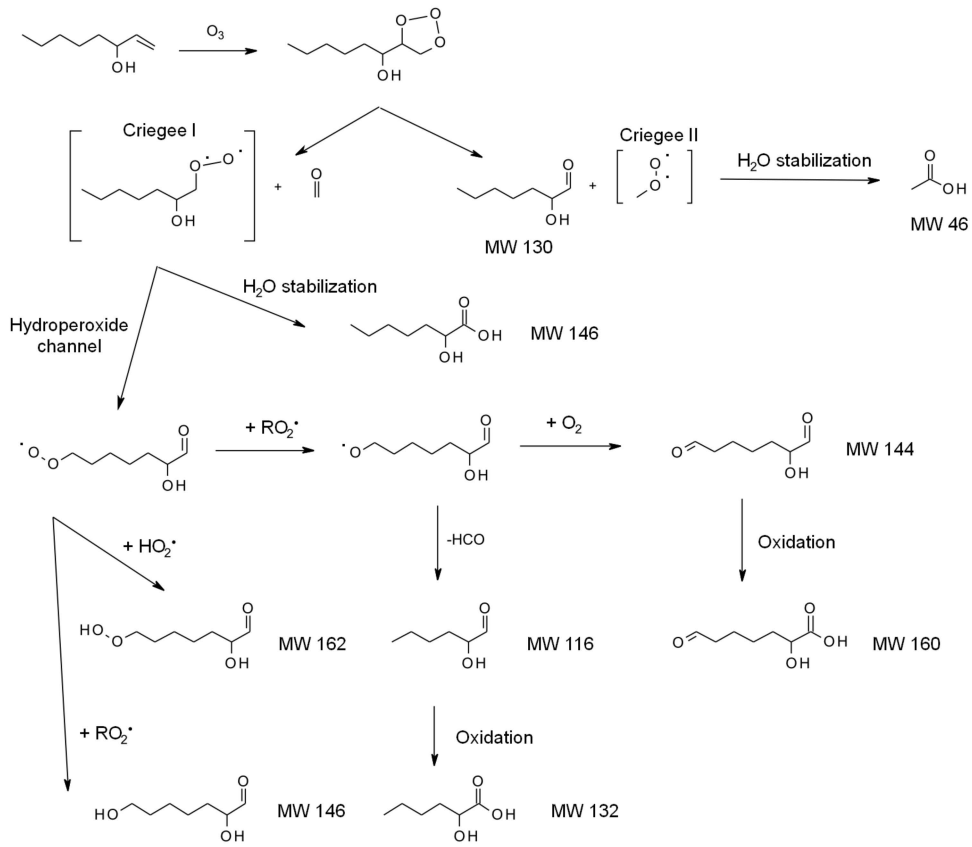

Scheme 53. Mechanism of multiphase ozonolysis of 1-octen-3-ol in a smog chamber [48]. Products with specified MW values were identified in chamber SOA samples using NIR-LDI-AMS approach.

7. Atmospheric Impact of GLV

Holopainen et al. [72] provided a very recent concept review on the role of plant volatiles in the atmosphere-biosphere relations Like F.W. Went in his visionary approach from the 1960s [304,305], they elaborated on a framework linking plant emission with atmospheric processes and formation of soil components. However, that paper presented a general idea and did not go into a detailed treatment.

7.1. Atmospheric Lifetimes of GLV

An atmospheric lifetime of a given compound *C*, which decays in a gas-phase bimolecular reaction with an atmospheric oxidant *X*, is estimated based on the assumption that the rate of *C* decay follows Equation (22):

$$\frac{d\,[C]}{dt} = -k[X][C] \tag{22}$$

We assume that the concentration of *X* is constant, so Equation (22) becomes the explicitly integrable pseudo-first-order equation:

$$ln\left(\frac{[C]}{[C]_0}\right) = -kt \tag{23}$$

For the simplicity of comparison, we assume that the atmospheric lifetime is the time ratio $[C]/[C]_0$ that will be equal to e. After rearrangement, we obtain:

$$t_{atmos} = \frac{1}{k[X]} \tag{24}$$

By analogy, the atmospheric lifetime of a compound due to the gas-phase photolysis is:

$$t_{atmos} = \frac{1}{j} \tag{25}$$

where j is the rate constant of the photolytic decay of this compound.

The atmospheric lifetimes of GLV reported in the literature or calculated from reported rate constants are collected in Table 41.

Sarang et al. [163] analyzed the atmospheric significance of the aqueous-phase reactions of 1-penten-3-ol, (*Z*)-2-hexen-1-ol, and (*E*)-2-hexen-1-al with OH, NO_3, and SO_4^- radicals. The aqueous-phase reactions reduced the atmospheric lifetimes of GLV at sufficiently high liquid water contents (LWC). The radical concentrations in the aqueous phase predicted by CAPRAM modeling [306] were: [OH] = 3.5×10^{-15}–3×10^{-12} M, [NO_3] = 1.9×10^{-15}–8.6×10^{-14} M, [SO_4^-] = 2.3×10^{-15}–3.6×10^{-13} M. LWC ranged from 10^{-12} to 10^{-4} m^3 m^{-3} (aerosol to storm). Henry's equilibria governed the partitioning of reactants between the phases. Fluxes of 1-penten-3-ol and (*Z*)-2-hexen-1-ol removed by the gas-phase and aqueous-phase reactions were comparable only in urban and remote clouds with high liquid water content. (*E*)-2-hexenal was removed faster by gas-phase processing in all clouds. Generally, the aqueous-phase processes did not influence the GLV lifetimes in systems with LWC lower than 10^{-6} m^3 m^{-3} that is most clouds and all aerosol systems. In systems with high LWC, like storms, the lifetime of 1-penten-3-ol decreased markedly due to the aqueous-phase reactions with OH radicals. Similarly, the lifetimes of all three GLV studied decreased due to the reactions with NO_3. Aqueous-phase reactions of GLV with SO_4^- radicals could decrease the GLV lifetimes from years to hours at high LWC and radical concentrations. The authors estimated that the removal of GLV from the atmosphere by the aqueous-phase reaction with SO_4^- was faster than the removal by combined gas and aqueous phase reactions with OH or NO_3 in clouds and rains of high LWC, provided those radicals were in sufficient proportion to OH and NO_3 radicals. For 1-penten-3-ol the proportions were: [OH]/[SO_4^-] $\leq$ 0.16, and [NO_3]/[SO_4^-] < 6.5; for (*Z*)-2-hexen-1-ol–[OH]/[SO_4^-] $\leq$ 0.40, and [NO_3]/[SO_4^-] < 3; and for (*E*)-2-hexen-1-al–[OH]/[SO_4^-] $\leq$ 0.11, and [NO_3]/[SO_4^-] < 1.

7.2. SOA Potential of GLV

There is strong evidence that GLV contribute to the formation of ambient SOA (Section 6). Several smog-chamber experiments (Section 6.1) demonstrated the SOA formation from individual GLV, GLV mixtures, and plant emissions. To date, several compounds identified in ambient aerosol samples are known to form by reactions of GLV with atmospheric oxidants (Section 6.2).

Hamilton [65] estimated that the global SOA production from GLV (namely (*Z*)-3-hexen-1-ol and (*Z*)-3-hexenyl acetate) was 1–5 TgC yr^{-1}. The calculation based on SOA mass yields from the OH photooxidation of isoprene and each GLV in the smog chamber experiments (1.2%, 3.1%, and 0.93%, resp., Section 6.1) scaled up to 3%, 7.5%, and 2.25%. The scaled GLV yields were totaled and applied to the yearly emission of a group of bVOC, including hexenal, hexenol, hexenyl acetate, and six non-GLV compounds estimated as 10–50 TgC yr^{-1} [45]. However, it is not clear whether that range regarded the whole group or each of its members. Thus, the estimated production of 1–5 TgC yr^{-1} of SOA from GLV is somewhat imprecise and uncertain. Furthermore, the chamber yields reflected the masses of SOA carbon obtained from the parent compounds. They cannot convert any amount of a parent compound to the amount of derived SOA if the molecular composition of that compound is unknown.

Table 41. Atmospheric lifetimes of GLV at 298 K due to gas-phase reactions with OH (2×10^6 molecules cm^{-3}), NO_3, (5×10^8 molecules cm^{-3}), O_3 (7×10^{11} molecules cm^{-3}), and Cl (1×10^4 molecules cm^{-3}).

GLV	OH		NO_3		O_3		Cl		Photolysis		
	τ h	Ref.	τ h	Ref.	τ h	Ref.	τ h	Ref.	τ h	Zenith Angle, °	Ref.
Pentan-1-ol	24 [b]	[184]									
1-penten-3-ol	2.1	[185]	40	[192] [a]	23.5	[201]	118	[205] [a]	174–120 [c]		[57]
	2.83	[57] [b]			22.3	[237] [a]					
	1.95	[228] [a]			24.3	[243] [b]					
(*Z*)-2-penten-1-ol	1.3	[185]	3.6	[192] [a]	3.7	[201]	93	[245]			
					2.5	[237] [a]	92.6	[205] [a]			
					2.1	[243] [b]					
(*E*)-2-penten-1-ol	2.05	[57] [a]									
(*E*)-2-pentenal	5.9	[85] [a]	28.8	[230] [a]	309	[244] [b]	212	[246] [b]	0.73	26	[162]
	3.23	[173] [a]									
1-penten-3-one	1.18	[57] [b]	16.4	[215] [a]	29.2	[201]			77–20 [ac]		[57]
hexanal	4.4	[85] [a]	32	[232] [a]			97	[246] [b]	24.4–13.4 [ac]		[159]
	5.0	[159] [a]									
(*Z*)-2-hexen-1-ol	1.25	[217] [b]	3.6	[231]	5.3	[238]					
	4.27	[171] [b]	1.5	[230]							
(*E*)-2-hexen-1-ol	1.4	[176]	4.3	[231]	6.7	[175]	81	[245]			
	4.04	[171] [b]			2.4	[238]	81	[249]			
	2.26	[57] [a]									
(*Z*)-3-hexen-1-ol	1.3	[174,228] a	2.1	[231]	3.8	[237,240] [a]	91	[245]	17.4–11.8 [ac]		[57]
	1.0	[176]	2.0	[174]	2.8	[243] [b]	95	[249]			
	4.78	[57] [b]			6.6	[175]					
	5.05	[171] [b]			6.2	[174]					
					7.2	[238]					
(*E*)-3-hexen-1-ol	1.2	[176]	1.3	[231]	6.9	[175]	86	[245]			
	1.25	[175]			6.4	[238]	81	[249]			
	1.75	[217] [b]			6.6	[243] [a]					
	4.55	[171] [b]									

Table 41. *Cont.*

GLV	OH		NO_3		O_3		Cl		Photolysis		
	τ h	Ref.	τ h	Ref.	τ h	Ref.	τ h	Ref.	τ h	Zenith Angle, °	Ref.
(*Z*)-4-hexen-1-ol	3.92	[171] [b]	1.9	[231]	5.6	[238]					
(*E*)-4-hexen-1-ol	3.57	[171] [b]			3.8	[238]					
(*Z*)-2-hexenal			40.8	[230] [a]							
(*E*)-2-hexenal	3.12	[174] [b]	81.2	[174]	192	[174]	145	[246] [b]	0.48	26	[162]
	2.97	[159] [a]	41	[230]	274	[244] [b]			2.7		[161]
			10	[235]							
			125	[193]							
(*Z*)-3-hexenal					11.5	[160] [a]			13.3		[161]
									5.6	30	[160]
(*Z*)-3-hepten-1-ol	1.09	[175]					73	[249]			
1-octen-3-ol							69	[245]			
(*Z*)-3-octen-1-ol	0.94	[175]					67	[249]			
2-methyl-3-buten-2-ol	3.56	[224] [a]	26.5	[234] [b]	39.9	[237] [a]	130	[251] [a]	>5 yrs		[165]
	2.01	[179] [a]	46	[236]	47.8	[242] [a]	59.1	[224] [a]			
	2.17	[165] [a]			46.1	[224] [a]	84.2	[179] [a]			
	2.5	[177]									
(*E*)-2-hexenylacetate	2	[186]					9.0	[186]			
(*Z*)-3-hexenyl formate	3	[222] [b]			9.8	[241]	113.5	[222]			
(*Z*)-3-hexenyl acetate	1.76	[174] [b]	2.3	[174]	7.3	[174]					
					6.9	[241]					
					4.0	[196] [a]					
(*Z*)-3-hexenyl propionate					5.2	[241]					
(*Z*)-3-hexenyl butyrate					3.2	[241]					
Methyl salicylate	70.88	[190]			99192	[164] [b]	15378	[164] [b]			
					11.3 yrs		1.64 yr				
					15.6 yrs	[189] [a]	275 [b]	[209]			

[a] calculated using the rate constant from the reference; [b] recalculated from the reference values to another concentration; [c] at 0–10 km above Earth's surface.

Better estimates of global annual emissions are available for (*Z*)-3-hexenal (4.9 Tg yr^{-1}), (*Z*)-3-hexenol (2.9 Tg yr^{-1}), and MBO (2.2 Tg yr^{-1})—claimed to be the most abundant GLV (Section 1, [50]). Yields of SOA from OH-initiated processing of (*Z*)-3-hexen-1-ol in smog chambers ranged from 2% [279] to the scaled-up value of 7.5% [65]. The corresponding global annual formation of SOA from (*Z*)-3-hexen-1-ol ranges from 0.058 to 0.218 Tg yr^{-1}. The maximum SOA yield from the smog-chamber ozonolysis of (*Z*)-3-hexenol was 5.2% [279], which gives 0.151 Tg yr^{-1} of SOA globally. Smog-chamber yields of SOA from 2-methyl-3-buten-2-ol were 0.7% for OH reactions and 0.3–1.8% for ozonolysis. Respective global annual production of SOA is 0.015 Tg yr^{-1} and 0.007–0.040 Tg yr^{-1}, respectively. We can assume that the chamber SOA yields from the oxidation of (Z)-3-hexanal are the same as for (*Z*)-3-hexen-1-ol. Then, the atmospheric SOA yields from(Z)-3-hexanal are 0.098–0.368 Tg yr^{-1} from the OH reactions and 0.255 Tg yr^{-1} from the ozonolysis. Thus, the estimated overall SOA yields from (*Z*)-3-hexen-1-ol, MBO, and (*Z*)-3-hexenal would be 0.58–1.05 Tg yr^{-1}.

Besides overall global estimates, one can calculate SOA emission from individual sources. The annual SOA production from C_6 GLV alcohols and aldehydes emitted by cut grass in Sydney and Melbourne was 0.1–0.2 Gg yr^{-1}, based on the emission estimates [19] (Section 2.3) and assumed 5% SOA yield. The annual global production of 940 μg m^{-2} yr^{-1} SOA from grass mowing [92] multiplied by 55.5 × 10^6 km^2 of the total area of world grassland [307] translates into 52 Gg yr^{-1} of SOA.

Switchgrass, grown to produce biofuels, produces 0.7 kg ha^{-1} yr^{-1} of 1-penten-3-ol, hexenols, and hexanals during growth and harvest (based on [88], Table 2). If the SOA yield from GLV is assumed at 5% and the total cultivation area is 9.5 × 10^6 km^2 (data for 16 major countries in 2013, [308]), the total SOA input is 33 Gg yr^{-1}. That number can increase because the available marginal land suitable for switchgrass cultivation amounts to 22.3 × 10^6 km^2 [309].

Estimating SOA production from GLV based on SOA yields from smog-chamber experiments and GLV emission is somewhat approximate. The formation and growth of aerosol in the atmosphere depends on many factors that differ between the chamber and atmospheric conditions like the concentration of reactants, time of reactions, competition by other reactants, and influence of meteorological phenomena.

The global yield of SOA should increase due to the aqueous-phase processing of GLV. Based on the calculated values of the Henry's constant, Hansel et al. [21] concluded that the intermediate and final products of MeJa and MeSa reactions with OH radicals were better soluble in water than the parent compounds and were plausible candidates for components of aqueous SOA.

Richards-Henderson et al. [22] estimated that for typical atmospheric conditions, the reactions of (*Z*)-3-hexen-1-ol, (*Z*)-3-hexenyl acetate, MeSa, MeJa, and MBO with OH radicals in the aqueous phase produced SOA, albeit about 15 times less than the gas phase reactions. The primary reason was low solubility of GLV in water. One can expect this ratio to change if the GLV solubility increases due to factors such as ionic strength or the presence of other organic compounds.

Richards-Henderson et al. [265] estimated the aqueous-phase reactions of singlet oxygen $^1O_2$ * with (*Z*)-3-hexen-1-ol, cis-3-hexenyl acetate, MeSa, MeJa, and MBO were relatively insignificant atmospherically. In contrast, the reactions of ^{3}DMB * with (*Z*)-3-hexenyl acetate, MeSa, and MeJa produced a more aqueous SOA. They showed that the aqueous-phase reactions of MeJa with OH and ^{3}DMB * are the major conversion paths creating SOA, while other GLV convert to SOA mostly in the gas-phase reactions with OH and O_3.

Hansel et al. [21] found that MeJa and MeSa oxidation products in the aqueous phase were much less volatile than the parent compounds, so they were likely to remain in the condensed phases as SOA components.

8. Conclusions

This review proves the substantial interest in Green Leaf Volatiles chemistry among atmospheric scientists. GLV should remain mainly in the atmospheric gas phase because of limited solubility in water. Their aqueous-phase reactions may be significant in atmospheric systems of high liquid water contents. GLV processing at the interfaces, both air-water, and air-particle, is practically a terra incognita. A few papers indicate it may play a role [156,157,269].

The SOA formation from GLV has been proved and warrants further research. Although the previous estimates of SOA production were overestimated (1–5 TgC yr^{-1} [65]), the values estimated in this work are still substantial and range from 0.58 to 1.05 Tg yr^{-1} from (*Z*)-hexen-1-ol, (*Z*)-3-hexenal and MBO jointly, 33 Gg yr^{-1} from switch grass cultivation for biofuels, or 52 Gg yr^{-1} from grass mowing. All calculations utilize SOA yields determined in smog-chamber experiments, which consequently deserve research attention.

The GLV transformation in the atmosphere may be minor globally, compared to major players like isoprene or monoterpenes (mostly α-pinene). The main reason is far smaller GLV emission fluxes. However, the GLV influence on the air quality may be very significant under local scenarios, including high emissions of GLV, like harvesting, switchgrass cultivation, or lawn mowing. It may increase if fumigation of plants with GLV is widely introduced to agriculture, horticulture, and forestry.

Further research should focus on better estimation of SOA yields in smog-chamber experiments, including the influence of relative humidity and acidity of particles, better introduction of GLV to air quality models, at least for local scenarios, and better estimation of GLV emissions for the latter purpose. Aqueous-phase studies should pay more attention to interfacial processes and product characterization. More experimental data on solubility and air-water partitioning of GLV would certainly be welcomed.

The health effects of GLV and GLV atmospheric transformation products have not been studied and warrant further research via abiotic and biotic experiments. The results may be significant to social groups exposed to high GLV emissions like farmers and residents of houses with grass yards.

Author Contributions: Conceptualization, K.J.R.; data mining, K.S. and K.J.R.; writing, K.S., K.J.R., and R.S. All authors have read and agreed to the published version of the manuscript.

Funding: Kumar Sarang received funding for the scientific work from the European Commission Horizon 2020 research and innovation program under the Marie Sklodowska-Curie grant agreements number 711859, and from the financial resources for science in the years 2017–2021 awarded by the Polish Ministry of Science and Higher Education for the implementation of an international cofinanced project.

Institutional Review Board Statement: Not applicable.

Informed Consent Statement: Not applicable.

Data Availability Statement: Not applicable.

Acknowledgments: The authors acknowledge the invitation from Atmosphere Editors to contribute to the Special Issue "Plant-Derived Volatiles and Their Contribution to Secondary Organic Aerosol".

Conflicts of Interest: The authors declar no conflict of interest.

Abbreviations

AAT	alcohol acyltransferase
ADH	alcohol dehydrogenase
AMS	aerosol mass spectrometry
AOC	allene oxide cyclase

AOS	allene oxide synthase
Aqu	aqueous
BVOC	biogenic volatile organic compounds
CEAS	cavity-enhanced absorption spectroscopy
CRAC	smog chamber at the University of Cork
DFT	density functional theory
DHIP	dihydroxoisopropanol
DMAPP	dimethylallyl pyrophosphate (dimethylallyl diphosphate)
DW	dry weight (mass)
EI	electron ionization (in mass spectrometry)
EUPHORE	environmental smog chamber in Valencia, Spain
EVK	ethyl vinyl ketone (1-penten-3-one)
FID	flame ionization detector (in gas chromatography)
FTIR	Fourier transform infrared spectroscopy
GC	gas chromatography
GLV	green leaf volatiles
HMW	higher molecular weight
JA	jasmonic acid
LC	liquid chromatography
LDI	laser desorption ionization (in mass spectrometry)
LFER	linear free energy relation
LISA	smog chamber at the Laboratoire Interuniversitaire des Systèmes Atmosphériques in Paris
LOX	lipoxygenase
LWC	liquid water contents, m^3 (water) m^{-3} (air)
MBO	2-methyl-3-buten-2-ol
MEGAN	Model of Emission of Gases and Aerosols from Nature
MeJa	methyl jasmonate
MeSa	methyl salicylate
MS	mass spectrometry
MW	molecular weight
NIR	near infra-red (spectroscopy)
PAR	photosynthetically active radiation
PI	photoionization detector
PLP-LIF	pulsed laser photolysis—laser-induced fluorescence
PLP-RF	pulse laser photolysis—resonance fluorescence
PM	particulate matter, ambient aerosol
RH	relative humidity (%)
RRKM	Rice–Ramsperger–Kassel–Marcus theory
SAR	structure-activity relation
SMPS	scanning mobility particle sizer
SOA	secondary organic aerosol
SPME	solid-phase microextraction
SRR	structure-reactivity relation
TOF	time of flight analyzer (in mass spectrometry)
UV	ultraviolet
VOC	volatile organic compounds
yr, yrs	year, years

References

1. Matsui, K.; Koeduka, T. Green leaf volatiles in plant signaling and response. In *Lipids in Plant and Algae Development*; Nakamura, Y., LiBeisson, Y., Eds.; Springer: New York, NY, USA, 2016; Volume 86, pp. 427–443.
2. Dong, F.; Fu, X.M.; Watanabe, N.; Su, X.G.; Yang, Z.Y. Recent Advances in the Emission and Functions of Plant Vegetative Volatiles. *Molecules* **2016**, *21*, 124. [CrossRef] [PubMed]
3. Holopainen, J.K. Can forest trees compensate for stress-generated growth losses by induced production of volatile compounds? *Tree Physiology* **2011**, *31*, 1356–1377. [CrossRef]
4. Baldwin, I.T.; Halitschke, R.; Paschold, A.; von Dahl, C.C.; Preston, C.A. Volatile Signaling in Plant-Plant Interactions: "Talking Trees" in the Genomics Era. *Science* **2006**, *311*, 812–815. [CrossRef]

5. Arimura, G.; Pearse, I.S. Chapter One—From the Lab Bench to the Forest: Ecology and Defence Mechanisms of Volatile-Mediated 'Talking Trees'. In *Advances in Botanical Research*; Becard, G., Ed.; Academic Press: Cambridge, MA, USA, 2017; Volume 82, pp. 3–17.
6. Farmer, E.E. Surface-to-air signals. *Nature* **2001**, *411*, 854–856. [CrossRef]
7. Shulaev, V.; Silverman, P.; Raskin, I. Airborne signalling by methyl salicylate in plant pathogen resistance. *Nature* **1997**, *385*, 718–721. [CrossRef]
8. Loreto, F.; Schnitzler, J.-P. Abiotic stresses and induced BVOCs. *Trends Plant Sci.* **2010**, *15*, 154–166. [CrossRef] [PubMed]
9. Shen, J.Y.; Tieman, D.; Jones, J.B.; Taylor, M.G.; Schmelz, E.; Huffaker, A.; Bies, D.; Chen, K.S.; Klee, H.J. A 13-lipoxygenase, TomloxC, is essential for synthesis of C5 flavour volatiles in tomato. *J. Exp. Bot.* **2014**, *65*, 419–428. [CrossRef] [PubMed]
10. Hatanaka, A. The biogeneration of green odor by green leaves. *Phytochemistry* **1993**, *34*, 1201–1218. [CrossRef]
11. Matsui, K.; Sugimoto, K.; Mano, J.; Ozawa, R.; Takabayashi, J. Differential Metabolisms of Green Leaf Volatiles in Injured and Intact Parts of a Wounded Leaf Meet Distinct Ecophysiological Requirements. *PLoS ONE* **2012**, *7*, e10036433. [CrossRef]
12. de Gouw, J.A.; Howard, C.J.; Custer, T.G.; Fall, R. Emissions of volatile organic compounds from cut grass and clover are enhanced during the drying process. *Geophys. Res. Lett.* **1999**, *26*, 811–814. [CrossRef]
13. Jardine, K.; Barron-Gafford, G.A.; Norman, J.P.; Abrell, L.; Monson, R.K.; Meyers, K.T.; Pavao-Zuckerman, M.; Dontsova, K.; Kleist, E.; Werner, C.; et al. Green leaf volatiles and oxygenated metabolite emission bursts from mesquite branches following light-dark transitions. *Photosynth. Res.* **2012**, *113*, 321–333. [CrossRef]
14. Loreto, F.; Barta, C.; Brilli, F.; Nogues, I. On the induction of volatile organic compound emissions by plants as consequence of wounding or fluctuations of light and temperature. *Plant Cell Environ.* **2006**, *29*, 1820–1828. [CrossRef]
15. Brilli, F.; Ruuskanen, T.M.; Schnitzhofer, R.; Muller, M.; Breitenlechner, M.; Bittner, V.; Wohlfahrt, G.; Loreto, F.; Hansel, A. Detection of Plant Volatiles after Leaf Wounding and Darkening by Proton Transfer Reaction "Time-of-Flight" Mass Spectrometry (PTR-TOF). *PLoS ONE* **2011**, *6*, e0020419. [CrossRef] [PubMed]
16. Jardine, K.J.; Chambers, J.Q.; Holm, J.; Jardine, A.B.; Fontes, C.G.; Zorzanelli, R.F.; Meyers, K.T.; de Souza, V.F.; Garcia, S.; Gimenez, B.O.; et al. Green leaf volatile emissions during high temperature and drought stress in a Central Amazon rainforest. *Plants* **2015**, *4*, 678. [CrossRef]
17. Karl, T.; Harren, F.; Warneke, C.; de Gouw, J.; Grayless, C.; Fall, R. Senescing grass crops as regional sources of reactive volatile organic compounds. *J. Geophys. Res. Atmos.* **2005**, *110*, 12. [CrossRef]
18. Kirstine, W.; Galbally, I.; Ye, Y.R.; Hooper, M. Emissions of volatile organic compounds (primarily oxygenated species) from pasture. *J. Geophys. Res. Atmos.* **1998**, *103*, 10605–10619. [CrossRef]
19. Kirstine, W.V.; Galbally, I.E. A simple model for estimating emissions of volatile organic compounds from grass and cut grass in urban airsheds and its application to two Australian cities. *J. Air Waste Manag. Assoc.* **2004**, *54*, 1299–1311. [CrossRef]
20. Scala, A.; Allmann, S.; Mirabella, R.; Haring, M.; Schuurink, R. Green Leaf Volatiles: A Plant's Multifunctional Weapon against Herbivores and Pathogens. *Int. J. Mol. Sci.* **2013**, *14*, 17781. [CrossRef]
21. Hansel, A.K.; Ehrenhauser, F.S.; Richards-Henderson, N.K.; Anastasio, C.; Valsaraj, K.T. Aqueous-phase oxidation of green leaf volatiles by hydroxyl radical as a source of SOA: Product identification from methyl jasmonate and methyl salicylate oxidation. *Atmos. Environ.* **2015**, *102*, 43–51. [CrossRef]
22. Richards-Henderson, N.K.; Hansel, A.K.; Valsaraj, K.T.; Anastasio, C. Aqueous oxidation of green leaf volatiles by hydroxyl radical as a source of SOA: Kinetics and SOA yields. *Atmos. Environ.* **2014**, *95*, 105–112. [CrossRef]
23. Maffei, M.E. Sites of synthesis, biochemistry and functional role of plant volatiles. *S. Afr. J. Bot.* **2010**, *76*, 612–631. [CrossRef]
24. Fisher, A.J.; Baker, B.M.; Greenberg, J.P.; Fall, R. Enzymatic Synthesis of Methylbutenol from Dimethylallyl Diphosphate in Needles of Pinus sabiniana. *Arch. Biochem. Biophys.* **2000**, *383*, 128–134. [CrossRef]
25. Guenther, A.; Geron, C.; Pierce, T.; Lamb, B.; Harley, P.; Fall, R. Natural emissions of non-methane volatile organic compounds; carbon monoxide, and oxides of nitrogen from North America. *Atmos. Environ.* **2000**, *34*, 2205–2230. [CrossRef]
26. Mochizuki, S.; Sugimoto, K.; Koeduka, T.; Matsui, K. Arabidopsis lipoxygenase 2 is essential for formation of green leaf volatiles and five-carbon volatiles. *FEBS Lett.* **2016**, *590*, 1017–1027. [CrossRef] [PubMed]
27. Fisher, A.J.; Grimes, H.D.; Fall, R. The biochemical origin of pentenol emissions from wounded leaves. *Phytochemistry* **2003**, *62*, 159–163. [CrossRef]
28. Mayland, H.F.; Flath, R.A.; Shewmaker, G.E. Volatiles from Fresh and Air-Dried Vegetative Tissues of Tall Fescue (*Festuca arundinacea* Schreb.): Relationship to Cattle Preference. *J. Agric. Food Chem.* **1997**, *45*, 2204–2210. [CrossRef]
29. Fall, R.; Karl, T.; Jordon, A.; Lindinger, W. Biogenic C5VOCs: Release from leaves after freeze-thaw wounding and occurrence in air at a high mountain observatory. *Atmos. Environ.* **2001**, *35*, 3905–3916. [CrossRef]
30. López-Gresa, M.P.; Lisón, P.; Campos, L.; Rodrigo, I.; Rambla, J.L.; Granell, A.; Conejero, V.; Bellés, J.M. A Non-targeted Metabolomics Approach Unravels the VOCs Associated with the Tomato Immune Response against Pseudomonas syringae. *Front. Plant Sci.* **2017**, *8*, 1188. [CrossRef]
31. Connor, E.C.; Rott, A.S.; Zeder, M.; Juttner, F.; Dorn, S. (13)C-labelling patterns of green leaf volatiles indicating different dynamics of precursors in Brassica leaves. *Phytochemistry* **2008**, *69*, 1304–1312. [CrossRef] [PubMed]
32. Matsui, K. Green leaf volatiles: Hydroperoxide lyase pathway of oxylipin metabolism. *Curr. Opin. Plant Biol.* **2006**, *9*, 274–280. [CrossRef]

33. Fall, R.; Karl, T.; Hansel, A.; Jordan, A.; Lindinger, W. Volatile organic compounds emitted after leaf wounding: On-line analysis by proton-transfer-reaction mass spectrometry. *J. Geophys. Res. Atmos.* **1999**, *104*, 15963–15974. [CrossRef]
34. Engelberth, J.; Alborn, H.T.; Schmelz, E.A.; Tumlinson, J.H. Airborne signals prime plants against insect herbivore attack. *Proc. Natl. Acad. Sci. USA* **2004**, *101*, 1781–1785. [CrossRef]
35. Croft, K.P.C.; Juttner, F.; Slusarenko, A.J. Volatile products of the lipoxygenase pathway evolved from *Phaseolus-vulgaris* (L.) leaves inoculated with *Pseudomonas syringae* pv *phaseolicola*. *Plant Physiol.* **1993**, *101*, 13–24. [CrossRef] [PubMed]
36. Fukui, Y.; Doskey, P.V. Identification of nonmethane organic compound emissions from grassland vegetation. *Atmos. Environ.* **2000**, *34*, 2947–2956. [CrossRef]
37. Rose, U.; Manukian, A.; Heath, R.R.; Tumlinson, J.H. Volatile Semiochemicals Released from Undamaged Cotton Leaves (A Systemic Response of Living Plants to Caterpillar Damage). *Plant Physiol.* **1996**, *111*, 487–495. [CrossRef]
38. Matsui, K.; Minami, A.; Hornung, E.; Shibata, H.; Kishimoto, K.; Ahnert, V.; Kindl, H.; Kajiwara, T.; Feussner, I. Biosynthesis of fatty acid derived aldehydes is induced upon mechanical wounding and its products show fungicidal activities in cucumber. *Phytochemistry* **2006**, *67*, 649–657. [CrossRef] [PubMed]
39. Matsui, K.; Kurishita, S.; Hisamitsu, A.; Kajiwara, T. A lipid-hydrolysing activity involved in hexenal formation. *Biochem. Soc. Trans.* **2000**, *28*, 857–860. [CrossRef]
40. Peterson, D.L.; Böröczky, K.; Tumlinson, J.; Cipollini, D. Ecological fitting: Chemical profiles of plant hosts provide insights on selection cues and preferences for a major buprestid pest. *Phytochemistry* **2020**, *176*, 112397. [CrossRef] [PubMed]
41. Zhang, Q.-H.; Birgersson, G.; Zhu, J.; Löfstedt, C.; Löfqvist, J.; Schlyter, F. Leaf Volatiles from Nonhost Deciduous Trees: Variation by Tree Species, Season and Temperature, and Electrophysiological Activity in Ips typographus. *J. Chem. Ecol.* **1999**, *25*, 1923–1943. [CrossRef]
42. Gaquerel, E.; Weinhold, A.; Baldwin, I.T. Molecular Interactions between the Specialist Herbivore Manduca sexta (Lepidoptera, Sphigidae) and Its Natural Host Nicotiana attenuata. VIII. An Unbiased GCxGC-ToFMS Analysis of the Plant's Elicited Volatile Emissions. *Plant Physiol.* **2009**, *149*, 1408–1423. [CrossRef]
43. Kessler, A.; Baldwin, I.T. Defensive function of herbivore-induced plant volatile emissions in nature. *Science* **2001**, *291*, 2141–2144. [CrossRef] [PubMed]
44. Blande, J.D.; Korjus, M.; Holopainen, J.K. Foliar methyl salicylate emissions indicate prolonged aphid infestation on silver birch and black alder. *Tree Physiol.* **2010**, *30*, 404–416. [CrossRef] [PubMed]
45. Wiedinmyer, C.; Guenther, A.; Harley, P.; Hewitt, N.; Geron, C.; Artaxo, P.; Steinbrecher, R.; Rasmussen, R. Global organic emissions from vegetation. In *Emissions of Atmospheric Trace Compound*; Granier, C., Artaxo, P., Reeves, C.E., Eds.; Springer: Dordrecht, The Netherlands, 2004; pp. 115–170. [CrossRef]
46. Karl, T.G.; Spirig, C.; Rinne, J.; Stroud, C.; Prevost, P.; Greenberg, J.; Fall, R.; Guenther, A. Virtual disjunct eddy covariance measurements of organic compound fluxes from a subalpine forest using proton transfer reaction mass spectrometry. *Atmos. Chem. Phys.* **2002**, *2*, 279–291. [CrossRef]
47. Geron, C.D.; Daly, R.W.; Arnts, R.R.; Guenther, A.B.; Mowry, F.L. Canopy level emissions of 2-methyl-3-buten-2-ol, monoterpenes, and sesquiterpenes from an experimental Pinus taeda plantation. *Sci. Total Environ.* **2016**, *565*, 730–741. [CrossRef] [PubMed]
48. Fischer, K.B.; Gold, C.S.; Harvey, R.M.; Petrucci, A.N.; Petrucci, G.A. Ozonolysis Chemistry and Phase Behavior of 1-Octen-3-ol-Derived Secondary Organic Aerosol. *ACS Earth Space Chem.* **2020**, *4*, 1298–1308. [CrossRef]
49. Creelman, R.A.; Mullet, J.E. Biosynthesis and action of jasmonates in plants. *Annu. Rev. Plant Physiol. Plant Mol. Biol.* **1997**, *48*, 355–381. [CrossRef]
50. Guenther, A.B.; Jiang, X.; Heald, C.L.; Sakulyanontvittaya, T.; Duhl, T.; Emmons, L.K.; Wang, X. The Model of Emissions of Gases and Aerosols from Nature version 2.1 (MEGAN2.1): An extended and updated framework for modeling biogenic emissions. *Geosci. Model Dev.* **2012**, *5*, 1471–1492. [CrossRef]
51. Sindelarova, K.; Granier, C.; Bouarar, I.; Guenther, A.; Tilmes, S.; Stavrakou, T.; Müller, J.F.; Kuhn, U.; Stefani, P.; Knorr, W. Global data set of biogenic VOC emissions calculated by the MEGAN model over the last 30 years. *Atmos. Chem. Phys.* **2014**, *14*, 9317–9341. [CrossRef]
52. Su, Q.; Yang, F.; Zhang, Q.; Tong, H.; Hu, Y.; Zhang, X.; Xie, W.; Wang, S.; Wu, Q.; Zhang, Y. Defence priming in tomato by the green leaf volatile (Z)-3-hexenol reduces whitefly transmission of a plant virus. *Plant Cell Environ.* **2020**, *43*, 2797–2811. [CrossRef] [PubMed]
53. Guo, R.-Z.; Yan, H.-Y.; Li, X.-X.; Zou, X.-X.; Zhang, X.-J.; Yu, X.-N.; Ci, D.-W.; Wang, Y.-F.; Si, T. Green leaf volatile (Z)-3-hexeny-1-yl acetate reduces salt stress in peanut by affecting photosynthesis and cellular redox homeostasis. *Physiol. Plant.* **2020**, *170*, 75–92. [CrossRef]
54. Wakai, J.; Kusama, S.; Nakajima, K.; Kawai, S.; Okumura, Y.; Shiojiri, K. Effects of trans-2-hexenal and cis-3-hexenal on post-harvest strawberry. *Sci. Rep.* **2019**, *9*, 10112. [CrossRef] [PubMed]
55. Cofer, T.M.; Engelberth, M.; Engelberth, J. Green leaf volatiles protect maize (Zea mays) seedlings against damage from cold stress. *Plant Cell Environ.* **2018**, *41*, 1673–1682. [CrossRef] [PubMed]
56. Payá, C.; López-Gresa, M.P.; Intrigliolo, D.S.; Rodrigo, I.; Bellés, J.M.; Lisón, P. (Z)-3-Hexenyl Butyrate Induces Stomata Closure and Ripening in Vitis vinifera. *Agronomy* **2020**, *10*, 1122. [CrossRef]
57. Jiménez, E.; Lanza, B.; Antiñolo, M.; Albaladejo, J. Photooxidation of leaf-wound oxygenated compounds, 1-penten-3-ol, (Z)-3-hexen-1-ol, and 1-penten-3-one, initiated by OH radicals and sunlight. *Environ. Sci. Technol.* **2009**, *43*, 1831–1837. [CrossRef]

58. Yli-Pirilä, P.; Copolovici, L.; Kännaste, A.; Noe, S.; Blande, J.D.; Mikkonen, S.; Klemola, T.; Pulkkinen, J.; Virtanen, A.; Laaksonen, A.; et al. Herbivory by an Outbreaking Moth Increases Emissions of Biogenic Volatiles and Leads to Enhanced Secondary Organic Aerosol Formation Capacity. *Environ. Sci. Technol.* **2016**, *50*, 11501–11510. [CrossRef]
59. Tsigaridis, K.; Daskalakis, N.; Kanakidou, M.; Adams, P.J.; Artaxo, P.; Bahadur, R.; Balkanski, Y.; Bauer, S.E.; Bellouin, N.; Benedetti, A.; et al. The AeroCom evaluation and intercomparison of organic aerosol in global models. *Atmos. Chem. Phys.* **2014**, *14*, 10845–10895. [CrossRef]
60. Khan, M.A.H.; Jenkin, M.E.; Foulds, A.; Derwent, R.G.; Percival, C.J.; Shallcross, D.E. A modeling study of secondary organic aerosol formation from sesquiterpenes using the STOCHEM global chemistry and transport model. *J. Geophys. Res. Atmos.* **2017**, *122*, 4426–4439. [CrossRef]
61. Hodzic, A.; Kasibhatla, P.S.; Jo, D.S.; Cappa, C.D.; Jimenez, J.L.; Madronich, S.; Park, R.J. Rethinking the global secondary organic aerosol (SOA) budget: Stronger production, faster removal, shorter lifetime. *Atmos. Chem. Phys.* **2016**, *16*, 7917–7941. [CrossRef]
62. Carlton, A.G.; Wiedinmyer, C.; Kroll, J.H. A review of secondary organic aerosol (SOA) formation from isoprene. *Atmos. Chem. Phys.* **2009**, *9*, 4987–5005. [CrossRef]
63. Lim, H.-J.; Carlton, A.G.; Turpin, B.J. Isoprene Forms Secondary Organic Aerosol through Cloud Processing: Model Simulations. *Environ. Sci. Technol.* **2005**, *39*, 4441–4446. [CrossRef]
64. Lin, G.; Penner, J.E.; Zhou, C. How will SOA change in the future? *Geophys. Res. Lett.* **2016**, *43*, 1718–1726. [CrossRef]
65. Hamilton, J.F.; Lewis, A.C.; Carey, T.J.; Wenger, J.C.; Garcia, E.B.I.; Munoz, A. Reactive oxidation products promote secondary organic aerosol formation from green leaf volatiles. *Atmos. Chem. Phys.* **2009**, *9*, 3815–3823. [CrossRef]
66. Dicke, M.; Loreto, F. Induced plant volatiles: From genes to climate change. *Trends Plant Sci.* **2010**, *15*, 115–117. [CrossRef] [PubMed]
67. Peñuelas, J.; Staudt, M. BVOCs and global change. *Trends Plant Sci.* **2010**, *15*, 133–144. [CrossRef] [PubMed]
68. Holopainen, J.K.; Gershenzon, J. Multiple stress factors and the emission of plant VOCs. *Trends Plant Sci.* **2010**, *15*, 176–184. [CrossRef]
69. Noziere, B.; Kalberer, M.; Claeys, M.; Allan, J.; D'Anna, B.; Decesari, S.; Finessi, E.; Glasius, M.; Grgic, I.; Hamilton, J.F.; et al. The molecular identification of organic compounds in the atmosphere: State of the art and challenges. *Chem. Rev.* **2015**, *115*, 3919–3983. [CrossRef]
70. Herrmann, H.; Schaefer, T.; Tilgner, A.; Styler, S.A.; Weller, C.; Teich, M.; Otto, T. Tropospheric aqueous-phase chemistry: Kinetics, mechanisms, and its coupling to a changing gas phase. *Chem. Rev.* **2015**, *115*, 4259–4334. [CrossRef] [PubMed]
71. Mellouki, A.; Wallington, T.J.; Chen, J. Atmospheric chemistry of oxygenated volatile organic compounds: Impacts on air quality and climate. *Chem. Rev.* **2015**, *115*, 3984–4014. [CrossRef] [PubMed]
72. Holopainen, J.K.; Kivimäenpää, M.; Nizkorodov, S.A. Plant-derived Secondary Organic Material in the Air and Ecosystems. *Trends Plant Sci.* **2017**, *22*, 744–753. [CrossRef] [PubMed]
73. Ameye, M.; Allmann, S.; Verwaeren, J.; Smagghe, G.; Haesaert, G.; Schuurink, R.C.; Audenaert, K. Green leaf volatile production by plants: A meta-analysis. *New Phytol.* **2018**, *220*, 666–683. [CrossRef]
74. López-Gresa, M.P.; Payá, C.; Ozáez, M.; Rodrigo, I.; Conejero, V.; Klee, H.; Bellés, J.M.; Lisón, P. A New Role for Green Leaf Volatile Esters in Tomato Stomatal Defense Against *Pseudomonas syringe* pv. *tomato*. *Front. Plant Sci.* **2018**, *9*, 1855. [CrossRef] [PubMed]
75. Kivimäenpää, M.; Babalola, A.B.; Joutsensaari, J.; Holopainen, J.K. Methyl Salicylate and Sesquiterpene Emissions Are Indicative for Aphid Infestation on Scots Pine. *Forests* **2020**, *11*, 573. [CrossRef]
76. Niinemets, Ü.; Kännaste, A.; Copolovici, L. Quantitative patterns between plant volatile emissions induced by biotic stresses and the degree of damage. *Front. Plant Sci.* **2013**, *4*, 262. [CrossRef] [PubMed]
77. Mattiacci, L.; Rocca, B.A.; Scascighini, N.; D'Alessandro, M.; Hern, A.; Dorn, S. Systemically induced plant volatiles emitted at the time of "danger". *J. Chem. Ecol.* **2001**, *27*, 2233–2252. [CrossRef] [PubMed]
78. Engelberth, J. Primed to grow: A new role for green leaf volatiles in plant stress responses. *Plant Signal. Behav.* **2020**, *15*, 1701240. [CrossRef]
79. Arimura, G.-I.; Kost, C.; Boland, W. Herbivore-induced, indirect plant defences. *Biochim. Biophys. Acta (BBA) Mol. Cell Biol. Lipids* **2005**, *1734*, 91–111. [CrossRef] [PubMed]
80. Cui, H.; Wei, J.; Su, J.; Li, C.; Ge, F. Elevated O_3 increases volatile organic compounds via jasmonic acid pathway that promote the preference of parasitoid Encarsia formosa for tomato plants. *Plant Sci.* **2016**, *253*, 243–250. [CrossRef] [PubMed]
81. Pinto, D.M.; Nerg, A.M.; Holopainen, J.K. The role of ozone-reactive compounds, terpenes, and green leaf volatiles (GLVs), in the orientation of *Cotesia plutellae*. *J. Chem. Ecol.* **2007**, *33*, 2218–2228. [CrossRef] [PubMed]
82. Hanley, M.E.; Shannon, R.W.R.; Lemoine, D.G.; Sandey, B.; Newland, P.L.; Poppy, G.M. Riding on the wind: Volatile compounds dictate selection of grassland seedlings by snails. *Ann. Bot.* **2018**, *122*, 1075–1083. [CrossRef] [PubMed]
83. Dudareva, N.; Negre, F.; Nagegowda, D.A.; Orlova, I. Plant volatiles: Recent advances and future perspectives. *Crit. Rev. Plant Sci.* **2006**, *25*, 417–440. [CrossRef]
84. Engelberth, J.; Engelberth, M. Variability in the Capacity to Produce Damage-Induced Aldehyde Green Leaf Volatiles among Different Plant Species Provides Novel Insights into Biosynthetic Diversity. *Plants* **2020**, *9*, 213. [CrossRef]
85. Albaladejo, J.; Ballesteros, B.; Jiménez, E.; Martén, P.; Marténez, E. A PLP–LIF kinetic study of the atmospheric reactivity of a series of C4–C7 saturated and unsaturated aliphatic aldehydes with OH. *Atmos. Environ.* **2002**, *36*, 3231–3239. [CrossRef]

86. König, G.; Brunda, M.; Puxbaum, H.; Hewitt, C.N.; Duckham, S.C.; Rudolph, J. Relative contribution of oxygenated hydrocarbons to the total biogenic VOC emissions of selected mid-European agricultural and natural plant species. *Atmos. Environ.* **1995**, *29*, 861–874. [CrossRef]
87. García-Plazaola, J.I.; Portillo-Estrada, M.; Fernández-Marín, B.; Kännaste, A.; Niinemets, Ü. Emissions of carotenoid cleavage products upon heat shock and mechanical wounding from a foliose lichen. *Environ. Exp. Bot.* **2017**, *133*, 87–97. [CrossRef]
88. Eller, A.S.D.; Sekimoto, K.; Gilman, J.B.; Kuster, W.C.; de Gouw, J.A.; Monson, R.K.; Graus, M.; Crespo, E.; Warneke, C.; Fall, R. Volatile organic compound emissions from switchgrass cultivars used as biofuel crops. *Atmos. Environ.* **2011**, *45*, 3333–3337. [CrossRef]
89. Heiden, A.C.; Hoffmann, T.; Kahl, J.; Kley, D.; Klockow, D.; Langebartels, C.; Mehlhorn, H.; Sandermann, H., Jr.; Schraudner, M.; Schuh, G.; et al. Emission of volatile organic compounds from ozone-exposed plants. *Ecol. Appl.* **1999**, *9*, 1160–1167. [CrossRef]
90. Helmig, D.; Klinger, L.F.; Guenther, A.; Vierling, L.; Geron, C.; Zimmerman, P. Biogenic volatile organic compound emissions (BVOCs) I. Identifications from three continental sites in the U.S. *Chemosphere* **1999**, *38*, 2163–2187. [CrossRef]
91. Semiz, G.; Blande, J.D.; Heijari, J.; Işık, K.; Niinemets, Ü.; Holopainen, J.K. Manipulation of VOC emissions with methyl jasmonate and carrageenan in the evergreen conifer *Pinus sylvestris* and evergreen broadleaf *Quercus ilex*. *Plant Biol.* **2012**, *14*, 57–65. [CrossRef]
92. Harvey, R.M.; Zahardis, J.; Petrucci, G.A. Establishing the contribution of lawn mowing to atmospheric aerosol levels in American suburbs. *Atmos. Chem. Phys.* **2014**, *14*, 797–812. [CrossRef]
93. Giacomuzzi, V.; Cappellin, L.; Nones, S.; Khomenko, I.; Biasioli, F.; Knight, A.L.; Angeli, S. Diel rhythms in the volatile emission of apple and grape foliage. *Phytochemistry* **2017**, *138*, 104–115. [CrossRef]
94. Fukui, Y.; Doskey, P.V. Air-surface exchange of nonmethane organic compounds at a grassland site: Seasonal variations and stressed emissions. *J. Geophys. Res. Atmos.* **1998**, *103*, 13153–13168. [CrossRef]
95. Arey, J.; Winer, A.M.; Atkinson, R.; Aschmann, S.M.; Long, W.D.; Lynn Morrison, C. The emission of (Z)-3-hexen-1-ol, (Z)-3-hexenylacetate and other oxygenated hydrocarbons from agricultural plant species. *Atmos. Environ. Part A Gen. Top.* **1991**, *25*, 1063–1075. [CrossRef]
96. Bamberger, I.; Hortnagl, L.; Schnitzhofer, R.; Graus, M.; Ruuskanen, T.M.; Muller, M.; Dunkl, J.; Wohlfahrt, G.; Hansel, A. BVOC fluxes above mountain grassland. *Biogeosciences* **2010**, *7*, 1413–1424. [CrossRef]
97. Gray, D.W.; Lerdau, M.T.; Goldstein, A.H. Influences of temperature history, water stress, and needle age on methylbutenol emissions. *Ecology* **2003**, *84*, 765–776. [CrossRef]
98. Harley, P.; Eller, A.; Guenther, A.; Monson, R.K. Observations and models of emissions of volatile terpenoid compounds from needles of ponderosa pine trees growing in situ: Control by light, temperature and stomatal conductance. *Oecologia* **2014**, *176*, 35–55. [CrossRef]
99. Juráň, S.; Pallozzi, E.; Guidolotti, G.; Fares, S.; Šigut, L.; Calfapietra, C.; Alivernini, A.; Savi, F.; Večeřová, K.; Křůmal, K.; et al. Fluxes of biogenic volatile organic compounds above temperate Norway spruce forest of the Czech Republic. *Agric. For. Meteorol.* **2017**, *232*, 500–513. [CrossRef]
100. Baker, B.; Guenther, A.; Greenberg, J.; Goldstein, A.; Fall, R. Canopy fluxes of 2-methyl-3-buten-2-ol over a ponderosa pine forest by relaxed eddy accumulation: Field data and model comparison. *J. Geophys. Res. Atmos.* **1999**, *104*, 26107–26114. [CrossRef]
101. Schade, G.W.; Goldstein, A.H. Fluxes of oxygenated volatile organic compounds from a ponderosa pine plantation. *J. Geophys. Res. Atmos.* **2001**, *106*, 3111–3123. [CrossRef]
102. Baker, B.; Guenther, A.; Greenberg, J.; Fall, R. Canopy Level Fluxes of 2-Methyl-3-buten-2-ol, Acetone, and Methanol by a Portable Relaxed Eddy Accumulation System. *Environ. Sci. Technol.* **2001**, *35*, 1701–1708. [CrossRef]
103. Arnts, R.R.; Mowry, F.L.; Hampton, G.A. A high-frequency response relaxed eddy accumulation flux measurement system for sampling short-lived biogenic volatile organic compounds. *J. Geophys. Res. Atmos.* **2013**, *118*, 4860–4873. [CrossRef]
104. Schade, G.W.; Goldstein, A.H.; Gray, D.W.; Lerdau, M.T. Canopy and leaf level 2-methyl-3-buten-2-ol fluxes from a ponderosa pine plantation. *Atmos. Environ.* **2000**, *34*, 3535–3544. [CrossRef]
105. Harley, P.; Fridd-Stroud, V.; Greenberg, J.; Guenther, A.; Vasconcellos, P. Emission of 2-methyl-3-buten-2-ol by pines: A potentially large natural source of reactive carbon to the atmosphere. *J. Geophys. Res. Atmos.* **1998**, *103*, 25479–25486. [CrossRef]
106. Karl, T.; Guenther, A.; Turnipseed, A.; Patton, E.G.; Jardine, K. Chemical sensing of plant stress at the ecosystem scale. *Biogeosciences* **2008**, *5*, 1287–1294. [CrossRef]
107. Copolovici, L.; Kännaste, A.; Remmel, T.; Niinemets, Ü. Volatile organic compound emissions from *Alnus glutinosa* under interacting drought and herbivory stresses. *Environ. Exp. Bot.* **2014**, *100*, 55–63. [CrossRef] [PubMed]
108. Brilli, F.; Hortnagl, L.; Bamberger, I.; Schnitzhofer, R.; Ruuskanen, T.M.; Hansel, A.; Loreto, F.; Wohlfahrt, G. Qualitative and quantitative characterization of volatile organic compound emissions from cut grass. *Environ. Sci. Technol.* **2012**, *46*, 3859–3865. [CrossRef]
109. Karl, T.; Guenther, A.; Lindinger, C.; Jordan, A.; Fall, R.; Lindinger, W. Eddy covariance measurements of oxygenated volatile organic compound fluxes from crop harvesting using a redesigned proton-transfer-reaction mass spectrometer. *J. Geophys. Res. Atmos.* **2001**, *106*, 24157–24167. [CrossRef]
110. Karl, T.; Guenther, A.; Jordan, A.; Fall, R.; Lindinger, W. Eddy covariance measurement of biogenic oxygenated VOC emissions from hay harvesting. *Atmos. Environ.* **2001**, *35*, 491–495. [CrossRef]

111. de Carvalho, A.B.; Kato, M.; Rezende, M.M.; Pereira, P.; de Andrade, J.B. Determination of carbonyl compounds in the atmosphere of charcoal plants by HPLC and UV detection. *J. Sep. Sci.* **2008**, *31*, 1686–1693. [CrossRef] [PubMed]
112. Karl, T.; Fall, R.; Jordan, A.; Lindinger, W. On-line analysis of reactive VOCs from urban lawn mowing. *Environ. Sci. Technol.* **2001**, *35*, 2926–2931. [CrossRef] [PubMed]
113. Gentner, D.R.; Ormeno, E.; Fares, S.; Ford, T.B.; Weber, R.; Park, J.H.; Brioude, J.; Angevine, W.M.; Karlik, J.F.; Goldstein, A.H. Emissions of terpenoids, benzenoids, and other biogenic gas-phase organic compounds from agricultural crops and their potential implications for air quality. *Atmos. Chem. Phys.* **2014**, *14*, 5393–5413. [CrossRef]
114. Goldan, P.D.; Kuster, W.C.; Fehsenfeld, F.C.; Montzka, S.A. The observation of a C5 alcohol emission in a North American pine forest. *Geophys. Res. Lett.* **1993**, *20*, 1039–1042. [CrossRef]
115. Guenther, A.; Karl, T.; Harley, P.; Wiedinmyer, C.; Palmer, P.I.; Geron, C. Estimates of global terrestrial isoprene emissions using MEGAN (Model of Emissions of Gases and Aerosols from Nature). *Atmos. Chem. Phys.* **2006**, *6*, 3181–3210. [CrossRef]
116. Heiden, A.C.; Kobel, K.; Langebartels, C.; Schuh-Thomas, G.; Wildt, J. Emissions of oxygenated volatile organic compounds from plants - part I: Emissions from lipoxygenase activity. *J. Atmos. Chem.* **2003**, *45*, 143–172. [CrossRef]
117. US_EPA. *Estimation Programs Interface Suite™ for Microsoft®Windows, v 4.11*; United States Environmental Protection Agency: Washington, DC, USA, 2012.
118. Hine, J.; Mookerjee, P.K. Structural effects on rates and equilibriums. XIX. Intrinsic hydrophilic character of organic compounds. Correlations in terms of structural contributions. *J. Org. Chem.* **1975**, *40*, 292–298. [CrossRef]
119. Altschuh, J.; Bruggemann, R.; Santl, H.; Eichinger, G.; Piringer, O.G. Henry's law constants for a diverse set of organic chemicals: Experimental determination and comparison of estimation methods. *Chemosphere* **1999**, *39*, 1871–1887. [CrossRef]
120. Sander, R. Compilation of Henry's law constants (version 4.0) for water as solvent. *Atmos. Chem. Phys.* **2015**, *15*, 4399–4981. [CrossRef]
121. Staudinger, J.; Roberts, P.V. A critical review of Henry's law constants for environmental applications. *Crit. Rev. Environ. Sci. Technol.* **1996**, *26*, 205–297. [CrossRef]
122. Sangster, J. Octanol-water partition coefficients of simple organic compounds. *J. Phys. Chem. Ref. Data* **1989**, *18*, 1111–1229. [CrossRef]
123. Abraham, M.H.; Le, J.; Acree, W.E.; Carr, P.W.; Dallas, A.J. The solubility of gases and vapours in dry octan-1-ol at 298 K. *Chemosphere* **2001**, *44*, 855–863. [CrossRef]
124. Shunthirasingham, C.; Cao, X.S.; Lei, Y.D.; Wania, F. Large bubbles reduce the surface sorption artifact of the inert gas stripping method. *J. Chem. Eng. Data* **2013**, *58*, 792–797. [CrossRef]
125. Hansch, C.; Quinlan, J.E.; Lawrence, G.L. Linear free-energy relationship between partition coefficients and aqueous solubility of organic liquids. *J. Org. Chem.* **1968**, *33*, 347. [CrossRef]
126. Suzuki, T. Development of an automatic estimation system for both the partition-coefficient and aqueous solubility. *J. Comput.-Aided Mol. Des.* **1991**, *5*, 149–166. [CrossRef]
127. Karl, T.; Yeretzian, C.; Jordan, A.; Lindinger, W. Dynamic measurements of partition coefficients using proton-transfer-reaction mass spectrometry (PTR–MS). *Int. J. Mass Spectrom.* **2003**, *223–224*, 383–395. [CrossRef]
128. Sander, R. *Compilation of Henry's Law Constants for Inorganic and Organic Species of Potential Importance in Environmental Chemistry*; Max-Planck Institute of Chemistry: Mainz, Germany, 1999; p. 107.
129. Zhou, X.; Mopper, K. Apparent partition coefficients of 15 carbonyl compounds between air and seawater and between air and freshwater; implications for air-sea exchange. *Environ. Sci. Technol.* **1990**, *24*, 1864–1869. [CrossRef]
130. Vempati, H.; Vaitilingom, M.; Zhang, Z.H.; Liyana-Arachchi, T.P.; Stevens, C.S.; Hung, F.R.; Valsararj, K.T. Physico-chemical properties of green leaf volatiles (GLV) for ascertaining atmospheric fate and transport in fog. *Adv. Environ. Res.* **2018**, *7*, 139–159. [CrossRef]
131. Buttery, R.G.; Bomben, J.L.; Guadagni, D.G.; Ling, L.C. Volatilities of organic flavor compounds in foods. *J. Agric. Food Chem.* **1971**, *19*, 1045–1048. [CrossRef]
132. Nozière, B.; Voisin, D.; Longfellow, C.A.; Friedli, H.; Henry, B.E.; Hanson, D.R. The Uptake of Methyl Vinyl Ketone, Methacrolein, and 2-Methyl-3-butene-2-ol onto Sulfuric Acid Solutions. *J. Phys. Chem. A* **2006**, *110*, 2387–2395. [CrossRef]
133. Iraci, L.T.; Baker, B.M.; Tyndall, G.S.; Orlando, J.J. Measurements of the Henry's Law Coefficients of 2-Methyl-3-buten-2-ol, Methacrolein, and Methylvinyl Ketone. *J. Atmos. Chem.* **1999**, *33*, 321–330. [CrossRef]
134. Roberts, D.D.; Pollien, P. Analysis of aroma release during microwave heating. *J. Agric. Food Chem.* **1997**, *45*, 4388–4392. [CrossRef]
135. Meylan, W.M.; Howard, P.H. Estimating octanol-air partition coefficients with octanol-water partition coefficients and Henry's law constants. *Chemosphere* **2005**, *61*, 640–644. [CrossRef]
136. Yalkowsky, S.H.; Valvani, S.C. Solubility and partitioning. 1. Solubility of non-electrolytes in water. *J. Pharm. Sci.* **1980**, *69*, 912–922. [CrossRef] [PubMed]
137. Riddick, J.A.; Bunger, W.B.; Sakano, T.K. *Organic Solvents: Physical Properties and Methods of Purification*, 4th ed.; John Wiley and Sons: New York, NY, USA, 1986.
138. Mackay, D.; Yeun, A.T.K. Mass-transfer coefficient correlations for volatilization of organic solutes from water. *Environ. Sci. Technol.* **1983**, *17*, 211–217. [CrossRef]
139. Daubert, T.E.; Danner, R.P. *Physical and Thermodynamic Properties of Pure Chemicals: Data Compilation*; Taylor & Francis: Washington, DC, USA, 1989.

140. Amoore, J.E.; Buttery, R.G. Partition-coefficients and comparative olfactometry. *Chem. Sens. Flavour* **1978**, *3*, 57–71. [CrossRef]
141. Yalkowsky, S.H.; Dannenfelser, R. *Aquasol Database of Aqueous Solubility, Version 5*; College of Pharmacy, University of Arizona: Tuscon, AR, USA, 1992.
142. Yaws, C.L. *Handbook of Vapor Pressure*; Gulf Pub. Co.: Houston, TX, USA, 1994.
143. Butler, J.A.V.; Ramchandani, C.N.; Thomson, D.W. 58. The solubility of non-electrolytes. Part I. The free energy of hydration of some aliphatic alcohols. *J. Chem. Soc.* **1935**, 280–285. [CrossRef]
144. Buttery, R.G.; Ling, L.; Guadagni, D.G. Food volatiles. Volatilities of aldehydes, ketones, and esters in dilute water solution. *J. Agric. Food Chem.* **1969**, *17*, 385–389. [CrossRef]
145. Hwang, Y.L.; Olson, J.D.; Keller, G.E. Steam stripping for removal of organic pollutants from water. 2. Vapor-liquid-equilibrium data. *Ind. Eng. Chem. Res.* **1992**, *31*, 1759–1768. [CrossRef]
146. Li, J.J.; Carr, P.W. Measurement of water-hexadecane partition-coefficients by headspace gas-chromatography and calculation of limiting activity-coefficients in water. *Anal. Chem.* **1993**, *65*, 1443–1450. [CrossRef]
147. Mackay, D.; Shiu, W.-Y.; Shiu, W.-Y.; Lee, S.C. *Handbook of Physical-Chemical Properties and Environmental Fate for Organic Chemicals*, 2nd ed.; CRC Press: Boca Raton, FL, USA, 2006. [CrossRef]
148. Rytting, J.H.; Huston, L.P.; Higuchi, T. Thermodynamic group contributions for hydroxyl, amino, and methylene groups. *J. Pharm. Sci.* **1978**, *67*, 615–618. [CrossRef]
149. Buttery, R.G.; Guadagni, D.G.; Okano, S. Air-water partition coefficients of some aldehydes. *J. Sci. Food Agric.* **1965**, *16*, 691–692. [CrossRef]
150. Sieg, K.; Fries, E.; Puttmann, W. Analysis of benzene, toluene, ethylbenzene, xylenes and n-aldehydes in melted snow water via solid-phase dynamic extraction combined with gas chromatography/mass spectrometry. *J. Chromatogr. A* **2008**, *1178*, 178–186. [CrossRef] [PubMed]
151. Gupta, A.K.; Teja, A.S.; Chai, X.S.; Zhu, J.Y. Henry's constants of n-alkanols (methanol through n-hexanol) in water at temperatures between 40 degrees C and 90 degrees C. *Fluid Phase Equilib.* **2000**, *170*, 183–192. [CrossRef]
152. Falabella, J.B.; Nair, A.; Teja, A.S. Henry's constants of 1-alkanols and 2-ketones in salt solutions. *J. Chem. Eng. Data* **2006**, *51*, 1940–1945. [CrossRef]
153. Harvey, A.H. Applications of Near-Critical Dilute-Solution Thermodynamics. *Ind. Eng. Chem. Res.* **1998**, *37*, 3080–3088. [CrossRef]
154. Teja, A.S.; Gupta, A.K.; Bullock, K.; Chai, X.-S.; Zhu, J. Henry's constants of methanol in aqueous systems containing salts. *Fluid Phase Equilib.* **2001**, *185*, 265–274. [CrossRef]
155. Dohnal, V.; Fenclova, D.; Vrbka, P. Temperature dependences of limiting activity coefficients, Henry's law constants, and derivative infinite dilution properties of lower (C-1-C-5) 1-alkanols in water. Critical compilation, correlation, and recommended data. *J. Phys. Chem. Ref. Data* **2006**, *35*, 1621–1651. [CrossRef]
156. Liyana-Arachchi, T.P.; Hansel, A.K.; Stevens, C.; Ehrenhauser, F.S.; Valsaraj, K.T.; Hung, F.R. Molecular modeling of the green leaf volatile methyl salicylate on atmospheric air/water interfaces. *J. Phys. Chem. A* **2013**, *117*, 4436–4443. [CrossRef]
157. Liyana-Arachchi, T.P.; Zhang, Z.; Vempati, H.; Hansel, A.K.; Stevens, C.; Pham, A.T.; Ehrenhauser, F.S.; Valsaraj, K.T.; Hung, F.R. Green leaf volatiles on atmospheric air/water interfaces: A combined experimental and molecular simulation study. *J. Chem. Eng. Data* **2014**, *59*, 3025–3035. [CrossRef]
158. Kerr, J.B.; Fioletov, V.E. Surface ultraviolet radiation. *Atmos. Ocean.* **2008**, *46*, 159–184. [CrossRef]
159. Jiménez, E.; Lanza, B.; Martínez, E.; Albaladejo, J. Daytime tropospheric loss of hexanal and trans-2-hexenal: OH kinetics and UV photolysis. *Atmos. Chem. Phys.* **2007**, *7*, 1565–1574. [CrossRef]
160. Xing, J.-H.; Ono, M.; Kuroda, A.; Obi, K.; Sato, K.; Imamura, T. Kinetic Study of the Daytime Atmospheric Fate of (Z)-3-Hexenal. *J. Phys. Chem. A* **2012**, *116*, 8523–8529. [CrossRef] [PubMed]
161. O'Connor, M.P.; Wenger, J.C.; Mellouki, A.; Wirtz, K.; Munoz, A. The atmospheric photolysis of E-2-hexenal, Z-3-hexenal and E,E-2,4-hexadienal. *Phys. Chem. Chem. Phys.* **2006**, *8*, 5236–5246. [CrossRef] [PubMed]
162. Kalalian, C.; Samir, B.; Roth, E.; Chakir, A. UV absorption spectra of trans-2-pentenal, trans-2-hexenal and 2-methyl-2-pentenal. *Chem. Phys. Lett.* **2019**, *718*, 22–26. [CrossRef]
163. Sarang, K.; Otto, T.; Rudzinski, K.; Grgić, I.; Nestorowicz, K.; Herrmann, H.; Szmigielski, R. Reaction kinetics of green leaf volatiles with sulfate, hydroxyl and nitrate radicals in tropospheric aqueous-phase. *Environ. Sci. Technol.* **2021**. [CrossRef]
164. Canosa-Mas, C.E.; Duffy, J.M.; King, M.D.; Thompson, K.C.; Wayne, R.P. The atmospheric chemistry of methyl salicylate—reactions with atomic chlorine and with ozone. *Atmos. Environ.* **2002**, *36*, 2201–2205. [CrossRef]
165. Rudich, Y.; Talukdar, R.; Burkholder, J.B.; Ravishankara, A.R. Reaction of Methylbutenol with the OH Radical: Mechanism and Atmospheric Implications. *J. Phys. Chem.* **1995**, *99*, 12188–12194. [CrossRef]
166. Tang, Y.; Zhu, L. Wavelength-Dependent Photolysis of n-Hexanal and n-Heptanal in the 280−330-nm Region. *J. Phys. Chem. A* **2004**, *108*, 8307–8316. [CrossRef]
167. Atkinson, R.; Arey, J. Gas-phase tropospheric chemistry of biogenic volatile organic compounds: A review. *Atmos. Environ.* **2003**, *37* (Supp. 2), 197–219. [CrossRef]
168. Atkinson, R.; Arey, J. Atmospheric Degradation of Volatile Organic Compounds. *Chem. Rev.* **2003**, *103*, 4605–4638. [CrossRef] [PubMed]
169. Vereecken, L.; Francisco, J.S. Theoretical studies of atmospheric reaction mechanisms in the troposphere. *Chem. Soc. Rev.* **2012**, *41*, 6259–6293. [CrossRef] [PubMed]

170. Atkinson, R. Atmospheric chemistry of VOCs and NOx. *Atmos. Environ.* **2000**, *34*, 2063–2101. [CrossRef]
171. Gai, Y.; Lin, X.; Ma, Q.; Hu, C.; Gu, X.; Zhao, W.; Fang, B.; Zhang, W.; Long, B.; Long, Z. Experimental and Theoretical Study of Reactions of OH Radicals with Hexenols: An Evaluation of the Relative Importance of the H-Abstraction Reaction Channel. *Environ. Sci. Technol.* **2015**, *49*, 10380–10388. [CrossRef]
172. Du, B.; Zhang, W. Atmospheric reaction of OH radicals with 2-methyl-3-buten-2-ol (MBO): Quantum chemical investigation on the reaction mechanism. *Comput. Theor. Chem.* **2012**, *999*, 109–120. [CrossRef]
173. Davis, M.E.; Gilles, M.K.; Ravishankara, A.R.; Burkholder, J.B. Rate coefficients for the reaction of OH with (E)-2-pentenal, (E)-2-hexenal, and (E)-2-heptenal. *Phys. Chem. Chem. Phys.* **2007**, *9*, 2240–2248. [CrossRef]
174. Atkinson, R.; Arey, J.; Aschmann, S.M.; Corchnoy, S.B.; Shu, Y. Rate constants for the gas-phase reactions of cis-3-Hexen-1-ol, cis-3-Hexenylacetate, trans-2-Hexenal, and Linalool with OH and NO_3 radicals and O_3 at 296 $\pm$ 2 K, and OH radical formation yields from the O_3 reactions. *Int. J. Chem. Kinet.* **1995**, *27*, 941–955. [CrossRef]
175. Gibilisco, R.G.; Blanco, M.a.B.; Bejan, I.; Barnes, I.; Wiesen, P.; Teruel, M.A. Atmospheric Sink of (E)-3-Hexen-1-ol, (Z)-3-Hepten-1-ol, and (Z)-3-Octen-1-ol: Rate Coefficients and Mechanisms of the OH-Radical Initiated Degradation. *Environ. Sci. Technol.* **2015**, *49*, 7717–7725. [CrossRef] [PubMed]
176. Gibilisco, R.G.; Santiago, A.N.; Teruel, M.A. OH-initiated degradation of a series of hexenols in the troposphere. Rate coefficients at 298 K and 1 atm. *Atmos. Environ.* **2013**, *77*, 358–364. [CrossRef]
177. Carrasco, N.; Doussin, J.F.; O'Connor, M.; Wenger, J.C.; Picquet-Varrault, B.; Durand-Jolibois, R.; Carlier, P. Simulation Chamber Studies of the Atmospheric Oxidation of 2-Methyl-3-Buten-2-ol: Reaction with Hydroxyl Radicals and Ozone Under a Variety of Conditions. *J. Atmos. Chem.* **2007**, *56*, 33–55. [CrossRef]
178. Alvarado, A.; Tuazon, E.C.; Aschmann, S.M.; Arey, J.; Atkinson, R. Products and mechanisms of the gas-phase reactions of OH radicals and O_3 with 2-methyl-3-buten-2-ol. *Atmos. Environ.* **1999**, *33*, 2893–2905. [CrossRef]
179. Ferronato, C.; Orlando, J.J.; Tyndall, G.S. Rate and mechanism of the reactions of OH and Cl with 2-methyl-3-buten-2-ol. *J. Geophys. Res. Atmos.* **1998**, *103*, 25579–25586. [CrossRef]
180. Reisen, F.; Aschmann, S.M.; Atkinson, R.; Arey, J. Hydroxyaldehyde Products from Hydroxyl Radical Reactions of Z-3-Hexen-1-ol and 2-Methyl-3-buten-2-ol Quantified by SPME and API-MS. *Environ. Sci. Technol.* **2003**, *37*, 4664–4671. [CrossRef]
181. Orlando, J.J.; Tyndall, G.S. Laboratory studies of organic peroxy radical chemistry: An overview with emphasis on recent issues of atmospheric significance. *Chem. Soc. Rev.* **2012**, *41*, 6294–6317. [CrossRef] [PubMed]
182. Fantechi, G.; Jensen, N.R.; Hjorth, J.; Peeters, J. Mechanistic studies of the atmospheric oxidation of methyl butenol by OH radicals, ozone and NO_3 radicals. *Atmos. Environ.* **1998**, *32*, 3547–3556. [CrossRef]
183. Aschmann, S.M.; Shu, Y.; Arey, J.; Atkinson, R. Products of the gas-phase reactions of cis-3-hexen-1-ol with OH radicals and O_3. *Atmos. Environ.* **1997**, *31*, 3551–3560. [CrossRef]
184. Cavalli, F.; Barnes, I.; Becker, K.H. FT-IR kinetic and product study of the OH radical-initiated oxidation of 1-pentanol. *Environ. Sci. Technol.* **2000**, *34*, 4111–4116. [CrossRef]
185. Orlando, J.J.; Tyndall, G.S.; Ceazan, N. Rate coefficients and product yields from reaction of OH with 1-penten-3-ol, (Z)-2-penten-1-ol, and allyl alcohol (2-propen-1-ol). *J. Phys. Chem. A* **2001**, *105*, 3564–3569. [CrossRef]
186. Gaona-Colmán, E.; Blanco, M.B.; Teruel, M.A. Kinetics and product identification of the reactions of (E)-2-hexenyl acetate and 4-methyl-3-penten-2-one with OH radicals and Cl atoms at 298 K and atmospheric pressure. *Atmos. Environ.* **2017**, *161*, 155–166. [CrossRef]
187. Chan, A.W.H.; Galloway, M.M.; Kwan, A.J.; Chhabra, P.S.; Keutsch, F.N.; Wennberg, P.O.; Flagan, R.C.; Seinfeld, J.H. Photooxidation of 2-Methyl-3-Buten-2-ol (MBO) as a Potential Source of Secondary Organic Aerosol. *Environ. Sci. Technol.* **2009**, *43*, 4647–4652. [CrossRef]
188. Bowman, J.H.; Barket, D.J.; Shepson, P.B. Atmospheric chemistry of nonanal. *Environ. Sci. Technol.* **2003**, *37*, 2218–2225. [CrossRef]
189. Priya, A.M.; Senthilkumar, L. Reaction of OH radical and ozone with methyl salicylate–a DFT study. *J. Phys. Org. Chem.* **2015**, *28*, 542–553. [CrossRef]
190. Seif, A.; Domingo, L.R.; Mazarei, E.; Zahedi, E.; Ahmadi, T.S. Atmospheric Oxidation Reactions of Methyl Salicylate as Green Leaf Volatiles by OH Radical: Theoretical Kinetics and Mechanism. *Chem. Sel.* **2020**, *5*, 12535–12547. [CrossRef]
191. Noda, J.; Hallquist, M.; Langer, S.; Ljungström, E. Products from the gas-phase reaction of some unsaturated alcohols with nitrate radicals. *Phys. Chem. Chem. Phys.* **2000**, *2*, 2555–2564. [CrossRef]
192. Pfrang, C.; Romero, M.T.B.; Cabanas, B.; Canosa-Mas, C.E.; Villanueva, F.; Wayne, R.P. Night-time tropospheric chemistry of the unsaturated alcohols (Z)-pent-2-en-1-ol and pent-1-en-3-ol: Kinetic studies of reactions of NO_3 and N2O5 with stress-induced plant emissions. *Atmos. Environ.* **2007**, *41*, 1652–1662. [CrossRef]
193. Kerdouci, J.; Picquet-Varrault, B.; Durand-Jolibois, R.; Gaimoz, C.; Doussin, J.F. An Experimental Study of the Gas-Phase Reactions of NO_3 Radicals with a Series of Unsaturated Aldehydes: Trans-2-Hexenal, trans-2-Heptenal, and trans-2-Octenal. *J. Phys. Chem. A* **2012**, *116*, 10135–10142. [CrossRef] [PubMed]
194. Horie, O.; Moortgat, G.K. Gas-Phase Ozonolysis of Alkenes. Recent Advances in Mechanistic Investigations. *Acc. Chem. Res.* **1998**, *31*, 387–396. [CrossRef]
195. Johnson, D.; Marston, G. The gas-phase ozonolysis of unsaturated volatile organic compounds in the troposphere. *Chem. Soc. Rev.* **2008**, *37*, 699–716. [CrossRef]

196. Li, J.; Sun, Y.; Cao, H.; Han, D.; He, M. Mechanisms and kinetics of the ozonolysis reaction of cis-3-hexenyl acetate and trans-2-hexenyl acetate in atmosphere: A theoretical study. *Struct. Chem.* **2014**, *25*, 71–83. [CrossRef]
197. Li, J.J. Criegee mechanism of ozonolysis. In *Name Reactions: A Collection of Detailed Mechanisms and Synthetic Applications*; Springer: Berlin/Heidelberg, Germany, 2009; p. 161. [CrossRef]
198. Jain, S.; Zahardis, J.; Petrucci, G.A. Soft Ionization Chemical Analysis of Secondary Organic Aerosol from Green Leaf Volatiles Emitted by Turf Grass. *Environ. Sci. Technol.* **2014**, *48*, 4835–4843. [CrossRef] [PubMed]
199. Grosjean, D.; Grosjean, E. Carbonyl products of the ozone-unsaturated alcohol reaction. *J. Geophys. Res. Atmos.* **1995**, *100*, 22815–22820. [CrossRef]
200. Grosjean, E.; Grosjean, D. The Gas Phase Reaction of Unsaturated Oxygenates with Ozone: Carbonyl Products and Comparison with the Alkene-Ozone Reaction. *J. Atmos. Chem.* **1997**, *27*, 271–289. [CrossRef]
201. O'Dwyer, M.A.; Carey, T.J.; Healy, R.M.; Wenger, J.C.; Picquet-Varrault, B.; Doussin, J.F. The gas-phase ozonolysis of 1-penten-3-ol, (z)-2-penten-1-ol and 1-penten-3-one: Kinetics, products and secondary organic aerosol formation. *Z. FPhys. Chem.* **2010**, *224*, 1059–1080. [CrossRef]
202. Uchida, R.; Sato, K.; Imamura, T. Gas-phase Ozone Reactions with Z-3-Hexenal and Z-3-Hexen-1-ol: Formation Yields of OH Radical, Propanal, and Ethane. *Chem. Lett.* **2015**, *44*, 457–458. [CrossRef]
203. Grosjean, E.; Grosjean, D.; Seinfeld, J.H. Gas-phase reaction of ozone with trans-2-hexenal, trans-2-hexenyl acetate, ethylvinyl ketone, and 6-methyl-5-hepten-2-one. *Int. J. Chem. Kinet.* **1996**, *28*, 373–382. [CrossRef]
204. Fantechi, G.; Jensen, N.R.; Saastad, O.; Hjorth, J.; Peeters, J. Reactions of Cl Atoms with Selected VOCs: Kinetics, Products and Mechanisms. *J. Atmos. Chem.* **1998**, *31*, 247–267. [CrossRef]
205. Rodríguez, A.; Rodríguez, D.; Garzón, A.; Soto, A.; Aranda, A.; Notario, A. Kinetics and mechanism of the atmospheric reactions of atomic chlorine with 1-penten-3-ol and (Z)-2-penten-1-ol: An experimental and theoretical study. *Phys. Chem. Chem. Phys.* **2010**, *12*, 12245–12258. [CrossRef] [PubMed]
206. Zhang, W.C.; Zhang, D.J. Theoretical investigation of the oxidation pathways of the Cl-initiated reaction of 2-methyl-3-buten-2-ol. *Mol. Phys.* **2012**, *110*, 2901–2917. [CrossRef]
207. Takahashi, K.; Xing, J.H.; Hurley, M.D.; Wallington, T.J. Kinetics and Mechanism of Chlorine-Atom-Initiated Oxidation of Allyl Alcohol, 3-Buten-2-ol, and 2-Methyl-3-buten-2-ol. *J. Phys. Chem. A* **2010**, *114*, 4224–4231. [CrossRef]
208. Shashikala, K.; Janardanan, D. Degradation mechanism of trans-2-hexenal in the atmosphere. *Chem. Phys. Lett.* **2020**, *759*. [CrossRef]
209. Priya, A.M.; Senthilkumar, L. Degradation of methyl salicylate through Cl initiated atmospheric oxidation—A theoretical study. *RSC Adv.* **2014**, *4*, 23464–23475. [CrossRef]
210. Lendar, M.; Aissat, A.; Cazaunau, M.; Daele, V.; Mellouki, A. Absolute and relative rate constants for the reactions of OH and Cl with pentanols. *Chem. Phys. Lett.* **2013**, *582*, 38–43. [CrossRef]
211. Wallington, T.J.; Kurylo, M.J. The gas-phase reactions of hydroxyl radicals with a series of aliphatic-alcohols over the temperature-range 240-440-K. *Int. J. Chem. Kinet.* **1987**, *19*, 1015–1023. [CrossRef]
212. Nelson, L.; Rattigan, O.; Neavyn, R.; Sidebottom, H.; Treacy, J.; Nielsen, O.J. Absolute and relative rate constants for the reactions of hydroxyl radicals and chlorine atoms with a series of aliphatic-alcohols and ethers at 298-K. *Int. J. Chem. Kinet.* **1990**, *22*, 1111–1126. [CrossRef]
213. Wu, H.; Mu, Y.J.; Zhang, X.S.; Jiang, G.B. Relative rate constants for the reactions of hydroxyl radicals and chlorine atoms with a series of aliphatic alcohols. *Int. J. Chem. Kinet.* **2003**, *35*, 81–87. [CrossRef]
214. Oh, S.; Andino, J.M. Kinetics of the gas-phase reactions of hydroxyl radicals with C-1-C-6 aliphatic alcohols in the presence of ammonium sulfate aerosols. *Int. J. Chem. Kinet.* **2001**, *33*, 422–430. [CrossRef]
215. Grosjean, D.; Williams, E.L. Environmental persistence of organic compounds estimated from structure-reactivity and linear free-energy relationships. Unsaturated aliphatics. *Atmos. Environment. Part A Gen. Top.* **1992**, *26*, 1395–1405. [CrossRef]
216. Aschmann, S.M.; Atkinson, R. Kinetics of the gas-phase reactions of the OH radical with selected glycol ethers, glycols, and alcohols. *Int. J. Chem. Kinet.* **1998**, *30*, 533–540. [CrossRef]
217. Peirone, S.A.; Barrera, J.A.; Taccone, R.A.; Cometto, P.M.; Lane, S.I. Relative rate coefficient measurements of OH radical reactions with (Z)-2-hexen-1-ol and (E)-3-hexen-1-ol under simulated atmospheric conditions. *Atmos. Environ.* **2014**, *85*, 92–98. [CrossRef]
218. D'Anna, B.; Andresen, Ø.; Gefen, Z.; Nielsen, C.J. Kinetic study of OH and NO_3 radical reactions with 14 aliphatic aldehydes. *Phys. Chem. Chem. Phys.* **2001**, *3*, 3057–3063. [CrossRef]
219. Papagni, C.; Arey, J.; Atkinson, R. Rate constants for the gas-phase reactions of a series of C3 C6 aldehydes with OH and NO_3 radicals. *Int. J. Chem. Kinet.* **2000**, *32*, 79–84. [CrossRef]
220. Plagens, H. Untersuchugen zum atmosphärenchemischen Abbau langkettiger Aldehyde. Ph.D. Thesis, Bergische Univerität, Wuppertal, Germany, 2001.
221. Gao, T.T.; Andino, J.M.; Rivera, C.C.; Marquez, M.F. Rate Constants of the Gas-Phase Reactions of OH Radicals with trans-2-Hexenal, trans-2-Octenal, and trans-2-Nonenal. *Int. J. Chem. Kinet.* **2009**, *41*, 483–489. [CrossRef]
222. Rodríguez, D.; Rodríguez, A.; Bravo, I.; Garzón, A.; Aranda, A.; Diaz-de-Mera, Y.; Notario, A. Kinetic study of the gas-phase reactions of hydroxyl radicals and chlorine atoms with cis-3-hexenylformate. *Int. J. Environ. Sci. Technol.* **2015**, *12*, 2881–2890. [CrossRef]

223. Papagni, C.; Arey, J.; Atkinson, R. Rate constants for the gas-phase reactions of OH radicals with a series of unsaturated alcohols. *Int. J. Chem. Kinet.* **2001**, *33*, 142–147. [CrossRef]
224. Fantechi, G.; Jensen, N.R.; Hjorth, J.; Peeters, J. Determination of the rate constants for the gas-phase reactions of methyl butenol with OH radicals, ozone, NO_3 radicals, and Cl atoms. *Int. J. Chem. Kinet.* **1998**, *30*, 589–594. [CrossRef]
225. Imamura, T.; Iida, Y.; Obi, K.; Nagatani, I.; Nakagawa, K.; Patroescu-Klotz, I.; Hatakeyama, S. Rate coefficients for the gas-phase reactions of OH radicals with methylbutenols at 298 K. *Int. J. Chem. Kinet.* **2004**, *36*, 379–385. [CrossRef]
226. Baasandorj, M.; Stevens, P.S. Experimental and Theoretical Studies of the Kinetics of the Reactions of OH and OD with 2-Methyl-3-buten-2-ol between 300 and 415 K at Low Pressure. *J. Phys. Chem. A* **2007**, *111*, 640–649. [CrossRef] [PubMed]
227. Ren, Y.G.; McGillen, M.R.; Daele, V.; Casas, J.; Mellouk, A. The fate of methyl salicylate in the environment and its role as signal in multitrophic interactions. *Sci. Total Environ.* **2020**, *749*. [CrossRef]
228. Davis, M.E.; Burkholder, J.B. Rate coefficients for the gas-phase reaction of OH with (Z)-3-hexen-1-ol, 1-penten-3-ol, (E)-2-penten-1-ol, and (E)-2-hexen-1-ol between 243 and 404 K. *Atmos. Chem. Phys.* **2011**, *11*, 3347–3358. [CrossRef]
229. Atkinson, R. A structure-activity relationship for the estimation of rate constants for the gas-phase reactions of OH radicals with organic compounds. *Int. J. Chem. Kinet.* **1987**, *19*, 799–828. [CrossRef]
230. Zhao, Z.J.; Husainy, S.; Smith, G.D. Kinetics studies of the gas-phase reactions of NO_3 radicals with series of 1-alkenes, dienes, cycloalkenes, alkenols, and alkenals. *J. Phys. Chem. A* **2011**, *115*, 12161–12172. [CrossRef] [PubMed]
231. Pfrang, C.; Martin, R.; Canosa-Mas, C.; Wayne, R. Gas-phase reactions of NO_3 and N2O5 with (Z)-hex-4-en-1-ol, (Z)-hex-3-en-1-ol ('leaf alcohol'), (E)-hex-3-en-1-ol, (Z)-hex-2-en-1-ol and (E)-hex-2-en-1-ol. *Phys. Chem. Chem. Phys.* **2006**, *8*, 354–363. [CrossRef]
232. D'Anna, B.; Nielsen, J.C. Kinetic study of the vapour-phase reaction between aliphatic aldehydes and the nitrate radical. *J. Chem. Soc. Faraday Trans.* **1997**, *93*, 3479–3483. [CrossRef]
233. Noda, J.; Holm, C.; Nyman, G.; Langer, S.; Ljungstrom, E. Kinetics of the gas-phase reaction of n-C-6-C-10 aldehydes with the nitrate radical. *Int. J. Chem. Kinet.* **2003**, *35*, 120–129. [CrossRef]
234. Hallquist, M.; Langer, S.; Ljungström, E.; Wängberg, I. Rates of reaction between the nitrate radical and some unsaturated alcohols. *Int. J. Chem. Kinet.* **1996**, *28*, 467–474. [CrossRef]
235. Cabañas, B.; Salgado, S.; Martín, P.; Baeza, M.T.; Martínez, E. Night-time Atmospheric Loss Process for Unsaturated Aldehydes: Reaction with NO_3 Radicals. *J. Phys. Chem. A* **2001**, *105*, 4440–4445. [CrossRef]
236. Rudich, Y.; Talukdar, R.K.; Fox, R.W.; Ravishankara, A.R. Rate Coefficients for Reactions of NO_3 with a Few Olefins and Oxygenated Olefins. *J. Phys. Chem.* **1996**, *100*, 5374–5381. [CrossRef]
237. Grosjean, E.; Grosjean, D. Rate constants for the gas-phase reactions of ozone with unsaturated aliphatic-alcohols. *Int. J. Chem. Kinet.* **1994**, *26*, 1185–1191. [CrossRef]
238. Lin, X.; Ma, Q.; Yang, C.; Tang, X.; Zhao, W.; Hu, C.; Gu, X.; Fang, B.; Gai, Y.; Zhang, W. Kinetics and mechanisms of gas phase reactions of hexenols with ozone. *RSC Adv.* **2016**, *6*, 83573–83580. [CrossRef]
239. Gibilisco, R.G.; Bejan, I.; Barnes, I.; Wiesen, P.; Teruel, M.A. FTIR gas kinetic study of the reactions of ozone with a series of hexenols at atmospheric pressure and 298K. *Chem. Phys. Lett.* **2015**, *618*, 114–118. [CrossRef]
240. Grosjean, D.; Grosjean, E.; Williams II, E.L. Rate constants for the gas-phase reactions of ozone with unsaturated alcohols, esters, and carbonyls. *Int. J. Chem. Kinet.* **1993**, *25*, 783–794. [CrossRef]
241. Zhang, Q.; Lin, X.; Gai, Y.; Ma, Q.; Zhao, W.; Fang, B.; Long, B.; Zhang, W. Kinetic and mechanistic study on gas phase reactions of ozone with a series of cis-3-hexenyl esters. *RSC Adv.* **2018**, *8*, 4230–4238. [CrossRef]
242. Klawatsch-Carrasco, N.; Doussin, J.F.; Carlier, P. Absolute rate constants for the gas-phase ozonolysis of isoprene and methyl-butenol. *Int. J. Chem. Kinet.* **2004**, *36*, 152–156. [CrossRef]
243. Kalalian, C.; El Dib, G.; Singh, H.J.; Rao, P.K.; Roth, E.; Chakir, A. Temperature dependent kinetic study of the gas phase reaction of ozone with 1-penten-3-ol, cis-2-penten-1-ol and trans-3-hexen-1-ol: Experimental and theoretical data. *Atmos. Environ.* **2020**, *223*, 117306. [CrossRef]
244. Kalalian, C.; Roth, E.; Chakir, A. Rate Coefficients for the Gas-Phase Reaction of Ozone with C5 and C6 Unsaturated Aldehydes. *Int. J. Chem. Kinet.* **2018**, *50*, 47–56. [CrossRef]
245. Grira, A.; Amarandei, C.; Romanias, M.N.; El Dib, G.; Canosa, A.; Arsene, C.; Bejan, I.G.; Olariu, R.I.; Coddeville, P.; Tomas, A. Kinetic Measurements of Cl Atom Reactions with C5–C8 Unsaturated Alcohols. *Atmosphere* **2020**, *11*, 256. [CrossRef]
246. Rodriguez, D.; Rodriguez, A.; Notario, A.; Aranda, A.; Diaz-de-Mera, Y.; Martinez, E. Kinetic study of the gas-phase reaction of atomic chlorine with a series of aldehydes. *Atmos. Chem. Phys.* **2005**, *5*, 3433–3440. [CrossRef]
247. Teruel, M.A.; Achad, M.; Blanco, M.B. Kinetic study of the reactions of Cl atoms with alpha, beta-unsaturated carbonyl compounds at atmospheric pressure and structure activity relations (SARs). *Chem. Phys. Lett.* **2009**, *479*, 25–29. [CrossRef]
248. Kaiser, E.W.; Wallington, T.J.; Hurley, M.D. Products and Mechanism of the Reaction of Chlorine Atoms with 3-Pentanone in 700-950 Torr of N-2/O-2 Diluent at 297-515 K. *J. Phys. Chem. A* **2010**, *114*, 343–354. [CrossRef]
249. Gibilisco, R.G.; Bejan, I.; Barnes, I.; Wiesen, P.; Teruel, M.A. Rate coefficients at 298 K and 1 atm for the tropospheric degradation of a series of C6, C7 and C8 biogenic unsaturated alcohols initiated by Cl atoms. *Atmos. Environ.* **2014**, *94*, 564–572. [CrossRef]
250. Cuevas, C.A.; Notario, A.; Martinez, E.; Albaladejo, J. Temperature-dependence study of the gas-phase reactions of atmospheric Cl atoms with a series of aliphatic aldehydes. *Atmos. Environ.* **2006**, *40*, 3845–3854. [CrossRef]

251. Rodríguez, A.; Rodríguez, D.; Soto, A.; Notario, A.; Aranda, A.; Díaz-de-Mera, Y.; Bravo, I. Relative rate measurements of reactions of unsaturated alcohols with atomic chlorine as a function of temperature. *Atmos. Environ.* **2007**, *41*, 4693–4702. [CrossRef]
252. NCAR. Tropospheric Ultra Visible Model. Available online: https://www2.acom.ucar.edu/modeling/tropospheric-ultraviolet-and-visible-tuv-radiation-model (accessed on 8 August 2021).
253. Kwok, E.S.C.; Atkinson, R. Estimation of hydroxyl radical reaction rate constants for gas-phase organic compounds using a structure-reactivity relationship: An update. *Atmos. Environ.* **1995**, *29*, 1685–1695. [CrossRef]
254. Peeters, J.; Boullart, W.; Pultau, V.; Vandenberk, S.; Vereecken, L. Structure−Activity Relationship for the Addition of OH to (Poly)alkenes: Site-Specific and Total Rate Constants. *J. Phys. Chem. A* **2007**, *111*, 1618–1631. [CrossRef] [PubMed]
255. King, M.D.; Canosa-Mas, C.E.; Wayne, R.P. A structure–activity relationship (SAR) for predicting rate constants for the reaction of NO_3, OH and O_3 with monoalkenes and conjugated dienes. *Phys. Chem. Chem. Phys.* **1999**, *1*, 2239–2246. [CrossRef]
256. Pfrang, C.; King, M.D.; Canosa-Mas, C.E.; Wayne, R.P. Structure–activity relations (SARs) for gas-phase reactions of NO_3, OH and O_3 with alkenes: An update. *Atmos. Environ.* **2006**, *40*, 1180–1186. [CrossRef]
257. Pfrang, C.; King, M.D.; Canosa-Mas, C.E.; Wayne, R.P. Correlations for gas-phase reactions of NO_3, OH and O_3 with alkenes: An update. *Atmos. Environ.* **2006**, *40*, 1170–1179. [CrossRef]
258. Pfrang, C.; King, M.D.; Braeckevelt, M.; Canosa-Mas, C.E.; Wayne, R.P. Gas-phase rate coefficients for reactions of NO_3, OH, O_3 and O(3P) with unsaturated alcohols and ethers: Correlations and structure–activity relations (SARs). *Atmos. Environ.* **2008**, *42*, 3018–3034. [CrossRef]
259. Kerdouci, J.; Picquet-Varrault, B.; Doussin, J.-F. Prediction of Rate Constants for Gas-Phase Reactions of Nitrate Radical with Organic Compounds: A New Structure–Activity Relationship. *Chem. Phys. Chem.* **2010**, *11*, 3909–3920. [CrossRef]
260. Ezell, M.J.; Wang, W.; Ezell, A.A.; Soskin, G.; Finlayson-Pitts, B.J. Kinetics of reactions of chlorine atoms with a series of alkenes at 1 atm and 298 K: Structure and reactivity. *Phys. Chem. Chem. Phys.* **2002**, *4*, 5813–5820. [CrossRef]
261. McGillen, M.R.; Archibald, A.T.; Carey, T.; Leather, K.E.; Shallcross, D.E.; Wenger, J.C.; Percival, C.J. Structure–activity relationship (SAR) for the prediction of gas-phase ozonolysis rate coefficients: An extension towards heteroatomic unsaturated species. *Phys. Chem. Chem. Phys.* **2011**, *13*, 2842–2849. [CrossRef] [PubMed]
262. Doussin, J.F.; Monod, A. Structure–activity relationship for the estimation of OH-oxidation rate constants of carbonyl compounds in the aqueous phase. *Atmos. Chem. Phys.* **2013**, *13*, 11625–11641. [CrossRef]
263. Monod, A.; Doussin, J.F. Structure-activity relationship for the estimation of OH-oxidation rate constants of aliphatic organic compounds in the aqueous phase: Alkanes, alcohols, organic acids and bases. *Atmos. Environ.* **2008**, *42*, 7611–7622. [CrossRef]
264. Monod, A.; Poulain, L.; Grubert, S.; Voisin, D.; Wortham, H. Kinetics of OH-initiated oxidation of oxygenated organic compounds in the aqueous phase: New rate constants, structure–activity relationships and atmospheric implications. *Atmos. Environ.* **2005**, *39*, 7667–7688. [CrossRef]
265. Richards-Henderson, N.K.; Pham, A.T.; Kirk, B.B.; Anastasio, C. Secondary organic aerosol from aqueous reactions of green leaf volatiles with organic triplet excited states and singlet molecular oxygen. *Environ. Sci. Technol.* **2015**, *49*, 268–276. [CrossRef] [PubMed]
266. Mael, L.E.; Jacobs, M.I.; Elrod, M.J. Organosulfate and Nitrate Formation and Reactivity from Epoxides Derived from 2-Methyl-3-buten-2-ol. *J. Phys. Chem. A* **2015**, *119*, 4464–4472. [CrossRef]
267. Liu, Z.; Ge, M.; Wang, W.; Yin, S.; Tong, S. The uptake of 2-methyl-3-buten-2-ol into aqueous mixed solutions of sulfuric acid and hydrogen peroxide. *Phys. Chem. Chem. Phys.* **2011**, *13*, 2069–2075. [CrossRef]
268. Ren, H.; Sedlak, J.A.; Elrod, M.J. General Mechanism for Sulfate Radical Addition to Olefinic Volatile Organic Compounds in Secondary Organic Aerosol. *Environ. Sci. Technol.* **2021**, *55*, 1456–1465. [CrossRef]
269. Liyana-Arachchi, T.P.; Stevens, C.; Hansel, A.K.; Ehrenhauser, F.S.; Valsaraj, K.T.; Hung, F.R. Molecular simulations of green leaf volatiles and atmospheric oxidants on air/water interfaces. *Phys. Chem. Chem. Phys.* **2013**, *15*, 3583–3592. [CrossRef] [PubMed]
270. Heath, A.; Valsaraj, K.T. An experimental study of the atmospheric oxidation of a biogenic organic compound (methyl jasmonate) in a thin water film as in fog or aerosols. *Open J. Air Pollut.* **2017**, *6*, 44–51. [CrossRef]
271. Hansel, A.K. Reaction of Green Leaf Volatiles as a Source of Secondary Organic Aerosols in Fog Droplets. Master's Thesis, Louisiana State University, Baton Rouge, LA, USA, 2013.
272. Hamilton, J.F.; Lewis, A.C.; Carey, T.J.; Wenger, J.C. Characterization of polar compounds and oligomers in secondary organic aerosol using liquid chromatography coupled to mass spectrometry. *Anal. Chem.* **2008**, *80*, 474–480. [CrossRef]
273. Jaoui, M.; Kleindienst, T.E.; Offenberg, J.H.; Lewandowski, M.; Lonneman, W.A. SOA formation from the atmospheric oxidation of 2-methyl-3-buten-2-ol and its implications for PM2.5. *Atmos. Chem. Phys.* **2012**, *12*, 2173–2188. [CrossRef]
274. Novelli, A.; Kaminski, M.; Rolletter, M.; Acir, I.H.; Bohn, B.; Dorn, H.P.; Li, X.; Lutz, A.; Nehr, S.; Rohrer, F.; et al. Evaluation of OH and HO2 concentrations and their budgets during photooxidation of 2-methyl-3-butene-2-ol (MBO) in the atmospheric simulation chamber SAPHIR. *Atmos. Chem. Phys.* **2018**, *18*, 11409–11422. [CrossRef]
275. Lewandowski, M.; Piletic, I.R.; Kleindienst, T.E.; Offenberg, J.H.; Beaver, M.R.; Jaoui, M.; Docherty, K.S.; Edney, E.O. Secondary organic aerosol characterisation at field sites across the United States during the spring–summer period. *Int. J. Environ. Anal. Chem.* **2013**, *93*, 1084–1103. [CrossRef]
276. Edney, E.O.; Kleindienst, T.E.; Conver, T.S.; McIver, C.D.; Corse, E.W.; Weathers, W.S. Polar organic oxygenates in PM2.5 at a southeastern site in the United States. *Atmos. Environ.* **2003**, *37*, 3947–3965. [CrossRef]

277. Hettiyadura, A.P.S.; Al-Naiema, I.M.; Hughes, D.D.; Fang, T.; Stone, E.A. Organosulfates in Atlanta, Georgia: Anthropogenic influences on biogenic secondary organic aerosol formation. *Atmos. Chem. Phys.* **2019**, *19*, 3191–3206. [CrossRef]
278. Hansen, A.M.K.; Kristensen, K.; Nguyen, Q.T.; Zare, A.; Cozzi, F.; Nøjgaard, J.K.; Skov, H.; Brandt, J.; Christensen, J.H.; Ström, J.; et al. Organosulfates and organic acids in Arctic aerosols: Speciation, annual variation and concentration levels. *Atmos. Chem. Phys.* **2014**, *14*, 7807–7823. [CrossRef]
279. Barbosa, T.S.; Riva, M.; Chen, Y.Z.; da Silva, C.M.; Ameida, J.C.S.; Zhang, Z.; Gold, A.; Arbilla, G.; Bauerfeldt, G.F.; Surratt, J.D. Chemical characterization of organosulfates from the hydroxyl radical-initiated oxidation and ozonolysis of cis-3-hexen-1-ol. *Atmos. Environ.* **2017**, *162*, 141–151. [CrossRef]
280. Nguyen, Q.T.; Christensen, M.K.; Cozzi, F.; Zare, A.; Hansen, A.M.K.; Kristensen, K.; Tulinius, T.E.; Madsen, H.H.; Christensen, J.H.; Brandt, J.; et al. Understanding the anthropogenic influence on formation of biogenic secondary organic aerosols in Denmark via analysis of organosulfates and related oxidation products. *Atmos. Chem. Phys.* **2014**, *14*, 8961–8981. [CrossRef]
281. Kristensen, K.; Bilde, M.; Aalto, P.P.; Petaja, T.; Glasius, M. Denuder/filter sampling of organic acids and organosulfates at urban and boreal forest sites: Gas/particle distribution and possible sampling artifacts. *Atmos. Environ.* **2016**, *130*, 36–53. [CrossRef]
282. Hettiyadura, A.P.S.; Stone, E.A.; Kundu, S.; Baker, Z.; Geddes, E.; Richards, K.; Humphry, T. Determination of atmospheric organosulfates using HILIC chromatography with MS detection. *Atmos. Meas. Tech.* **2015**, *8*, 2347–2358. [CrossRef]
283. Hettiyadura, A.P.S.; Jayarathne, T.; Baumann, K.; Goldstein, A.H.; de Gouw, J.A.; Koss, A.; Keutsch, F.N.; Skog, K.; Stone, E.A. Qualitative and quantitative analysis of atmospheric organosulfates in Centreville, Alabama. *Atmos. Chem. Phys.* **2017**, *17*, 1343–1359. [CrossRef]
284. Wang, Y.; Hu, M.; Guo, S.; Wang, Y.; Zheng, J.; Yang, Y.; Zhu, W.; Tang, R.; Li, X.; Liu, Y.; et al. The secondary formation of organosulfates under interactions between biogenic emissions and anthropogenic pollutants in summer in Beijing. *Atmos. Chem. Phys.* **2018**, *18*, 10693–10713. [CrossRef]
285. Huang, R.J.; Cao, J.; Chen, Y.; Yang, L.; Shen, J.; You, Q.; Wang, K.; Lin, C.; Xu, W.; Gao, B.; et al. Organosulfates in atmospheric aerosol: Synthesis and quantitative analysis of PM2.5 from Xi'an, northwestern China. *Atmos. Meas. Tech.* **2018**, *11*, 3447–3456. [CrossRef]
286. Le Breton, M.; Wang, Y.; Hallquist, Å.M.; Pathak, R.K.; Zheng, J.; Yang, Y.; Shang, D.; Glasius, M.; Bannan, T.J.; Liu, Q.; et al. Online gas- and particle-phase measurements of organosulfates, organosulfonates and nitrooxy organosulfates in Beijing utilizing a FIGAERO ToF-CIMS. *Atmos. Chem. Phys.* **2018**, *18*, 10355–10371. [CrossRef]
287. Olson, C.N.; Galloway, M.M.; Yu, G.; Hedman, C.J.; Lockett, M.R.; Yoon, T.; Stone, E.A.; Smith, L.M.; Keutsch, F.N. Hydroxycarboxylic Acid-Derived Organosulfates: Synthesis, Stability, and Quantification in Ambient Aerosol. *Environ. Sci. Technol.* **2011**, *45*, 6468–6474. [CrossRef]
288. Hughes, D.D.; Christiansen, M.B.; Milani, A.; Vermeuel, M.P.; Novak, G.A.; Alwe, H.D.; Dickens, A.F.; Pierce, R.B.; Millet, D.B.; Bertram, T.H.; et al. PM2.5 chemistry, organosulfates, and secondary organic aerosol during the 2017 Lake Michigan Ozone Study. *Atmos. Environ.* **2021**, *244*, 117939. [CrossRef]
289. Shalamzari, M.S.; Vermeylen, R.; Blockhuys, F.; Kleindienst, T.E.; Lewandowski, M.; Szmigielski, R.; Rudzinski, K.J.; Spólnik, G.; Danikiewicz, W.; Maenhaut, W.; et al. Characterization of polar organosulfates in secondary organic aerosol from the unsaturated aldehydes 2-E-pentenal, 2-E-hexenal, and 3-Z-hexenal. *Atmos. Chem. Phys.* **2016**, *16*, 7135–7148. [CrossRef]
290. Safi Shalamzari, M.; Ryabtsova, O.; Kahnt, A.; Vermeylen, R.; Hérent, M.-F.; Quetin-Leclercq, J.; Van der Veken, P.; Maenhaut, W.; Claeys, M. Mass spectrometric characterization of organosulfates related to secondary organic aerosol from isoprene. *Rapid Commun. Mass Spectrom.* **2013**, *27*, 784–794. [CrossRef] [PubMed]
291. Brüggemann, M.; Xu, R.; Tilgner, A.; Kwong, K.C.; Mutzel, A.; Poon, H.Y.; Otto, T.; Schaefer, T.; Poulain, L.; Chan, M.N.; et al. Organosulfates in Ambient Aerosol: State of Knowledge and Future Research Directions on Formation, Abundance, Fate, and Importance. *Environ. Sci. Technol.* **2020**, *54*, 3767–3782. [CrossRef]
292. Tolocka, M.P.; Turpin, B. Contribution of Organosulfur Compounds to Organic Aerosol Mass. *Environ. Sci. Technol.* **2012**, *46*, 7978–7983. [CrossRef] [PubMed]
293. Zhang, H.; Worton, D.R.; Lewandowski, M.; Ortega, J.; Rubitschun, C.L.; Park, J.-H.; Kristensen, K.; Campuzano-Jost, P.; Day, D.A.; Jimenez, J.L.; et al. Organosulfates as Tracers for Secondary Organic Aerosol (SOA) Formation from 2-Methyl-3-Buten-2-ol (MBO) in the Atmosphere. *Environ. Sci. Technol.* **2012**, *46*, 9437–9446. [CrossRef] [PubMed]
294. Shalamzari, M.S.; Kahnt, A.; Vermeylen, R.; Kleindienst, T.E.; Lewandowski, M.; Cuyckens, F.; Maenhaut, W.; Claeys, M. Characterization of polar organosulfates in secondary organic aerosol from the green leaf volatile 3-z-hexenal. *Environ. Sci. Technol.* **2014**, *48*, 12671–12678. [CrossRef]
295. Faiola, C.L.; Pullinen, I.; Buchholz, A.; Khalaj, F.; Ylisirniö, A.; Kari, E.; Miettinen, P.; Holopainen, J.K.; Kivimäenpää, M.; Schobesberger, S.; et al. Secondary Organic Aerosol Formation from Healthy and Aphid-Stressed Scots Pine Emissions. *ACS Earth Space Chem.* **2019**, *3*, 1756–1772. [CrossRef] [PubMed]
296. Waza, A.A. *Effect of Green Leaf Volatiles (GLVS) on Secondary Organic Aerosol Formation*; University of Eastern Finland: Joensuu, Finland, 2014.
297. Joutsensaari, J.; Loivamäki, M.; Vuorinen, T.; Miettinen, P.; Nerg, A.M.; Holopainen, J.K.; Laaksonen, A. Nanoparticle formation by ozonolysis of inducible plant volatiles. *Atmos. Chem. Phys.* **2005**, *5*, 1489–1495. [CrossRef]

298. Zhang, H.; Zhang, Z.; Cui, T.; Lin, Y.-H.; Bhathela, N.A.; Ortega, J.; Worton, D.R.; Goldstein, A.H.; Guenther, A.; Jimenez, J.L.; et al. Secondary Organic Aerosol Formation via 2-Methyl-3-buten-2-ol Photooxidation: Evidence of Acid-Catalyzed Reactive Uptake of Epoxides. *Environ. Sci. Technol. Lett.* **2014**, *1*, 242–247. [CrossRef] [PubMed]
299. Knap, H.C.; Schmidt, J.A.; Jørgensen, S. Hydrogen shift reactions in four methyl-buten-ol (MBO) peroxy radicals and their impact on the atmosphere. *Atmos. Environ.* **2016**, *147*, 79–87. [CrossRef]
300. Gomez-Gonzalez, Y.; Surratt, J.D.; Cuyckens, F.; Szmigielski, R.; Vermeylen, R.; Jaoui, M.; Lewandowski, M.; Offenberg, J.H.; Kleindienst, T.E.; Edney, E.O.; et al. Characterization of organosulfates from the photooxidation of isoprene and unsaturated fatty acids in ambient aerosol using liquid chromatography/(-) electrospray ionization mass spectrometry. *J. Mass Spectrom.* **2008**, *43*, 371–382. [CrossRef]
301. Rudziński, K.J.; Gmachowski, L.; Kuznietsova, I. Reactions of isoprene and sulphoxy radical-anions–A possible source of atmospheric organosulphites and organosulphates. *Atmos. Chem. Phys.* **2009**, *9*, 2129–2140. [CrossRef]
302. Wach, P.; Spolnik, G.; Surratt, J.D.; Blaziak, K.; Rudzinski, K.J.; Lin, Y.H.; Maenhaut, W.; Danikiewicz, W.; Claeys, M.; Szmigielski, R. Structural Characterization of Lactone-Containing MW 212 Organosulfates Originating from Isoprene Oxidation in Ambient Fine Aerosol. *Environ. Sci. Technol.* **2020**, *54*, 1415–1424. [CrossRef]
303. Wach, P.; Spólnik, G.; Rudziński, K.J.; Skotak, K.; Claeys, M.; Danikiewicz, W.; Szmigielski, R. Radical oxidation of methyl vinyl ketone and methacrolein in aqueous droplets: Characterization of organosulfates and atmospheric implications. *Chemosphere* **2019**, *214*, 1–9. [CrossRef]
304. Rudzinski, K. Heterogeneous and aqueous-phase transformations of isoprene. In *Environmental Simulation Chambers: Application to Atmospheric Chemical Processes*; Barnes, I., Rudzinski, K., Eds.; Springer: Berlin/Heidelberg, Germany, 2006; Volume 62, pp. 261–277.
305. Went, F.W. Blue Hazes in the Atmosphere. *Nature* **1960**, *187*, 641–643. [CrossRef]
306. Herrmann, H.; Hoffmann, D.; Schaefer, T.; Bräuer, P.; Tilgner, A. Tropospheric aqueous-phase free-radical chemistry: Radical sources, spectra, reaction kinetics and prediction tools. *Chem. Phys. Chem.* **2010**, *11*, 3796–3822. [CrossRef] [PubMed]
307. White, R.P.; Murray, S.; Rohweder, M. *Grassland Ecosystems*; World Research Institute: Washington, DC, USA, 2000.
308. Kang, S.; Nair, S.S.; Kline, K.L.; Nichols, J.A.; Wang, D.; Post, W.M.; Brandt, C.C.; Wullschleger, S.D.; Singh, N.; Wei, Y. Global simulation of bioenergy crop productivity: Analytical framework and case study for switchgrass. *GCB Bioenergy* **2014**, *6*, 14–25. [CrossRef]
309. Fan, P.; Hao, M.; Ding, F.; Jiang, D.; Dong, D. Quantifying Global Potential Marginal Land Resources for Switchgrass. *Energies* **2020**, *13*, 6197. [CrossRef]